

Technische Universität München  
Fakultät für Physik  
Institut für Festkörperphysik und Technische Physik E20

**Vibrational spectroscopy studies  
of clean and adsorbate-covered Si(100) surfaces:  
Surface phonon dispersions  
and adsorbate induced vibrations**

**Borislav Naydenov**

Vollständiger Abdruck der von der Fakultät für Physik der Technischen Universität München  
zur Erlangung des akademischen Grades eines

**Doktors der Naturwissenschaften**

genehmigten Dissertation.

Vorsitzender: Univ.-Prof. Dr. A. Groß  
Prüfer der Dissertation: 1. Univ.-Prof. Dr. W. Widdra, Technische Universität Berlin  
2. Univ.-Prof. Dr. R. L. Gross

Die Dissertation wurde am 18.07.02 bei der Technischen Universität München eingereicht und  
durch die Fakultät für Physik am 10.09.02 angenommen.

”Schwingungspektroskopische Untersuchungen von reinen und adsorbatbedeckten Si(100)-Oberflächen: Dispersion von Oberflächenphononen und Adsorbat-induzierte Schwingungen”.

Disertation

Institut für Festkörperphysik und Technische Physik E20,  
Fakultät für Physik,  
Technische Universität München.

To my Family



# Contents

<b>Introduction</b>	<b>7</b>
<b>1 Physical background</b>	<b>9</b>
1.1 Surface phonons . . . . .	9
1.2 Adsorbate related vibrations . . . . .	12
1.3 Electron scattering on surfaces . . . . .	13
1.3.1 High resolution electron energy loss spectroscopy (HREELS) . . . . .	14
1.3.2 Comparison of the vibrational spectroscopies . . . . .	17
1.4 Thermal desorption spectroscopy . . . . .	19
<b>2 Experiment</b>	<b>21</b>
2.1 UHV setting . . . . .	21
2.2 Sample holder and temperature control . . . . .	21
2.3 Gas dosing system . . . . .	24
2.4 HREEL spectrometer . . . . .	25
2.5 Quadrupole mass spectrometer and LEED device. . . . .	26
<b>3 The Si(100) surface</b>	<b>29</b>
3.1 The surface structure . . . . .	29
3.1.1 The nominally flat surface . . . . .	29
3.1.2 Vicinal surfaces . . . . .	31
3.2 Preparation, quality control and orientation . . . . .	33
3.3 Passivation of the Si(100)-(2×1) surface by atomic hydrogen(deuterium) . . . . .	39
3.3.1 Results . . . . .	40
3.3.2 Discussion . . . . .	45
<b>4 Surface phonons</b>	<b>51</b>
4.1 Overview . . . . .	51
4.2 Phonons on bare Si(100) surfaces . . . . .	53
4.3 Phonons on Si(100)-(2×1)-H(D) surfaces . . . . .	64
4.4 Summary . . . . .	73
<b>5 Benzene adsorption on Si(100) surfaces</b>	<b>77</b>
5.1 Benzene adsorption on a vicinal Si(100)-(2×1) surface . . . . .	78
5.2 Benzene adsorption on a nominally flat Si(100)-(2×1) surface . . . . .	88

5.3 Discussion . . . . .	94
<b>Summary and conclusions</b>	<b>103</b>
<b>Appendix A</b>	<b>107</b>
<b>List of Figures</b>	<b>111</b>
<b>List of Tables</b>	<b>115</b>
<b>References</b>	<b>117</b>
<b>Publications</b>	<b>129</b>
<b>Acknowledgements</b>	<b>131</b>

# Introduction

The physics of semiconductors, more precisely the conductivity modulation by doping, was first applied in the transistor invented at the end of the 1940s. This marked the birth of solid-state electronics which subsequently underwent a rapid evolution. Today silicon is the dominant semiconductor material because of its high mechanical stability as well as its good electric isolation and thermal conductivity. The importance of Si is best illustrated by the following quotations:

”Today, Si is used in about 95% of all electronic applications. They touch nearly all facets of our lives and culture. We can safely say that we are well into the Silicon Age”, H.C. Gatos 1994 [1],

”Silicon technology is expected to continue as the most powerful driver of the information age for at least the next 100 years”, An Electrochemical Society (ECS) Centennial Series Article, 2002 [2].

The invention of the transistor and the introduction of the planar technology at the beginning of the 1960s were the keys to a device minimization which constituted the microelectronics. Apart from dopants, it was found that the surface has a strong influence on the semiconductor device properties. The remarkable electronic and structural properties of semiconductor surfaces and interfaces result from the existence of surface and interface states, respectively [3]. Today’s state-of-the-art dynamic random access memories (DRAMs) have critical dimensions of 130 nm, and industry plans to deliver 22 nm (2016) [4]. The smallest feature size in the integrated circuits, namely the microprocessor transistor gate length, is projected to be  $\sim 9$  nm (2016) [4]. This size minimization leads to conversion of the device operation from the classical to the quantum regime where a microscopic approach is essential.

The quantum-mechanical many-particle approach to the rigorous treatment of a solid surface includes the investigation of the electronic and vibrational properties of the periodic arrangement of atoms. The atomic vibrations (phonons) are direct characteristics of the crystal dynamics. Similar to bulk phonons, the investigation of surface-localized phonon modes provides information of the bonding structure, the interatomic force constants, and the atomic geometry in the topmost layers. In analogy to the role of inelastic neutron scattering for bulk lattice dynamics, a progress in the inelastic surface scattering methods was made in the early 1980s by the development of high-resolution electron energy loss spectroscopy (HREELS) and helium atom scattering (HAS). Thus the experimental possibility for full characterization of the vibrational states of the surface becomes a stimulus and an ultimate check for the renewed theoretical approaches of the surface dynamics [5]. Semiconductor surface dynamics have been studied with increasing intensity during the last decade supported by the refinement of the

experimental techniques (HAS, HREELS), the advances achieved within the *ab initio* calculations based on a density-functional theory (DFT), and the availability of supercomputers [6]. Technologically, the most important silicon surface is the (100) oriented plane. Based on its low atom coordination and small unit cell (as described in chapter 3), it is also a model surface for fundamental theoretical and experimental investigations. Numerous theoretical studies of the vibrations on a Si(100) surface are available in the literature quoted in chapter 4. In contrast, as far as we know, only two experimental studies of the phonon dispersions on Si(100) have been performed [7, 8]. The first work was a Brillouin light scattering approach of the acoustic part of the surface vibrational modes [7]. The second work was a HREELS surface phonon investigation on a flat Si(001) surface with orientation providing access to an inseparable phonon dispersion mixture of the  $\overline{\Gamma\overline{J}}$  and  $\overline{\Gamma\overline{J}'}$  directions in the  $(2\times 1)$  surface Brillouin zone (SBZ) [8]. Our HREELS investigation of the phonon dispersions on bare and H(D) passivated, nominally flat and vicinal, Si(100) surfaces presented in chapter 4 is addressed to a detailed vibrational characterization of these surfaces covering all high-symmetry points of the  $(2\times 1)$  SBZ.

Many technologically important processes, like epitaxial layer growth, dopant incorporation, and the patterning of semiconductor surfaces by self assembly, proceed through semiconductor surface reactions. This has important implications for the structural and electronic properties and reveals the key role of specific surface sites and local response to adsorbate species [9]. A portion of the wide range of investigation on the important Si(100) surface concerns its chemical reaction with organic molecules which is a basis for new technological opportunities in microelectronics. The studies of this organic-inorganic system may provide possibilities to bond a wide range of useful organic molecules directly on the dangling bonds of the surface [10]. As a prototype for understanding the aromatic hydrocarbon adsorption on semiconductor surfaces, benzene adsorption on a Si(100) surface has attracted considerable scientific interest in the last ten years. Despite of the various theoretical and experimental approaches reviewed in the introduction of chapter 5 the structure of the benzene phases on a real Si(100) surface remains under debate. The present TPD and HREELS study is directed to characterize the chemisorption phases of benzene on vicinal and nominally flat Si(100)- $(2\times 1)$  surfaces and is presented in chapter 5.

A short overview of the physics underlying the phenomena involved in the present work is given in chapter 1. The experimental layout is depicted in chapter 2. A description of the Si(100) surface together with the surface preparation and quality control, is made in chapter 3. In the latter chapter experimental data for surfaces passivated by atomic hydrogen(deuterium) are also included.

# Chapter 1

## Physical background

Since all real solids have boundaries the surface effects belong to the fundamental scientific subjects. In its simplest sense the surface is the outermost atom layer of a semi-infinite solid. As far as our considerations in the following will be restricted to a single crystal, the surface can be expressed as a plane where the three-dimensional periodicity is reduced to a two-dimensional one. However, surfaces are complex and their characterization requires consideration of the atoms in the layers below the surface, i.e. the whole region where the geometrical, chemical, electronic and vibrational properties differ from those of the bulk. Thus the surface analysis embraces depths of about 1 nm and up to a few adsorbed monolayers. These analysis provide detailed information on the chemical binding states, the precise geometric positions of the atoms in relation to the crystal structure, the surface homogeneity and the state of adsorbates. Thus in the last decades surface science has removed the frontier between chemistry and physics and lead to strong interrelations between the theoretical and experimental investigations.

### 1.1 Surface phonons

The phonon is the quantum unit of a crystal vibration with energy  $\hbar\omega$ . For a periodic crystal all vibrations can be described by wave vectors ( $\mathbf{k}$ ) that lie within the first Brillouin zone in reciprocal space

$$-\frac{\pi}{a} < k \leq \frac{\pi}{a} \quad (1.1.1)$$

where  $a$  is the lattice constant. The phonons are divided into acoustic, whose frequency varies linearly with the wave-vector at small  $\mathbf{k}$ , and optic, whose frequency remains finite as  $\mathbf{k}$  approaches zero.

The surface phonon is a vibrational excitation of the crystal atoms whose displacement amplitudes nearly exponentially decrease from the surface to the bulk. The surface phonon determination provides knowledge of the atomic geometry, bonding structure and interatomic force constants in the topmost layers. Thus the investigation of the surface vibrational excitations essentially contributes to a better understanding of the surface nature.

The vibrational modes can be classified with respect to their polarization and the square of the amplitudes in the different crystal layers. Moving away from the surface into the substrate, the bulk modes do not change significantly the atom amplitudes, while the atom amplitudes

associated with true surface modes decrease essentially exponentially. The frequencies of the latter appear in the gaps of the bulk modes projection into the phonon dispersion plots of the two-dimensional surface Brillouin zone or in the bulk frequency region as long as the surface mode eigenvector has a symmetry different from the eigenvector of the nearby bulk phonons. For phonon resonances the amplitudes do not decay as they approach the layers into the bulk. They, however, exhibit larger amplitudes in the surface region with frequencies located in the bulk continuum.

If the parallel component of the phonon wave-vector is oriented along a high-symmetry direction of the crystal, the polarization of the mode is either strictly sagittal (SP) with non-vanishing components of the eigenvector only in the sagittal plane, defined by the surface normal and the wave-vector, or shear horizontal (SH) with all atoms moving exclusively perpendicularly to that sagittal plane. The sagittal modes are coherent mixtures of two polarizations, namely transverse (which is normal to the surface) and longitudinal which is perpendicular to the surface normal. For non-high-symmetry directions the sagittal and shear horizontal polarizations are mixed in general. Based on the fact that the surface atoms have less neighboring bonding partners, the effective force constants are generally softened in the outermost layers and thus the surface vibrations appear at lower frequencies compared to the bulk modes from which they originate. Due to surface relaxation or reconstruction, the effective force constants of the near-surface atoms can be increased and localized modes frequencies can appear above the bulk phonon continuum.

The problem of surface vibrational excitations on a crystal solid was first investigated by Lord Rayleigh in 1887. Till the 1960s not many theoretical studies of that problem were developed in contrast to the studies of bulk vibrational excitations. In the last few decades due to the appearance of new experimental techniques for surface phonon investigations (subsection 1.3.2) and the availability of super-computers, a great increase of the theoretical effort in the field of surface vibrations has been made. In the beginning the focus was on ionic and metal crystals but in the last decade the theory became able to comprise also the more complicated case of semiconductors. The covalent nature (directed bonds) of the semiconductors requires to include in the theoretical investigations three-body interactions that comprise bond-angle deformations over a wide range. Moreover, the surface unsaturated bonds cause substantial changes in the atomic equilibrium positions which allow the energy of the electronic system and the surface to decrease. As a result characteristic electronic states and vibrational modes occur, which are closely related to the relaxed or reconstructed surface. With the exception of some macroscopic excitations like the Rayleigh (acoustic) and the Fuchs-Kliwer (optical) modes, most of the surface vibrations cannot be explained with the continuum theory and are only accessible by means of a microscopic examination. A comprehensive introduction and a more detailed illustration of the progress in the computation of surface phonons is given in a series of reviews, including those of Maradudin [11], Kress and de Wette [5], Desjonquères and Spanjaard [12], Wallis and Tong [13], Fritsch and Schröder [6]. Here I will present only a short survey of the theoretical methods based on the above-cited authors.

To describe the surface dynamics one must solve the equation of motion. Since the electron mass is much smaller compared to the atomic mass, the electrons are assumed to follow

instantaneously the motion of the atoms. The adiabatic potential as a function of the atomic position determines the vibrational properties of the crystal and can be represented by a sum of an electronic part and a pure ionic contribution:

$$V_{ad}(\{\mathbf{R}'_{\bar{l}\alpha}\}) = V_{ion}(\{\mathbf{R}'_{\bar{l}\alpha}\}) + E_{el}(\{\mathbf{R}'_{\bar{l}\alpha}\}) \quad (1.1.2)$$

where the time dependent position of the atom is

$$\mathbf{R}'_{\bar{l}\alpha} = \mathbf{R}_{\bar{l}\alpha} + \mathbf{u}_{\bar{l}\alpha}(t) \quad (1.1.3)$$

and  $\mathbf{u}_{\bar{l}\alpha}(t)$  is the displacement from the equilibrium position  $\mathbf{R}_{\bar{l}\alpha}$  of the  $\alpha$ th atom in the  $\bar{l}$ th unit cell. The concept of a small atomic displacements from the equilibrium positions  $\mathbf{R}_{\bar{l}\alpha}$  makes the first order terms of the adiabatic potential series over the displacement to vanish. The second order derivatives of the potential define the harmonic force constants.

The slab model examines a finite number of infinite layers. The translational symmetry parallel to the surface is preserved and solutions in the Bloch form are substituted in the equation of motion. In the resulting equation the force constants enter in a dynamical matrix. Diagonalization of this matrix yields vibrational eigenstates. For  $n$  atoms in the slab unit cell the dynamic matrix has dimensions  $(3n \times 3n)$ . Diagonalization of this matrix for each wavevector  $\bar{\mathbf{q}}$  in the SBZ yields  $3n$  real and non-negative eigenvalues  $\omega^2(\bar{\mathbf{q}})$  corresponding to  $3n$  eigenvectors, i.e.  $3n$  normal modes. Only a small number of these modes are related to localized and resonance vibrations; most are bulk branches with density depending on the number of slab layers.

Green's function approach treats the surface as a two-dimensional perturbation of an ideal crystal, thus allowing one to determine the surface vibrations of a semi-infinite system. This method permits easier and more precise identification of deeply penetrating and resonant phonon modes.

Molecular-dynamics simulations extract the dynamical properties of the surface from finite-temperature particle trajectories which are computed for a sufficiently large period of time by solving the equation of motion for all atoms in the slab. Temperature effects and anharmonicity are directly accessible within this method. The method has limited frequency resolution and weakly excited modes can remain hidden. A significant improvement is the self-consistent multiple signal-classification method in which the separation of the received data into signal and noise subspaces is used.

In order to achieve a rigorous treatment of the electronic and vibrational properties of the semiconductors, the quantum-mechanical many-particle problem including all electrons and nuclei has to be solved by minimizing the total energy of the system with respect to the electronic and atomic coordinates. In general this problem is too complicated to be solved, hence, simplifications and approximations are necessary to reduce the complexity and then use efficient numerical methods. The adiabatic approximation reduces the many-particle problem to determination of the electronic ground-state for a given and fixed atomic configuration. Further in the pseudopotential approach, the electronic system is divided into chemically active (valence) electrons and inert (core) electrons. The latter together with the nuclei form the ionic cores. Then the density-functional theory (DFT) is built where the electronic energy is expressed as a functional of the single-particle density which is minimal at the ground-state

density. The construction of the energy functional is done assuming noninteracting electrons in an effective potential. Additional simplifications like the local density approximation (LDA) exists for determination of the effective potential [6]. In the end the electronic eigenstates have to be determined by solving the Kohn-Sham equations.

To determine the vibrational excitations in the framework of the density-functional theory one should treat both, the ion and electron systems. If the adiabatic approximation is not valid, couplings between phonons and electron excitations are possible giving rise to the so-called Kohn anomalies. Currently, in the adiabatic case three methods are mainly used, namely molecular-dynamics simulations, the frozen-phonon technique, and the linear-response formalism [14].

All above-mentioned theoretical methods of surface dynamics treatment have their advantages and restrictions. The choice of one of them is very case-specific and a comparison between the results of different calculations is required. However, the major criterion for the theoretical result's accuracy is the experiment.

## 1.2 Adsorbate related vibrations

The presence of an adsorbate on a crystal surface influences the surface phonon spectrum by modifying the interactions between the substrate atoms which can as well lead to surface reconstruction. The altered interatomic forces can change the frequency of the substrate modes or induce spill-out of modes off the bulk bands. Also new modes will appear because of the extra degree of freedom connected with the motion of the adatoms or of the admolecules. For example, hindered translations and rotations appear, which are not present in the gas phase of the adsorbate. If the adparticles interact with each other, either directly or via the substrate, their vibrations will disperse with the parallel wave vector. The adsorbate modes may lie in the frequency domain of the substrate and hybridise with modes of the same symmetry. When the hybridisation involves bulk modes, the adsorbate vibrations become resonances and their energies leak into the crystal, giving rise to a finite linewidth. Moreover, new surface bands can be generated if the adsorbate induces higher-order symmetry resulting in a surface Brillouin zone backfolding .

The adsorbate-substrate systems can be divided into two classes with respect to the preservation of the periodicity parallel to the interface. In the first class which is characterized by missing periodicity, can be collected the cases of single adparticle and adlayers forming lattices that are incommensurate with the substrate. The lattice mismatch gives rise to the problem of coupling the phonons of two different periodic lattices through the non-periodic interface. The investigation of this problem is difficult from the theoretical as well as from the experimental point of view. The low-coverage limit and high-frequency mode investigation could be comprised by use of the single adparticle approach and it is widely used in calculations with relatively big success. The straight approach is to use group theory which gives correlation tables for the reduction of the gas phase symmetries after adsorption on the surface, where the mirror plane parallel to the surface is in principle broken. Thus, from the experimental spectra it is possible to determine the orientation and symmetry of the adsorbed molecule. In the framework of isolated adparticles the full theoretical description of the vibrational properties

of the adsorbate-substrate system is built by determination of the eigenvalues and eigenvectors, solving the Schrödinger equation. For the equilibrium geometry defined by total potential energy minimization in the adiabatic approximation the central issue is to analyze the normal modes of the vibrational Hamiltonian:

$$\mathcal{H} = \mathcal{H}_M + \mathcal{H}_S + V \quad (1.2.4)$$

where  $\mathcal{H}_M$  is the vibrational Hamiltonian of the adsorbate,  $\mathcal{H}_S$  that of the substrate, and  $V$ -the coupling terms between the adsorbate and the substrate. In the limits of the harmonic approximation for adsorbed molecule with  $N$  atoms on a substrate of  $N_S$  atoms, one has to diagonalize the dynamic matrix with size  $3(N + N_S) \times 3(N + N_S)$ , which in the case of a macroscopic crystal is impossible. Consequently, simple models and approximations have to be involved. The finite cluster model gives good results for vibrational modes with frequencies above the substrate phonon branches, but for frequencies below the maximal substrate frequency slab or semi-infinite crystal models must be introduced.

The second class, which includes adlayer lattices matching those of the substrate, represents a natural extension of the surface dynamics problem of a crystal with surface layer containing atoms different from the bulk. Hence, the theoretical methods used for a clean surface can be applied also for these adsorbate-substrate systems ( see sec. 1.1).

The vibrational properties of the crystal surface in the presence of adsorbates have been reported in a number of articles and reviews, among them are the works of Ibach and Mills [15], Alldredge, Allen and de Wette [16], Li, Tong and Mills [17], and Rozenbaum and Lin [18]. A broad current data collection can be found in the review of Rocca [19].

### 1.3 Electron scattering on surfaces

If one considers the interaction of an electron from vacuum with a semi-infinite rigid crystal lattice, then the elastic scattered electrons undergo diffraction. The diffraction spot positions reflect the symmetry and geometric arrangement of near surface atoms. This is the basis of the low-energy electron diffraction (LEED) measurements [20, 21, 22] with a layout described in section 2.5 of the present work. In the framework of the kinematic theory the condition for a Bragg spot appearance is given by equation 1.3.6, which connects the scattering vector components parallel to the surface with the two dimensional reciprocal lattice vector  $\mathbf{G}_{\parallel}$ . Thus the Erwald construction reduced to the two-dimensional case, together with the LEED spot positions, provides a method for  $\mathbf{G}_{\parallel}$  determination. Then the surface unit cell vectors can be obtained by reciprocal to real space conversion. LEED patterns can be used to find a superstructure formed on a reconstructed bare or adsorbate-covered surface. Information about crystallographic defects such as a regular array of atomic steps or faceting can also be obtained. Through observation of the spot sharpness and background intensity LEED is used for checking the crystallographic quality of the surface. As a standard tool, the LEED is present in almost every surface physics laboratory.

If the effect of the presence of lattice vibrations is considered, the intensity of the Bragg beam is reduced by a Debye-Waller factor because the electron near the surface may emit or

absorb one or more phonons. Since in the latter case wave vector components parallel to the surface are conserved to within a reciprocal lattice vector  $\mathbf{G}_{\parallel}$ , the electron is deflected away from one of the Bragg directions. This inelastic electron scattering is the basis of the high resolution electron energy loss spectroscopy (HREELS). Its layout is given in section 2.4, while here we will in short describe the theory of inelastic electron scattering mechanisms.

### 1.3.1 High resolution electron energy loss spectroscopy (HREELS)

Electron energy loss spectroscopy is a technique in which the vibrational motions of atoms and molecules on and near the surface are studied through the analysis of the energy spectrum of low-energy electrons backscattered from the surface. The base relation is  $E_s = E_i - \hbar\omega$  where  $E_i$  and  $E_s$  are the energies of the incident and backscattered electron and  $\hbar\omega$  is the energy of a surface excitation. In the usual incident electron energy region (2–250 eV) the penetration depth is approximately several atomic layers [21], which in the short range regime provides the technique with information only of the very surface volume. In the long range scattering regime (up to 1000 Å) information from interfaces can also be obtained. Detailed information about the chemical bounding and geometry of the bare and adsorbate-covered surface can be extracted from the electron energy loss spectra. To extract this information one must be able to prepare and analyze a well-defined monoenergetic electron beam (see section 2.4). Also, a detailed knowledge of the interaction of the electron with the surface is required. For facilitation of theoretical calculations, as well as for experimental interpretations, the problem of the inelastic scattering of electrons by excitations in the crystal is artificially divided into two parts. The electron may be scattered inelastically from the long-range electric field fluctuations present in the vacuum outside the crystal, or it may be also scattered inelastically while it is near or inside the crystal where it interacts directly with the ion cores and electron distribution of the crystal. The long-range interaction of the electron with the vibrating substrate is a dipole scattering. The short-range interactions are split into scattering via an intermediate negative ion resonance and impact scattering from a vibrating entity [15]. In the dipole dominated regime, the cross section of scattering may be accurately described by a phenomenological theory, while in the impact dominated regime a fully microscopic approach is required.

The scattering via a negative ion resonance is well observed in gas phase experiments [23]. Resonances are also observed on surfaces, but mainly for physisorbed molecule layers [24, 25]. For the chemisorbed molecules, with some exceptions [26], the resonances are quenched by strong coupling of the negative ion state with the surface. Therefore, the case of scattering via a negative ion resonance will be omitted in this work.

#### The dipole scattering regime:

We construct the  $xy$  plane to be parallel to the surface, with the sample in the half space  $z < 0$  and vacuum above. With subscript  $\parallel$  we will denote the vectors that lie in the  $xy$  plane. We consider an incident electron with wave vector  $\mathbf{k}^{(I)}$  that scatters to a final state with wave vector  $\mathbf{k}^{(S)}$  and we introduce a vector  $\mathbf{Q}_{\parallel} = \mathbf{k}^{(I)\parallel} - \mathbf{k}^{(S)\parallel}$ . Retardation effects are ignored if the relation  $\omega_o/Q_{\parallel} \ll c$  is satisfied with  $c$  (the velocity of light) and  $\omega_o$  (the frequency of the considered vibration). For a given value of  $\mathbf{Q}_{\parallel}$  and energy transfer  $\hbar\omega = E_I - E_S$ , the direction of the outgoing electron is uniquely determined. Because the potential must obey Laplace's

equation in the vacuum above the crystal, it extends into a distance roughly equal to  $Q_{\parallel}^{-1}$ . This is the long-range interaction at small scattering angles. An important consequence is that the maximal efficiency takes place at an angle of  $\hbar\omega_o/2E_I$  which in the normal experiment condition  $\hbar\omega_o \ll E_i$  peaks the maximum near the specular direction, the so-called dipolar lobe in the angular distribution. It is also possible to deduce that the potential is produced by charge fluctuations which extend down to a distance approximately equal to  $Q_{\parallel}^{-1}$ , i.e. the electron scattering with change of the parallel components of its wave vector by the amount  $\mathbf{Q}_{\parallel}$  is probing down the medium roughly the distance  $Q_{\parallel}^{-1}$ .

The next step is to insert the potential  $\varphi_1(\mathbf{x}, t)$  into the Schrödinger equation and use the perturbation theory to calculate the scattering cross section. In the small-angle regime two scattering processes, both involving only one specular reflection from the surface, are dominant and are retained in the probability amplitude for scattering [15]. A convenient resulting quantity is the scattering efficiency  $d^2S/d\Omega(\hat{k}_S)d\hbar\omega$ . The combination  $(d^2S/d\Omega(\hat{k}_S)d\hbar\omega)d\Omega(\hat{k}_S)d\hbar\omega$  is dimensionless and gives the probability that an electron will scatter from its initial state into a final state in the solid angle  $d\Omega(\hat{k}_S)$ , and in the energy range  $d\hbar\omega$ . If in the small angle inelastic electron scattering from surfaces the energy transfer  $\hbar\omega$  is a small fraction of the incident energy  $E_I$ , for the scattering efficiency we have [15]

$$\frac{d^2S}{d\Omega(\hat{k}_S)d\hbar\omega} = \frac{2m^2e^2v_{\perp}^4}{\pi\hbar^5\cos(\theta_I)} \left(\frac{k_S}{k_I}\right) \frac{|R_I|^2P(\mathbf{Q}_{\parallel}, \omega)}{[v_{\perp}^2\mathbf{Q}_{\parallel}^2 + (\omega - \mathbf{v}_{\parallel} \cdot \mathbf{Q}_{\parallel})^2]^2}, \quad (1.3.5)$$

where  $\theta_i$  is the incidence angle with respect to the surface normal,  $v_{\perp}$  is the magnitude of the normal component of the incoming electron velocity,  $\mathbf{v}_{\parallel}$  is the parallel velocity and  $|R_I|^2$  is the intensity of the specularly reflected, elastic beam normalized to the incident intensity. All factors which enter in Eq.(1.3.5), except  $P(\mathbf{Q}_{\parallel}, \omega)$ , are fully determined by either the scattering geometry or are directly measurable. Thus in the limits of dipole scattering the consideration is reduced to obtain the form of  $P(\mathbf{Q}_{\parallel}, \omega)$  which contains the fluctuations of the charge density  $\rho_1(\mathbf{x}_{\parallel}z, t)$  in the surface region. To obtain this form one must turn to a model description of the surface. One approach is to relate  $P(\mathbf{Q}_{\parallel}, \omega)$  to the dielectric properties of the substrate, considering a semi-infinite substrate with a complex, but isotropic dielectric constant  $\varepsilon_b(\omega)$ . With appropriate choice of  $\varepsilon_b(\omega)$  one may discuss scattering from a metal or semiconductor with free carriers present, or from an insulator, where interband electronic transitions are dominating in the dielectric constant. If in the model a surface layer of thickness  $d$  and dielectric constant  $\varepsilon_s(\omega)$  is added, one may describe a layer of adsorbate molecules, or one may model a semiconductor with a depletion or accumulation layer near the surface. A general expression of the dipole scattering efficiency dependence on the dielectric constant is obtained by Ibach and Mills, page 75 at al.[15]. In this book a detailed discussion of the above-mentioned cases by the dielectric approach is given. An important consequence is that the excitation cross section decreases as the impact energy  $E_I$  increases. Also, the cross section is proportional to the intensity of the specular beam, which permits data normalization and comparison.

Finally the dipole selection rule can be formulated. It states that only vibrational modes with symmetry that generates an oscillating electric dipole moment with non-zero components perpendicular to the surface, namely totally symmetric modes, will produce small-angle scattering peaked around the specular direction, confined within the angular range  $\hbar\omega_o/2E_I$ .

### The impact scattering regime:

The description of the impact scattering of electrons from the surface requires a microscopic approach. Hence, one must consider the atomic structure of the crystal by the position vectors  $\{\mathbf{R}\}$  of the nuclei. In the quantum-mechanics scattering theory, the basic quantity is the scattering amplitude  $f(\mathbf{k}^{(S)}, \mathbf{k}^{(I)}, \{\mathbf{R}\})$  that describes the amplitude of the wave that radiates outward from the scattering center. If the semi-infinite substrate is perfectly periodic with frozen atoms, we have only Bragg scattering with  $E_I = E_S$  and nonzero amplitude when

$$\mathbf{k}_{\parallel}^{(S)} = \mathbf{k}_{\parallel}^{(I)} + \mathbf{G}_{\parallel}, \quad (1.3.6)$$

where  $\mathbf{G}_{\parallel}$  is the reciprocal lattice vector associated with a two-dimensional surface unit cell. One can consider the atomic vibrations by assuming that the incoming electron finds a disordered structure described by the position vector  $\mathbf{R}_i = \mathbf{R}_i^{(0)} + \mathbf{u}_i$ , where  $\mathbf{R}_i^{(0)}$  is the vector to the equilibrium site and  $\mathbf{u}_i$  is the displacement from this site. Thus a certain fraction of the electron beam is scattered away from the Bragg directions, emerging with energy  $E_S = E_I \pm \hbar\omega_s$ , where  $\omega_s$  is the frequency of the emitted or absorbed vibrational quantum with wave vector

$$\mathbf{Q}_{\parallel} = \mathbf{k}_{\parallel}^{(S)} - \mathbf{k}_{\parallel}^{(I)} - \mathbf{G}_{\parallel}, \quad (1.3.7)$$

which is the momentum conservation in the periodic plane parallel to the surface. The subtraction of the reciprocal lattice vector  $\mathbf{G}_{\parallel}$  brings, if necessary, the product  $\mathbf{k}_{\parallel}^{(S)} - \mathbf{k}_{\parallel}^{(I)}$  into the first Brillouin zone. The probability that a vibrational quantum ( $\mathbf{Q}_{\parallel}\alpha$ ) scatters the electron in a solid angle  $d\Omega$  from a surface area  $A$  is [15] :

$$\frac{dS_{\alpha}(\mathbf{k}^{(I)}, \mathbf{k}^{(S)})}{d\Omega} = \frac{mE_I \cos \theta_S}{2\pi^2 \hbar^2 \cos \theta_I} A |M(\mathbf{k}^{(I)}, \mathbf{k}^{(S)}; \mathbf{Q}_{\parallel}\alpha)|^2. \quad (1.3.8)$$

In case of emitted phonons and small displacement we have for the matrix element

$$M(\mathbf{k}^{(I)}, \mathbf{k}^{(S)}; +s) = (n_s + 1)^{1/2} \left( \frac{\hbar}{2N\omega_s} \right)^{1/2} \left( \frac{\partial f}{\partial \mathbf{Q}_s} \right), \quad (1.3.9)$$

where

$$\left( \frac{\partial f}{\partial \mathbf{Q}_s} \right) = \sum_{i\alpha} \left( \frac{\partial f}{\partial R_{i\alpha}} \right)_0 \frac{\xi_{i\alpha}^{(s)}}{\sqrt{M_i}}, \quad (1.3.10)$$

$N$  is the number of unit cells,  $n_s$  the number of present vibrational quanta, and  $\xi_{i\alpha}^{(s)}$  denotes the amplitude of the displacement of nucleus  $i$  in Cartesian direction  $\alpha$ . From the lattice theory of the surface region one can obtain the vibrational frequencies  $\omega_s$  and the eigenvectors  $\xi_{i\alpha}^{(s)}$ , then one must calculate the derivatives  $(\partial f / \partial R_{i\alpha})_0$  of the scattering amplitude with atomic displacement. The latter requires a detailed theory of how the electron interacts with the atoms of the crystal, when they are displaced from their equilibrium positions by vibrations. Models which provide opportunity for calculation of the eigenvectors  $\xi_{i\alpha}^{(s)}$  as well as the energy and angular variations of the impact scattering cross section have been developed. One of these approaches is the muffin tin model developed by Li, Tong and Mills *et al.* [17]. This model is constructed by a spherical potential surrounding the nuclei and a constant potential between the lattice sites. The electric dipole moment generation and screening is neglected, which

makes this model incompatible with dipole scattering. The scattering amplitude derivatives are expressed by the following [17]:

$$\left(\frac{\partial f}{\partial \mathbf{Q}_s}\right) = \left\langle \mathbf{k}^{(S)} \left| \underbrace{(G + GT_0G)}_{g_{PE}^{(F)}} \frac{\partial V(\{\mathbf{R}\})}{\partial R_{i\alpha}} \underbrace{(1 + GT_0)}_{|\psi_{LEED}^{(I)}\rangle} \right| \mathbf{k}^{(I)} \right\rangle, \quad (1.3.11)$$

where  $|\mathbf{k}^{(I)}\rangle$  and  $|\mathbf{k}^{(S)}\rangle$  are the plane waves of the incoming and outgoing electrons with respect to the crystal,  $G$  is the Green's free space function for the electron,  $T_0$  is the  $t$  matrix for multiple scattering with nuclei in equilibrium positions. The notation  $g_{PE}^{(F)}$  of the underbraced terms is Green's function describing the emitted electron in the theory of photoemission, while the notation  $|\psi_{LEED}^{(I)}\rangle$  is the wave function encountered in the theory of low-energy electron diffraction. In the model considered all quantities in Eq.(1.3.11) may be expressed in terms of certain matrix elements of  $G$ , the phase shift for scattering off the spherical potentials, and the radial solution of Schrödinger's equation within the muffin tin which contains the displaced nucleus [17]. From these model calculations of the scattering efficiency some characteristics of the impact regime can be extracted. The scattering cross section, in contrast to the dipole regime, is no longer proportional to the intensity of the specular beam, and normalization to this intensity is not possible. Also, the total excitation efficiency increases as the electron impact energy increases. Hence, it is more favorable to study large-angle inelastic electron scattering at impact energies substantially larger than those used in small-angle scattering. Additionally, the scattering cross section variation with the impact energy has structures sensitive to the surface geometry and thus the energy dependency studies are a source of information on the surface structure.

A selection rule for the impact scattering can be obtained using symmetry and time-reversal invariance [17]. The statement is that the scattering amplitude vanishes for electrons scattered in the sagittal plane by vibrational modes with polarization odd to this plane. Also the impact scattering amplitude vanishes along the specular direction for modes with polarization odd to the plane perpendicular to the sagittal [15, 17]. The sagittal plane is the plane defined from the phonon wave vector and the surface normal.

### 1.3.2 Comparison of the vibrational spectroscopies

The existing vibrational spectroscopies are divided into optical and particle scattering techniques [12]. The optical methods include infrared absorption spectroscopy (IRAS) and Raman spectroscopy (RS). The particle scattering methods are Helium atom scattering (HAS), high-resolution electron energy loss spectroscopy (HREELS) and neutron scattering. The most important characteristics of the above-mentioned methods which have been applied for surface investigations, are summarized [12, 27, 15, 5] in Table 1.1. It is obvious that the major disadvantage of the electron spectroscopy is the low resolution in comparison with the other techniques, but it is comparable with the typical intrinsic width of surface vibrations ( $\sim 10\text{cm}^{-1}$ ). In many cases this problem can be overcome by exploring the large impact energy range for cross section modulation of modes with adjacent frequencies, which are inseparable with the resolution. The most prominent advantage of the HREELS is that it can examine, with constant resolution, the

Method acronym	RS	IRAS	HAS	HREELS
Primary beam	photons	photons	He atoms	electrons
Resolution	$1 - 5 \text{ cm}^{-1}$	$1 - 5 \text{ cm}^{-1}$	$1.6 \text{ cm}^{-1}$	$7 - 20 \text{ cm}^{-1}$
Examined frequency range	no limits	min. limit $600 \text{ cm}^{-1}$	achieved max. $480 \text{ cm}^{-1}$	no limits
Primary beam energy	$20 - 100 \text{ meV}$	$20 - 600 \text{ meV}$	$20 - 60 \text{ meV}$	$2 - 250 \text{ eV}$
Probing sample depth	surface + bulk volume	surface + bulk volume	deflection above the surface	imp.scatt. $0.7 - 20 \text{ \AA}$
Measurable phonon dispersion	only the $\Gamma$ point	only the $\Gamma$ point	the whole SBZ	the whole SBZ
Accessible vibrational modes	Raman active	only the dipole active modes	all modes	all modes
Data interpretation	complex	simple	simple	middle
Operating pressure	$\leq 1 \text{ atm}$	$\leq 1 \text{ atm}$	$\leq 10^{-7} \text{ mbar}$	$\leq 10^{-6} \text{ mbar}$

Table 1.1: Characteristics of the available vibrational spectroscopies for surface analysis.

entire frequency region, where surface and adsorbate vibrations can appear. From one spectrum it is possible to analyze single mode positions, coupling effects, overtones and multiphonon losses. Additionally, based on the two operating scattering mechanisms, all vibrational modes of the investigated surface region are accessible. The impact scattering regime probes only the surface region and varying the incidence electron energy and surface azimuthal orientation all  $\mathbf{k}$ -points of the SBZ are approachable. The dipole scattering regime additionally allows one to investigate buried interfaces.

Thus the analysis of the characteristics in Tab. 1.1 makes it possible to conclude that HREELS is a universal method for vibrational investigation of the surface region under UHV conditions. With this method it is possible to study clean and adsorbate-covered metal and semiconductor single crystals.

## 1.4 Thermal desorption spectroscopy

The interaction between a gas and a solid is electromagnetic in nature. Thus the adsorption phenomena can be deduced by comparison of the ionization energy  $E_I$  and the electron affinity level  $E_A$  of the free atom or molecule with the electronic structure of the substrate [28]. When the electrons of the particle interact with those of the solid forming a chemical bond, we have chemisorption. If  $E_A$  is very small or even negative and  $E_I$  is large compared to the work function of the surface, the electronic configuration of the adsorbate is slightly changed to the extent of an overall polarization. In this case the adsorption can be modeled by an attractive van der Waals type potential and we have physisorption. In the adsorption process on semiconductors, the chemisorption is usually restricted to the monolayer where all "dangling" bonds of the surface can be used, then additional particles can be subject to physisorption or condensation.

The characterization of an adsorbate-substrate system is provided by investigation of the equilibrium state and the adsorption-desorption kinetics. In various experimental techniques (HREELS, LEED) the system is in equilibrium and the kinetic parameters are not accessible. To assess the kinetics a time dependent non-equilibrium processes must be examined. One of the most frequently used experimental method for kinetic measurements is thermal desorption [29, 30, 22]. In this method the energy necessary to desorb a particle from the adsorbate comes from the solid as thermal energy. The thermal desorption can be analyzed as a chemical reaction by using the Polanyi-Wigner equation for the desorption rate

$$R_d = \dot{\Theta} = -\frac{d\Theta}{dt} = \Theta^n \nu_n \exp\left(-\frac{E_a}{RT}\right), \quad (1.4.12)$$

where  $\Theta$  is the adsorbate coverage,  $\nu$  the pre-exponential factor (to first order equal to the frequency of attempts of the system to move in the reaction direction), the exponential term represents the relative number of these attempts having the necessary minimum energy,  $E_a$  the activation energy, and  $n$  the order of the reaction interpreted as indication of the rate-determining elementary step mechanism. The concept of the desorption order has limited meaning because in principle  $\nu$  and  $E_a$  are coverage-dependent. The different orders of the desorption process could be illustrated with simple models as follows: a zero order desorption is present, when condensation occurs, a fractional order is related to a reaction on adsorbate cluster edges [31], a first order arises from independent single particles. If two equal mobile atoms desorb by recombination and the latter step is rate-determining, the reaction is of the second order.

The goal of thermal desorption studies is to determine the kinetic parameters  $n$ ,  $\nu$ , and  $E_a$  by using the Polanyi-Wigner equation 1.4.12. There are a variety of procedures which can be divided into two groups [32]. The first group contains the integral approach, based on the fundamental contribution of Redhead [33] which relates the kinetic parameters to the peak shape and peak maximum position. The integral method can be applied if the parameters are coverage-independent, where also a correlation between the number of peaks and adsorbate sites exists. The second group consists of differential methods involving construction of Arrhenius

plot of  $\ln(-\dot{\Theta}/\Theta^n)$  vs  $1/T$  based on a presentation of Eq. 1.4.12 in a form

$$\frac{d\ln(-\dot{\Theta}/\Theta^n)}{d(1/T)} = \frac{-E_a(\Theta)}{R} + \frac{d\Theta}{d(1/T)} \times \left[ \frac{\partial \ln \nu(\Theta)}{\partial \Theta} - \frac{1}{RT} \frac{\partial E_a(\Theta)}{\partial \Theta} \right]_T. \quad (1.4.13)$$

The slope of the plot, in the general case, contains derivatives of  $E_a(\Theta)$  and  $\nu(\Theta)$  with respect to  $\Theta$ . Since in simple experiments it is impossible to evaluate the derivatives, the Arrhenius plot should be applied only in cases where these terms may be legitimately ignored. The latter is obeyed in three cases. The first is when  $E_a$  and  $\nu$  are constants and Eq.1.4.13 is reduced to

$$\ln(-\dot{\Theta}/\Theta^n) = \ln \nu - \frac{E_a}{RT}, \quad (1.4.14)$$

The slope of the  $\ln(-\dot{\Theta}/\Theta^n)$  vs  $1/T$  plot gives directly  $E_a$  and its intercept gives  $\nu$ . The second case is the procedure proposed by Habenschaden and Küppers *et al.* [34] in which  $d\Theta/d(1/T)$  may be vanishingly small at the onset of the desorption, where the initial coverage  $\Theta_o$  drops only by a few percent. Hence, by varying the initial coverage,  $E_a(\Theta_o)$  and  $\nu(\Theta_o)$  can be evaluated for the entire coverage range. The third case is when, in a given coverage range, a compensation effect occurs manifested by such a variation of  $E_a$  and  $\nu$  with  $\Theta$  that the sum of the derivatives in Eq.1.4.13 becomes zero.

Apart from the determination of the main kinetic parameters  $n$ ,  $E_a$ , and  $\nu$ , an important stationary property is the total relative adsorbate coverage determined by the rate integral over the time or over the temperature as in the temperature programmable desorption. In modern UHV systems with large pumping speed and when the heating rates are not too large, the pressure rise ( $\Delta P$ ) over the background is proportional to the desorption rate [29]. Thus, the thermal desorption experiments are relatively simple and well established. The layout of the experiment is presented in section 2.5.

# Chapter 2

## Experiment

Surface science deals with investigations of atomically clean surfaces or surfaces covered with up to several adsorbate layers. This demands stringent requirements for the experimental layout and performance. For instance, the pressure in which the surface area will be covered by a monolayer in one hour is in the range of  $10^{-10}$  mbar. Ultrahigh vacuum is thus essential. Additionally, the investigation techniques using free particles must operate in conditions where their mean free path in the gas phase is in the metric range. Owing to the surface science and vacuum techniques development in the last decades, the larger part of the basic experimental preparation is routine work, but still a lot of details should be developed in each specific case. In this chapter the specific details of our experimental layout will be presented.

### 2.1 UHV setting

Our experiments were performed in a two-chamber ultrahigh vacuum system (Fig. 2.1). The chambers are vertically arranged and the sample is transported between them with a manipulator through a gate valve orifice. The upper level houses standard four grid LEED optics (section 2.5), a quadrupole mass spectrometer (section 2.5), an Ar<sup>+</sup>-ion sputter gun and gas dosing facilities (section 2.3). The lower level houses a high resolution electron energy loss spectrometer (VSI Delta 0.5, section 2.4). The preparation chamber is pumped by a 500 l/s turbomolecular drag pump and a titanium sublimation pump. The HREELS chamber is pumped by a 300 l/s diode type ion pump and an additional titanium sublimation pump. The vacuum was controlled with a Bayard-Alpert ionization gauge (x-ray limit of about  $2 \times 10^{-11}$  mbar). The base pressure in the system was less than  $5 \times 10^{-11}$  mbar.

### 2.2 Sample holder and temperature control

In surface science experiments there are many requirements for the mounting of small single-crystal sample under ultrahigh vacuum, discussed in details by H. Schlichting and D. Menzel [35]. Fulfilling these requirements is not a trivial task because some of them are conflicting but there exist strongly case-specific solutions. Some required features for the silicon crystal holder can be summarized as follows: uniform temperature over the whole surface area in the entire

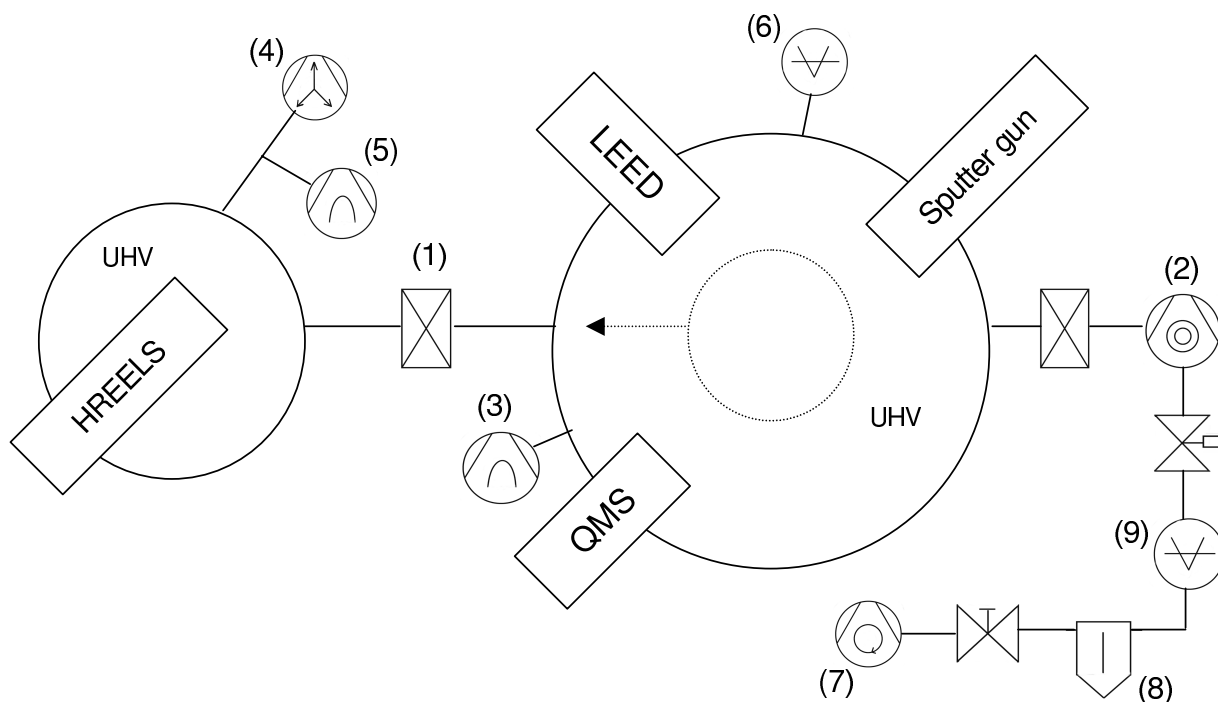


Figure 2.1: UHV setting: (1) Gate valve, (2) Turbomolecular drag pump, (3) Titanium sublimation pump, (4) Ion pump, (5) Titanium sublimation pump, (6) Bayard-Alpert ionization pump, (7) Primary mechanical pump, (8) Catalyzer trap, (9) Pirani gauge head.

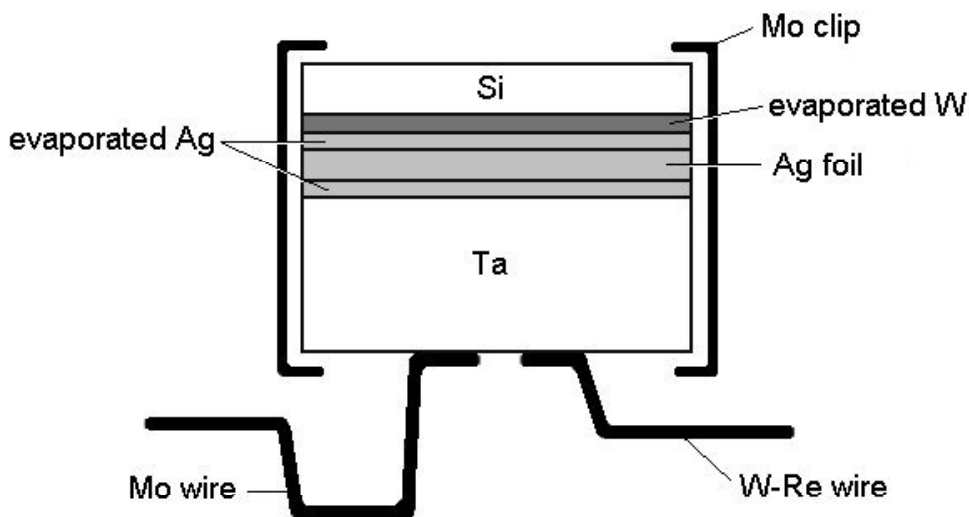


Figure 2.2: The Si crystal mounting.

20 ÷ 1250 K range, minimal thermal gradients during fast and well defined heating and cooling. We use a "sandwich" construction [36, 37] of the sample mounting and ohmic heating (Fig. 2.2). The Mo and W-Re wires are spot-welded to the back site of a thick Ta plate. Tantalum as a metal provides uniform thermal distribution over the whole area where the thermal coupling to the silicon crystal through a thin silver film is made. The tungsten evaporated on the back

site of the silicon is used to prevent the formation of Ag-Si alloy during annealing, which could cause breaking of the sample.

The tungsten and silver evaporation is made under high vacuum conditions using self-made evaporators (Fig. 2.3). One water cooled copper holder is used for the two constructions. The

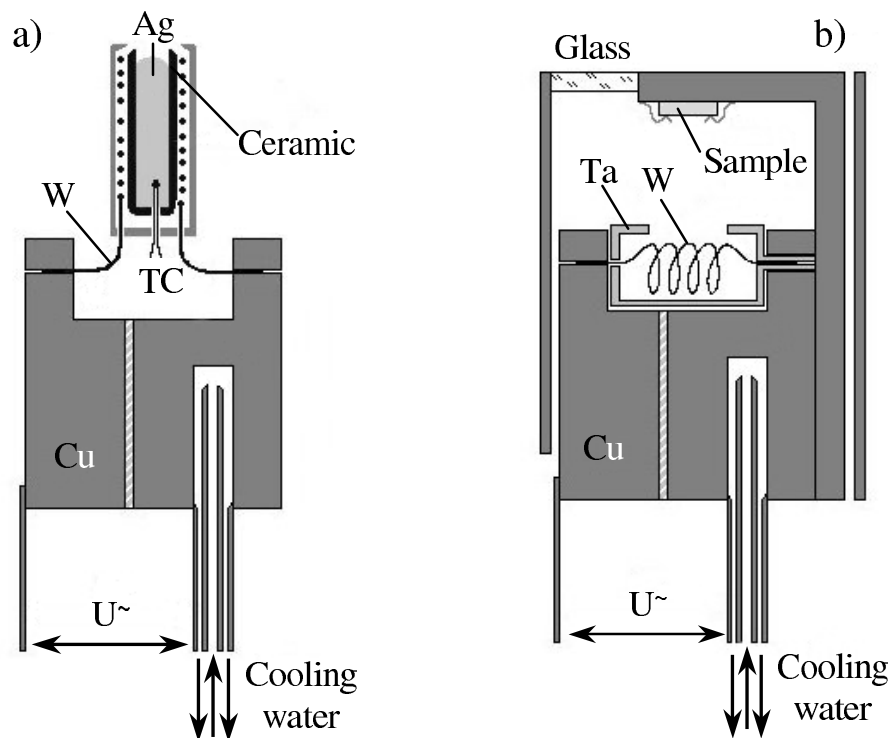


Figure 2.3: Evaporators: a) Ag source, b) W source.

silver source is a resistively heated ceramic cylindrical oven with chromel-alumel thermocouple attached to the melting metal (Fig. 2.3 a). The tungsten atomic flux is achieved by a W wire, resistively heated and held close to the melting point (Fig. 2.3(b)). The thickness (1000–1500 Å) of the obtained metal layers was determined by comparison of the coverage on a probe glass reference located near the target (Fig. 2.3 b). Temperatures of 30 K (liquid Helium) and of 85 K (liquid Nitrogen) are achieved by thermal coupling of the sample through Mo and W wires to a cryostat (silver head)(see Fig. 2.4). In Fig. 2.4 a cross section of the UHV part of the manipulator is presented. The construction is based on a stainless steel tube closed by a silver head (2). The cooling liquid flows in and out of the central tube through a siphon and cools the Ag-head. The heat of the sample (1) is transferred by Mo and W wires to the Ag-head. The thermal (electrically isolating) contact is provided by a sapphire plate. The resistive heating circuit involves all elements depicted in Fig. 2.4 except the central stainless steel cylinder and the Ag-head. Three stages of pre-cooling (3) are applied to the annealing circuit in order to prevent a heat flow to the sample coming from the Cu feedthroughs. Additional thermal decoupling of the sample from the chamber is achieved by introducing in the circuit stainless steel rods (4) with low thermal conductivity. The precise programmable annealing and cooling are obtained by ohmic heating using the scheme (Fig. 2.5) developed by Schlichting [38]. The temperature sensor in Fig. 2.5 is a chromel-alumel thermocouple, spot welded to the back side

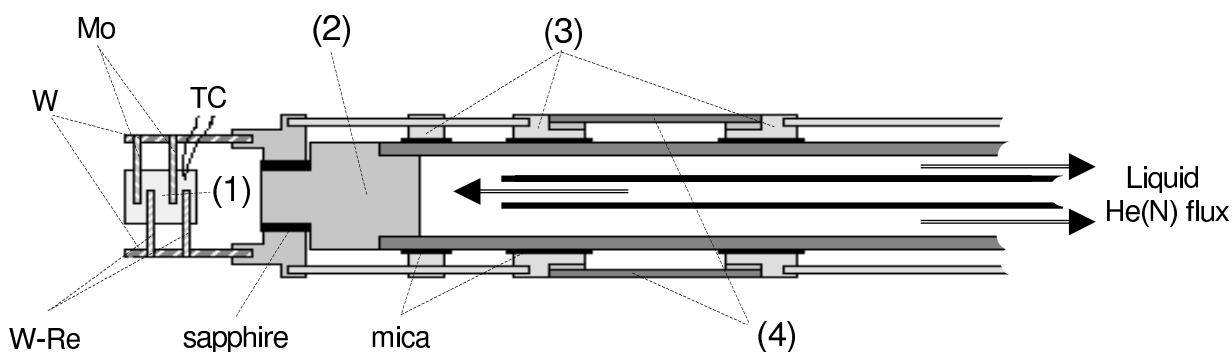


Figure 2.4: Cross section of the UHV side of the manipulator. Some of the elements are denoted by their materials and some are denoted by: (1) back view of Ta plate; (2) silver head; (3) pre-cooling stages, constructed by Cu blocks, which are in thermal but not in ohmic contact (mica) with the central stainless steel cylinder; and (4) stainless steel rods.

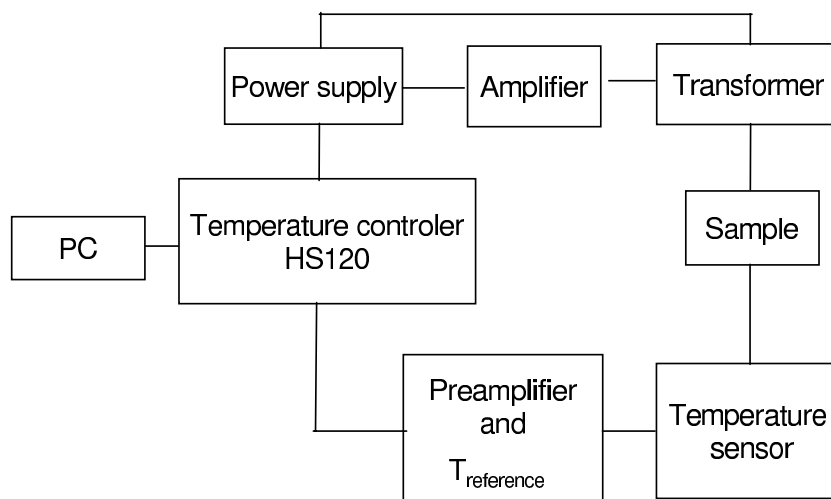


Figure 2.5: The temperature-control scheme.

of a Ta plate (marked as "TC" in Fig. 2.4). The crystal temperature is calibrated by a constant reference temperature.

The precise geometrical positioning of the sample surface in the chambers for analysis and preparation was provided by a single bellows manipulator with drives for three-dimensional translation and polar axis rotation. Additionally the whole manipulator was mounted on a rotatory flange with possibility for adjustment of the polar axis vertical.

### 2.3 Gas dosing system

A UHV system (see Fig. 2.6) connected to gas bottles through leak valves is used as a gas source for the preparation chamber. A base pressure of  $2 \times 10^{-8}$  mbar is obtained in the gas dosing system with a 50 l/s turbomolecular drag pump which is monitored by a Bayard-Alpert

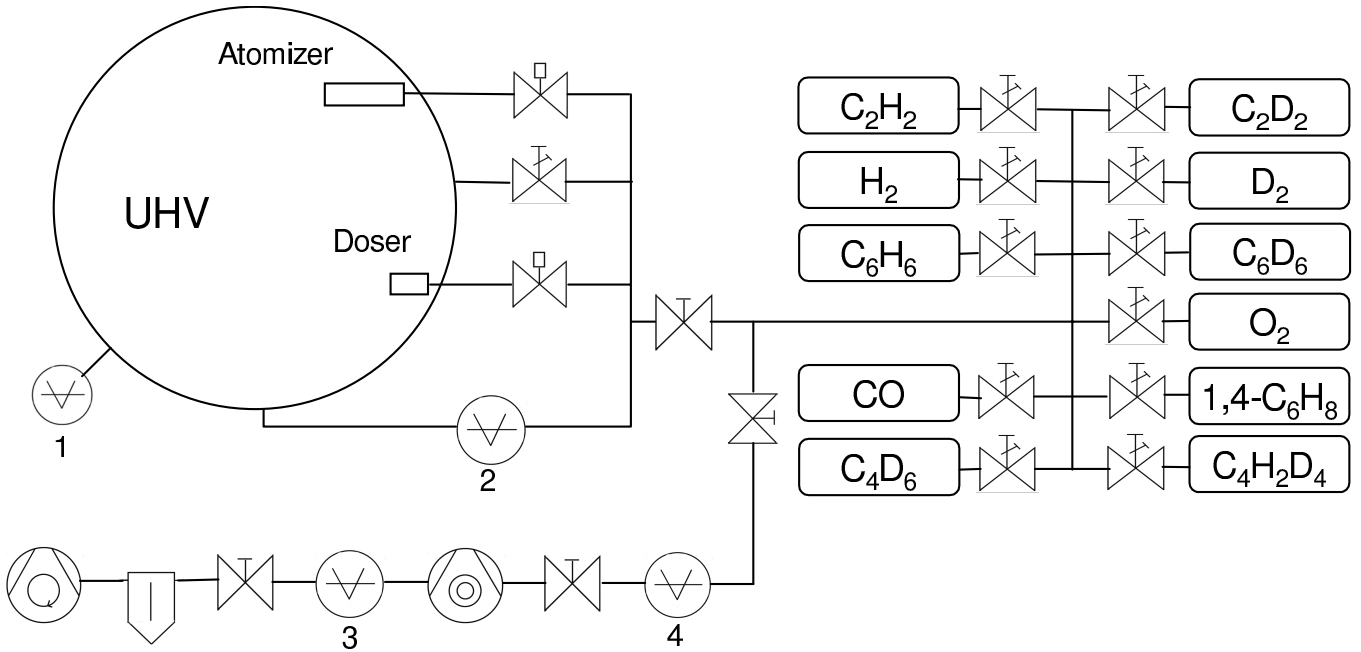


Figure 2.6: The gas dosing system. (1) and (3) denote Bayard-Alpert ionization gauges, (2) is a Baratron sensor, (4) is a Pirani gauge head.

ionization gauge. There are three gas inlets (Fig. 2.6) to the main UHV chamber: a capillary area doser, a simple capillary pipe and an atomizer. In the atomizer [36], a tungsten capillary thermally shielded and heated (up to 1850°C) by electron bombardment provides dissociation of the flowing gas molecules. Before dosing, the gas UHV system was disconnected from the turbomolecular pump and the ionization gauge, then it was filled with the selected gas and the pressure was monitored by a Baratron high accuracy sensor with a differential type of measurement. After establishment of the desired pressure the valve to one of the inlets to the main chamber was opened for a given period of time. The relative doses were determined from the difference of the Baratron readings before and after the dosing.

## 2.4 HREEL spectrometer

High resolution electron energy loss spectroscopy (HREELS) is an experimental technique in which a highly monochromatic electron beam is scattered from the sample surface, and the energy and angular distributions of the scattered electrons are measured. Production and analysis of such a monochromatic electron beam, where for example the space charge limit is considerable, requires a complex electron optical system [39]. The results of the long development in this field are incorporated in the HREEL spectrometer VSI Delta 0.5 whose principle scheme is presented in Fig. 2.7. The emission system (1) serves as a source of feed beam, focused into a small area and small angle aperture. A tungsten cathode tip is located in the center of a hemispherical repeller and thermo-emits electrons. The repelled beam passes through slot lenses with independent focusing in the two planes before reaching the pre-monochromator (2). All dispersive elements are cylindrical deflectors. The two monochromators (2) and (3) provide

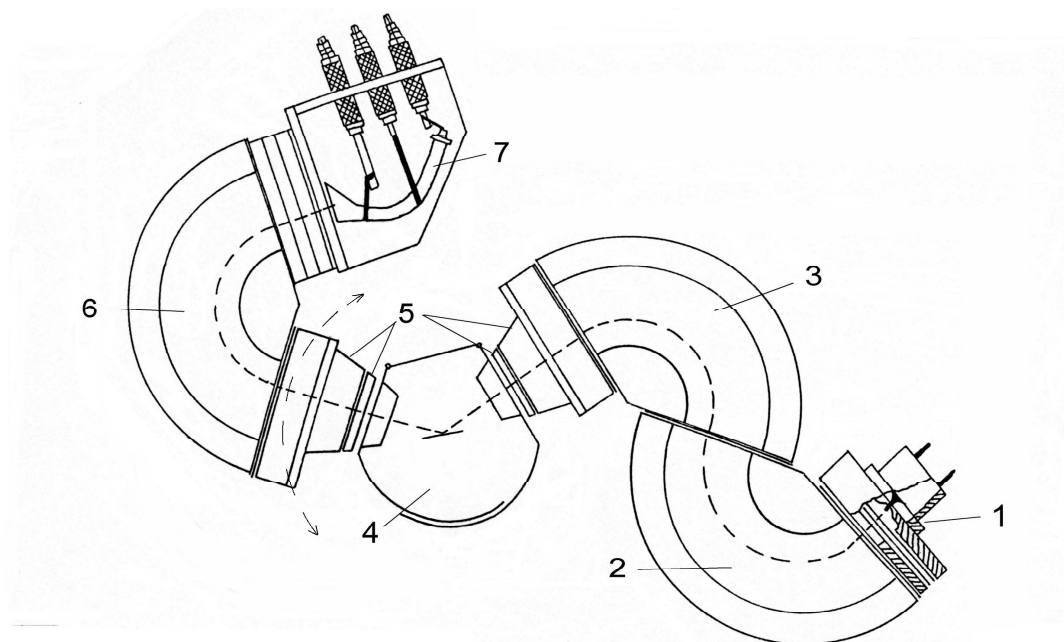


Figure 2.7: The high resolution electron energy loss spectrometer:(1) cathode emission system, (2) pre-monochromator, (3) monochromator, (4) scattering chamber; (5) lenses, (6) analyser, (7) Channeltron.

the monochromatic electron beam and the analyzer (6) sweeps the investigated energy region. The scattering chamber (4) has the same potential as the sample, to create a field-free space around the investigated surface and ensure well-defined parameters in the experiments. The energy and the focusing of the beam which strikes the sample is adjusted by the lenses located between the exit slit of the monochromator and the scattering chamber. Another set of lenses (5) which is with symmetric geometry and potentials is located on the outgoing beam path before the entrance slit of the analyzer. The electrons which leave the analyzer exit are then focused into the entrance of a channeltron multiplier and the signal is amplified and recorded. The analyzer together with the lenses in front of it can be rotated in the horizontal plane providing possibility for measurements with different scattering angles. All potentials of the spectrometer are remotely adjustable by a computer.

In the straight-through mode (without target deflection) 0.7 meV FWHM at an elastic peak intensity of 400 kcps was obtained. The same resolution have been achieved on a Ru(001) sample [40]. The best resolution on a bare Si(100) surface achieved in this work was 2.2 meV (at 200 kcps) and on a H/Si(100)-(3×1) surface 1.4 meV (at 120 kcps).

## 2.5 Quadrupole mass spectrometer and LEED device.

The temperature programmable desorption experiments were made with a commercial quadrupole mass spectrometer (Balzers QMG 112) equipped with a Feulner cup [41]. The scheme of the spectrometer includes an axially arranged ionization cell with two cathodes, a quadrupole dispersive element and collector. In the ionization cell, cathode emitted electrons

are used to ionize the analyzed particles. The ions are extracted in the dispersive element (quadrupole), containing four parallel rods. High frequency electric field separates the ions by mass and charge in the space between the rods. The selected ions then reach the electron multiplier and the collected signal is additionally amplified, recorded and displayed. Desorption spectra, namely the signal at one or more fixed  $m/e$  as a function of time or sample temperature were measured. Signal vs  $m/e$  spectra, containing peaks related to gas molecules and their cracking products, were used for analysis of the residual gas in the chamber and for control of the dosing gas cleanness.

The visual analysis of the low energy electron diffraction (LEED) from the surface were made using a standard system consisting of a coaxially positioned electron gun (Varian 981-2125) and Varian 4-grid retarding field optics. The electron gun provides a primary beam in the  $30 \div 300$  eV energy range with normal incidence to the investigated surface. The principle of the method is formation of a diffraction pattern based on the interference of electrons at the crystal surface. The geometry of the interference maxima and the intensity of the diffraction spots give information on the crystal surface structure. The reflexes are made visible on a hemispherical fluorescent screen which yields the two-dimensional surface periodicity. The gun and the collector first grid are grounded as is the sample. This ensures field-free space which prevents an electrostatic deflection. A negative potential with magnitude slightly smaller than the primary electron energy is applied to the second grid on the back-scattered electron trajectory. This potential repels the inelastically scattered electrons. The third grid is on the same potential as the second grid to reduce the field inhomogeneities in the meshes of the second grid, coming from the high voltages of the fluorescent screen. The fourth grid is used to improve the resolution properties of the optics. Diffraction patterns obtained in this way are visually observed through a window in the UHV chamber, positioned on the incident electron beam axis behind the sample. A photographic method is used for LEED pattern recording (Fig. 3.6 and 3.16).



# Chapter 3

## The Si(100) surface

Silicon is an elemental semiconductor from group IV of the periodic table of elements. It crystallizes in the diamond structure, i.e. the atoms are  $sp^3$  hybridized and directionally covalently bonded to four nearest neighbors in tetrahedral coordination. The bonding length is  $2.35\text{\AA}$ . The space lattice is fcc with conventional cubic cell constant of  $5.43\text{\AA}$ [42].

The substrates used in this work are single crystals with (100) surface orientation. On the ideally-terminated (100) surface, each surface atom exhibits two unsaturated "dangling" bonds. The latter give rise to surface relaxation and reconstruction, described in the following section.

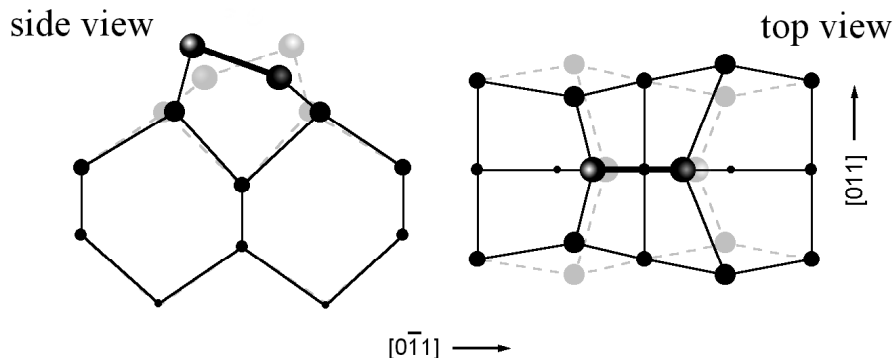
### 3.1 The surface structure

The silicon (100) surface is frequently denoted as nominally flat to differentiate it from the vicinal surface. The latter indicates surfaces with miscut of a few degrees from the (100) plane which must be strictly indicated by higher Miller indices. The following descriptions are based on this convention.

#### 3.1.1 The nominally flat surface

The ideal Si(100) surface consists of atoms, each left with two dangling bonds and back-bonded to two atoms of the second layer. The surface atoms form a lattice of perfect squares, thereby a  $(1 \times 1)$  LEED picture is expected. But starting with the experiments of Schlier and Farnsworth in 1959 [43], the most frequently reported LEED results from Si(100) surfaces are  $(2 \times 1)$  and  $c(4 \times 2)$  patterns. Following these observations, confirmed also by He diffraction measurements [44], many models have been proposed. A summary and comparison with STM images is presented in Ref.[45]. Among these models only the asymmetric (buckled) dimer model of Chadi *et al.* was consistent with the various experimental results [46, 47]. The introduction of partially ionic dimer atoms (charge transfer from one dimer atom to the other) made it compatible with the semiconducting band structures revealed by the angle-resolved photoemission spectroscopy [48]. After the work of Chadi several theoretical approaches have confirmed the minimal energy of the buckled dimer structure [49, 50]. Now it is generally accepted that the basic building block of the Si(100) reconstruction is the asymmetric surface dimer with a bond length of  $2.24 \pm 0.08\text{\AA}$  and an angle of  $19 \pm 2^\circ$  to the surface plane [51]. The building block is generated when

Figure 3.1: The two possible geometries (black and gray) of an asymmetric dimer (illuminated atoms) on a Si(100) surface. The atoms in the different layers are resized.



two neighboring atoms form  $\sigma$ - and  $\pi$ - bonds with each other giving rise to asymmetric dimer with charge transfer from the "down" atom to the "up" atom shown in Fig. 3.1. As a result the surface becomes covered with parallel dimer rows. The subsurface atom relaxation extends up to the fifth layer [52]. The dimer correlation between and along the rows determines, by long range ordering, various surface symmetry structures, represented in Fig. 3.2 in real space together with their corresponding surface Brillouin zones (SBZ). The structures are close in energy and differ by dimer buckling angle alternation, thus  $(2 \times 1)$  presents constant dimer bond orientation,  $p(2 \times 2)$  results from alternation along the rows, and if an additional antiphase between the neighboring rows exists, we have  $c(4 \times 2)$ . The theoretical calculations revealed  $c(4 \times 2)$  to be the most stable configuration, but in the STM experiments at room temperatures [45] all structures from Fig. 3.2 have been observed. Elucidation of these experimental results has been made by LEED. Observation of a  $c(4 \times 2)$  to  $(2 \times 1)$  order-disorder transition at about 200 K [53] was made, confirmed later by low-temperature STM measurements [54]. The proposal was that the symmetric dimer in the STM experiment results from time averaging observation of dimers switching between the two asymmetric geometries shown in Fig. 3.1. This flip-flop motion of the dimer was obtained also in the surface dynamics calculations [55, 56] and experimentally resolved [57]. The flip-flop motion can be suppressed by a pinning effect near defects and steps, and as a consequence local buckled dimers can be observed in room temperature STM [45, 54]. Point defects are always present on Si(100) surfaces. These defects are mainly missing dimers with different configuration in relation with the dimer rows [58] and depending on the sample preparation can vary in density from lower than 1% to up to 10%. In the lower defect limit, at temperatures below 200 K, the surface can be almost entirely  $c(4 \times 2)$  reconstructed [59]. An increase of defect density reduces the  $c(4 \times 2)$  reconstructed surface area at low temperatures and in the upper limit a  $(2 \times n)$  reconstruction with dimer vacancy chains could be produced [60]. Suppression of the low-temperature  $c(4 \times 2)$  area can appear also from the strain field of the present steps [61].

LEED investigations of highly oriented Si(100) surfaces reveal not only  $(2 \times 1)$  patterns, but also  $(1 \times 2)$ . This illustrates the presence of two domains with orthogonal dimer directions which originate from the bonding geometry rotation by  $90^\circ$  on the successive (100) layers in the tetrahedral crystal structure. The domains are equally populated and are separated by single atomic steps. The steps can be of two types, regarding the dimerization axis on the upper terrace near a step, namely normal ( $S_A$ ) and parallel ( $S_B$ ) to the step edge. Single-layer  $S_A$ -type have been calculated to have the lowest formation energy [62].

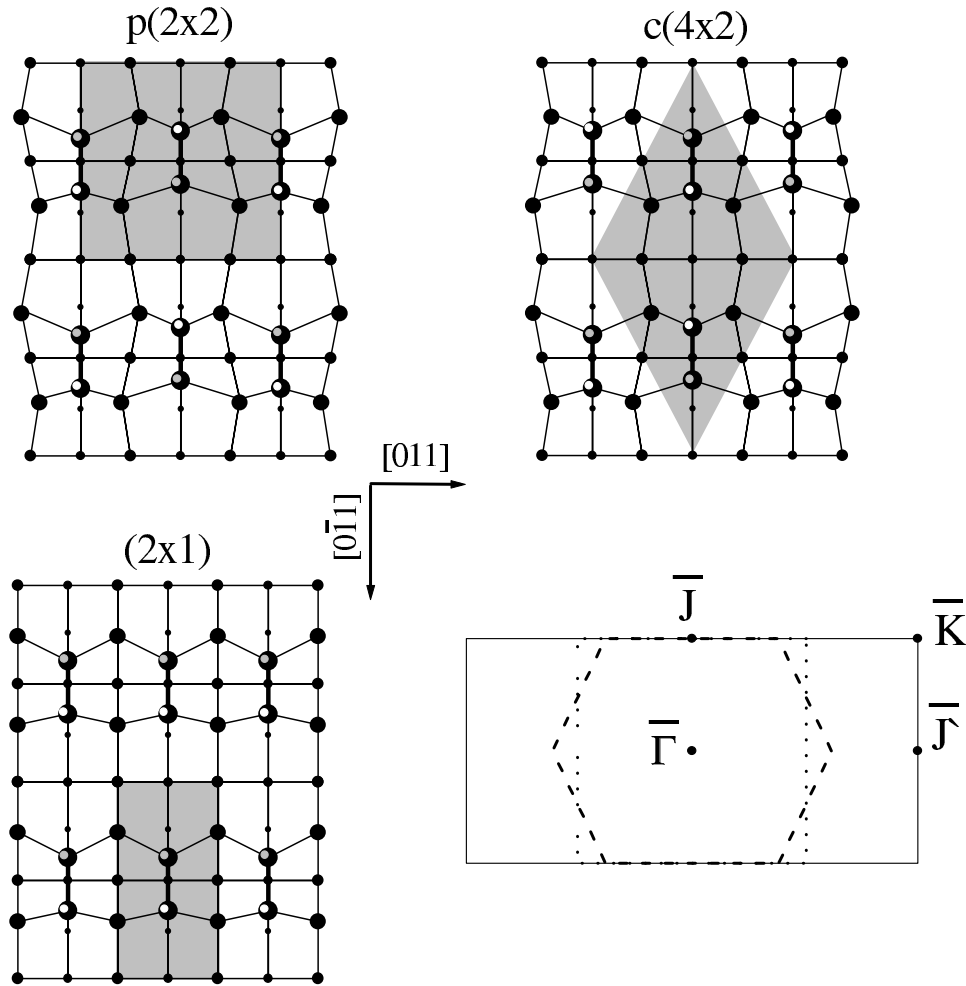


Figure 3.2: Top view of asymmetric dimer arrangements, atom relaxation and corresponding surface Brillouin zones (SBZ) on the Si(100) surface. The atoms in the different layers are resized, and the dimer atoms are illuminated. Shaded areas indicate the surface unit cell in real space. In reciprocal space the  $(2 \times 1)$ ,  $c(4 \times 2)$  and  $p(2 \times 2)$  surface Brillouin zones are presented by solid, dashed and dotted lines, respectively, together with the  $(2 \times 1)$  symmetry points.

### 3.1.2 Vicinal surfaces

For the surface analytical techniques the two domains rotated by  $90^\circ$  which are present on a nominally flat Si(100) surface result in measurement of mixed dispersions in the  $\mathbf{k}$ -space. Exception is the direction rotated by  $45^\circ$  from the  $\overline{\Gamma\bar{J}}$ . Also, this surface configuration is a source of antiphase disorder in thin-films growth. A solution of this problem was found by preparation of Si(100) surfaces misoriented towards  $[011]$  or  $[0\bar{1}1]$  axes. Earlier LEED investigations of vicinal Si(100) after sufficient heat treatment have revealed a primitive  $(2 \times 1)$  structure with double step array [63]. The predominance of double layer steps lead to equal dimer orientation on all surface terraces. Chadi has calculated various step formation energies and has determined the most stable bilayer step as  $D_B$ -type with dimer bond parallel to the step and rebonded lower step edge atoms [62]. This theoretical result has been soon confirmed

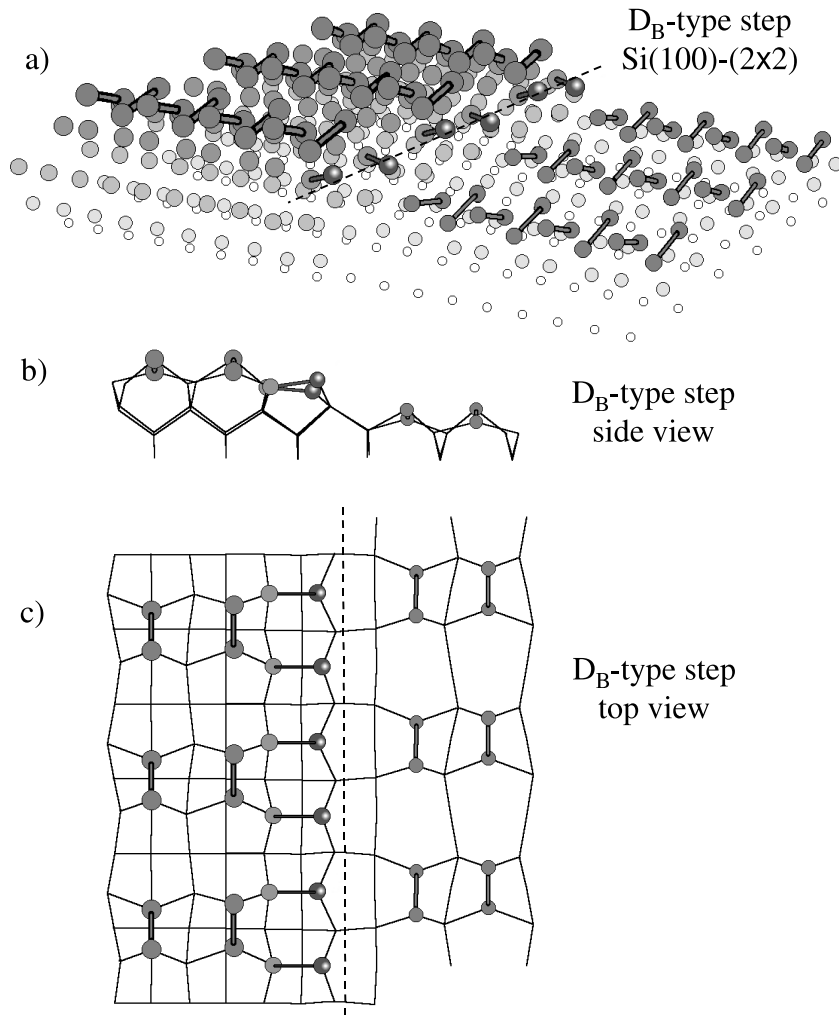


Figure 3.3: The single-domain Si(100)-(2x2) surface. The atoms in the different layers are resized. In (a) only the dimer bonds and the lower step edge atom (illuminated) bonds are shown. In (b) and (c) all bonds up to the fifth layer are presented. The  $D_B$  step is marked by a dashed line.

by the STM observation of a buckled rebonded geometry at the double layer steps on Si(001) with a miscut of  $4^\circ$  in the  $[1\bar{1}0]$  direction [64]. The angle of  $2^\circ$  has been determined as critical for the equilibrium transition between single and double steps by phase diagram calculations [65] of vicinal Si(100) as a function of temperature and misorientation angle towards  $[011]$ . Similar conclusions have been reached on the basis of the relative population of the  $(1 \times 2)$  domain and the concentration of double steps as a function of vicinality measured from STM images [66]. The experimentally observed buckling of the rebonded atoms favours the  $(2 \times 2)$  structure on the upper terrace near the step, which is well distinguished in the STM images [67]. The relaxed structure of the vicinal Si(100)-(2x2) surface is presented in Fig. 3.3. A recent review of the vicinal Si(001) surface properties in relation with energy and thermodynamical parameters can be found in the work of Zandvliet [68].

## 3.2 Preparation, quality control and orientation

The basic requirement for every scientific study is that the initial conditions must be well defined and reproducible. In this way different experiments with the same or various samples must be compared and analyzed. In this sense the Si(100) surface with its high chemical activity and reconstruction sensitivity to defects and contaminants represents a difficult task. Based on the numerous studies of Si(100) surfaces, the preparation processes can be categorized as follows: chemical etching with subsequent annealing ( $\sim 1200$  K) in vacuum, sputter etching and annealing to a variety of temperatures up to 1450 K, and pure annealing treatment up to 1500 K without etching.

The quality and the cleanness of the surface are usually controlled by AES, LEED or STM. Auger electron spectroscopy (AES) is not sensitive to impurity clusters. Conventional LEED gives sharp patterns with low background from samples with up to 10% density of random spot defects [69]. Therefore among these techniques STM is the most sensitive and provides real space images of the very surface. STM has been used to reveal the pure annealing treatment as the best method for new sample preparation in comparison with chemical etching and annealing; it leaves small area islands of SiC on the surface [69].

The criterion for a Si(100) surface quality is the concentration of point defects (missing dimers). In the case of cleaning by pure annealing it has been found that the rate of cooling plays a significant role. Thus cooling with rates  $< 2^\circ/\text{s}$  from 1200 K produces surfaces with defect concentration below 0.1% [70]. In contrast quenching the heating at 1200 K increases the defect density and leads to formation of  $(2 \times n)$  structure with vacancy chains perpendicular to the dimer rows after multiple quenching [71]. Two explanations of the  $(2 \times n)$  structures driving forces have been proposed, namely: defect interaction [60] and nickel contaminant segregation in the surface region [72]. The nickel atoms have been found to diffuse in the Si bulk at temperatures above 600 K and to segregate (even in  $< 0.01$  ML Ni) with quenching temperature above 1000 K [72]. This conclusion has been confirmed by STM/AES derived correlation between the nickel concentration and the "split off dimer" defect density [73]. Sources of Ni on the Si surface have been determined to be the crystal support and mainly the chromel-alumel thermocouples, if present [73]. This is why the silicon crystal must be kept out of contact with Ni containing alloys, *in* as well as *ex situ*.

Apart from nickel, carbon can be present in the bulk and surface region of the silicon crystal. It is impossible to remove the carbon by thermal desorption, thus sputtering and annealing is necessary. The temperature behaviour of adsorbed carbon atoms monitored by XPS indicated that above 800 K migration into subsurface sites is present, leading to a narrow layer of a highly C-concentrated SiC-alloy [74, 75]. Clean Si samples annealed in the 850-1050 K range in UHV conditions obtained a  $c(4 \times 4)$  reconstruction (RHEED) which was attributed to carbon contamination determined by SIMS [76]. The same assignment of the  $c(4 \times 4)$  structure have been confirmed by XPD [77] and XPS and LEED [78] investigations. STM results revealed a  $c(4 \times 4)$  surface symmetry after carbon ( $< 1/2$  ML) deposition at temperatures above 800 K [79, 80]. Recently, combined STM, LEED and AES techniques have revealed a deposited amount of 0.07 ML carbon to be enough to produce full  $c(4 \times 4)$  surface reconstruction with results consistent with subsurface C-sites [81]. In this way the surface purity can be monitored

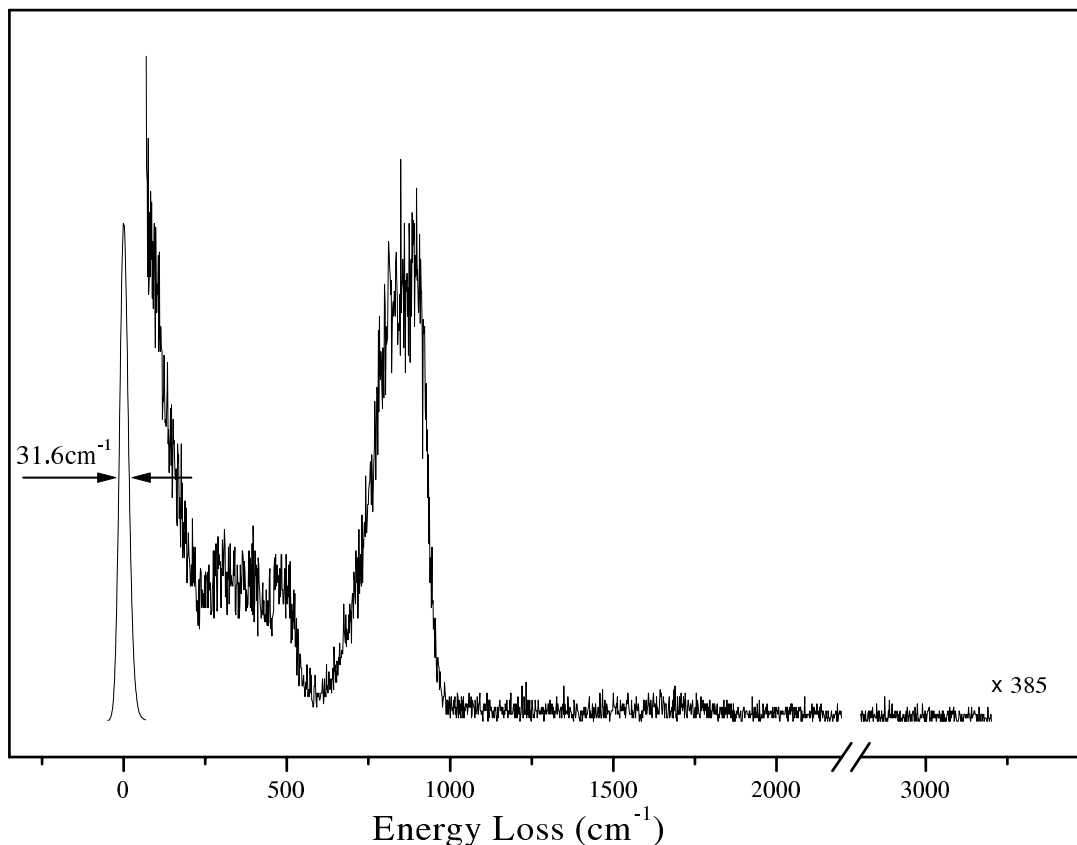


Figure 3.4: HREELS of a Si(100)-(2 $\times$ 1) surface after adsorption and decomposition (1200 K) of acetylene.

by LEED in combination with vibrational spectroscopy (HREELS) for carbon related modes, detectable in concentrations below the AES sensitivity. On Si terminated SiC(001) an intensive Fuchs-Kliwer surface optical phonon was observed at 936/945  $cm^{-1}$  [82, 83]. On a Si(100) surface implanted with carbon atoms and annealed to 1200 K a broad structure at 600-1000  $cm^{-1}$  together with a sharp peak at 795  $cm^{-1}$  appear in the FTIR spectra [84]. The surface carbonization upon chemical vapor deposition gives rise to various vibrational modes, depending on the employed gas and the annealing temperature. After acetylene adsorption and decomposition (1000 K) a broad peak at 800  $cm^{-1}$  appeared [85]. Dissociation of diethylsilane (900 K), diethyldichlorosilane (900 K) or biacetyl (1050 K) led to vibrations at 750  $cm^{-1}$ , 780  $cm^{-1}$  or 860  $cm^{-1}$  respectively [86, 87]. Annealing (1095 K) of  $C_{60}$  on the Si(100) surface produced SiC with strong Fuchs-Kliwer mode at 920  $cm^{-1}$  and a prominent shoulder at 806  $cm^{-1}$  [88]. Summarizing the above results one can expect vibrational modes with frequencies around 800  $cm^{-1}$  or in the 900–980  $cm^{-1}$  range if the Si(100) surface and subsurface are contaminated with carbon. This is demonstrated in Fig. 3.4 where a spectrum of an acetylene-covered Si(100)-(2 $\times$ 1) surface annealed to 1200 K is presented. The broad structure centered around 800  $cm^{-1}$  and 900  $cm^{-1}$  represents the Si-C related vibrations after the acetylene thermal decomposition.

An important requirement during surface preparation is that the vacuum must be kept in the  $10^{-10}$  mbar range during sample annealing at high temperatures [69, 70]. Hence outgasing of the crystal together with the sample holder for several hours at temperatures below the  $SiO_2$

desorption temperature (1150 K) is necessary.

Molecular hydrogen which is a residual gas has a very low sticking coefficient of  $0.5 \times 10^{-5}$  at 300 K [89]. For vicinal Si(100) surfaces reported values were  $s_0^{step} \approx 10^{-5}$  and  $s_0^{terrace} < 10^{-10}$  at 300 K and  $s_0^{step} \approx 10^{-4}$  and  $s_0^{terrace} \approx 10^{-8}$  at 550 K [90]. Therefore the hydrogen(deuterium) molecular chemisorption on Si(100) under UHV conditions and the time scale of our experiment has negligible contribution.

Carbon monoxide adsorbs nondissociatively on the Si(100) surface at low temperatures, forming a weak bond (Si-CO stretching at  $811 \text{ cm}^{-1}$ , SiC-O stretching at  $2080 \text{ cm}^{-1}$ ), and desorbs molecularly at 180 K, thus at temperatures above 220 K no CO is present on the surface [91].

Structure	Mode	Theory	Experiment
(HSi-SiOH) <sup>a</sup> <sub>isolated</sub>	$\delta(\text{Si-H})$	612/615	612/618
	$\nu(\text{Si-OH})$	794	798
	$\delta(\text{Si-O-H})$	870-920	883/890
	$\nu(\text{Si-H})$	2084	–
	$\nu(\text{SiO-H})$	3682	3682
(HSi-SiOH) <sup>a</sup> <sub>coupled</sub>	$\delta(\text{Si-H})$	604/617/620/627	602/618/628
	$\nu(\text{Si-OH})$	783/814	787/814
	$\delta(\text{Si-O-H})$	870-920	883/890
	$\nu(\text{Si-H})$	2076/2087	2089
	$\nu(\text{SiO-H})$	3656/3673	3655/3676
(HSi-Si*) <sup>a</sup>	$\delta(\text{Si-H})$	617/627	618/628
	$\nu(\text{Si-H})$	2100	2098
(HSi-SiH) <sup>b</sup>	$\nu(\text{Si-H})$	2091/2098	2090/2099
(HOSi-Si*) <sup>a</sup>	$\nu(\text{Si-OH})$	795	798
	$\nu(\text{SiO-H})$	3681	3682
(HSi-O-SiH) <sup>b</sup>	$\nu(\text{Si-OH})$	993	993
	$\nu(\text{OSi-H})$	2110/2113	2109/2117
(HSi-O-Si(O)H) <sup>b</sup>	$\nu(\text{Si-OH})$	1013/1046	1013/1042
	$\nu(\text{OSi-H})$	2110	2109
	$\nu(\text{O}_2\text{Si-H})$	2158	2165

Table 3.1: Vibrational frequencies related to water decomposition products on Si(100). The frequencies are in  $\text{cm}^{-1}$  and present results from [92]<sup>a</sup> and [93]<sup>b</sup>.

Water is the main contamination source of the Si(100) surface under UHV conditions. An earlier ellipsometric study of water adsorption of Si(100) concluded that the water adsorption is dissociative with a unity sticking coefficient up to a saturation of  $0.61 \pm 15\%$  ML [94]. The

proposed model was HSi-O-SiH with oxygen atom introduced in the dimer bond. In contrast molecular adsorption has been deduced from UPS experiments [95, 96]. The vibrational spectroscopies had supported the dissociative model by HREELS [97] and infrared [98] investigations. The latter has been confirmed by theoretical calculations [99] in which the electronic density of states was consistent with the previous UPS measurements but not with the proposed model of molecular chemisorption at RT [95]. Based on additional STM studies [100] and *ab initio* calculations [101] it is now accepted that water, in the temperature range 80–400 K, predominantly adsorbs dissociatively with close to unity sticking coefficient. After saturation of all surface dangling bonds at low temperatures it molecularly physisorbs. The dissociation products are monohydride Si-H and hydroxyl group Si-OH paired on a single dimer with preserved ( $2\times 1$ ) LEED pattern and saturation around half a monolayer. The initial chemisorption is on the terraces, not initiated by steps and defects [102, 100]. Further a saturated dimers coupling via hydrogen bonding between hydroxyl groups adjacent in the row was proposed [92] which can play a significant role in the surface oxidation via a hydroxyl group dissociation at elevated temperatures ( $>575$  K) [93]. Annealing up to 1200 K is sufficient to desorb all dissociative water products from the Si(100) surface [103, 104]. As a reference for the surface cleanness the vibrational frequencies of the plausible water decomposition products are summarized in Tab. 3.1. To illustrate a water contamination a spectrum of Si(100)-( $2\times 1$ ) after one month under UHV at RT is presented in Fig. 3.5 (a). The most intensive loss is the Si-OH stretching

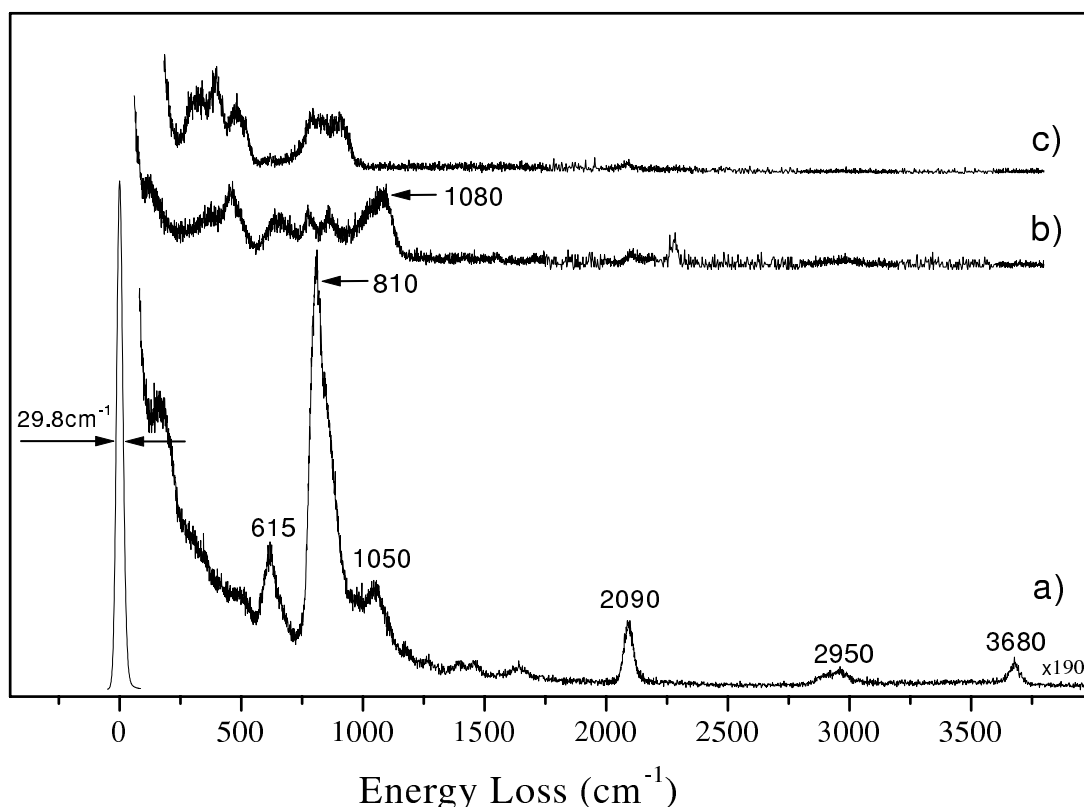


Figure 3.5: HREEL spectra of a Si(100)-( $2\times 1$ ) surface after one month under UHV at RT (a), successively annealed to 840 K (b) and to 1100 K (c). The measurements were made with 4 eV electron primary energy at 100 K.

mode at  $810\text{ cm}^{-1}$ . Well distinguished are the bending at  $615\text{ cm}^{-1}$  and the stretching at  $2090\text{ cm}^{-1}$  modes of the Si-H group. Silicon oxide and hydrocarbon related modes are visible at  $1050\text{ cm}^{-1}$  and around  $2950\text{ cm}^{-1}$  respectively. The vibration at  $3680\text{ cm}^{-1}$  is typical for water physisorbed at 100 K on the silicon surface with saturated dangling bonds. Annealing to 840K (Fig. 3.5 b) almost removes the hydrogen from the surface and leads to hydroxyl group dissociation with formation of silicon oxide with characteristic vibrations at about  $1080\text{ cm}^{-1}$ . Successive annealing to 1200 K cause the desorption of the oxide and in Fig. 3.5 (c) only the carbon associated modes around  $800\text{ cm}^{-1}$  and  $900\text{ cm}^{-1}$  are detectable above the surface

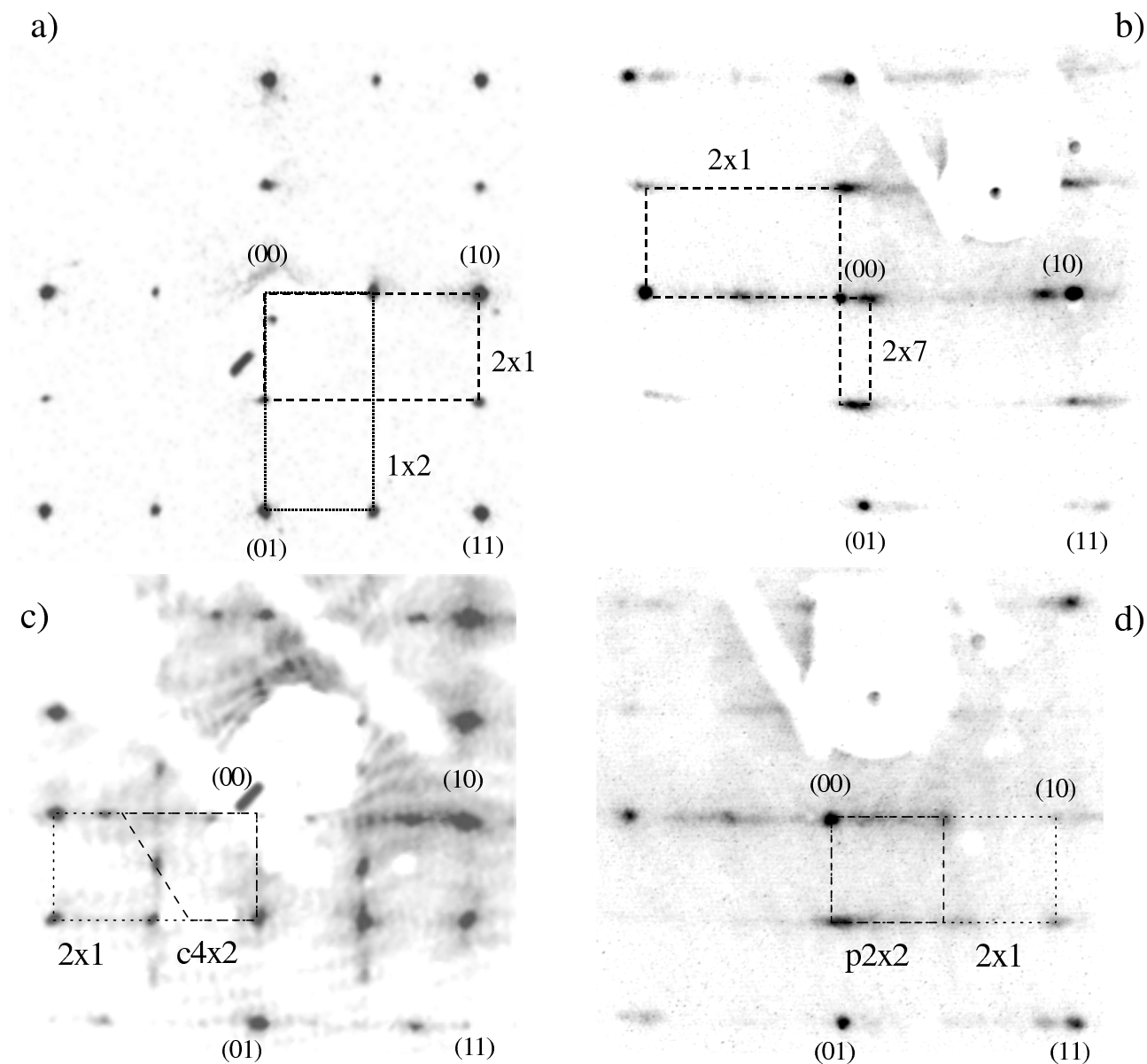


Figure 3.6: LEED patterns of (a, c) nominally flat (two domains) and (b, d) vicinal (single domain) Si(100) surfaces. (a, b) are at 300 K with 100 eV electron beam energy. (c, d) are at 90 K with 170 and 180 eV, respectively. The reciprocal unit cells are denoted by dashed and dotted lines.

phonon bands at  $550 \text{ cm}^{-1}$ .

In this study we use Si(100) samples ( $8 \times 10 \times 0.5 \text{ mm}$  and  $9 \times 11 \times 0.5 \text{ mm}$ ) cut from commercial polished wafers. The  $0.5 \text{ mm}$  thick wafers are: highly oriented (100) intrinsic Si and misoriented (miscut angle of  $5^\circ$  towards [011] direction) highly-doped n-type (phosphours) and p-type (boron) crystals. The crystals are *ex situ* oriented by x-ray diffraction, ultrasonically cleaned in Aceton (99.8%) and 2-Propanol (99.7%) and rinsed in deionized water. Tungsten and consequently silver are evaporated on the back side of the crystals under pressure below  $2 \times 10^{-6} \text{ mbar}$ . Then the sample is mounted with molybdenum clips on a tantalum plate (section 2.2). After introduction into the UHV chamber, the sample together with the holder are outgased at  $800 \text{ K}$  for 8-10 hours, until the pressure stays below  $3 \times 10^{-10} \text{ mbar}$ . Several cycles of argon ion sputtering (40-60 min,  $I_{Ar^+} \approx 1.5 \mu\text{A}$ ,  $800 \text{ eV}$  ion energy, angle =  $\pm 30^\circ$ ) at RT and  $800 \text{ K}$  and annealing up to  $1200 \text{ K}$  ( $\pm 2 \text{ K/s}$ , pressure in the  $10^{-10} \text{ mbar}$  range) were performed until sharp LEED patterns (see Fig. 3.6) and no contaminant-related features in the HREEL spectrum (see Fig. 3.7) were obtained. A cleaning procedure of sputtering

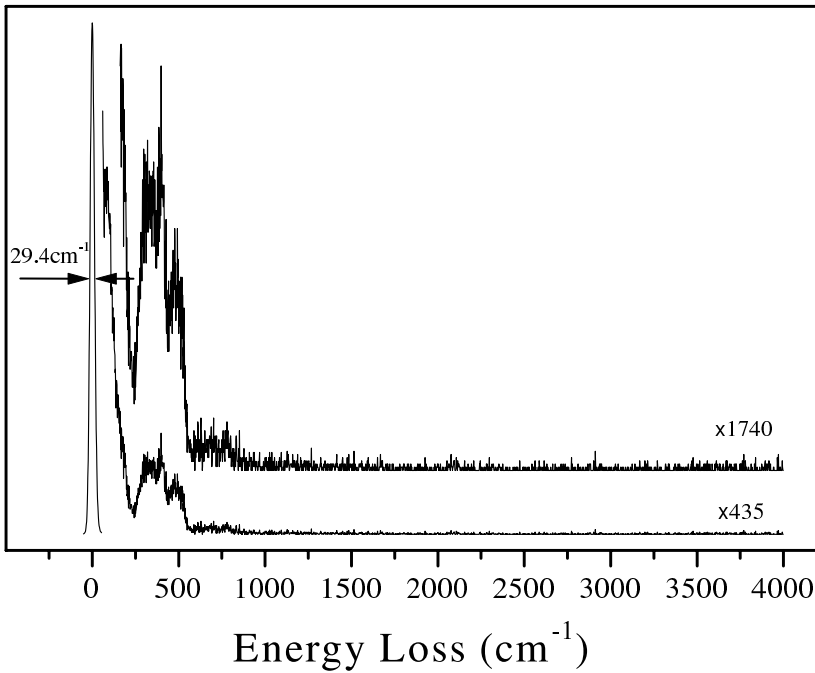
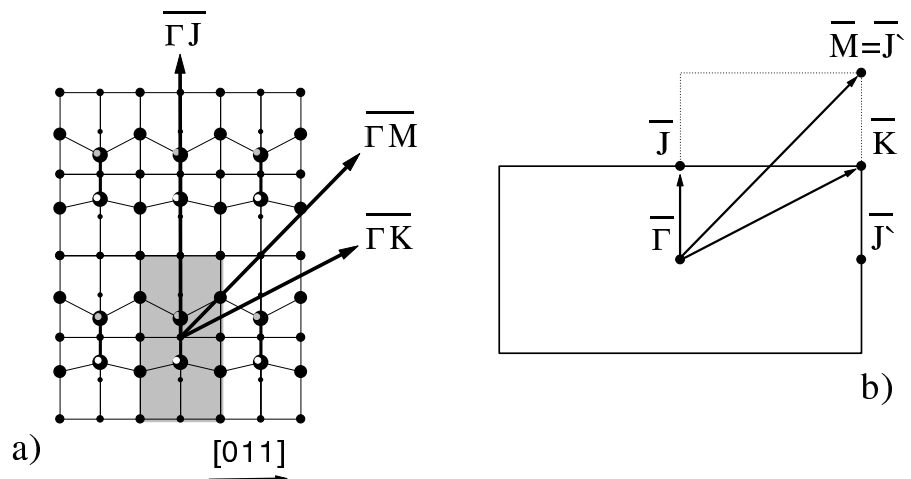


Figure 3.7: HREEL spectrum of a bare Si(100)-(2 $\times$ 1) surface. Electron primary energy  $4 \text{ eV}$ ,  $100 \text{ K}$ .

Figure 3.8: The measured HREELS scattering plane orientations are presented in a real space surface top view (a) and in the (2 $\times$ 1) SBZ (b).



(20 min) plus twice annealing ( $1200 \text{ K}$ ) was carried out before each experimental cycle. The

base pressure was below  $3 \times 10^{-11}$  mbar.

The samples were vertically positioned in order to have the HREELS scattering plane perpendicular to the surfaces and its projection azimuthally oriented in the desired direction which is controlled by LEED with an uncertainty of  $\pm 0.1^\circ$ . The scattering plane projections used in this work have been chosen with azimuthal directions (Fig. 3.8 a)  $\overline{\Gamma J}$ ,  $\overline{\Gamma M}$  and  $\overline{\Gamma K}$ . The notations are based on the  $(2 \times 1)$  SBZ symmetry points (Fig. 3.8 b). In the following text the HREELS scattering plane projection directions on a Si(100) with respect to the  $(2 \times 1)$  SBZ notations will be denoted as surface azimuthal orientation.

### 3.3 Passivation of the Si(100)- $(2 \times 1)$ surface by atomic hydrogen(deuterium)

Because of its importance for technology, hydrogen chemisorption on the Si(100)- $(2 \times 1)$  surface has been studied by a great number of researchers. This system also provides a possibility for both theoretical and experimental understanding of the chemisorption process. One of the methods for surface hydrogenation, predominantly used in the studies, is adsorption of atomic hydrogen prepared by hot-filament dissociation. After adsorption at 95 K, two peaks with first-order kinetics dominate the TPD spectra shown in Fig. 3.9, namely at 685 K and

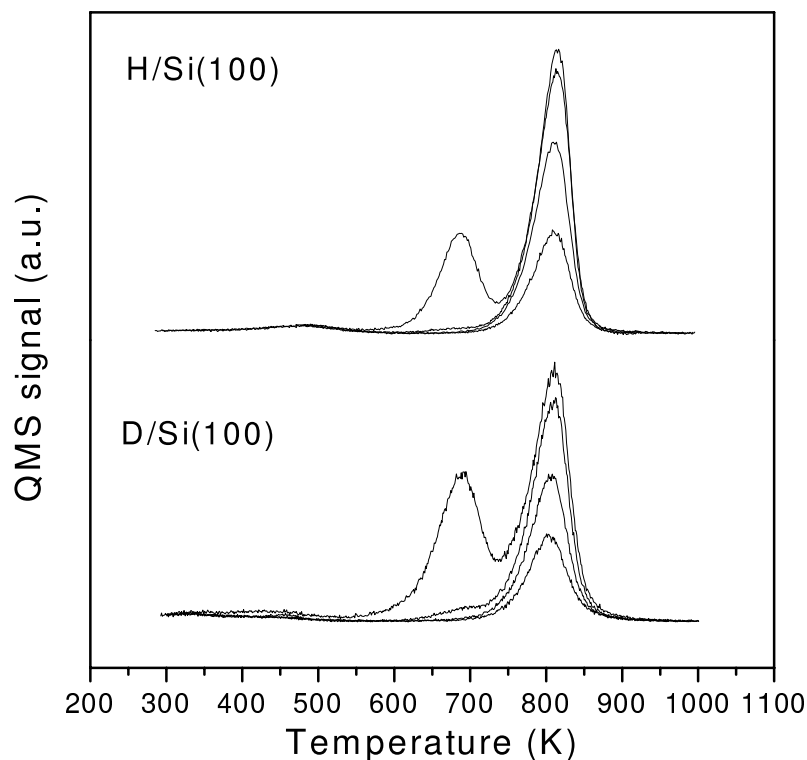


Figure 3.9: TPD spectra of successively increased atomic hydrogen(deuterium) deposition doses on Si(100) at 95 K.

at 810 K. The high-temperature peak is saturated before the onset of the low-temperature structure. Surface exposition at 650 K leaves only one phase on the surface with  $(2 \times 1)$  LEED pattern. It was identified [105, 106, 107] as monohydride on preserved silicon dimers as shown in Fig. 3.10 (a). A surprising first-order kinetics of the high-temperature (monohydride) peak was observed. By SHG [108] it was estimated to persist at coverages above 0.1 ML. A hot-precursor mechanism was proposed [109] leading to a hydrogen pairing on a silicon dimer as low

as 150 K, resulting in a first-order desorption. Saturation of the surface at temperatures below 350 K leads to a  $(1 \times 1)$  LEED pattern. This surface structure was investigated by UPS, LEED and TDS [105] and was determined as uniform dihydride phase. Later the proposed uniform dihydride was upheld by HREELS [106], by STM [110] and by theoretical [111] studies. Using IRS and LEED, Chabal and Raghavachari [112] discovered a  $(3 \times 1)$  surface arrangement after atomic hydrogen exposition at 400 K. They proposed a  $(3 \times 1)$  model containing alternating single dihydride- and monohydride-covered dimer rows as shown in Fig. 3.10 (b) Detailed STM

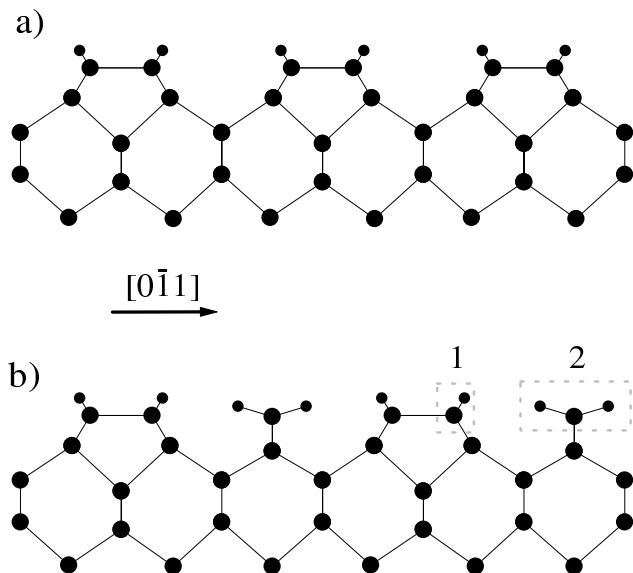


Figure 3.10: Atom configuration side views of hydrogen-saturated Si(100) surfaces. (a) uniform monohydride, (b) alternating rows of single dihydride- and monohydride-covered dimer. The mono- and di-hydride species are enclosed in dotted line boxes and labeled (1) and (2), respectively.

measurements [113] confirmed the  $(3 \times 1)$  structure and observed no uniform  $1 \times 1$  dihydride under any conditions [114]. After continuous exposition at 300 K a surface etching takes place together with trihydride formation [113, 115]. Thus now it is accepted that the continuous room temperature atomic adsorption leads to a  $(1 \times 1)$  disordered mixture of mono-, di- and trihydride on the Si(100) surface [116]. An elevated temperature adsorption is required for the two H/Si(100)- $(3 \times 1)$  [112] and H/Si(100)- $(2 \times 1)$  [107] arrangements namely exposition at 400 K and 650 K. The hydrogen coverages have been determined [115] as 1.0 ML, 1.4 ML and  $\sim 1.9$  ML for the  $(2 \times 1)$ ,  $(3 \times 1)$  and  $(1 \times 1)$  structures obtained by adsorption at 630 K, 400 K and 210 K respectively. Recently hydrogen diffusion into the bulk during atomic adsorption has been detected [117, 118] appearing as a structure in the TPD spectra above 840 K [117, 118, 119].

### 3.3.1 Results

The atomic hydrogen was obtained by molecular hydrogen dissociation in a tungsten capillary inlet, kept at 1860°C (see sec. 2.3) [120]. A water cooled shield was used to prevent sample temperature fluctuations due to illumination from the source during exposition. The surface was positioned 20-30 mm away from the capillary edge to ensure homogeneous atomic flux.

In Fig. 3.11 a HREEL spectrum of the monohydride Si(100)- $(2 \times 1)$ -H surface is presented. Above the end of the surface phonon bands at  $550 \text{ cm}^{-1}$  two strong loss peaks at  $621 \text{ cm}^{-1}$  and  $2098 \text{ cm}^{-1}$  are observed, associated with Si-H bending and stretching modes respectively [107, 106]. The structure around  $1248 \text{ cm}^{-1}$  are the bending mode overtones. No traces of C-H stretching, physisorbed water and Si-O vibrations around 3000, 3600 and  $1050 \text{ cm}^{-1}$ ,

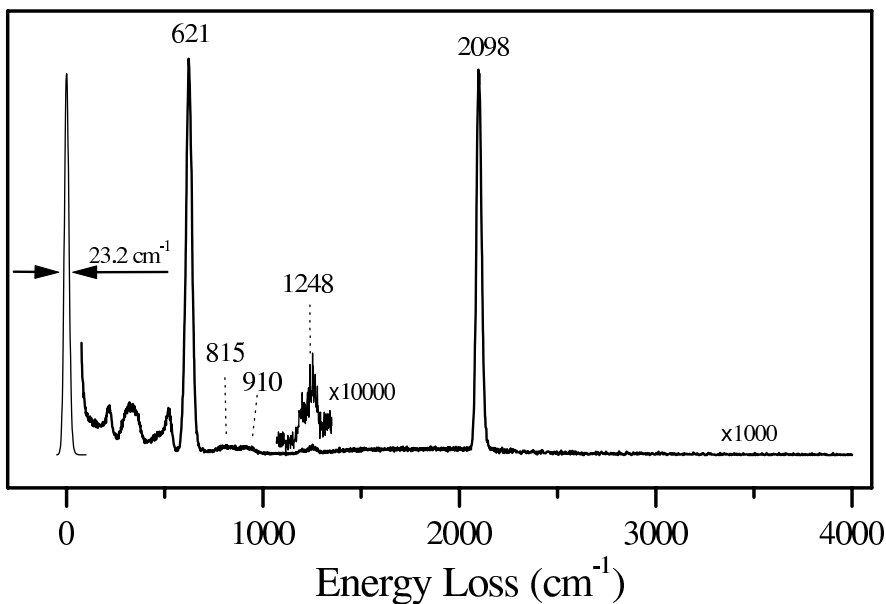


Figure 3.11: HREEL spectrum in the specular direction of a monohydride-saturated Si(100)-(2×1) surface. The electron primary energy is 4 eV and the measurement is on a vicinal sample with  $\overline{\Gamma J}$  azimuthal orientation at 100 K. The spectrum is taken after saturation of the surface with atomic hydrogen at 650 K.

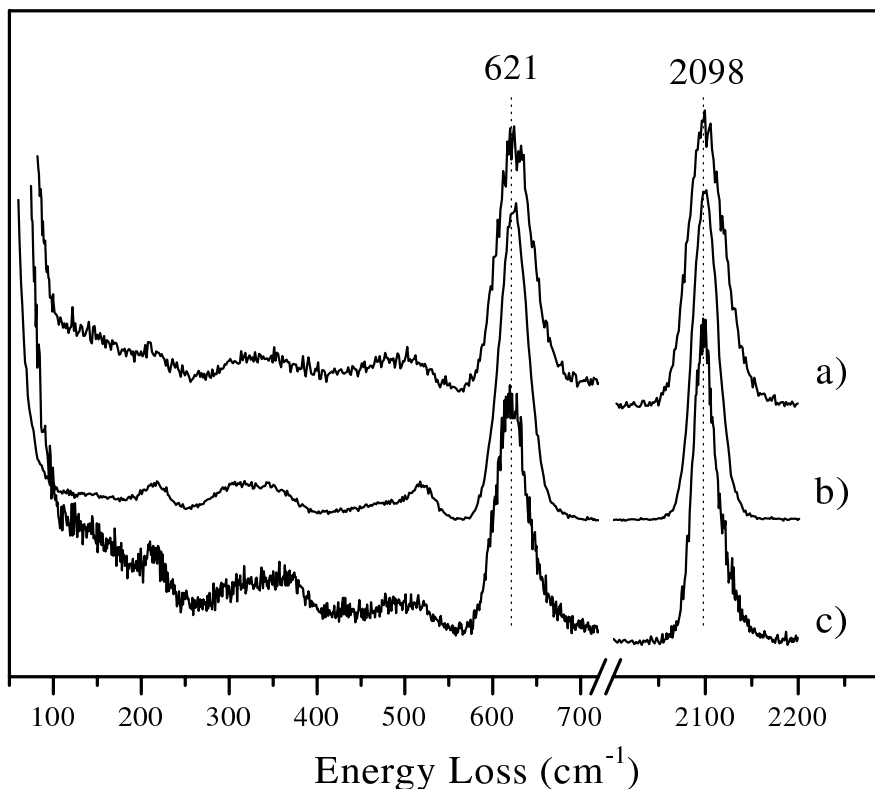


Figure 3.12: HREEL spectra of monohydride saturated vicinal and nominally flat Si(100)-(2×1) surfaces, recorded with 4 eV electron primary energy in the specular direction at 100 K. a) and b) vicinal samples with  $\overline{\Gamma K}$  and  $\overline{\Gamma J}$  azimuthal orientation respectively, c) nominally flat sample with  $\overline{\Gamma M}$  orientation. All spectra were taken after saturation of the surface with atomic hydrogen at 650 K.

respectively, are observed. The only surface contaminants with negligible concentration are chemisorbed water and carbon. The chemisorbed water with characteristic Si-OH stretching mode at  $\sim 815 \text{ cm}^{-1}$  could come from adsorption on defect sites during cooling which are depleted at 650 K. The broad weak structure at  $\sim 910 \text{ cm}^{-1}$  probably is carbon in the subsurface region as was discussed in section 3.2. The vibrational characteristics of the monohydride phase on vicinal and nominally flat Si(100) surfaces show equal features within our resolution of FWHM  $20 \div 30 \text{ cm}^{-1}$  following the same preparation procedure as is shown in Fig. 3.12.

Off-specular HREELS measurements of the monohydride phase on Si(100)-(2×1) were performed in three azimuthal directions. In Fig. 3.13 spectra taken with 250 eV electron primary

energy and scattering geometries corresponding to  $Q_{\parallel}$  in the  $0 \div 0.82 \text{ \AA}^{-1}$  range are presented.

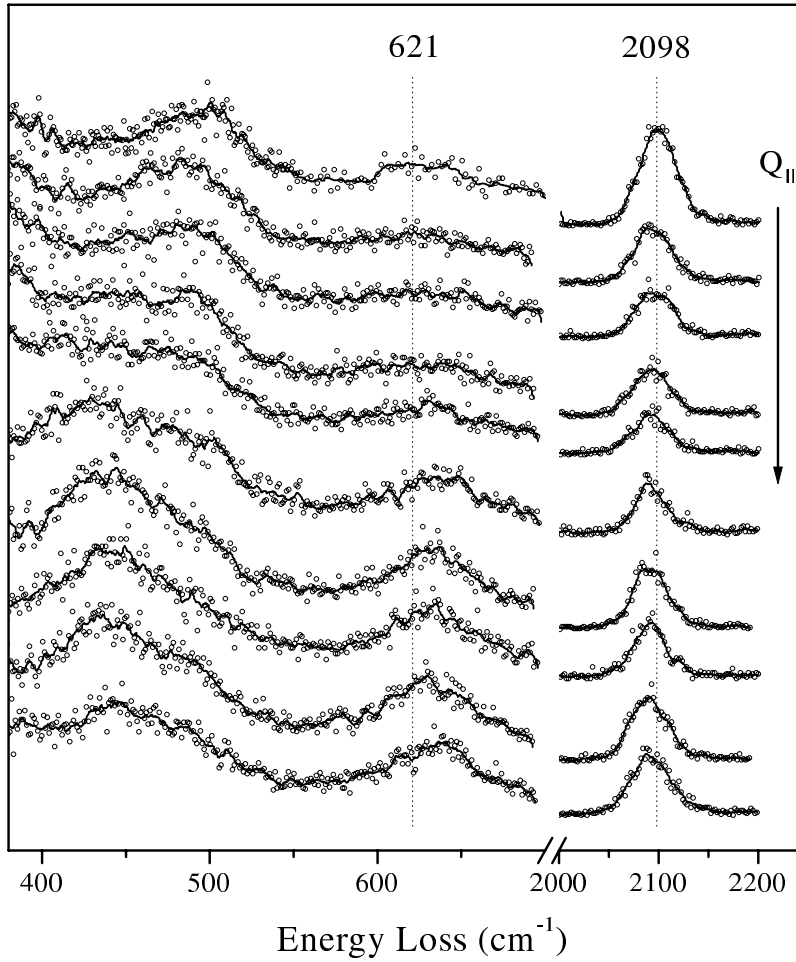


Figure 3.13: Off-specular HREELS measurements in the  $\bar{\Gamma}\bar{J}$  direction of the monohydride phase on a vicinal Si(100)-(2 $\times$ 1) surface with 250 eV electron primary energy.  $Q_{\parallel}$  is in the  $0 \div 0.82 \text{ \AA}^{-1}$  range, the arrow shows its increase direction.

A blue shift of the Si–H bending mode is observed together with a red shift of the Si–H stretching mode. On a vicinal surface in the  $\bar{\Gamma}\bar{K}$  direction with electron primary energy of 200 eV the same dispersion of both modes is observed (see Fig. 3.14). The Si–H bending mode shows a different dispersion on a nominally flat surface in the  $\bar{\Gamma}\bar{M}$  direction (see Fig. 3.15). The peak at  $621 \text{ cm}^{-1}$  quickly vanishes with the  $Q_{\parallel}$  increase and the peak at  $\sim 600 \text{ cm}^{-1}$  becomes dominant. Approaching large  $Q_{\parallel}$  dominant becomes a peak at  $\sim 630 \text{ cm}^{-1}$ . The dispersion of the Si–H stretching vibration shows a red shift. Using the fitting procedure described in Appendix A, the dispersions of the hydrogen related vibrations were obtained and are discussed in the next subsec. 3.3.2.

A second highly ordered hydrogen-covered Si(100) surface is the Si(100)-(3 $\times$ 1)-H surface. This reconstruction is obtainable after atomic hydrogen adsorption at 400 K. LEED patterns are demonstrated in Fig. 3.16. Since the Si(100)-(3 $\times$ 1)-H surface contains alternating rows of dihydride and monohydride (see Fig. 3.10 b), the vibrational spectrum is expected to contain vibrational modes of a mono- as well as of a dihydride species. In Fig. 3.17 HREELS spectra of ordered (2 $\times$ 1)-H and (3 $\times$ 1)-H phases on Si(100) are compared. Dotted lines indicate (3 $\times$ 1) spectra after corresponding (2 $\times$ 1) spectra subtraction. In the (3 $\times$ 1)-H phase the monohydride bending mode is preserved almost at the same  $621 \text{ cm}^{-1}$  position and a new mode appears at  $655 \text{ cm}^{-1}$ , associated with a dihydride wagging mode [106, 116]. Another new feature appears as a structure at  $\sim 907 \text{ cm}^{-1}$ , associated with a dihydride scissor mode [106, 116], the vibration

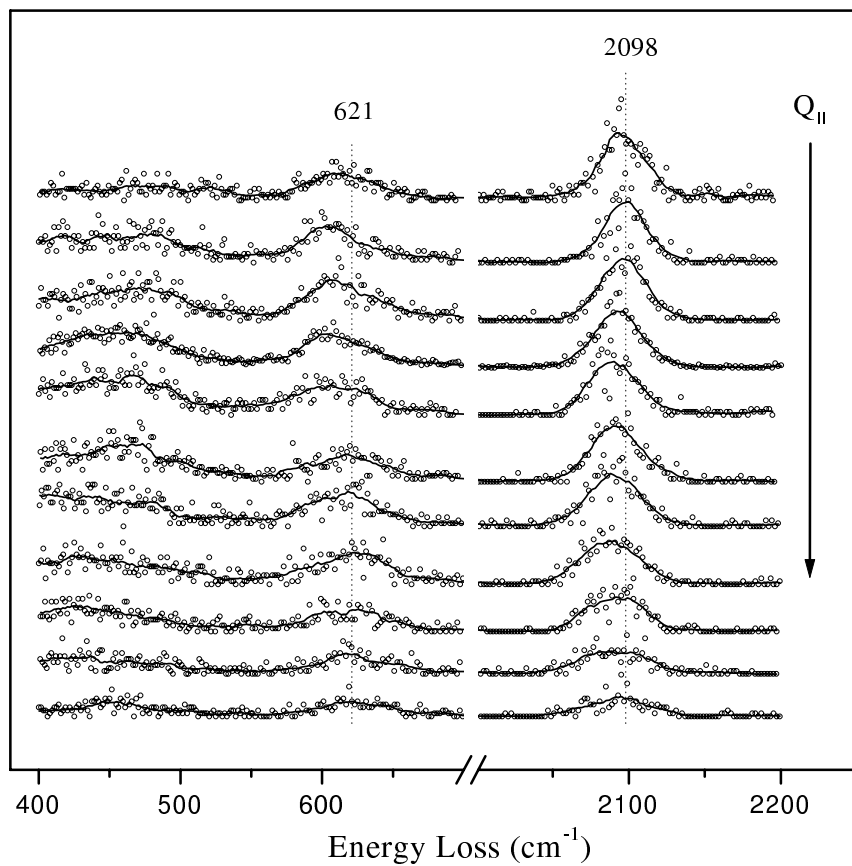


Figure 3.14: Off-specular HREELS measurements in the  $\overline{\Gamma K}$  direction of the monohydride phase on a vicinal Si(100)-(2 $\times$ 1) surface with 200 eV electron primary energy.  $Q_{||}$  is in the 0  $\div$  1.65  $\text{\AA}^{-1}$  range, the arrow shows its increase direction.

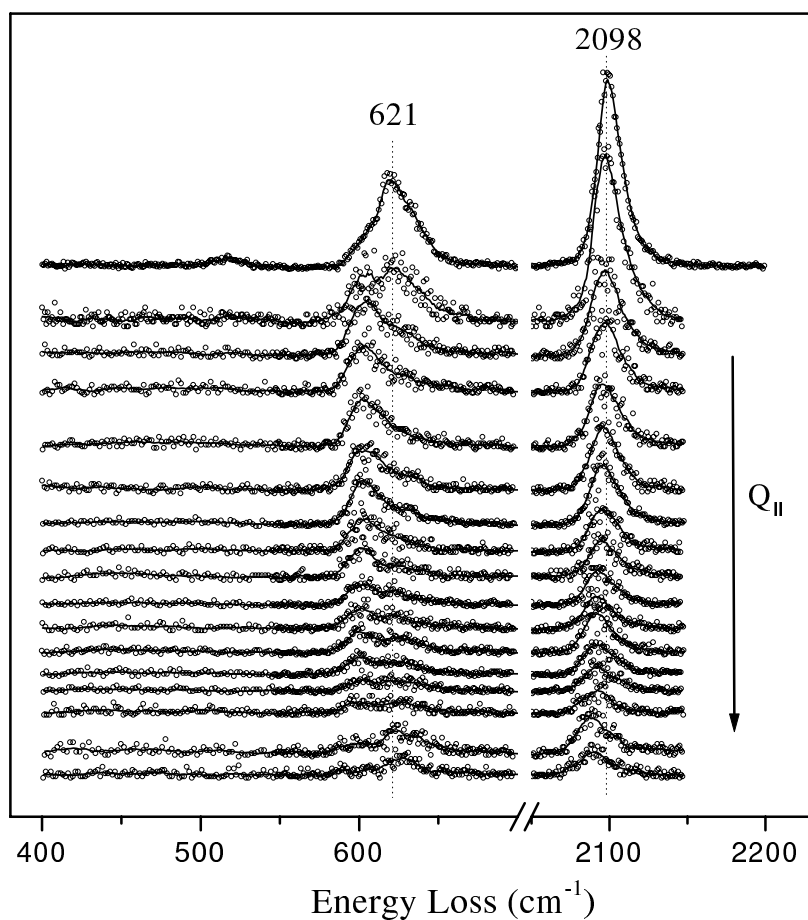


Figure 3.15: Off-specular HREELS measurements in the  $\overline{\Gamma M}$  direction of the monohydride phase on a vicinal Si(100)-(2 $\times$ 1) surface with 15 eV electron primary energy.  $Q_{||}$  is in the 0  $\div$  0.75  $\text{\AA}^{-1}$  range, the arrow shows its increase direction.

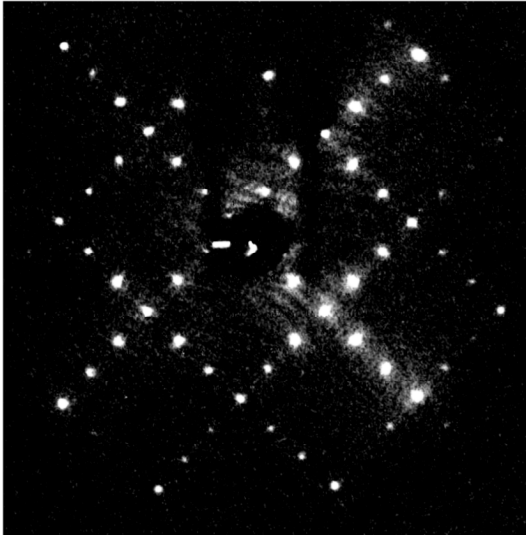


Figure 3.16: LEED patterns of a Si(100)-(3×1)-H surface, hydrogen saturated at 400 K.

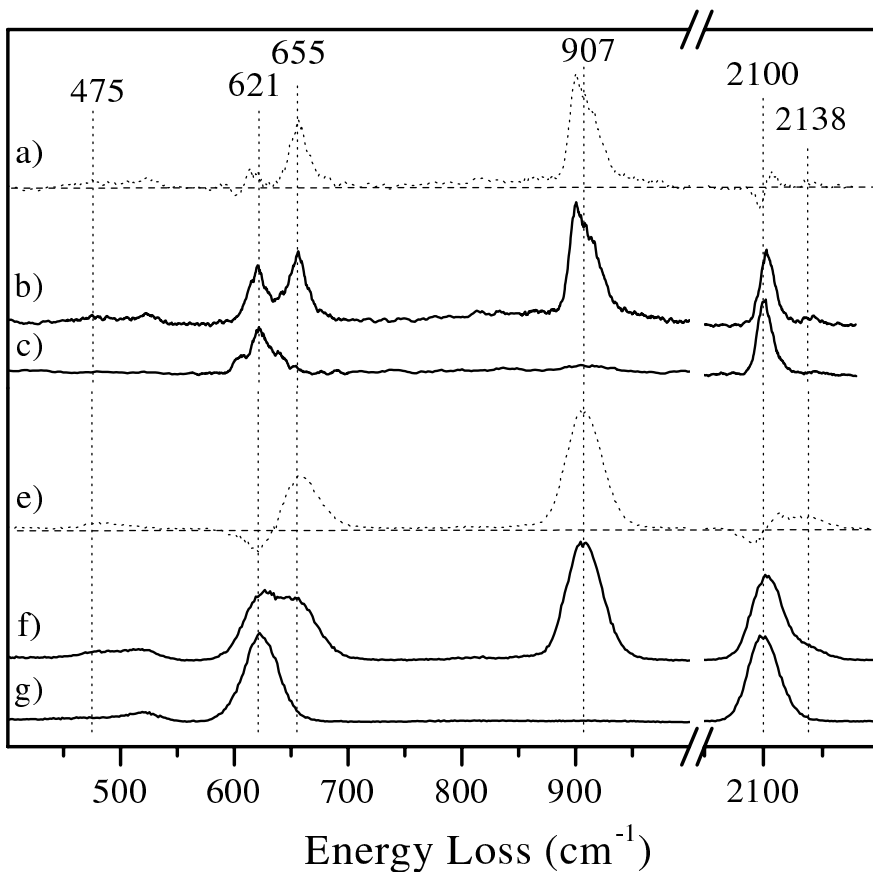


Figure 3.17: HREELS spectra of a Si(100)-(3×1)-H surface (b) and (f), compared with spectra of a Si(100)-(2×1)-H surface (c) and (g). (b) and (c) are spectra of a hydrogenated nominally flat  $\overline{\Gamma M}$  oriented sample, (f) and (g) are spectra of hydrogen adsorption on a vicinal  $\overline{\Gamma J}$  oriented substrate. (a) and (e) are difference spectra (dotted lines) of (b) and (c) and of (f) and (g), respectively.

at  $2098\text{ cm}^{-1}$  is shifted to  $2103\text{ cm}^{-1}$  and a structure around  $2138\text{ cm}^{-1}$  arises. The assignment of the latter is not straightforward and will be discussed in the next subsection.

Passivation of a Si(100) surface with deuterium leads to an isotope shift of all adsorbate-related vibrations. In Fig. 3.18 a HREELS spectrum of a Si(100)-(2×1)-H surface is presented. Above the substrate phonon bands only one strong peak at  $1527\text{ cm}^{-1}$  is observed. It is associated with the Si-D stretching mode [107]. Again, like in the (2×1)-H case, broad and weak features around  $815\text{ cm}^{-1}$  and  $930\text{ cm}^{-1}$  are detectable, indicating a negligible contamination with chemisorbed water and carbon on the surface and subsurface, respectively (see sec. 3.2). The vibrational characteristics of the uniform monodeuteride layer on a vicinal and nominally

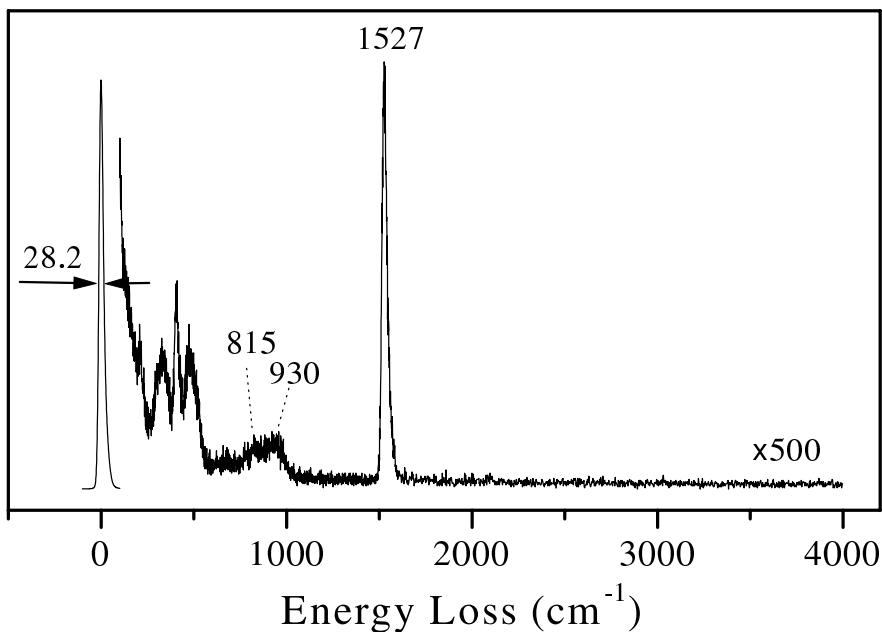


Figure 3.18: HREEL spectrum of the monodeuteride Si(100)-(2×1)-D surface. Recorded with 4 eV electron primary energy in the specular direction at 300 K. The sample is nominally flat with  $\overline{\Gamma M}$  azimuthal orientation.

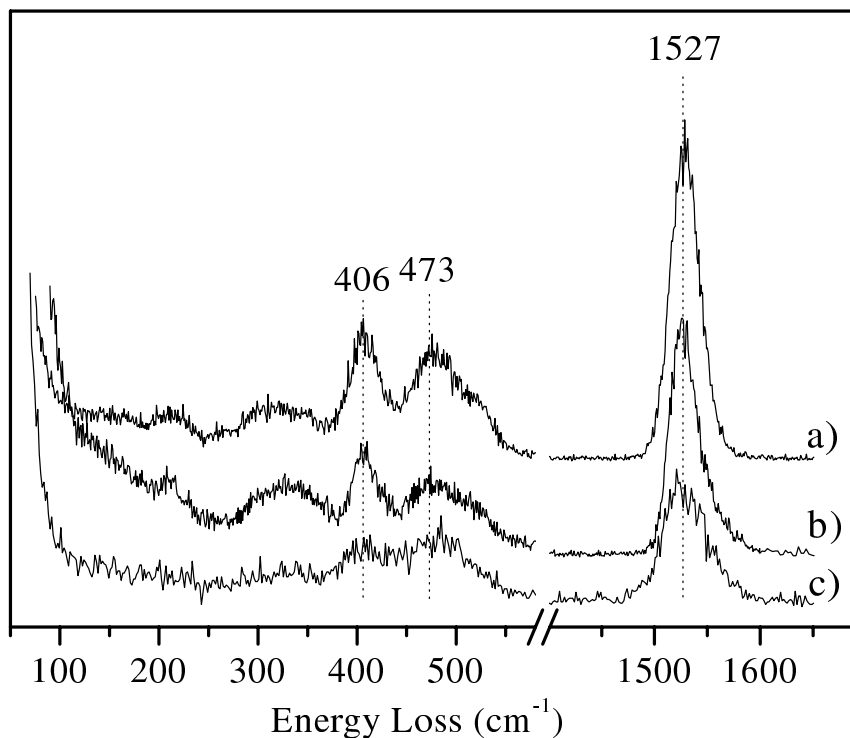


Figure 3.19: Comparison of HREEL spectra of monodeuteride (2×1)-D phases on vicinal and nominally flat Si(100) surfaces, recorded with 4 eV electron primary energy in the specular direction at 100 K. (a) and (c) are on vicinal samples with  $\overline{\Gamma J}$  and  $\overline{\Gamma K}$  azimuthal orientation, respectively, (b) is on a nominally flat sample with  $\overline{\Gamma M}$  orientation.

flat Si(100) shows no qualitative differences as is seen from the comparison in Fig. 3.19. The Si-D bending mode falls in the substrate phonon band and a strong coupling to the surface phonons is expected. Two peaks at  $406\text{ cm}^{-1}$  and  $473\text{ cm}^{-1}$  could be resolved in this region but the assignment is not obvious.

### 3.3.2 Discussion

In electron energy loss spectroscopy two scattering mechanisms are operating with their corresponding selection rules, namely dipole and impact scattering. Only totally symmetric modes are excited in a dipole scattering, while the impact scattering restriction concerns only modes odd with respect to the scattering plane (see subsec. 1.3.1). The dipole excited losses have a

lobe near the specular direction in contrast to the impact excited loss which could be spread in the entire measured off-specular range. The collecting angle of the spectrometer analyser is in the  $1\text{--}2^\circ$  range, depending on the electron primary energy and the adjustment. Thus specular measurements cover the dipole lobe and a  $\Delta k_{\parallel}$  area around the  $\Gamma$  point in the reciprocal space.

The electron losses of the dipole active modes detected in the  $\Delta k_{\parallel} = 0$  geometry in principle are expected to have a weak impact component. In general the losses reproduce the elastic peak shape if no damping processes due to energy or phase relaxation are present. Such processes could also shift the experimental frequency position of the vibrational loss. These damping mechanisms may take place by interactions with substrate phonons, surface defects and electron-hole pairs [121, 122] or/and by dipole-dipole coupling of an adsorbate [123]. As follows from the above-mentioned, the interpretation of the HREELS results is not straightforward and an involvement of surface symmetry models together with estimation of relaxation and coupling processes is required.

To address the intrinsic width of the adsorbate modes, the loss peaks have to be compared with the corresponding elastic peaks which represent the instrumental function. Fig. 3.20 shows the adsorbate loss peaks together with the shifted and scaled elastic peak. Additionally the difference spectra are given by crosses. Asymmetric broadening ( $6\pm 2\text{ cm}^{-1}$ ) of the Si-H stretching mode is observed in Fig. 3.20 (a), (b), and (d). The broadening factor compared with the corresponding elastic peak width is  $1.20\pm 0.05$  for all samples under investigation in the 90-300 K range. A red shift  $\sim 3\text{ cm}^{-1}$  of the loss structure maximum is observed between Fig. 3.20 (c) and (d) due to the temperature rise from 90 to 300 K in good agreement with a previously reported shift of  $4.1\text{ cm}^{-1}$  from 40 to 500 K [124]. The broadening on both vicinal and highly oriented samples allows us to ignore the surface point defects and steps as its potential sources. Energy and phase relaxation effects via interaction with electron-hole pairs can be also ruled out based on the unobserved influence of the sample doping (the vicinal substrates were n-type/phosphorus or p-type/boron crystals). Furthermore the concentration of charge carriers is many orders of magnitude smaller than in metals. Additionally a low charge concentration is expected in the surface region due to an energy band bending and the low temperature. Negligible dipole-dipole coupling between the Si-H stretching vibrations was previously estimated which leads to a vibrational lifetime of about  $10^{-3}\text{ cm}^{-1}$  [124]. In Ref. [124], the broadening of the infrared peak ( $< 1\text{ cm}^{-1}$ ) was attributed to pure dephasing via anharmonic coupling between the Si-H bending and Si-H stretching modes. The strong symmetric ( $2098.8\text{ cm}^{-1}$ ) and weak asymmetric ( $2087.5\text{ cm}^{-1}$ ) stretching modes, observed by FTIR [107], should lead to an asymmetry opposite to the one observed here. In principle the impact scattering mechanism presented in HREELS can affect the intensity ratio between the two modes which gives us a reason to apply a fitting of the structure around  $2100\text{ cm}^{-1}$  with two peaks. Similar procedure has also been applied in an other study [116]. The fitting results for all samples give values of  $\sim 2098.8\text{ cm}^{-1}$  and  $\sim 2115.5\text{ cm}^{-1}$  with an intensity ratio of  $3.5\pm 0.5$  and domination of the low-frequency vibration. These findings are not confirmed by the off-specular measurements shown in Fig. 3.13, 3.14, and 3.15 in which no clear separated peaks are observed.

Using the procedure described in Appendix A, the dispersions of the monohydride-related

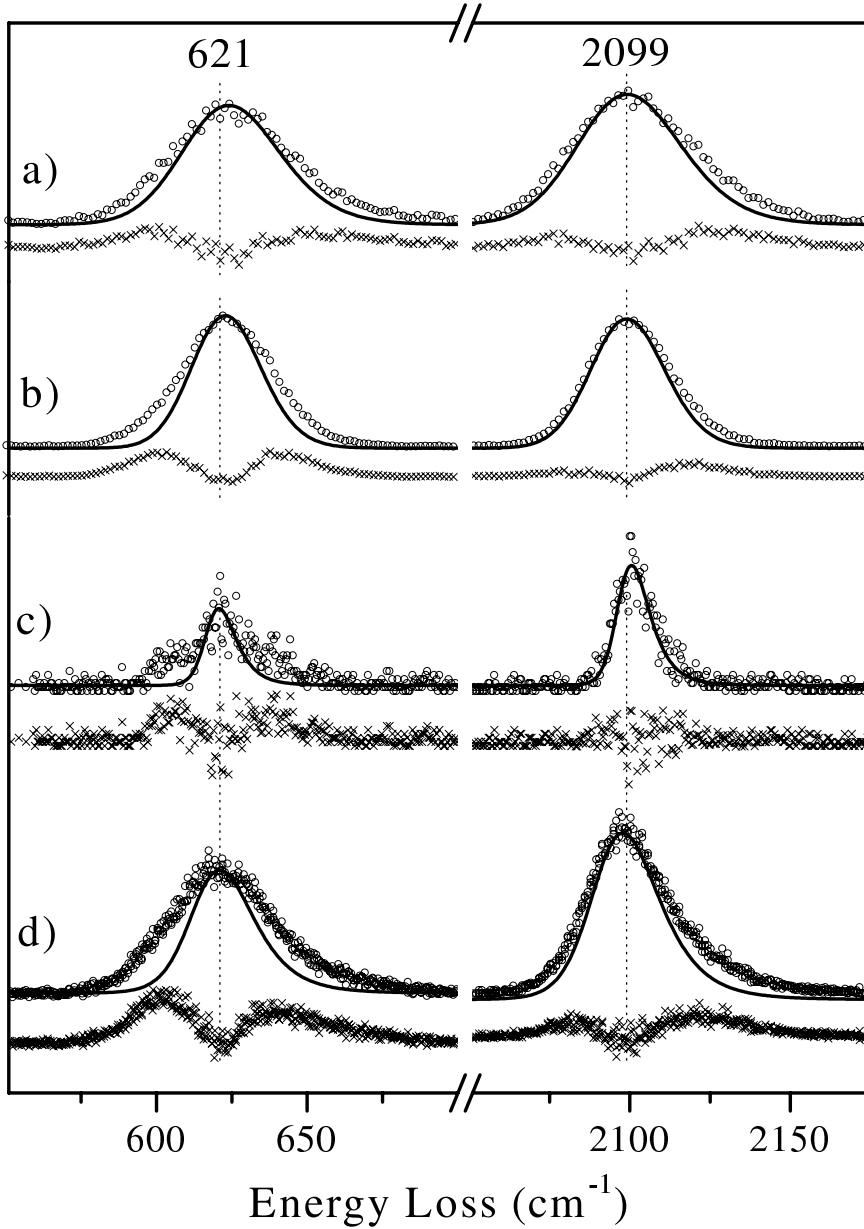


Figure 3.20: HREEL spectra (open circles) of the monohydride Si(100)-(2×1)-H surfaces compared with corresponding elastic peak profiles (solid lines) and their difference spectra (cross symbols). (a), and (b) are measured at 90 K on vicinal samples oriented in  $\bar{\Gamma K}$  and  $\bar{\Gamma J}$ , respectively. (c) and (d) are taken at 90 K and 300 K, respectively, on nominally flat substrate with  $\bar{\Gamma M}$  azimuthal orientation. The electron primary energy is 4 eV.

vibrations can be extracted from the off-specular data and are summarized in Fig. 3.21. Two bands are observed around 2095 and 620  $cm^{-1}$  related to the monohydride stretching and bending modes, respectively. The Si-H stretching band disperses as a compact structure in a  $\sim 10 cm^{-1}$  range suggesting a lateral interaction influence rather than a multi-mode structure. Based on these results we conclude that the structure with a center at 2099  $cm^{-1}$  in the  $\Gamma$ -point has a significant impact component in the specular EELS measurement with asymmetric broadening. The nature of the latter remains unclear and no evidence of multi-mode structure was obtained. The Si-H bending band around 620  $cm^{-1}$  in the spectra in Fig. 3.20 shows broadening by factors from 1.25 to 2.5 and with various asymmetries on the different samples. The variation of the shape could not be related to surface point defect and step variations. In this frequency range  $\Omega/\omega_{phonon}^{max} \approx 1.15$ , strong vibrational relaxation and coupling to substrate phonons is possible but considering the off-specular HREELS spectra, the structure appears as superposition of three-modes. The latter is best visible in Fig. 3.15. In the dispersion plot in Fig. 3.21 (c) well distinguished vibrations separated by  $\sim 30 cm^{-1}$  are observed together

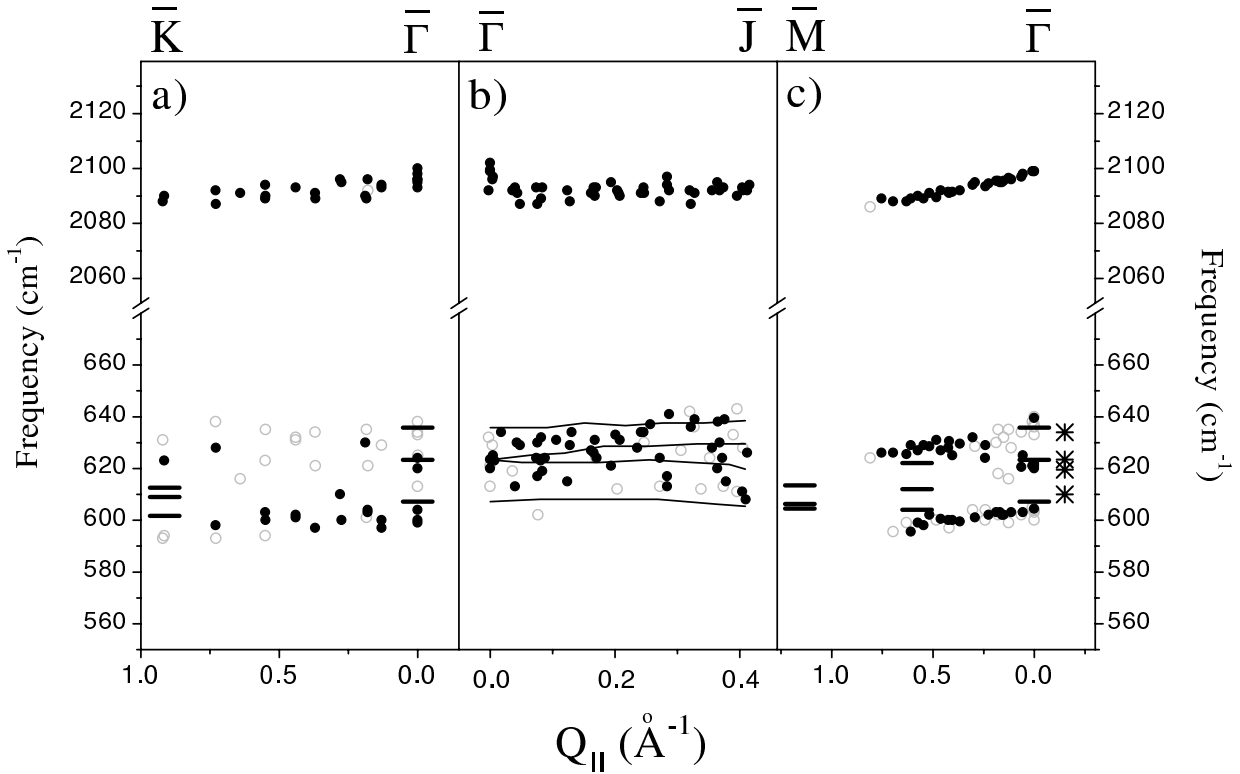


Figure 3.21: Dispersions of monohydride related vibrations on Si(100)-(2 $\times$ 1) surfaces. Distinct vibrations are marked by closed circles. Broad structures and shoulders are marked by open circles. Dispersions in  $\overline{\Gamma\bar{K}}$  (a) and  $\overline{\Gamma\bar{J}}$  (b) directions on vicinal samples and in  $\overline{\Gamma\bar{M}}$  direction (c) on a nominally flat surface are shown. Theoretical calculated vibrations are presented with lines and bars [125] and with stars [6].

with strong decay of the structure maximum. These observations support the conclusion of three-mode structure of the peak centered at  $621\text{ cm}^{-1}$  in the  $\Gamma$ -point. This conclusion is also supported by comparison with the theoretical predictions included in Fig. 3.21.

For the well-ordered (3 $\times$ 1)-H phase on Si(100), HREEL spectra are compared with the corresponding elastic peak profiles in Fig. 3.22. On this surface mono- and dihydride species coexist (see Fig. 3.10), consequently the vibrational characteristics of the two species should be superimposed in the spectra if they do not couple with each other. Apart from the monohydride triplet around  $621\text{ cm}^{-1}$ , only one single peak with a frequency of  $655\text{ cm}^{-1}$  can be extracted from the data. It is associated with the dihydride wagging mode [106, 126, 116]. At the position of the dihydride scissor at  $\sim 907\text{ cm}^{-1}$  [126, 116] in our experiments a double peak constituted by vibrations at  $900$  and  $915\text{ cm}^{-1}$  can be resolved in Fig. 3.22. Beside the  $\sim 4\text{ cm}^{-1}$  blue shift of the Si-H stretch center, comparing the (2 $\times$ 1) and the (3 $\times$ 1) structures, a broad structure around  $2138\text{ cm}^{-1}$  is present in the spectra. This feature remains unchanged after annealing up to 600 K where all defect and step adsorbed hydrogen together with the trihydride are desorbed. The peak remains in parallel with a preserved sharp (3 $\times$ 1) LEED pattern. An assignment of the  $2138\text{ cm}^{-1}$  vibration as intrinsic of the ordered dihydride species, probably an asymmetric Si-H<sub>2</sub> stretching mode, is plausible. For the SiH<sub>2</sub> rocking mode a vibration of  $485\text{ cm}^{-1}$  has been reported [106] which is comparable with a peak at  $475\text{ cm}^{-1}$  in our investigation but this

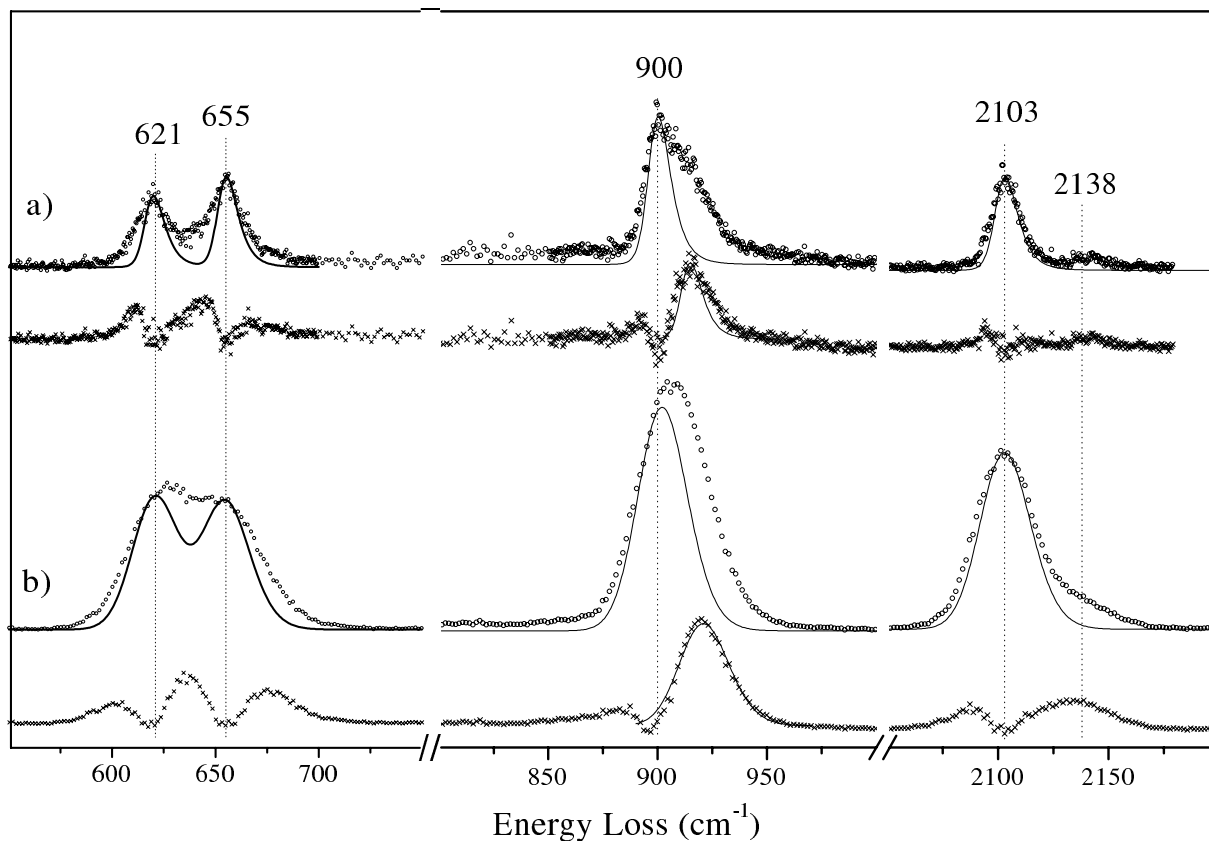


Figure 3.22: HREEL spectra (open circles) of H/Si(100)-(3 $\times$ 1) surfaces compared with corresponding elastic peak profiles (solid lines) and their subtraction products (cross symbols). The surface passivations were performed by atomic hydrogen exposition at 400 K. a) vicinal sample oriented in a  $\overline{\Gamma J}$  direction, b) nominally flat substrate with  $\overline{\Gamma M}$  azimuthal orientation. The electron primary energy was 4 eV and temperature 90 K.

assignment is not obvious because of the possible coupling to the substrate phonons.

Our results for the adsorbate related vibrations on Si(100)-(2 $\times$ 1)-H, Si(100)-(3 $\times$ 1)-H and Si(100)-(2 $\times$ 1)-D surfaces measured at 90 K are summarized and compared with the values reported in literature given in Tab. 3.2.

Modes	(2×1)				(3×1)		(1×1)
sym. Si-H str.	2099	2098.8 <sup>a</sup>			2103	2100.5 <sup>b</sup>	2083 <sup>c</sup>
		2100 <sup>c</sup>					2083 <sup>d</sup>
		2099 <sup>d</sup>					
		2100 <sup>g</sup>					
asym. Si-H str.	–	2087.5 <sup>a</sup>			–	2094.7 <sup>b</sup>	2070 <sup>c</sup>
		2085 <sup>c</sup>					2072 <sup>d</sup>
		2088 <sup>d</sup>					
Si-H bend.	639*	621 <sup>c</sup>	636 <sup>i</sup>	634 <sup>j</sup>	622		620 <sup>c</sup>
	621.5	635 <sup>g</sup>	623 <sup>i</sup>	623.5 <sup>j</sup>	~ 640*		630/640 <sup>c</sup>
	606*	640 <sup>h</sup>	607 <sup>i</sup>	619.5 <sup>j</sup>	~ 603*		
		624 <sup>h</sup>		610 <sup>j</sup>			
sym. Si-H <sub>2</sub> str.					–	2091.3 <sup>b</sup>	2107 <sup>d</sup>
						2091 <sup>d</sup>	2090 <sup>e</sup>
						2104 <sup>f</sup>	2120 <sup>g</sup>
asym. Si-H <sub>2</sub> str.					2138	2103.8 <sup>b</sup>	2118 <sup>c</sup>
						2104 <sup>d</sup>	2117 <sup>d</sup>
Si-H <sub>2</sub> scissor					900*	905 <sup>f</sup>	907 <sup>c</sup>
					915*	907 <sup>c</sup>	875 <sup>e</sup>
							915 <sup>g</sup>
Si-H <sub>2</sub> waging					655	657 <sup>f</sup>	658 <sup>c</sup>
							642 <sup>e</sup>
							650 <sup>g</sup>
Si-H <sub>2</sub> rocking					(475)		485 <sup>g</sup>
							400 <sup>e</sup>
sym. Si-H <sub>3</sub> str.							2131 <sup>c</sup>
							2129 <sup>d</sup>
asym. Si-H <sub>3</sub> str.							2142 <sup>c</sup>
							2139 <sup>d</sup>
sym. Si-H <sub>3</sub> scissor							858 <sup>c</sup>
asym. Si-H <sub>3</sub> scissor							933 <sup>c</sup>
sym. Si-D str.	1527	1528 <sup>a</sup>					
asym. Si-D str.		1519 <sup>a</sup>					
Si-D bend.	410						

Table 3.2: Vibrational modes of atomic hydrogen(deuterium) adsorbed on Si(100). The frequencies are in  $cm^{-1}$  and present results from this work (“\*” denotes data resulting from fitting), measured at 90 K and compared with data reported in the literature. [107]<sup>a</sup>, [112]<sup>b</sup>, [116]<sup>c</sup>, [127]<sup>d</sup>, [128]<sup>e</sup>, [126]<sup>f</sup>, [106]<sup>g</sup>, [129]<sup>h</sup>, [125]<sup>i</sup>+81  $cm^{-1}$  and [6]<sup>j</sup>+34  $cm^{-1}$ .

# Chapter 4

## Surface phonons

The details of the surface structural rearrangement are very important both from a scientific and technological point of view. The surface structural characteristics can be studied by examination of the surface vibrational properties which provide direct experimental access to the interaction between the surface structural degrees of freedom and the surface electronic system (see section 1.1). In this chapter an investigation of the vibrational properties of bare and H(D) passivated Si(100) surfaces is presented.

### 4.1 Overview

While inelastic scattering of He atoms and HREELS (see section 1.3 and subsection 1.3.2) have proved to be successful techniques for surface vibrational investigations by measuring phonon dispersion curves for numerous surfaces, as far as we know only two experimental studies of the phonon dispersions have been performed on Si(100) [7, 8]. In contrast, many theoretical investigations of the Si(100) surface vibrations are available: based on the tight-binding theory Allan and Mele investigated various reconstructions of clean and hydrogenated surfaces in a series of studies [130, 125, 131, 132, 133]; Mazur and Pollmann performed lattice-dynamical calculations on a semi-infinite system [134]; Weakliem and Carter analyzed the vibrations by molecular dynamics simulations [135]; Fritsch and Pavone applied an *ab initio* linear-response formalism based on density functional theory [52]; and recently Tütüncü, Jenkins and Srivastava used an adiabatic bond-charge model for the phonon dispersion determination [136]. Most of the above-mentioned theoretical studies considered a  $(2\times 1)$  reconstructed surface with buckled dimers. Characteristic vibrations of the Si(100)- $(2\times 1)$  are those involving dimer bond deformations following the dimer atoms motions. The displacement patterns of the typical surface phonon modes summarizing the theoretical calculations are shown in Fig. 4.1. The lowest phonon frequency range contains the acoustic band related to the Rayleigh waves (RW), demonstrated by example **A**. Above the acoustic band a dimer rocking mode (**r**) around 25 meV is predicted. The dimer swinging (**s**) and twisting (**t**) modes are expected around 44 and 54 meV, respectively. The dimer stretching (**ds**) modes are also localized in the latter frequency range. The higher frequency boundary of the surface phonon continuum is marked by a subsurface bond (**sb**) mode with dominant motions of the atoms in the second and third layer. The **sb**

mode is predicted to split off the bulk optical phonon bands. Most of the surface characteristic vibrations appear as resonances based on their location in the  $(2 \times 1)$  projection of the bulk phonon continuum. Surface phonons are the vibrations split off the bulk phonon continuum above and below it or in its gaps.

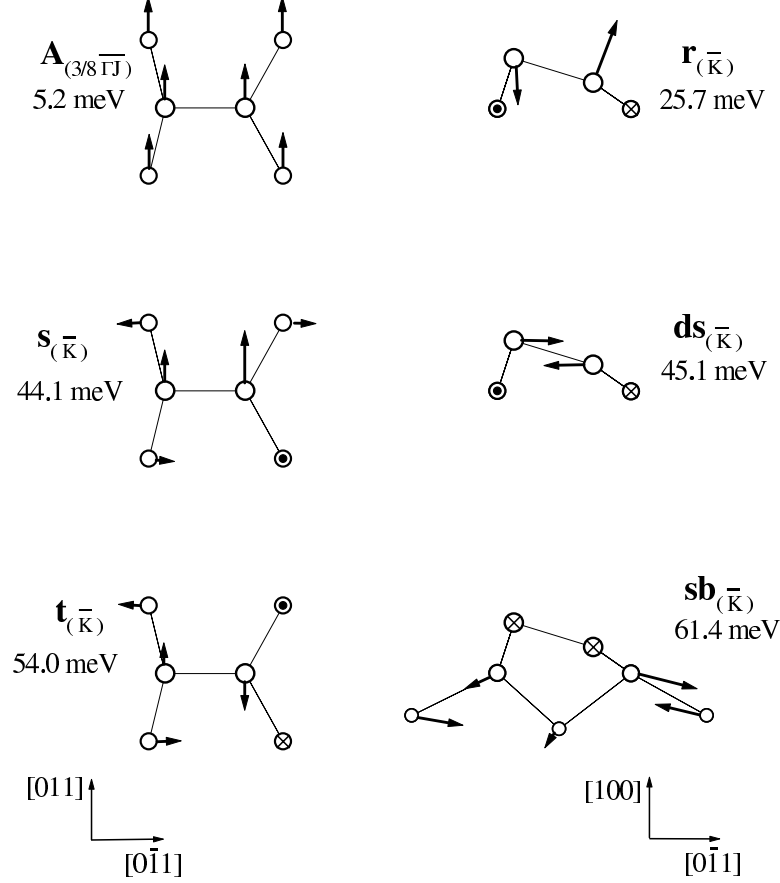


Figure 4.1: Displacement patterns of the characteristic vibrations on a Si(100)- $(2 \times 1)$  surface. "A" is an acoustic mode [137]; "r" is a dimer rocking mode [130]; "s" is a dimer swinging mode [130]; "ds" is a dimer stretching mode [137]; "t" is a dimer twisting mode [136]; and "sb" is a subsurface bond mode involving dominant motions of the second and third layer atoms [130].

The goal of the present work is to provide detailed experimental characterization of the vibrational properties of bare and H(D) passivated Si(100) surfaces. The experiments have been performed on vicinal and on nominally flat Si(100) crystals as is described in section 3.2. The phonon dispersions are determined from off-specular HREEL spectra taken in the following azimuthal directions of the  $(2 \times 1)$  SBZ (see Fig. 3.8): along  $\bar{\Gamma}\bar{J}$  and  $\bar{\Gamma}\bar{K}$  on single domain and along  $\bar{\Gamma}\bar{M}$  on double-domain Si(100) crystals. Thus all high-symmetry points of the  $(2 \times 1)$  SBZ are covered as the  $\bar{M}$  point is equivalent to the  $\bar{J}$  point. The wave vector  $Q_{\parallel}$  was calculated by

$$Q_{\parallel} = \mathbf{k}_{\parallel}^i - \mathbf{k}_{\parallel}^s = \frac{2m}{\hbar} \sqrt{E_p} (\sin\theta_i - \sin\theta_s), \quad (4.1.1)$$

where  $\mathbf{k}_{\parallel}^i$  and  $\mathbf{k}_{\parallel}^s$  are the projections of the incident and scattered electron wave vector onto

the plane parallel to the surface.  $\theta_i$  and  $\theta_s$  are the angles between the surface normal and the incoming and outgoing electron beams, respectively. In all HREELS experiments the electron scattering plane contained the surface normal and  $\theta_i$  was in the  $60\div 65^\circ$  range. The phonon dispersion measurement series were made for constant incident electron energy and k-vector swept by rotating the sample around an axis lying in the surface plane and perpendicular to the scattering plane. By rotating the sample with angle  $\varphi$  relative to the specular position the  $\theta_i + \theta_s$  value was kept constant ( $\sim 120^\circ$ ) and equal to  $\theta_i^{spec} + \theta_s^{spec}$ , where

$$\theta_i = \theta_i^{spec} + \varphi \quad \text{and} \quad \theta_s = \theta_s^{spec} + \varphi. \quad (4.1.2)$$

As the impact scattering cross-sections of the surface phonons in the off-specular measurements are hardly predictable, we examined the entire electron primary energy range from 4 to 250 eV with 10 eV steps and constant values of the corresponding  $Q_{\parallel}/\overline{\Gamma J}$ ,  $Q_{\parallel}/\overline{\Gamma K}$ , and  $Q_{\parallel}/\overline{\Gamma M}$  for the three azimuthal directions. Detailed measurements varying the wave vector were made only for electron primary energies where intensive spectral features appear in the substrate phonon region below  $550 \text{ cm}^{-1}$ . The elastic peak FWHM was between 15 and  $35 \text{ cm}^{-1}$  depending on the primary energy, the temperature, the azimuthal orientation and the doping of the substrate. All results presented here from  $\overline{\Gamma J}$  and  $\overline{\Gamma K}$  oriented samples were obtained at 90 K. From the  $\overline{\Gamma M}$  oriented sample measurements at 90 as well as at 300 K are described. The phonon dispersion data points are extracted from the HREEL spectra applying a fitting procedure outlined in Appendix A. Close symbols are used to denote strong well defined peaks in the HREEL spectra while open symbols are denoting broad or weak structures and also shoulders. This way of presentation will be used in all figures presenting phonon dispersion data.

## 4.2 Phonons on bare Si(100) surfaces

One of the fundamental requirements for an off-specular HREELS measurement is the calibration of the scattering geometry as it is essential for calculation of the parameter which enters in the phonon dispersion  $\omega(Q_{\parallel})$ . The selected azimuthal orientations (see Fig. 3.8) in our experiment allow us to cross electron diffraction spots (see Fig. 3.6). The electron diffraction maxima appear as peaks in the spectrum of the elastic beam intensity as a function of the off specular angle  $\varphi$ . Figure 4.2 shows electron elastic beam intensities as a function of  $Q_{\parallel}$ , normalized to the corresponding  $(2\times 1)$  SBZ boundaries. Even integers of the normalized  $Q_{\parallel}$  values correspond to diffraction maxima, referring to next  $\Gamma$ -points, while odd integers correspond to SBZ boundaries. The curve for a vicinal sample oriented parallel to the surface dimers (see Fig. 4.2 c) has sharp intensive peaks at  $Q_{\parallel}/|\overline{\Gamma J}|$  with values of 0 and 2, corresponding to diffraction maxima of a  $(2\times 1)$  unit cell. For the double domain substrate shown in Fig. 4.2 (b) the main features remain sharp together with a broad structure at  $Q_{\parallel}/|\overline{\Gamma J}|=1$ . The observed broad peak corresponds to a diffraction maximum of a  $p(2\times 2)$  unit cell where a  $\overline{M}$ -point of the  $(2\times 1)$  SBZ is a  $\overline{\Gamma}$ -point of the  $p(2\times 2)$  SBZ. The latter suggests that a minor area with a  $p(2\times 2)$  reconstruction is present on the flat surface. On a single domain crystal oriented along the  $\overline{\Gamma K}$  direction, a broadening of the peaks is visible in Fig. 4.2 (a). The broadening is due to the sample orientation which is close to the diffraction spot-split direction. This split is along

the  $\overline{\Gamma J}$  direction illustrated in the LEED pattern in Fig. 3.6 (b) and is a result of the periodic terraces and double-atomic steps formed on the surface.

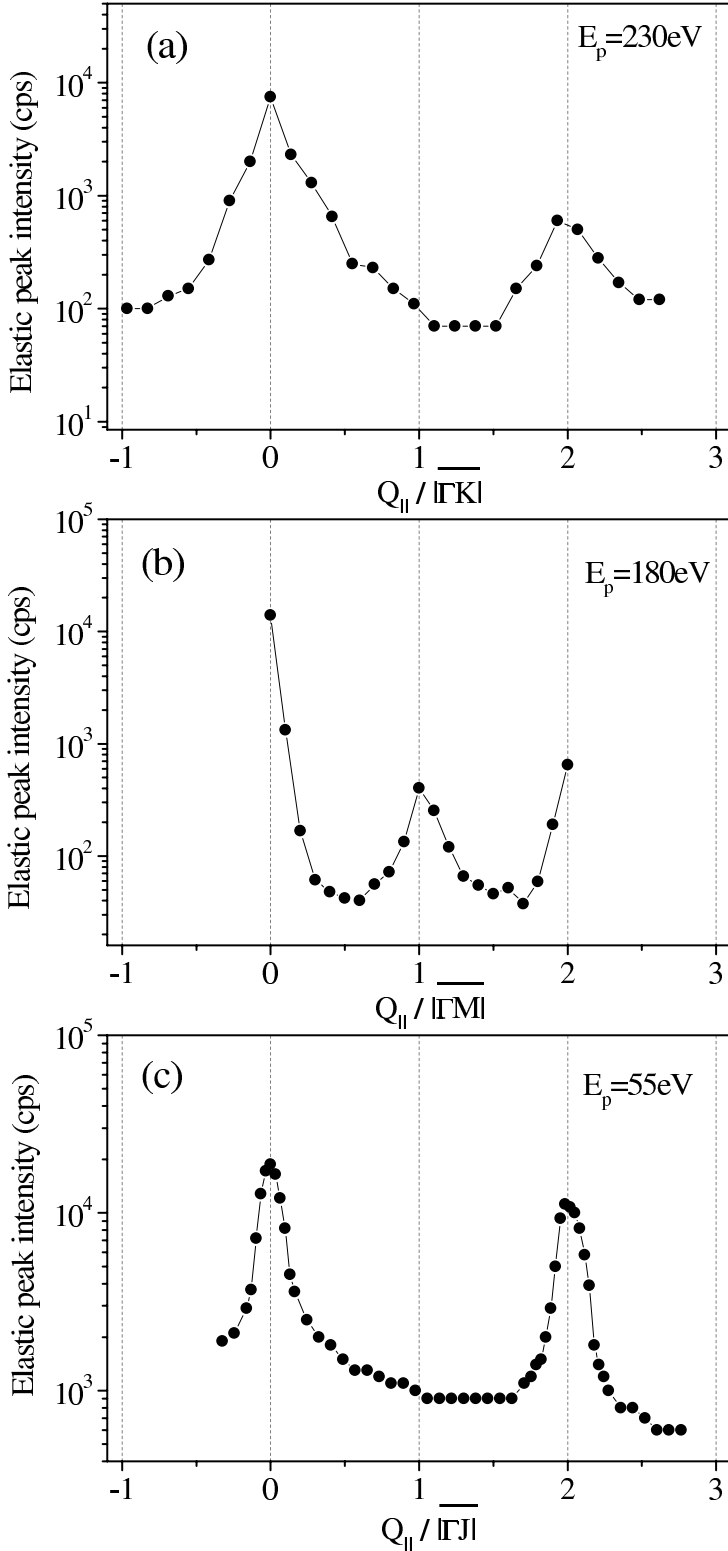


Figure 4.2: Elastic peak intensities on bare Si(100) surfaces as a function of the parallel wave vector  $Q_{||}$ , normalized by the corresponding SBZ boundaries. In (a) and (c) measurements at 90 K on vicinal Si(100) surfaces are presented with  $\overline{\Gamma K}$  and  $\overline{\Gamma J}$  azimuthal orientations, respectively. (b) shows results achieved at 300 K on a nominally flat surface oriented in the  $\overline{\Gamma M}$  direction.

Figure 4.3 shows HREEL spectra taken with different electron incident energies ( $E_p$ ) and for a constant  $Q_{||} / |\overline{\Gamma J}| = Q_{||} / |\overline{\Gamma K}| = Q_{||} / |\overline{\Gamma M}| = 0.8$ . Above  $200 \text{ cm}^{-1}$  no intense structures are observed in all three azimuthal directions. Below  $200 \text{ cm}^{-1}$  a multiple-peak structure is detected.

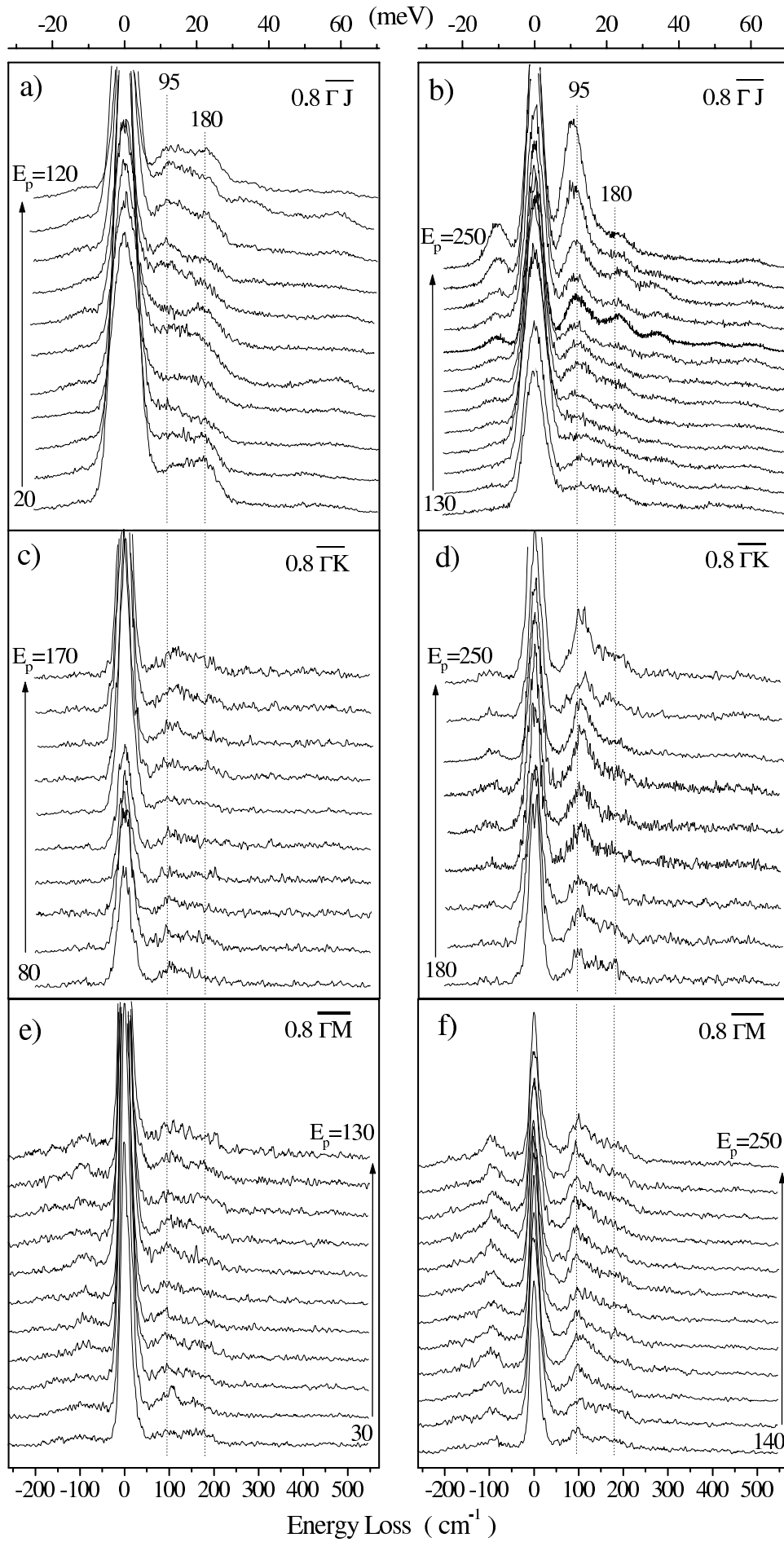


Figure 4.3: HREEL spectra on bare Si(100) surfaces for various electron primary energies ( $E_p$ ) along three different directions:  $\overline{\Gamma J}$ ,  $\overline{\Gamma K}$  and  $\overline{\Gamma M}$ . All spectra are with constant  $Q_{\parallel}/|\overline{\Gamma J}| = Q_{\parallel}/|\overline{\Gamma K}| = Q_{\parallel}/|\overline{\Gamma M}| = 0.8$ . The arrows indicate the direction of  $E_p$  (eV) in steps of 10 eV. (a) and (b) are taken at 90 K on a vicinal sample along the  $\overline{\Gamma J}$  direction. (c) and (d) are results from a single-domain substrate oriented along  $\overline{\Gamma K}$  at 90 K. (e) and (f) are measured at 300 K on a nominally flat surface along the  $\overline{\Gamma M}$  direction.

The prominent peak in this structure around  $95 \text{ cm}^{-1}$  has maxima at primary energies:  $\sim 250 \text{ eV}$  for  $0.8\overline{\Gamma J}$ ,  $\sim 230 \text{ eV}$  for  $0.8\overline{\Gamma K}$ ,  $\sim 170 \text{ eV}$  and  $\sim 210 \text{ eV}$  for  $0.8\overline{\Gamma M}$ . Small shifts of the peak with the electron incident energy variation are visible in Fig. 4.3 (b, d, f). These shifts cannot be due to dispersion because of the fixed position in the SBZ. Rather they are due to an intensity variation as a function of  $E_p$  of different close lying losses composing the peak. Another prominent peak in the  $0.8\overline{\Gamma J}$  spectra in Fig. 4.3 (a, b) located around  $180 \text{ cm}^{-1}$  can be resolved at  $E_p$  with values of 20, 80, 120 and 210 eV. The results presented in Fig. 4.3 demonstrate how the specific dependence on  $E_p$  of the different phonon cross sections can be used for the clear identification of the vibrational modes. Additionally, the cross-section dependence on the electron energy has been examined for  $2.0\overline{\Gamma J}$ ,  $0.4\overline{\Gamma K}$ ,  $0.3\overline{\Gamma M}$  and  $0.5\overline{\Gamma M}$ . Based on these loss intensity examinations, detailed phonon dispersion measurements have been performed for the following  $E_p$ : 8, 210 and 250 eV along  $\overline{\Gamma J}$ ; 150, 180 and 220 eV along  $\overline{\Gamma K}$ ; 30, 180, 220 and 250 eV along  $\overline{\Gamma M}$ . Examples of off-specular measurements along the three investigated azimuthal directions with constant incidence energy are presented in Fig. 4.4. An apparent dispersion of the RW from  $\sim 50$  to  $95/100 \text{ cm}^{-1}$  is visible. The RW intensity in Fig. 4.4 (b, c) decreases with the off-specular angle while the mode at  $\sim 190 \text{ cm}^{-1}$  in Fig. 4.4 (a) passes through an intensity maximum around  $Q_{\parallel}/|\overline{\Gamma J}| \approx 1$ . The value 1 of the normalized parallel momentum corresponds to the first SBZ boundary. With the applied electron energies presented in Fig. 4.4, the phonon dispersion can be followed also in the second and third SBZ. In this way, apart from the cross-section dependence on  $E_p$ , the loss intensity dependence on the off-specular angle can be used for better loss determination, as has been shown in Fig. 4.3 and by comparing spectra corresponding to equivalent points in different SBZ's.

The fitting procedure outlined in Appendix A is applied to extract the exact vibrational frequency from the HREEL spectra. The extracted phonon frequencies from all measurements (different primary energies and three orientations) on the Si(100) surfaces are summarized in Fig. 4.5. Above  $200 \text{ cm}^{-1}$  three vibrational bands are observed. They are most prominent along the  $\overline{\Gamma J}$  direction shown in Fig. 4.5 (b). Below  $200 \text{ cm}^{-1}$  two strong bands are detectable in the three examined directions. The lowest frequency band demonstrates an acoustic mode behaviour as its frequency tends to approach zero at the zone center. It is assigned to the Rayleigh wave (RW). The assignment of the other modes is not straightforward and a comparison with the theoretical calculations is necessary. Such a comparison will be made in the following discussion.

In Fig. 4.6 our data analysis is compared with the few experimental results available in

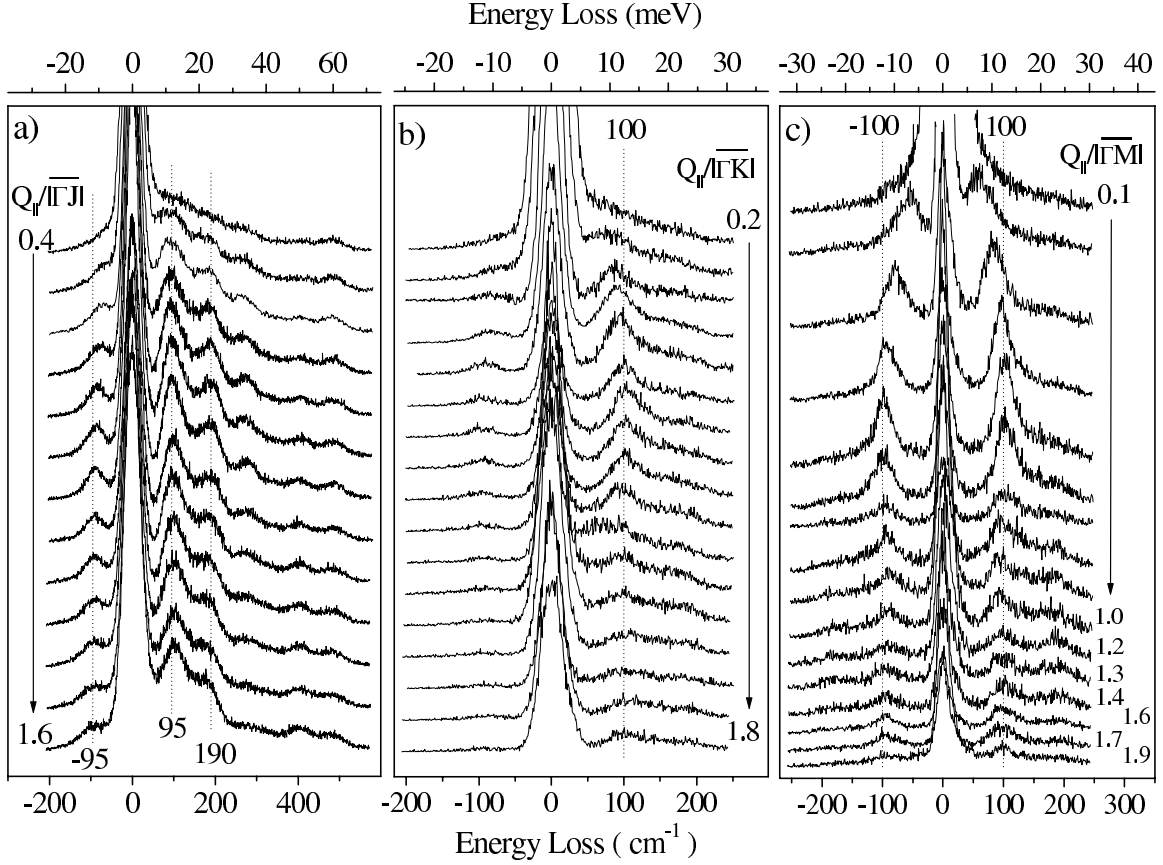


Figure 4.4: Off-specular HREEL spectra on bare Si(100) surfaces. The normalized  $Q_{\parallel}$  increase with 0.1 step is denoted by arrow. (a) and (b) present spectra take at 90 K with electron primary energy 210 and 230 eV on vicinal  $\overline{\Gamma J}$  and  $\overline{\Gamma K}$  oriented samples, respectively. (c) shows measurements at 300 K with incidence energy 250 eV on a double-domain  $\overline{\Gamma M}$  oriented surface.

literature. In Fig. 4.6 our phonon dispersions along the  $\overline{\Gamma J}$  direction, backfolded to the first SBZ, are compared with the HREELS measurements of Takagi *et al.* [8] and the Brillouin light scattering measurements of Dutcher *et al.* [7]. The six phonon bands observed by Takagi *et al.* [8] around the  $\overline{\Gamma}$  point are also detected in our measurements in approximately the same locations. At the  $\overline{\Gamma}$  point Takagi observed a loss around  $250 \text{ cm}^{-1}$  which was not observed by us. Instead we found a peak at about  $280\text{-}290 \text{ cm}^{-1}$ . At  $Q_{\parallel} \approx 0.15 \text{ \AA}^{-1}$  the Takagi's mode with highest frequency is located by  $\sim 45 \text{ cm}^{-1}$  above our upper band. Near the zone boundary the mode at  $\sim 190 \text{ cm}^{-1}$  is red-shifted by  $\sim 30 \text{ cm}^{-1}$  in Takagi's work similar to the RW red shift by  $\sim 20 \text{ cm}^{-1}$ . The observed differences between the phonon dispersions in this work and the results of Takagi *et al.* [8] are due to the fact that Takagi *et al.* have measured on a nominally flat Si(100) surface in an orientation where the two inequivalent  $\overline{\Gamma J}$  and  $\overline{\Gamma J'}$  directions of the  $90^\circ$  rotated domains overlap. Thus their vibrational spectra contain superimposed dispersions from two different directions in a reciprocal space. Additionally the data extraction in Ref. [8] from their spectra remains unclear especially concerning the background determination. Our Rayleigh mode data correspond to the Brillouin light scattering data [7] nicely, significantly

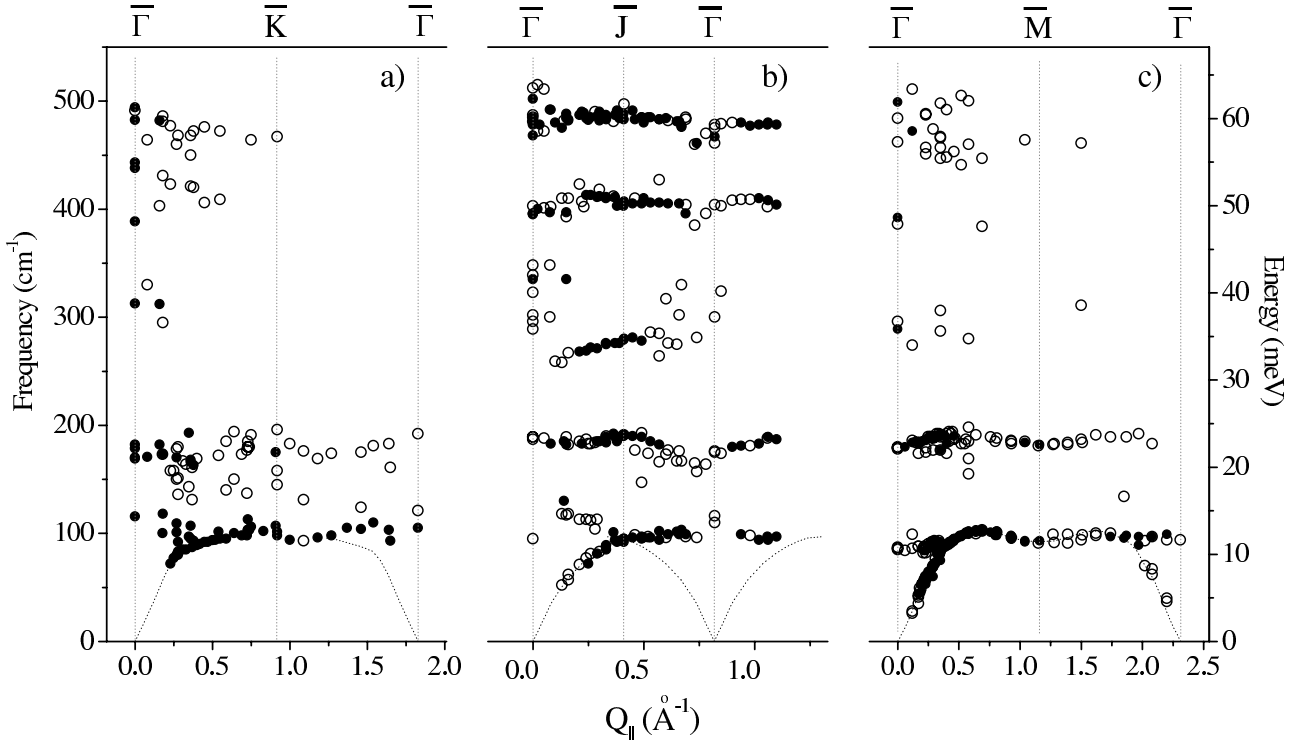


Figure 4.5: Phonon dispersions on Si(100) surfaces, measured in (a)  $\overline{\Gamma K}$ , (b)  $\overline{\Gamma J}$  and (c)  $\overline{\Gamma M}$  directions in the  $(2 \times 1)$  SBZ. The zone centers and boundaries are marked by the high-symmetry points of the  $(2 \times 1)$  SBZ.

better than those of Takagi *et al.* [8]. The small blue shift ( $\sim 10 \text{ cm}^{-1}$ ) in the lower  $Q_{\parallel}$  region could come from our fitting uncertainty (open circles in Fig. 4.6) related to the RW position in the steep tail of the elastic peak. Taking into account the above comparisons we can conclude that our results are in good agreement with the few published experimental results.

The surface phonons are expected to dominate a HREELS vibrational spectrum compared to the resonances and the bulk phonons. In Fig. 4.7 the phonon dispersions are summarized together with the projection of the bulk phonons in the  $(2 \times 1)$  SBZ. Most of the observed phonon bands fall into the bulk phonon projection which makes them resonance modes. The only exception is the lowest lying mode at  $\sim 100 \text{ cm}^{-1}$  around the  $\overline{K}$  and at the  $\overline{M}$  points. The split-off the bulk acoustic band makes this mode a surface vibration for the  $(2 \times 1)$  SBZ. Gaps exist in the bulk phonon projection near the zone boundaries where vibrational modes could appear as surface localized (see Fig. 4.7). When a vibration falls into one of these windows, it should be seen in the HREEL spectrum if it is not forbidden by the operating scattering selection rules and if its cross section is significant. At this  $Q_{\parallel}$ , far from the specular direction, only the impact scattering mechanism operates. In it odd modes related to the scattering plane are forbidden. In the orientations used in our study only in the  $\overline{\Gamma J}$  direction this selection rule couples with the  $(2 \times 1)$  surface symmetry. In the  $\overline{\Gamma K}$  and  $\overline{\Gamma M}$  no restriction from this selection rule is expected and if intense surface phonons exist in the phonon continuum gaps they should be sharp features in the electron loss spectrum. Additionally in all theoretical calculations mentioned in the beginning of this chapter such vibrational modes are predicted. In our experimental dispersions

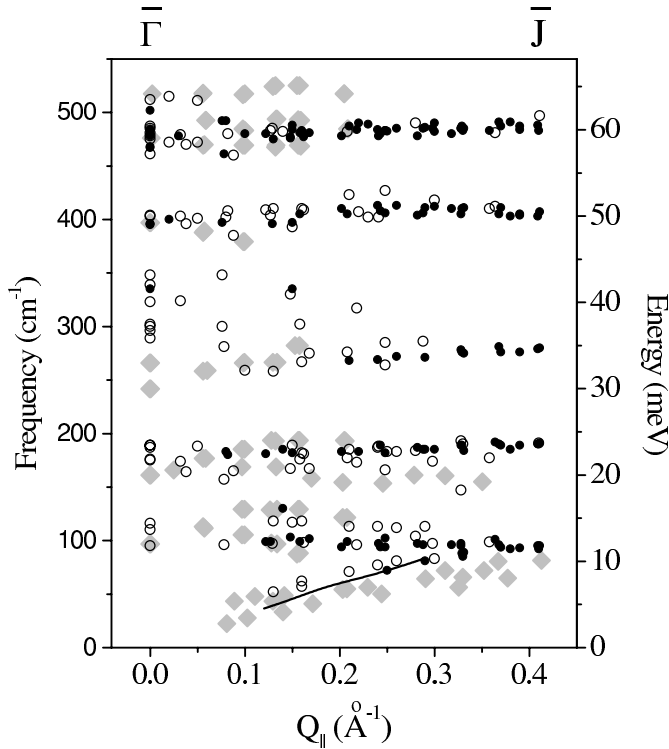


Figure 4.6: Comparison of our results with experimental phonon dispersions available in literature. The data presented are from this work (open and closed circles), from HREELS measurements [8] (grey squares) and from Brillouin light scattering measurements [7] (solid line).

there are no gap-modes at 90 K as well as at 300 K. The same is the result in the work of Takagi *et al.* [8]. Two explanations are plausible, either the surface reconstructs not in  $(2 \times 1)$  but in  $c(4 \times 2)$  or/and  $p(2 \times 2)$  symmetries (Fig. 3.2); or the cross sections are rather small. In the specular measurements where the dipole scattering mechanism could be dominant the experimental results can be compared with theoretical calculations of the dipole activity of the surface phonons as was suggested by Takagi. Such calculations for the phonon-assisted contribution to the surface conductivity for the  $(2 \times 1)$ ,  $c(4 \times 2)$  and  $p(2 \times 2)$  reconstructions on Si(100) are available in the work of Alerhand and Mele [132] and are presented in Fig. 4.7. The comparison of the structures in the surface conductivity and our phonon positions at the  $\bar{\Gamma}$ -point favour the two larger unit cells. There is no feature in our spectra which could be related to the structure at around  $250 \text{ cm}^{-1}$  of the  $(2 \times 1)$ -conductivity. In contrast we have good agreement with the  $c(4 \times 2)$ - and  $p(2 \times 2)$ -spectra in the same region. In the  $400\text{-}550 \text{ cm}^{-1}$  range a single structure in the  $(2 \times 1)$  curve becomes triple in the  $c(4 \times 2)$  and  $p(2 \times 2)$  curves, again the latter being in agreement with our data. Taking a surface conductivity envelope only over the vertical and along dimer bond polarizations in accord with measurements in  $\bar{\Gamma}\bar{J}$  (see Fig. 4.7(b)), a double structure appears, corresponding very well to the two phonon bands in the lower frequency range of the  $\bar{\Gamma}\bar{J}$  dispersions. For the other two investigated directions it is reasonable to use a conductivity envelope involving all polarizations (see Fig. 4.7(a,c)). In this polarization summation the only big difference in the curves of the two larger unit cells appears in the lower frequency range. This difference, however, cannot be resolved in our experiment. Thus, accounting only for the specular vibrational measurements and the comparison with the calculated dipole response function based on electron-phonon coupling [132], one can deduce that at low temperatures the phonon spectrum corresponds to a  $c(4 \times 2)$  or/and  $p(2 \times 2)$  symmetry. Additionally, the systematic discrepancy visible in Fig. 4.8 between the experimental frequencies of the characteristic  $\mathbf{RW}$ ,  $\mathbf{r}$ , and  $\mathbf{sb}$  modes and the theoretical

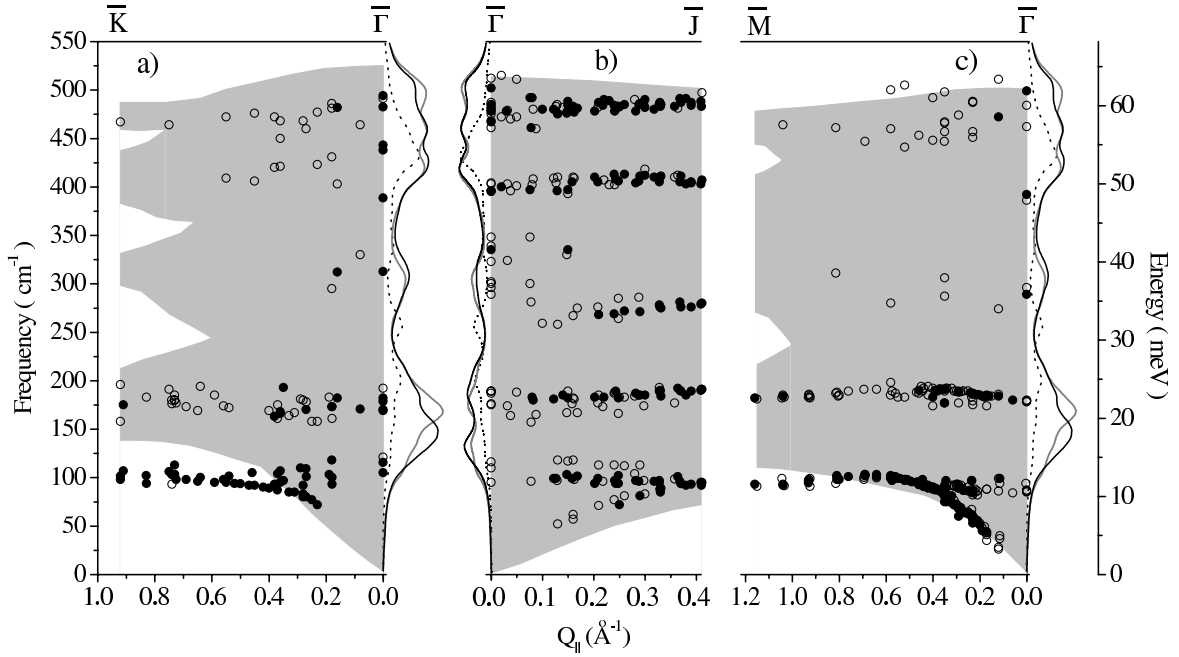


Figure 4.7: Phonon dispersion data (open and close circles) together with the bulk phonons projected (PBP) in a  $(2\times 1)$  SBZ (dark areas). All data measured out of the first SBZ are backfolded. The curves attached to the  $\bar{\Gamma}$ -points illustrate calculated phonon-assisted surface conductivities for  $(2\times 1)$  (dotted line),  $c(4\times 2)$  (black solid line) and  $p(2\times 2)$  (gray solid line) surface reconstructions [132]. (a) and (c) present phonon dispersions in the  $\bar{\Gamma}\bar{K}$  and the  $\bar{\Gamma}\bar{M}$  directions, respectively, together with full polarization summation of the conductivity. (b) shows phonon dispersions in the  $\bar{\Gamma}\bar{J}$  direction with conductivity summation over the vertical and along dimer bond polarizations.

calculations for the buckled  $(2\times 1)$  reconstruction [132, 134, 52, 136] supports the  $c(4\times 2)$  or  $p(2\times 2)$  structures. For the **RW**, which is predicted to be located below the acoustic bulk bands, the difference is  $>10 \text{ cm}^{-1}$  at all high symmetry SBZ points and  $>20 \text{ cm}^{-1}$  at the  $\bar{J}$  point. The highest frequency mode (**sb**) at the  $500\text{-}525 \text{ cm}^{-1}$  region, split off above the optical bulk band, is located  $>20 \text{ cm}^{-1}$  above the highest experimentally observed mode and at the  $\bar{J}$  point this difference become  $>40 \text{ cm}^{-1}$ . For the dimer rocking mode the discrepancy with the theoretical values is in average  $20 \text{ cm}^{-1}$ . This comparison suggests that the calculated surface phonon dispersion for the Si(100)- $(2\times 1)$  with asymmetric dimers is not applicable to the vibrational properties of the Si(100) surface at 90 K. This observation can be extended also to a real Si(100) surface at RT, as will be discussed below.

The buckling direction between neighboring dimers along or across the dimer rows is a source of an additional energy decrease. It is manifested by the  $p(2\times 2)$  and  $c(4\times 2)$  reconstruction geometries. The latter is favored by most of the theoretical investigations and is also observed as dominant at temperatures below 200 K (see the discussion and the works cited in section 3.1). Above 200 K an order-disorder transition occurs leading to  $(2\times 1)$  symmetry at 300 K with a flip-flop motion of the dimers between the two asymmetric geometries shown in Fig. 3.1. As a result the dimers appear symmetric in time averaging STM investigations. The defects

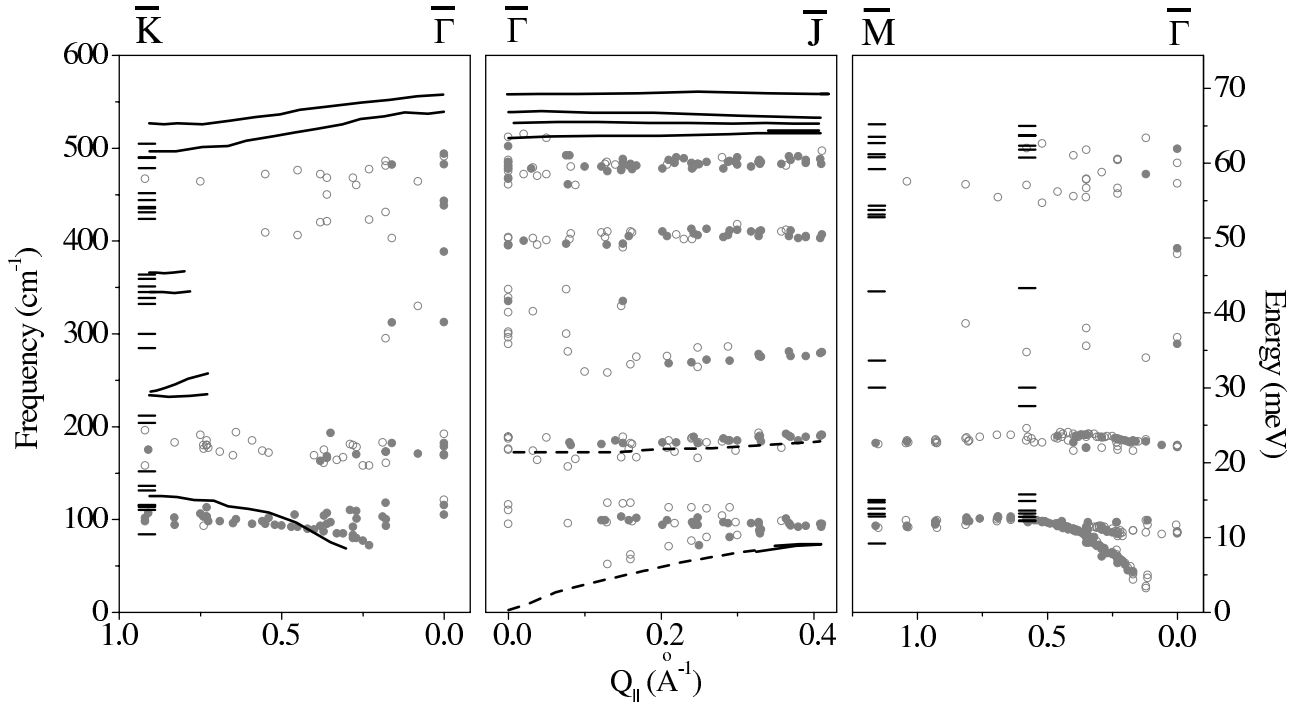


Figure 4.8: Comparison with calculated phonon dispersion for a  $(2 \times 1)$  reconstructed Si(100) surface. The experimental data from this work are shown with open and closed gray circles. The calculated surface phonons are presented with solid lines and horizontal bars and summarize results from Ref. [132, 134, 52, 136]. With dashed lines are plotted calculated resonant modes [52].

and steps present on real surfaces pin their surrounding configuration preventing the flip-flop motion and areas with a  $p(2 \times 2)$  or a  $c(4 \times 2)$  ordering can be observed at RT [45]. Based on finite-temperature *ab initio* molecular dynamics simulations, Shkrebtii *et al.* concluded that at 300 K the Si(100) structure corresponds to a mixture of the  $c(4 \times 2)$  and the  $p(2 \times 2)$  geometries [56]. As the scattering event probes the instantaneous configuration of the surface, we can expect to find phonon dispersions corresponding to the larger unit cell reconstructions also at 300 K. In Fig. 4.9 the results achieved on bare Si(100) with  $\overline{\Gamma M}$  azimuthal orientation at 86 and 300 K are compared. The elastic peak intensity in Fig. 4.9 (a) shows two maxima at  $Q_{\parallel} = 0$  and  $2 \overline{\Gamma M}$  corresponding to diffraction reflexes in all three reconstructions under consideration. The important feature is the structure at the  $\overline{M}$  point ( $Q_{\parallel} = |\overline{\Gamma M}|$ ) present at both temperatures, which can be a reflex coming only from a  $p(2 \times 2)$  unit cell on the surface. The missing temperature dependence of the latter maximum favours a pinning effect of the surface structural inhomogeneities (point defects and steps) over the dynamical coexistence. In the same figure the elastic peak intensity of the H-terminated Si(100)- $(2 \times 1)$ -H is shown where the dimer tilting and the  $p(2 \times 2)$  reconstruction are removed. The disappearance of the maximum at the  $\overline{M}$  point confirms our assignment. In Fig. 4.9(b) the phonon dispersions extracted from the HREEL spectra in Fig. 4.9(c) measured at 86 and 300 K are plotted. Close correspondence between the data at the two temperatures is observed. Following the dispersion of the lowest frequency mode (**RW**) we expect a decrease of its frequency approaching the  $\overline{M}$ -

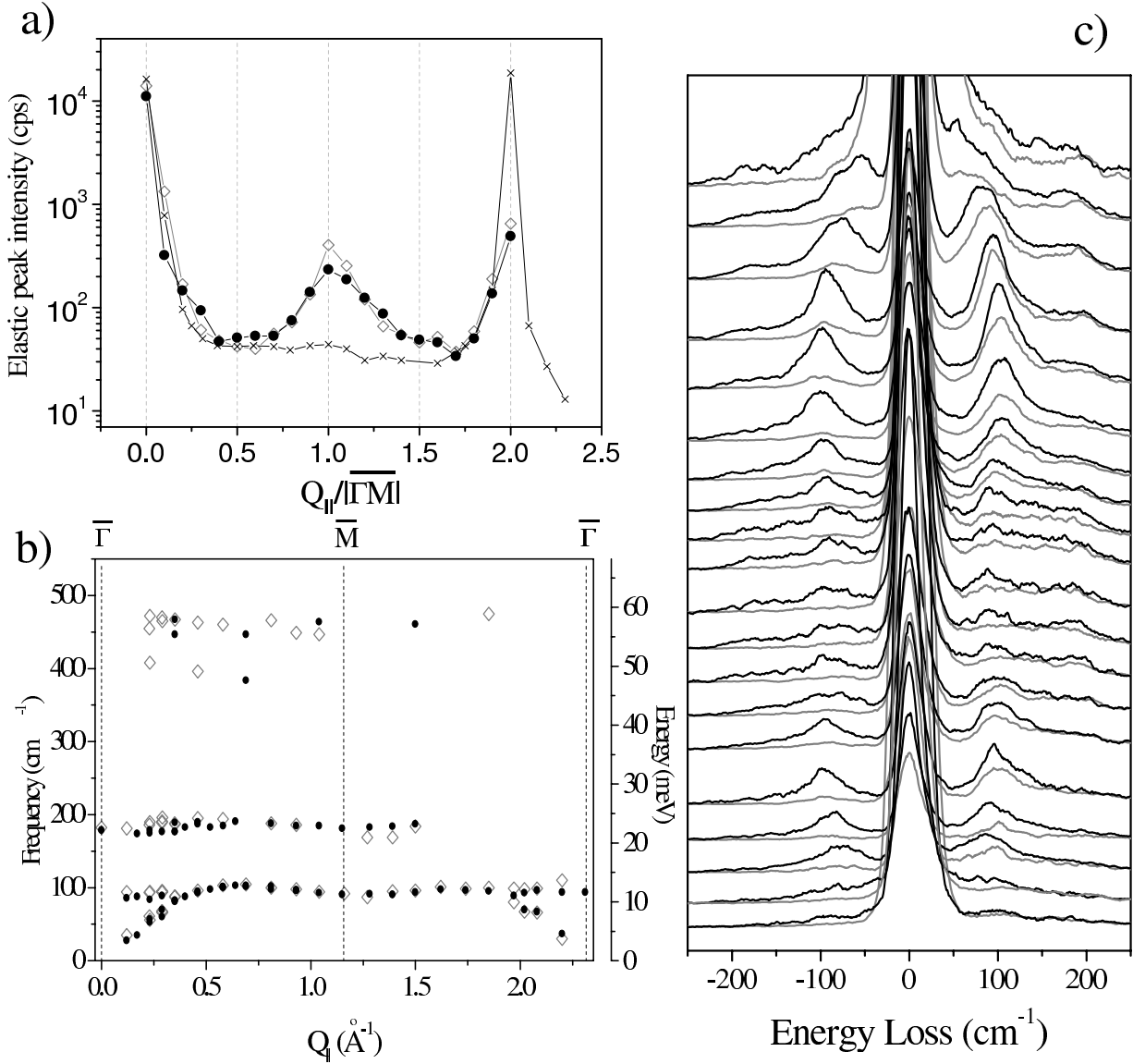


Figure 4.9: HREELS measurements on a bare nominally flat Si(100) surface with  $\overline{\Gamma M}$  azimuthal orientation. The measurements at 86 K are denoted with gray lines and gray open symbols. The investigations at 300 K are presented by black lines and closed symbols. Crosses mark measurements on a Si(100)-(2 $\times$ 1)-H surface. (a) shows the elastic peak intensity as a function of  $Q_{||}$  normalized by the (2 $\times$ 1) SBZ boundary. (b) is a plot of the phonon dispersions in the (2 $\times$ 1) SBZ extracted from the HREEL spectra (c) measured with electron primary energy 180 eV.

point because it is the  $\overline{\Gamma}$  point in the p(2 $\times$ 2) unit cell. Only a slight red shift is observed at this position in the SBZ. In contrast the **RW** frequency decrease appears approaching the next  $\overline{\Gamma}$  point as should be the case for all three geometries. The undetectable influence of the p(2 $\times$ 2) geometry on the RW is consistent with the minority of this phase suggested by the low intensity of its diffraction reflexes (seen in Fig. 4.9 a). However it might explain the peak broadening around the  $\overline{M}$  point in Fig. 4.9 (c). As a (2 $\times$ 1) converts to a c(4 $\times$ 2) reconstruction at 86 K, in detail discussed in chapter 3, the analysis of the results presented in Fig. 4.9 suggests a

domination of the latter phase in the phonon dispersion up to 300 K. Similar observations have been made by Stigler *et al.* for Ge(001) comparing DFT calculations of the phonon dispersion on  $(2 \times 1)$ ,  $c(4 \times 2)$  and  $p(2 \times 2)$  phases with inelastic He atom scattering measurements [138]. The theoretical vibrational studies have been made predominantly for the  $(2 \times 1)$  geometry. There is only one theoretical work containing phonon dispersions on  $p(2 \times 2)$  and  $c(4 \times 2)$  reconstructed Si(100) surfaces [137]. The very good correspondence of the calculations of this group for Ge(100) with inelastic He scattering measurements [138] makes their method reliable as well for Si(100) which has similar features.

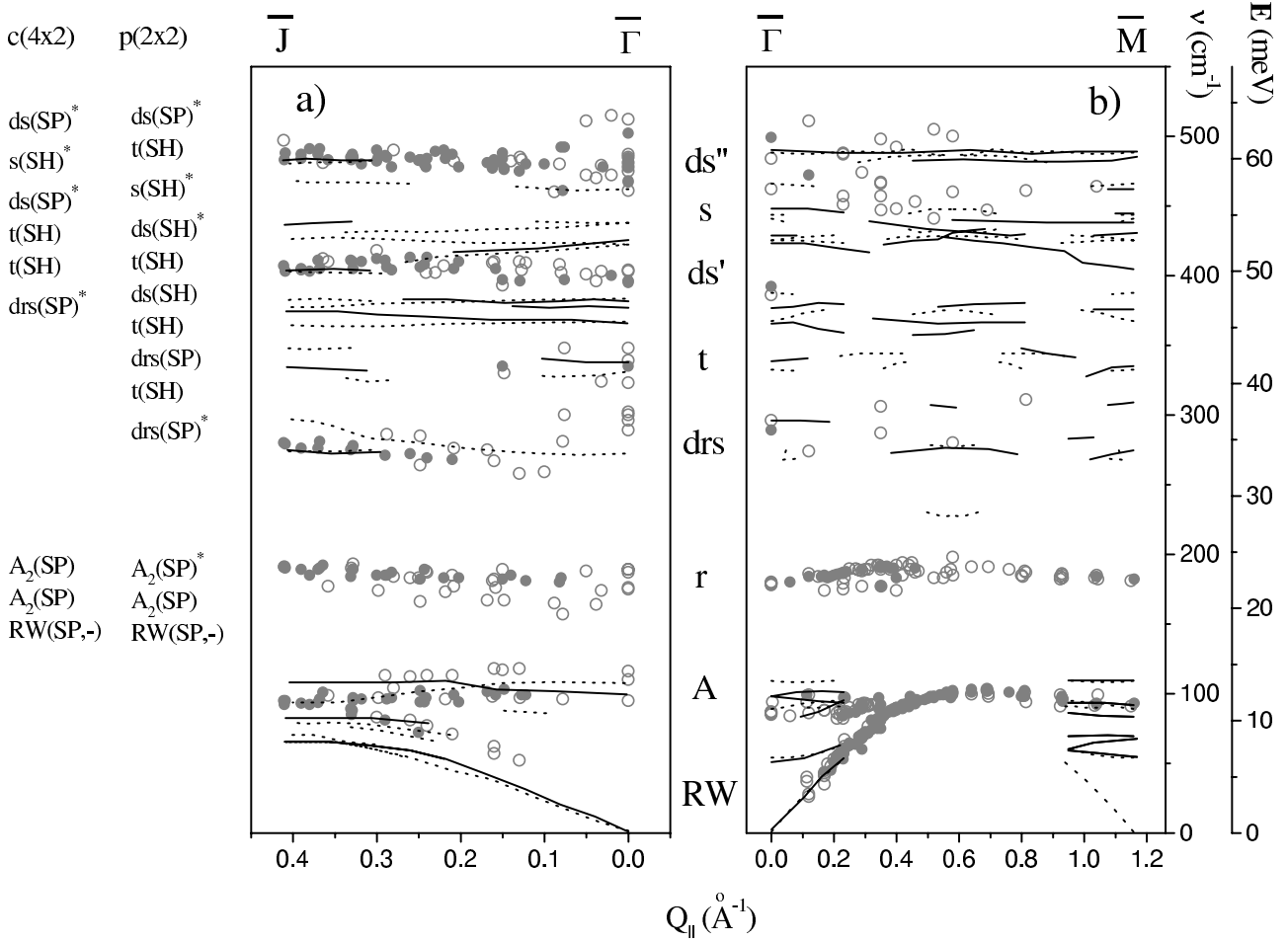


Figure 4.10: Comparison of our experimental phonon dispersions on (a) vicinal and (b) flat Si(100) surfaces with DFT calculations [137]. The experimental data are plotted with open and closed circles. Calculated dispersions are presented for  $c(4 \times 2)$  (solid line) and  $p(2 \times 2)$  (dotted line) symmetries. In the  $\bar{\Gamma}\bar{J}$  direction (a) only even theoretical modes are presented, except the **RW**. The assignment of the theoretical modes at the  $\bar{J}$ -point are on the left-hand side of the figure. The modes coinciding with the experiment are marked with “\*”. Based on this coincidence the measured phonon bands are labeled as is shown in the space between (a) and (b).

In Fig. 4.10 the experimental phonon dispersions are compared with the calculations of Stigler [137] for  $c(4 \times 2)$  and  $p(2 \times 2)$  symmetries on a Si(100) surface. The vibrational modes

involve atoms from the outermost crystal layers and are labeled according to the involved characteristic dimer atom motions as is shown in Fig. 4.1. Only the **drs** mode which involves dimer rocking and swinging is not described in Fig. 4.1. Additionally, the modes are characterized by their polarizations which are in the scattering(sagittal) plane or perpendicular to it. All calculated vibrations [137] are phonon resonances except **A** and **RW** at the  $\bar{J}$ -point for both symmetries and at  $\bar{M}$ -point for a  $c(4\times 2)$  reconstruction. All measured phonon frequencies are in the corresponding bulk phonon projection even at  $\bar{J}$  and  $\bar{M}$ . Eight phonon bands are detected on the real Si(100) surface. In the  $\bar{\Gamma}\bar{M}$  direction (seen in Fig. 4.10 b) the predominance of a  $c(4\times 2)$  phase is confirmed by the **RW** behaviour which does not tend to zero approaching  $\bar{M}$ . The lack of theoretically predicted modes between  $110$  and  $220\text{ cm}^{-1}$  is not because there are no vibrations but because they have not been presented in Ref. [137]. It was only mentioned as an area where a dimer rocking mode exists. The rocking mode value of  $161\div 171\text{ cm}^{-1}$  found in the DFT work of Fritsch *et al.* [52] is close to the experimental value of  $175\div 195\text{ cm}^{-1}$  which is labeled by **r**. Apart from the **RW** and **r** modes, which are detectable in all examined regions of the SBZ, three other bands are prominent along the  $\bar{\Gamma}\bar{J}$ . Namely, the **drs** at  $255\div 300\text{ cm}^{-1}$ , the **ds'** at  $385\div 415\text{ cm}^{-1}$ , and the **ds''** at  $465\div 480\text{ cm}^{-1}$ . Less defined bands are the  $\mathbf{t}_{(\bar{\Gamma})}$  around  $\sim 335\text{ cm}^{-1}$  and the  $\mathbf{s}_{(0.5\bar{\Gamma}\bar{M})}$  around  $\sim 450\text{ cm}^{-1}$  on vicinal and flat surfaces, respectively. On both surfaces the reproducibility of the phonon frequencies at the  $\bar{\Gamma}$  point is within a  $5\text{ cm}^{-1}$  range except for the **A** mode which differs by  $\sim 18\text{ cm}^{-1}$ . Based on DF theory only small modifications in the frequencies and no substantial variations in the eigenvectors of the phonons have been observed in the  $c(4\times 2)$  structure compared to those in the  $p(2\times 1)$  structure [52]. The phonons in the various Si(100) surface reconstructions are the same and the differences come from the back folding of the SBZ. The appearance of the acoustic mode (**A**) at the zone center is a direct result of this back folding. Thus the observed shift of the **A** mode between the vicinal and the flat surfaces could be explained by variation of the phase ratio. An increase of the  $p(2\times 2)$  area and consequently a detectable influence on the phonon dispersion is plausible on a vicinal surface induced by the double steps atomic arrangement. The double step structure shown in Fig. 3.3 reveals an indication for a step induced preferential  $p(2\times 2)$  reconstruction on the terraces.

### 4.3 Phonons on Si(100)-(2×1)-H(D) surfaces

The influence of the dimer asymmetry on the Si(100) phonon dispersions is a very interesting point because it can reveal the vibrations unique for the tilted structure. The driving force of the buckling are the unsaturated silicon bonds left after the surface dimerization which tend to interact with each other by charge transfer from the dimer down to the dimer up atom. A saturation of these bonds with hydrogen or deuterium removes this source of instability leading to symmetric flat-lying dimers with  $(2\times 1)$  symmetry on the surface. The monohydride related vibrations (bending and stretching) lie well above the substrate phonon continuum whereas the monodeuteride bending mode falls in this continuum. The atomic mass ratios between the adsorbate and substrate atoms are small ( $1:32$  for H and  $2:32$  for D), hence a negligible mass effect on the dimer vibrations is expected. Thus the observed dispersion changes with respect

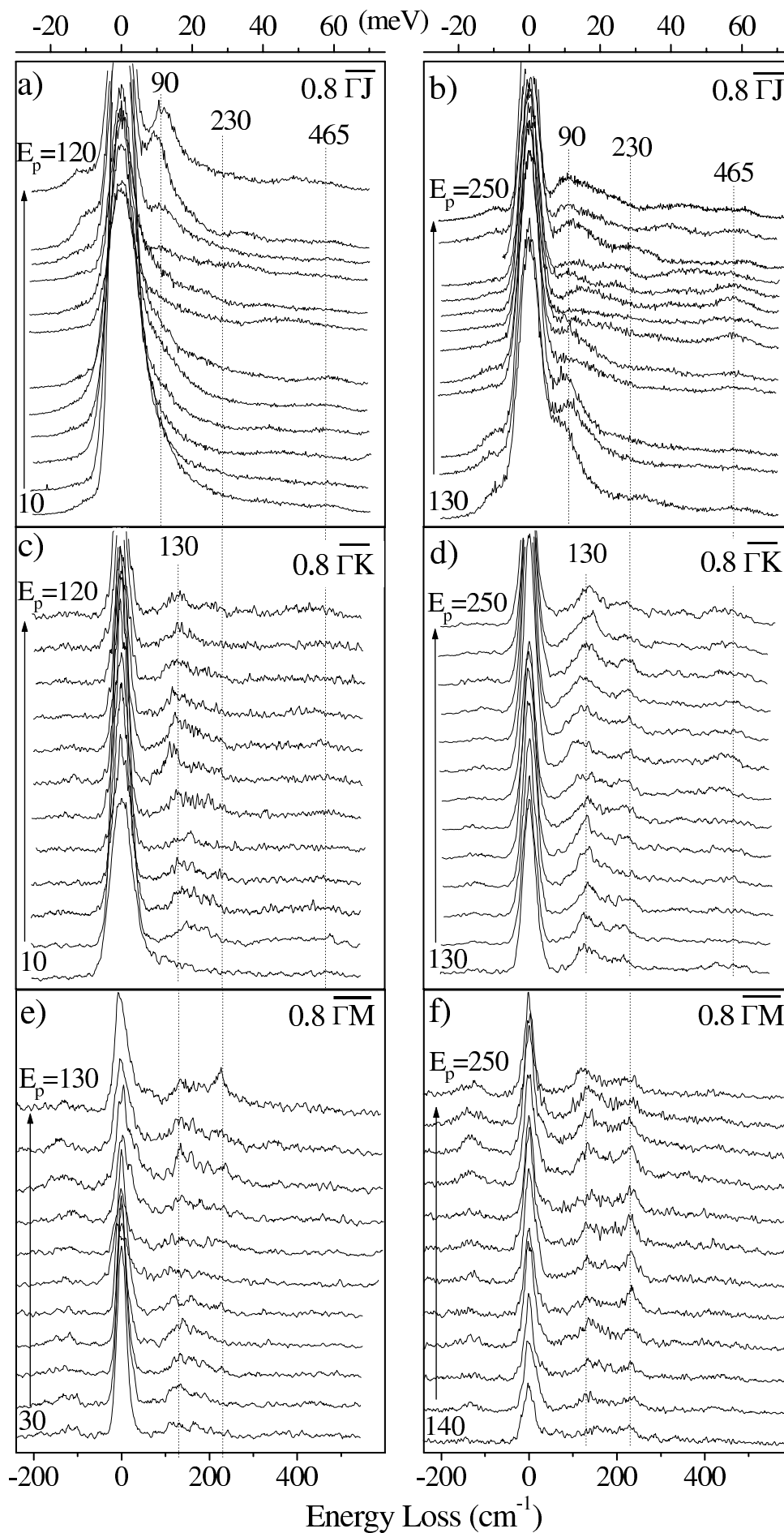


Figure 4.11: HREEL spectra on monohydride Si(100)-(2×1)-H surfaces with various electron primary energies ( $E_p$ ) along three different directions:  $\overline{\Gamma J}$ ,  $\overline{\Gamma K}$  and  $\overline{\Gamma M}$ . All spectra are with constant  $Q_{\parallel}/|\overline{\Gamma J}| = Q_{\parallel}/|\overline{\Gamma K}| = Q_{\parallel}/|\overline{\Gamma M}| = 0.8$ . The arrows indicate the direction of  $E_p$ (eV) in steps of 10 eV. (a) and (b) are taken at 90 K on a vicinal sample along the  $\overline{\Gamma J}$  direction. (c) and (d) are results from a vicinal substrate oriented along  $\overline{\Gamma K}$  at 90 K. (e) and (f) are measured at 300 K on a nominally flat surface along the  $\overline{\Gamma M}$  direction.

to the bare surface could be ascribed to the dimer symmetrisation.

Similar to the phonon dispersion studies using HREELS described in the previous section, studies on the monohydride (monodeuteride) Si(100)-(2×1)-H(D) surfaces have been performed. The sample preparation was described earlier in sec. 3.3. As in the case of the bare surface the phonon cross section dependence on the electron incident energy ( $E_p$ ) has been examined. In Fig. 4.11 HREEL spectra with different  $E_p$  and constant  $Q_{\parallel}$  of  $0.8\overline{\Gamma J}$ ,  $0.8\overline{\Gamma K}$ , and  $0.8\overline{\Gamma M}$  are shown. The lowest frequency loss around  $90\text{ cm}^{-1}$  along  $\overline{\Gamma J}$  and around  $130\text{ cm}^{-1}$  along  $\overline{\Gamma K}$  and  $\overline{\Gamma M}$  shows a shift with  $E_p$  variation. As the position is fixed in the SBZ this shift indicates a multi-peak structure and as a consequence more than one spectrum is necessary for safe determination of such a multi-peak structure. A loss around  $230\text{ cm}^{-1}$  is detectable for  $E_p > 120\text{ eV}$  along  $\overline{\Gamma K}$  and  $\overline{\Gamma M}$  which also shows shifts due to intensity variations of the close lying losses. A weak and broad structure is located around  $465\text{ cm}^{-1}$  best visible in Fig. 4.11 (b). Based on this and similar loss intensity examinations with different fixed  $Q_{\parallel}$ , various  $E_p$  have been selected for detailed phonon dispersion investigations on both monohydride and monodeuteride surfaces.

Examples of off-specular measurements on Si(100)-(2×1)-H along the three investigated azimuthal directions with constant incidence energy are presented in Fig. 4.12 (a, b, c). The **RW** shows prominent dispersion from  $30$  to  $125/130\text{ cm}^{-1}$  and backward, best visible in the first and second SBZ in Fig. 4.12 (c). The phonon dispersion is followed up to the sixth SBZ along the  $\overline{\Gamma J}$  direction. Apart from the **RW** shift, a significant variations of its loss intensity as a function of  $Q_{\parallel}$  can be observed in Fig. 4.12 (a) which manifests the loss cross-section dependence on the off-specular angle. The same dependence is visible for the losses around  $215$ ,  $330$ , and  $230\text{ cm}^{-1}$  in Fig. 4.12 (a) and (c) which show no relation to the surface Brillouin zone periodicity. The intensities of the structures in the highest frequency region of the substrate phonon continuum are more prominent compared to the bare Si(100) surface.

Off-specular HREELS measurements with primary energies  $130$  and  $180\text{ eV}$  on monodeuteride Si(100)-(2×1)-D surfaces along  $\overline{\Gamma K}$  and  $\overline{\Gamma M}$ , respectively, are presented in Fig. 4.12 (d, e). The **RW** dispersion from  $30$  to  $140/130\text{ cm}^{-1}$  in the first SBZ and backward in the second SBZ is best visible in Fig. 4.12 (e). Near the zone centers a second peak on the higher frequency side of the **RW** around  $130\text{ cm}^{-1}$  can be resolved. At the zone boundaries these two losses overlap. A loss at  $225/230\text{ cm}^{-1}$  passes through an intensity maximum approaching the zone boundary in both directions shown in Fig. 4.12 (d, e). In the small  $Q_{\parallel}$  region a structure centered around  $472\text{ cm}^{-1}$  is visible along the  $\overline{\Gamma M}$  direction on the flat sample.

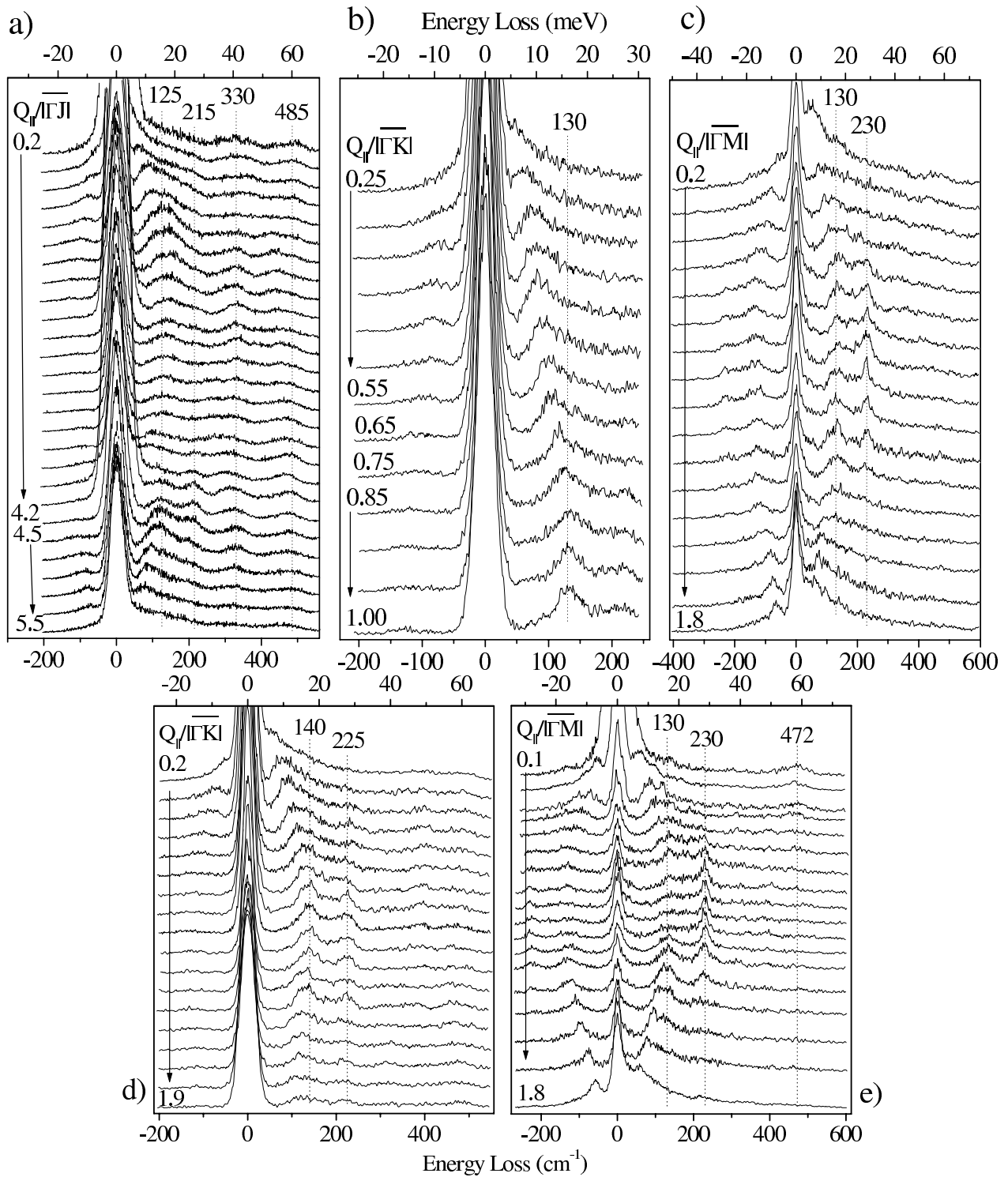


Figure 4.12: Off-specular HREEL spectra on monohydride (a, b, c) and monodeuteride (d, e) Si(100)-(2 $\times$ 1)-H(D) surfaces. The electron incident energy is fixed and the off-specular angle is varied. The arrows denote the  $Q_{\parallel}$  increase, normalized by the SBZ boundaries, with the following steps: 0.2 (a), 0.05 (b), and 0.1 (c, d, e). (a), (b), and (d) present spectra take at 90 K with primary energies 250, 200, and 130 eV on vicinal  $\overline{\Gamma J}$ ,  $\overline{\Gamma K}$ , and  $\overline{\Gamma K}$  oriented samples, respectively. (c) and (e) show measurements with incidence energies 220 and 180 eV on a double-domain  $\overline{\Gamma M}$  oriented surface at 300 K.

The fitting procedure outlined in Appendix A which has been applied for the HREEL spectra of bare Si(100) is applied to the spectra of Si(100)-(2×1)-H(D). The extracted phonon frequencies are summarized in Fig. 4.13.

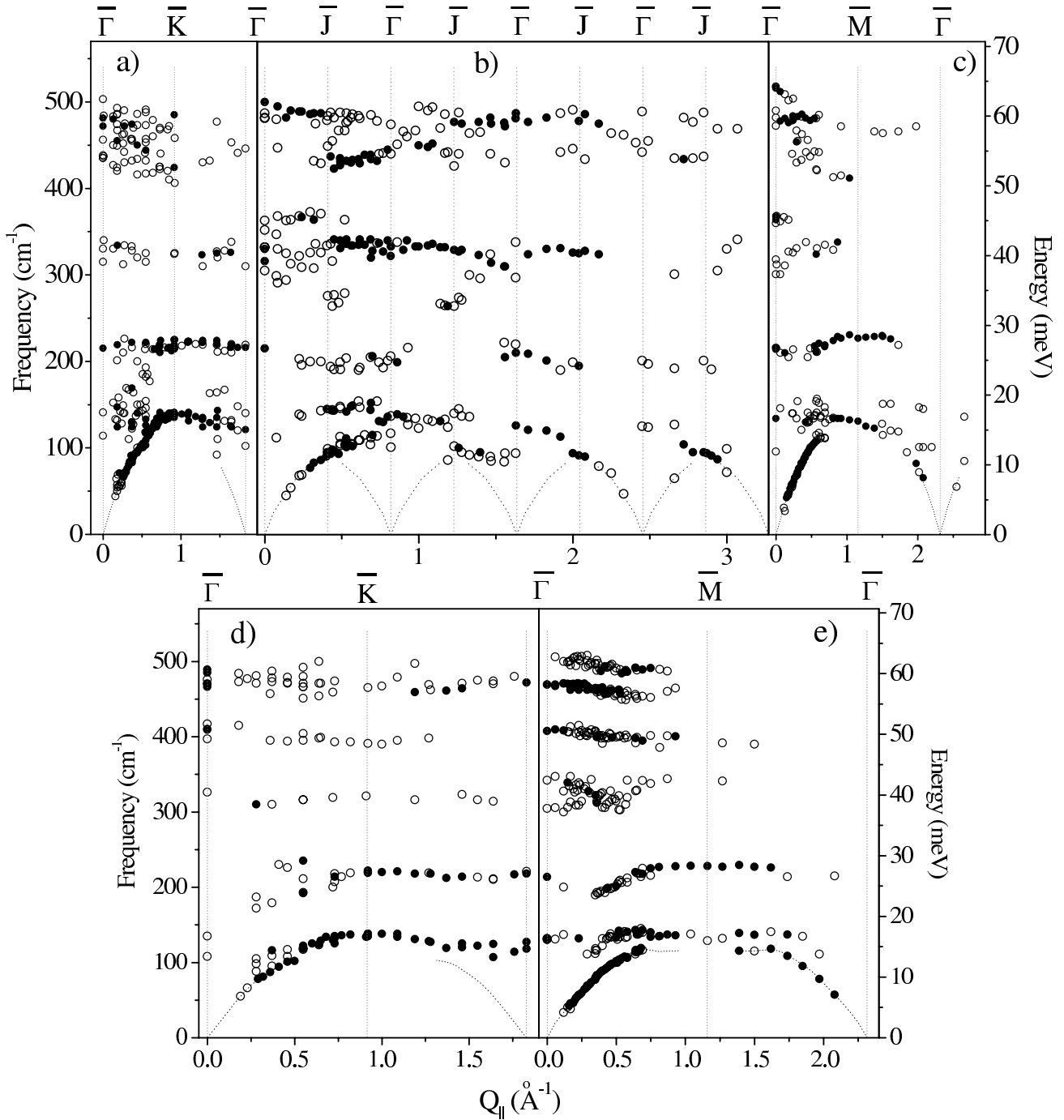


Figure 4.13: Phonon dispersions on monohydride (a, b, c) and monodeuteride (d, e) Si(100)-(2×1)-H(D) surfaces measured (a, d) in the  $\overline{\Gamma\overline{K}}$ , (b) in the  $\overline{\Gamma\overline{J}}$ , and (c, e) in the  $\overline{\Gamma\overline{M}}$  directions of the surface Brillouin zones. The dotted lines are extrapolations to  $0\text{ cm}^{-1}$  of the **RW** and are used to emphasize the dispersion periodicity in the different SBZ. The zone centers and boundaries are marked according to the (2×1) SBZ.

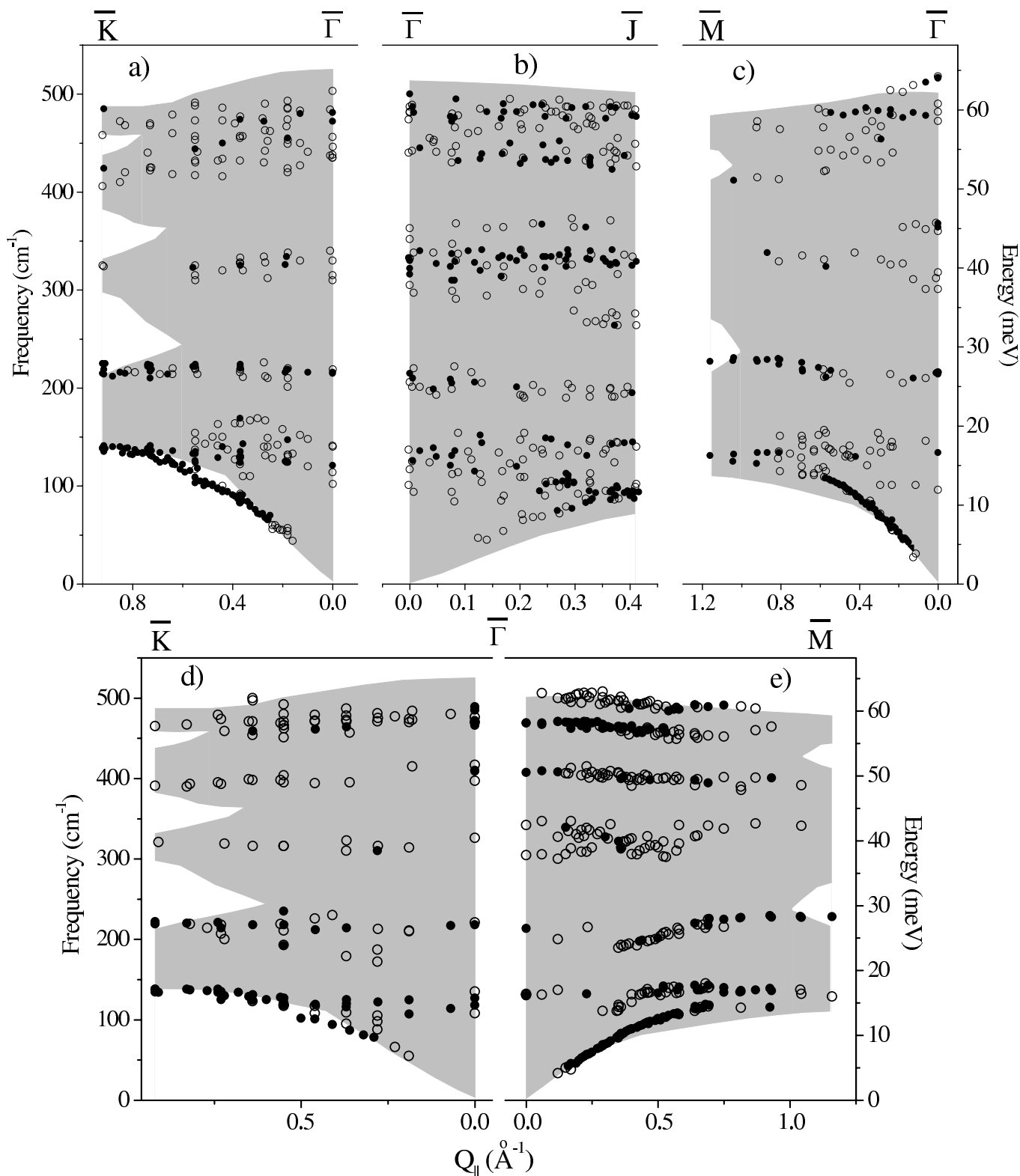


Figure 4.14: Phonon dispersion data (open and closed circles) on monohydride (a, b, c) and monodeuteride (d, e) Si(100)-(2×1)-H(D) surfaces together with the bulk phonons projected (BPP) in the (2×1) SBZ (dark areas). All data measured out of the first SBZ are back folded. (a, d) and (b) present phonon dispersions along the  $\bar{\Gamma}\bar{K}$  and the  $\bar{\Gamma}\bar{J}$  directions, respectively, on a vicinal sample. (c, e) show phonon dispersions along the  $\bar{\Gamma}\bar{M}$  direction on a nominally flat crystal.

Additionally dispersions have been measured up to the fifth SBZ along  $\overline{\Gamma J}$  on the Si(100)-(2×1)-H surface. Above  $250 \text{ cm}^{-1}$  two main bands centered roughly around  $330$  and  $460 \text{ cm}^{-1}$  are observed in the phonon dispersions on a hydrogenated surface shown in Fig. 4.13 (a, b, c). The bands are multi-component and their structure varies in the different surface Brillouin zones. In the phonon dispersions on the deuterated surface presented in Fig. 4.13 (d, e) these bands are better defined and split in three phonons at  $\sim 320$ ,  $\sim 395$ , and  $\sim 460 \text{ cm}^{-1}$  along the  $\overline{\Gamma K}$  direction. In the first SBZ along  $\overline{\Gamma M}$  three well resolved bands around  $400$ ,  $460$ , and  $490 \text{ cm}^{-1}$  are observed together with a structure located between  $305$  and  $340 \text{ cm}^{-1}$ , which indicates two-phonon composition. Below  $250 \text{ cm}^{-1}$  on both surfaces three well-defined phonon bands are observed. The lowest mode is the Rayleigh wave with its characteristic acoustic behaviour. Near all SBZ boundaries the **RW** overlaps with a phonon which shows dispersion in the  $105 \div 150 \text{ cm}^{-1}$  range. Above these two modes a phonon with frequency varying between  $190$  and  $230 \text{ cm}^{-1}$  is detected.

In Fig. 4.14 the data from Fig. 4.13 are back folded into the first (2×1) SBZ and are presented together with the bulk phonon projection (BPP). Most of the phonons appear as resonances falling in the BPP. The three exceptions on both surfaces are: the RW at  $\sim 0.5\overline{\Gamma K}$  which is split off the acoustic band; the highest mode near the zone center along  $\overline{\Gamma M}$ , split off the optical band; and the phonon at  $220$  and  $228 \text{ cm}^{-1}$  at the  $\overline{K}$  and  $\overline{M}$  points which falls in BPP gaps. A significant modification of the loss width was observed only for the phonon around  $225 \text{ cm}^{-1}$  (see Fig. 4.13 c, e), which could be related to a resonance to a surface localized phonon transition.

To examine the influence of the symmetric and asymmetric dimer on the vibrational features of the surface, the phonon dispersions on bare and hydrogenated Si(100) surfaces are compared in Fig. 4.15. For the bare Si(100)-(2×1) surface with tilted dimers the characteristic vibrations are the dimer rocking **r** and the subsurface bond **sb** modes [14]. The latter phonon involves a dimer stretch in the tilted dimer bond direction and is related to vibration in the fivefold ring defined by the dimer and the underlying second and third layer atoms shown in Fig. 4.1. This mode is expected to vanish on surfaces with symmetric dimers. As we have shown above, this mode is not present yet on a bare surface because of the  $c(4 \times 2)$  and  $p(2 \times 2)$  symmetries. The rocking mode was predicted by the DFT calculations of Fritsch *et al.* [14] to shift  $\sim 40 \text{ cm}^{-1}$  to higher frequencies along  $\overline{\Gamma J}$  due to dimer symmetrisation. In our experiment we find shifts between the bare and H-(2×1) surface also to higher frequencies: for vicinal samples  $\sim 36 \text{ cm}^{-1}$  at  $\overline{\Gamma}$ ,  $\sim 44 \text{ cm}^{-1}$  at  $\overline{K}$  and  $< 7 \text{ cm}^{-1}$  at  $\overline{J}$ , for nominally flat sample  $\sim 45 \text{ cm}^{-1}$  at  $\overline{\Gamma}$  and  $\sim 37 \text{ cm}^{-1}$  at  $\overline{M}$ . The agreement with theory is very good, hence we are allowed to apply the mode assignments in the DFT calculation to our results which was already done in the case of the bare surface where the assignments were based on the DFT calculation of Stigler [137]. The **RW** is also shifted up at the zone boundaries with  $\sim 37 \text{ cm}^{-1}$  at  $\overline{M}$  and  $\overline{K}$ , and no shift is observed at  $\overline{J}$ . A band which doesn't shows acoustic behaviour is labeled with **m** in Fig.4.15. The atomic motions involved in this mode remain unclear resulting from the lack of calculations for a (2×1) reconstructed surface with symmetric dimers. The twisting mode **t** is better defined and can be followed over the whole zone in the  $\overline{\Gamma J}$  direction accompanied by two weak satellites. The **ds''** band remains unchanged, which is not surprising if we assign this

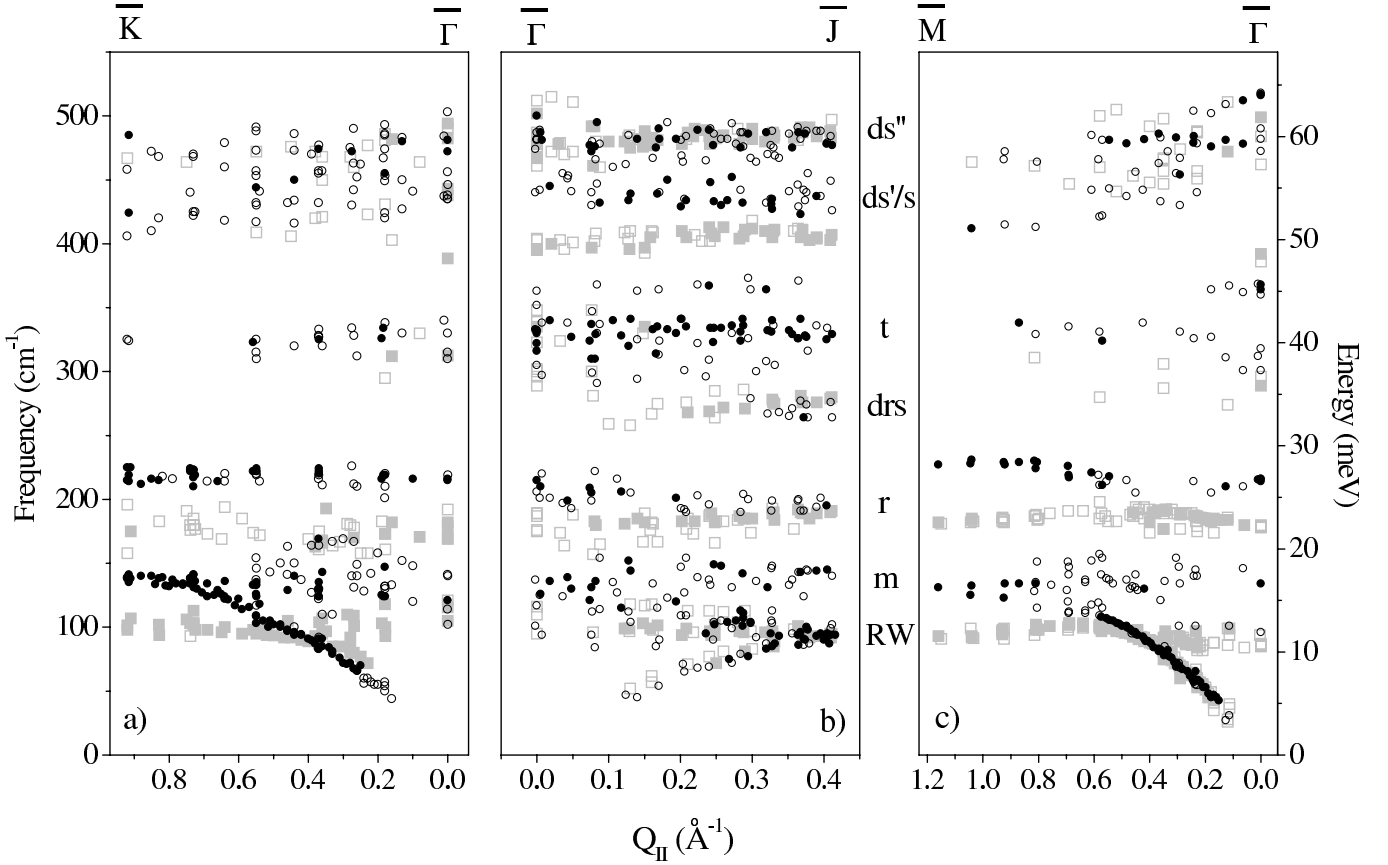


Figure 4.15: Comparison of the phonon dispersions on bare and monohydride-covered Si(100) surfaces. Results from vicinal surfaces in the  $\overline{\Gamma K}$  and  $\overline{\Gamma J}$  directions are presented in (a) and (b), respectively. Data for a double domain sample are plotted on (c) in the  $\overline{\Gamma M}$  direction. The dispersion on the hydrogenated surface is denoted by black open and closed circles and on the bare surface by open and closed gray squares.

mode to a subsurface bond stretchings localized in the second and third layer [125]. Thus it is less sensitive to the dimer buckling. The situation with the  $\mathbf{ds}'$  vibration is quite interesting. This mode should be very sensitive to the dimer tilting based on the involvement of vibrations localized in the top two layers with a large component of dimer stretching motion. The dimer stretching mode  $\mathbf{ds}'$  could be used as a fingerprint of the dimer tilting, alternative to the  $\mathbf{sb}$  mode missing on bare surfaces. The  $\mathbf{ds}'$  mode either vanishes or shifts up in frequency by  $\sim 48 \text{ cm}^{-1}$  and by  $\sim 33 \text{ cm}^{-1}$  at the  $\overline{\Gamma}$  and  $\overline{J}$  points, respectively. Another possibility is that  $\mathbf{ds}'$  is softened by  $35 \div 40 \text{ cm}^{-1}$  to the upper satellite of  $\mathbf{t}$  and as a partially twisting mode can also explain its dependence on the dimer asymmetry. Finally, if it vanishes, the band around  $440 \text{ cm}^{-1}$  can be related to vibrations involving a dimer swinging prominent in the  $(2 \times 1)$  symmetry. Therefore the band around  $420 \text{ cm}^{-1}$  is denoted as  $\mathbf{ds}'/s$ . In summary three modes ( $\mathbf{RW}$ ,  $\mathbf{r}$  and  $\mathbf{ds}'$ ) undergo strong changes from the bare Si(100) to the Si(100)-(2×1)-H surface. These modes appear to be very sensitive to the dimer asymmetry, two of them ( $\mathbf{r}$  and  $\mathbf{ds}'$ ) being characteristic for the dimer motions.

An isotope effect has been used to probe the adsorbate influence on the surface phonon dispersions by passivating the surface with deuterium. Similar to the monohydride the monodeuteride removes the dimer buckling and forms symmetric dimers on the Si(100) surface with  $(2\times 1)$  symmetry. The atomic mass of deuterium remains small related to the substrate atomic mass, hence again an influence on the surface phonon dispersion is expected mainly by the changed surface reconstruction. In Fig. 4.16 the experimentally achieved phonon dispersions on Si(100)- $(2\times 1)$ -H and Si(100)- $(2\times 1)$ -D surfaces are compared. Below  $380\text{ cm}^{-1}$  the main phonon bands on the hydrogenated surfaces are very well reproduced on the deuterated surface both on single and double domain Si(100). The dimer rocking ( $\mathbf{r}$ ) mode is reproduced in details according to its location and dispersion, best visible along the  $\overline{\Gamma M}$  direction in Fig. 4.16 (b). The  $\mathbf{RW}$  dispersion is also exactly repeated. The  $\mathbf{m}$  band is better resolved around  $0.3\text{ \AA}^{-1}$  along  $\overline{\Gamma K}$  on the deuterated surface compared with the broad band at the same position on the hydrogenated substrate. This difference could come from the better resolved two modes between the  $\mathbf{RW}$  and  $\mathbf{r}$  modes on the Si(100)- $(2\times 1)$ -D surface. In total the above observations support the assumption that the adsorbate in these particular cases causes a negligible mass effect in

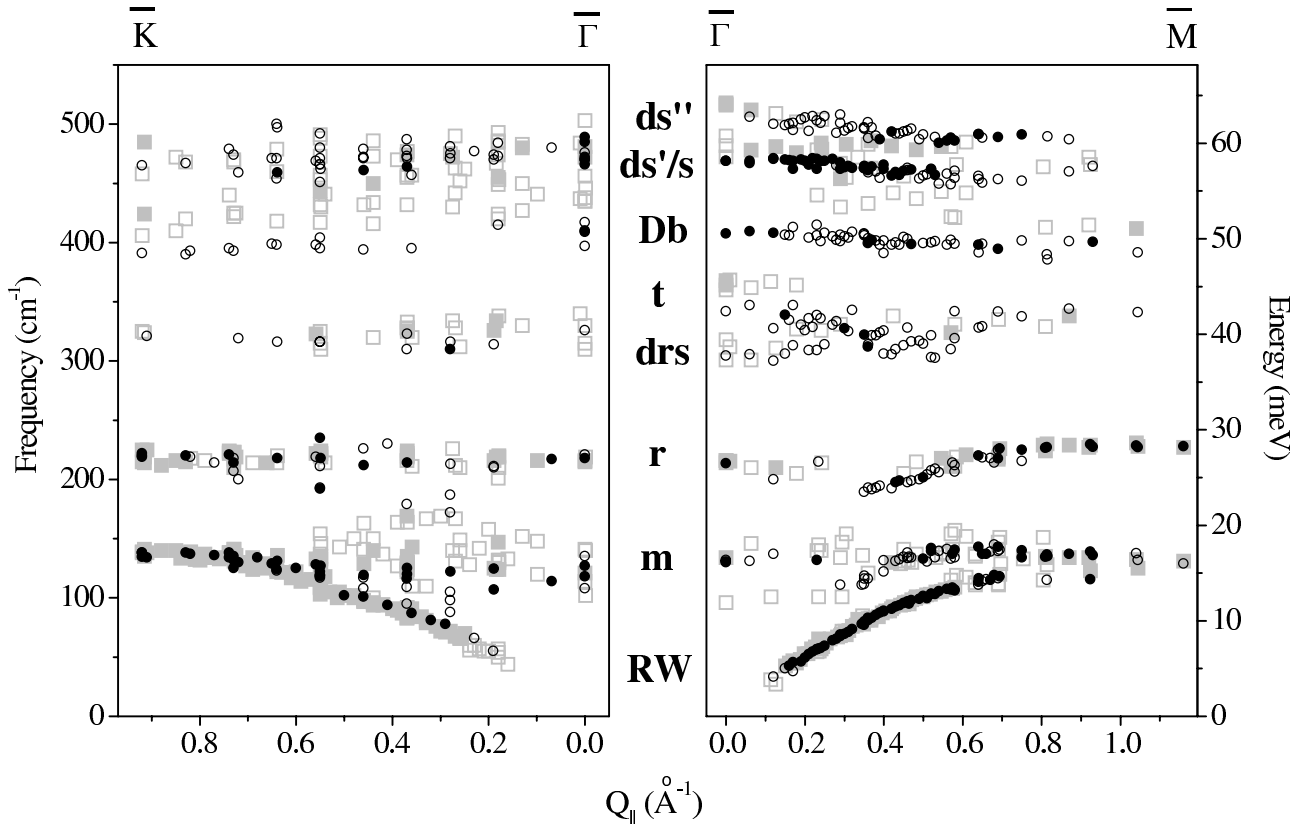


Figure 4.16: Comparison of the phonon dispersions on monohydride and monodeuteride-covered Si(100) surfaces. Results from a single domain surface in the  $\overline{\Gamma K}$  direction are presented in (a). Data for double domain sample are plotted in (b) in the  $\overline{\Gamma M}$  direction. The dispersions on a deuterated surface are denoted by black open and closed circles while those on a hydrogenated surface are denoted by open and closed gray squares.

the phonon dispersion and that the main contribution to the surface vibrations results from the surface reconstruction. Above  $380 \text{ cm}^{-1}$  the analyses are not straightforward. The reason is that for the monodeuteride, apart from the stretching vibrations located at  $1527 \text{ cm}^{-1}$ , the bending vibrations fall into the substrate phonon continuum and a strong coupling to phonon bands is expected. Therefore we attribute the new **Db** band in the  $400 \div 410 \text{ cm}^{-1}$  frequency range which is absent on the monohydride surface as a monodeuteride bending mode. Above the **Db** band the **ds''** phonon is preserved in both presented directions while the **ds'/s** is detected only in the  $\overline{\Gamma M}$  direction, probably because it is hidden between the **Db** and **ds''** peaks in the HREELS measurement with lower resolution made on a  $\overline{\Gamma K}$  oriented vicinal Si(100) surface. In summary we can conclude that a new mode related to the monodeuteride bending motion is found and that all other phonon dispersions on hydrogenated vicinal and nominally flat Si(100)-(2×1)-H surfaces are almost exactly reproduced after deuteration of these surfaces.

## 4.4 Summary

The vibrational properties of Si(100) surfaces have been investigated using high resolution electron energy loss spectroscopy (HREELS). The surface phonon dispersions have been studied on vicinal and nominally flat crystals along the  $\overline{\Gamma J}$ ,  $\overline{\Gamma K}$ , and  $\overline{\Gamma M}$  directions of the (2×1) SBZ at 90 and 300 K. Bare as well as monohydride- and monodeuteride-covered surfaces have been studied.

Mode	$\overline{\Gamma}_{(vicinal)}$	$\overline{\Gamma}_{(flat)}$	$\overline{J}_{(vicinal)}$	$\overline{K}_{(vicinal)}$	$\overline{M}(\overline{J})_{(flat)}$
<b>RW</b>			95 (11.8)	101 (12.5)	95 (11.8)
<b>A</b>	105 (13.0)	90 (11.2)	95 (11.8)	101 (12.5)	95 (11.8)
<b>r</b>	180 (22.3)	180 (22.3)	190 (23.6)	175 (21.7)	182 (22.6)
<b>drs</b>	305 (37.8)	290 (36.0)	280 (34.7)		
<b>t</b>	335 (41.5)				
<b>ds'</b>	395 (49.0)	390 (48.4)	405 (50.2)		
<b>s</b>	440 (54.6)				
<b>ds''</b>	485 (30.1)	490 (60.8)	485 (60.1)	467 (57.9)	465 (57.7)

Table 4.1: Surface phonon frequencies observed by HREELS on bare Si(100) surfaces at the high-symmetry (2×1) SBZ points, given in  $\text{cm}^{-1}$  and meV (in brackets), respectively.

On bare surfaces eight phonon bands are resolved. The comparison with the theoretical predictions reveals good agreement only with the calculations for a c(4×2) reconstruction for the flat surface [137]. On the vicinal surface the experimental results correspond to calculations

of  $c(4 \times 2)$  as well as to  $p(2 \times 2)$  unit cells [137]. The results for bare surfaces are summarized in Tab. 4.1 where the assignment of the modes is based on Ref. [137]. The most prominent phonons are the acoustic modes (**RW** and **A**) and the dimer rocking mode (**r**). Apart from the **RW** and **A** all other vibrations involve characteristic motions of the dimer atoms.

Mode	$\bar{\Gamma}_{(vicinal)}$	$\bar{\Gamma}_{(flat)}$	$\bar{J}_{(vicinal)}$	$\bar{K}_{(vicinal)}$	$\bar{M}(\bar{J}')_{(flat)}$
<b>RW</b>			95 (11.8)	140 (17.4)	130 (16.1)
<b>m</b>	125 (15.5)	134 (16.6)	95 (11.8)	140 (17.4)	130 (16.1)
<b>r</b>	215 (26.7)	215 (26.7)	195 (24.2)	220 (27.3)	227 (28.1)
<b>drs</b>		310 (38.4)	270 (33.5)		
<b>t</b>	331 (41.0)		329 (40.8)	325 (40.3)	
<b>ds'/s</b>	444 (55.1)		438 (54.3)	423 (52.5)	
<b>ds''</b>	483 (59.9)	483 (59.9)	479 (59.4)	486 (60.3)	

Table 4.2: Surface phonon frequencies observed by HREELS on the Si(100)-(2×1)-H surfaces at the high-symmetry (2×1) SBZ points, given in  $\text{cm}^{-1}$  and meV (in brackets), respectively.

Mode	$\bar{\Gamma}_{(vicinal)}$	$\bar{\Gamma}_{(flat)}$	$\bar{K}_{(vicinal)}$	$\bar{M}(\bar{J}')_{(flat)}$
<b>RW</b>			136 (16.9)	130 (16.1)
<b>m</b>	125 (15.5)	130 (16.1)	136 (16.9)	130 (16.1)
<b>r</b>	218 (27.0)	214 (26.5)	221 (27.4)	228 (28.3)
<b>drs</b>		305 (37.8)		
<b>t</b>	325 (40.3)	325 (40.3)	321 (39.8)	340 (42.2)
<b>Db</b>	410 (50.8)	408 (50.6)	392 (48.6)	395 (49.0)
<b>ds'/s</b>	470 (58.3)	469 (58.2)	466 (57.8)	
<b>ds''</b>	487 (60.4)	505 (62.6)		

Table 4.3: Surface phonon frequencies observed by HREELS on the Si(100)-(2×1)-D surfaces at the high-symmetry (2×1) SBZ points, given in  $\text{cm}^{-1}$  and meV (in brackets), respectively.

The surface phonon dispersion spectrum on monohydride Si(100)-(2×1)-H surfaces contains seven bands which are summarized in Tab. 4.2. In general related to the bare surfaces the **RW**,

**A**, **r**, and **ds'/s** phonons are blue-shifted while the other modes reproduce the location of their corresponding modes. The **ds'** and **s** modes probably coincide in the **ds'/s** mode on the hydrogenated surfaces and a new band (**m**) is present in the dispersion spectrum.

The results from the vibrational investigation on the monodeuteride Si(100)-(2×1)-D surfaces along  $\overline{\Gamma K}$  and  $\overline{\Gamma M}$  are shown in Tab. 4.3. In these two directions of the (2×1) SBZ the seven bands on the hydrogenated surface are exactly reproduced together with the appearance of the new band (**Db**). The observations are interpreted as a negligible isotope effect because the new mode is associated with a monodeuteride bending vibration.

In conclusion among all experimentally observed phonons on the bare Si(100) surface the **RW**, **r**, and **ds'** bands are the most sensitive to the silicon dimer tilting.



## Chapter 5

# Benzene adsorption on Si(100) surfaces

As a prototype for understanding the adsorption of aromatic hydrocarbons on semiconductor surfaces, benzene adsorption on a Si(100) surface has attracted considerable scientific interest in the last ten years. The investigations of this system were started by the pioneering experimental study of Taguchi *et al.* [139]. In this study based on TPD, HREELS, LEED and AES nondissociative chemisorption of benzene on a nominally flat Si(100)-(2×1) surfaces at 300 K was observed. Preservation of the silicon dimers was detected together with  $sp^3$ -hybridization of carbon atoms which form  $\sigma$ -bonds with the substrate atoms. Additionally the vibrational spectrum contained a vibration which was located in the carbon double bond stretching frequency region, suggesting the presence of  $sp^2$ -carbon atoms. A saturation coverage of  $\theta_{C_6H_6} = 0.27$  was determined. Proposed adsorbate geometries were 1,4-cyclohexadiene like or 1,3-cyclohexadiene like structures on a single silicon dimer (see Fig. 5.1 a,b). The carbon rehybridization and double bonds, lying nearly parallel to the surface, was later confirmed by the same authors using NEXAFS measurements [140]. The desorption spectrum reported in Ref. [139] contained two peaks related to chemisorbed benzene, corresponding to two adsorption sites and the high temperature desorption peak was attributed to defect induced configurations. Following these experimental results a theoretical study of the system was performed by Craig based on a SLAB-MINDO method [141]. A metastable 1,3-cyclohexadiene-like structure ( see Fig. 5.1 b) was determined and as most stable was established a benzene molecule four  $\sigma$ -bonded to two silicon atoms with one double bond left in the carbon ring were determined. Using a cluster model and semi-empirical PM3 calculations Jeong *et al.* determined as most stable a pedestal configuration with adsorbate four  $\sigma$ -bonded to two silicon dimers, adjacent in the row, and no double carbon bonds which is shown in Fig. 5.1 (c) [143]. The STM was used as a real-space observation technique to determine the actual benzene configurations. But apart from the consensus concerning the adsorption on top of the dimer rows, different stable configurations were proposed. Namely a butterfly [144] (Fig. 5.1 a), a 1,3-cyclohexadiene-like [145] (Fig. 5.1 b), and a tight bridge [146, 147] (Fig. 5.1 d) structure. This disagreement revealed the necessity of combined theoretical and experimental investigations of the benzene/Si(100) system. A combination of semi-empirical quantum cluster calculations, STM and FTIR was used [146, 147, 148, 149] to reveal a metastable butterfly structure (Fig. 5.1 a), as adsorption product at 300 K, with a time-dependent (hours) conversion to a more stable tight bridge configuration (Fig. 5.1 d). The lowest energy of the latter was deduced also by *ab initio* simulations

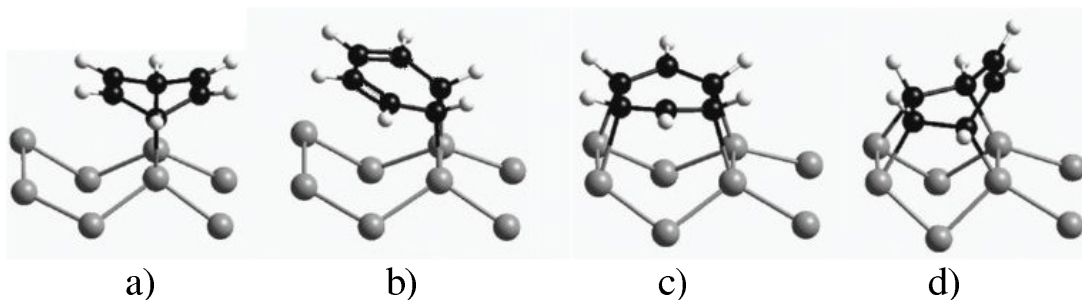


Figure 5.1: The stable structures of benzene on a Si(100) surface. (a) 1,4-cyclohexadienelike (butterfly), (b) 1,3-cyclohexadienelike (tilted), (c) symmetric bridge (pedestal), and (d) tight bridge configurations. The gray, black and white atoms correspond to silicon, carbon and hydrogen, respectively. [142]

[142]. The presence of a two-dimer bridge adsorption site was questioned by first-principles density-functional cluster calculations of electronic and vibrational structures of different geometric configurations [150]. The 1,4-cyclohexadiene-like adsorption complex, with a flat-lying benzene molecule which is di- $\sigma$  bonded to the two dangling bonds of a single silicon dimer (Fig. 5.1 a), was for the first time unambiguously determined by ARUPS measurements [151] and later confirmed by HREELS experiments [152] on a vicinal Si(100)-(2 $\times$ 1) surface. In this way the dominance of the butterfly structure of benzene adsorbed on a vicinal Si(100) surface was concluded. Not defined remains the second minor adsorbate structure, present as high temperature peak in the desorption spectrum. In the experiments a second structure was detected after a long time (hours) at 300 K [146] or after annealing to 350 K [153]. Additionally it was reported that 0.5 ML hydrogen preadsorption made the high temperature peak in the desorption spectrum to vanish and thus a step influenced adsorption site was proposed [151]. In contrast another assignment could be the tight bridge configuration (Fig. 5.1 e) which was found to be not defect- or step-associated [147]. Thus the more strongly bound benzene phase on a Si(100) surface remains under debate.

The present TPD and HREELS study is directed at characterizing the chemisorption phases of benzene on vicinal and nominally flat Si(100)-(2 $\times$ 1) surfaces.

## 5.1 Benzene adsorption on a vicinal Si(100)-(2 $\times$ 1) surface

TDS and HREELS investigations of a benzene low-temperature adsorption on a vicinal (miscut 4.75° along the [011] direction) Si(100)-(2 $\times$ 1) surface were performed. In Fig. 5.2 TPD spectra of hydrogenated and deuterated benzene adsorbed at 100 K on a vicinal Si(100) surface are presented. The physisorbed benzene desorbs below 150 K details can be found in Ref. [139, 151]. Because in this work we are focused on the chemisorption phase in Fig. 5.2, only the temperature range where this phase appears in the desorption spectrum is included. In the spectra of small doses shown in Fig. 5.2 (a, d) a single peak ( $\beta_3$ ) centered at 500 K is present. Before saturation

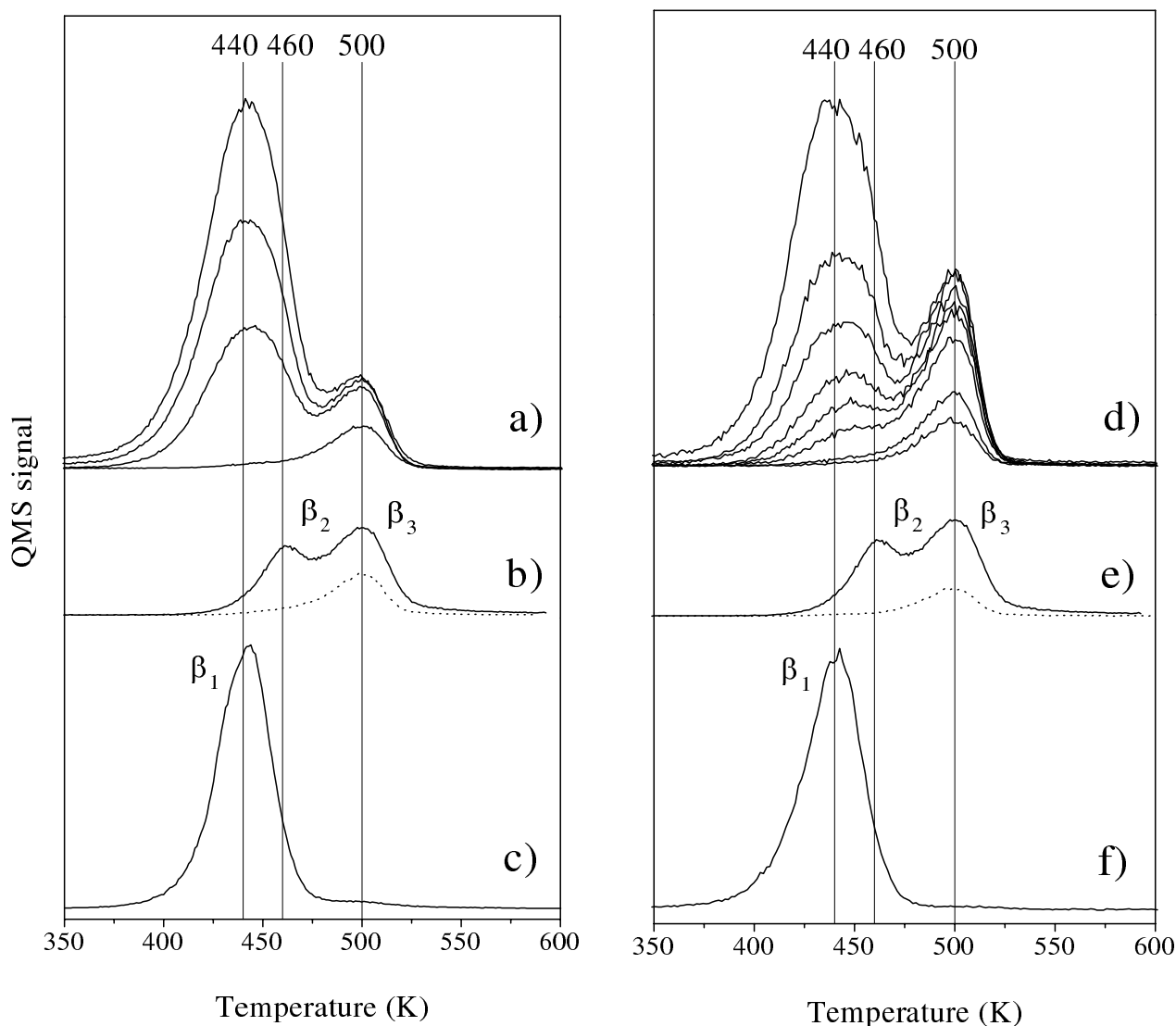


Figure 5.2: TPD spectra of hydrogenated (a, b, c) and deuterated (d, e, f) benzene adsorbed at 100 K on a vicinal Si(100) surface, measured with 5 K/s. Only the chemisorption temperature interval is included. (a) and (d) show spectra taken after successively increased doses. (b) and (e) are spectra of  $\theta = 1$  (solid line) and  $\theta = 0.2$  (dotted line) benzene coverages, both annealed up to 440 K. Here  $\theta = 1$  denotes a saturated chemisorption phase. (c) and (f) present results of a benzene-saturated surface, after its passivation with a half monolayer hydrogen at 650 K. The temperature center positions of the structures denoted by  $\beta_1$ ,  $\beta_2$  and  $\beta_3$  are shown on the top part of the figure.

of this peak a lower temperature broad structure starts to rise and saturates centered at about 440 K. Benzene is known to desorb molecularly [139] and a first-order desorption kinetics is expected with coverage independent peak position [33]. The coverage dependent shift of the second structure's center could be a result of lateral interactions (repulsion) between the adsorbed molecules on the surface [151]. Benzene saturation of the surface after its passivation (650 K) with half a monolayer hydrogen leads to a spectrum (see Fig. 5.2 c,f) with a sharp single peak ( $\beta_1$ ) at 440 K. Thus the adsorption sites for the  $\beta_3$ -structure are blocked and

the lateral interactions are suppressed. The desorption spectrum (Fig. 5.2 b,e/solid line) of a pre-annealed (440 K for a few seconds) saturated benzene coverage contains a well resolved double structure. The  $\beta_3$  peak is unchanged from the saturated coverage. In contrast the  $\beta_2$  peak centered at 460 K has no direct analog in the spectra in Fig. 5.2(a,d). The latter does not exclude the possibility that the  $\beta_2$  peak is a coverage-dependent product of  $\beta_1$ . As is demonstrated in Fig. 5.2, it is possible to prepare three well defined adsorbate phases on the Si(100) surface, which probably are elements of the saturated chemisorption coverage. For clarity in the following we base our notations on these TPD results. Namely, we denote as a low-temperature phase (LTP) a structure corresponding to  $\beta_1$ , as middle-temperature phase (MTP) we mark the  $\beta_2 + \beta_3$  configuration, and a high-temperature phase (HTP) indicates the presence only of  $\beta_3$  on the surface. The three phases are prepared by pre-adsorption of atomic hydrogen at 650 K (Fig. 5.2 c,f), by annealing up to 440 K of a saturated coverage (Fig. 5.2 b,e/solid line), and by annealing up to 440 K of  $\theta = 0.2$  benzene (Fig. 5.2 b,e /dotted line), respectively. With  $\theta = 1$  we will denote the saturated chemisorbed benzene coverage on a clean silicon surface.

We apply HREELS (subsection 1.3.2) to study the vibrational characteristics of the above-mentioned benzene phases on a vicinal Si(100) surface. The vicinal silicon crystal is oriented along the  $[0\bar{1}1]$  direction, relative to the electron scattering plane (see Fig. 3.8). In Fig. 5.3 HREEL spectra of the  $C_6H_6$  phases are presented. The observation of the three phases vibrational spectra (Fig. 5.3 a,c,d) firstly reveals a great similarity in the loss number, positions and intensities. The spectra of the MTP (c) and HTP (d) in Fig. 5.3 are essentially the same within  $\pm 2 \text{ cm}^{-1}$  and only the MTP peak at  $1255 \text{ cm}^{-1}$  vanishes in the HTP spectrum. A comparison of the MTP and HTP spectra with those of the LTP shows in general conservation of the intra-loss ratios but frequency shifts up to  $\sim 50 \text{ cm}^{-1}$  in some vibrational modes. In the spectrum of a saturated silicon surface, (b) in Fig. 5.3, all losses are broader, while the resolution is the same, indicating that this spectrum is a superposition of the three phases. The latter is obvious in the region around  $3000 \text{ cm}^{-1}$  where the three peaks are present corresponding to the two peaks in the LTP and MTP(HTP) spectra. Additionally the summation product (not plotted in Fig. 5.3) of the LTP and MTP spectra reproduces in detail curve (b) in Fig. 5.3. A presence of the three phases in the saturated coverage on the clean surface can be deduced in accordance with the desorption results shown in Fig. 5.2.

Because of the relatively small frequency shifts and the preserved intra-mode ratios for the moment an assignment, regarding the "butterfly" structure presented in Fig. 5.1 (a), of the observed vibrations will be addressed for all three adsorbate phases. A detailed vibrational modes assignment for a benzene-saturated vicinal Si(100) surface has been made by Stauffer *et al.* [152] and here we will base our considerations on these results. We will also use the notations involved in Ref. [152], namely: "Si<sub>d</sub>" for silicon dimer atoms involved in bonding with carbon atoms of the benzene, "C<sub>d</sub>" for  $sp^3$  hybridized carbon atoms bonded to the substrate, "C" for  $sp^2$  hybridized carbon atoms not bonded to silicon, "H" and "H<sub>d</sub>" for hydrogen attached to  $sp^2$ - and  $sp^3$ -carbon, respectively. The changes in the vibrations will be followed going from the LTP to the MTP. The high-energy edge of the MTP spectrum is characterized by two peaks located above and below  $3000 \text{ cm}^{-1}$ , belonging to C-H and C<sub>d</sub>-H<sub>d</sub> stretching modes,

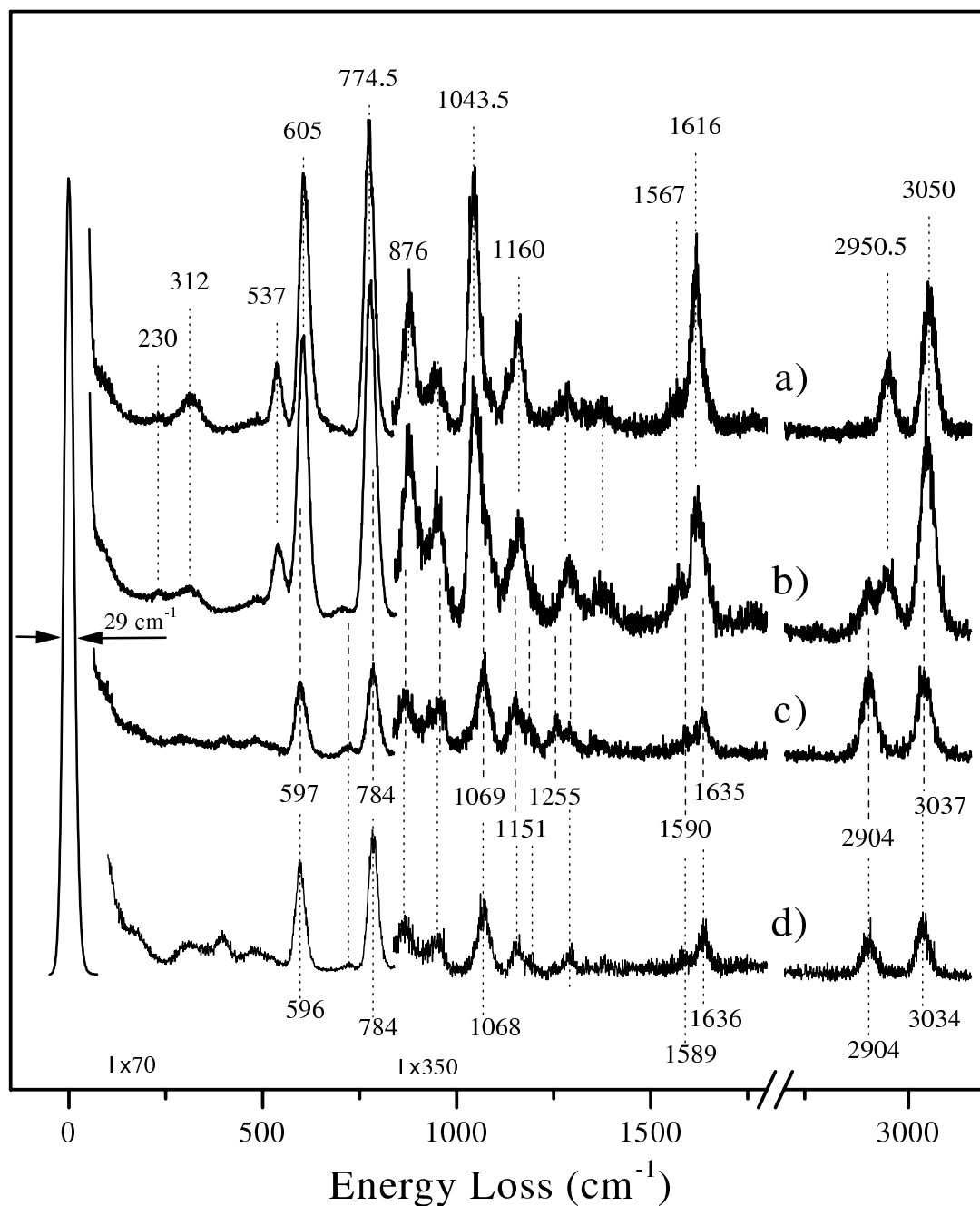


Figure 5.3: HREEL spectra of  $C_6H_6$  adsorbed on a vicinal Si(100) surface. The measurements are performed with 4 eV electron primary energy in the specular direction at 100 K substrate temperature. The spectra are taken on: (a) benzene saturated at 100 K, subsequently annealed to 300 K, after surface passivation (650 K) with 0.4 ML atomic hydrogen; (b) saturated at 100 K and annealed to 300 K clean surface;  $\theta = 0.2$  benzene annealed to (c) 430 K and to (d) 450 K. The frequencies of the main losses are denoted for curves (a), (c) and (d). The frequency values are presented above (a) and below (c,d) the corresponding spectra. The amplification factors are located in the low-frequency edge of the corresponding spectrum fragments and are shown at the bottom of the figure.

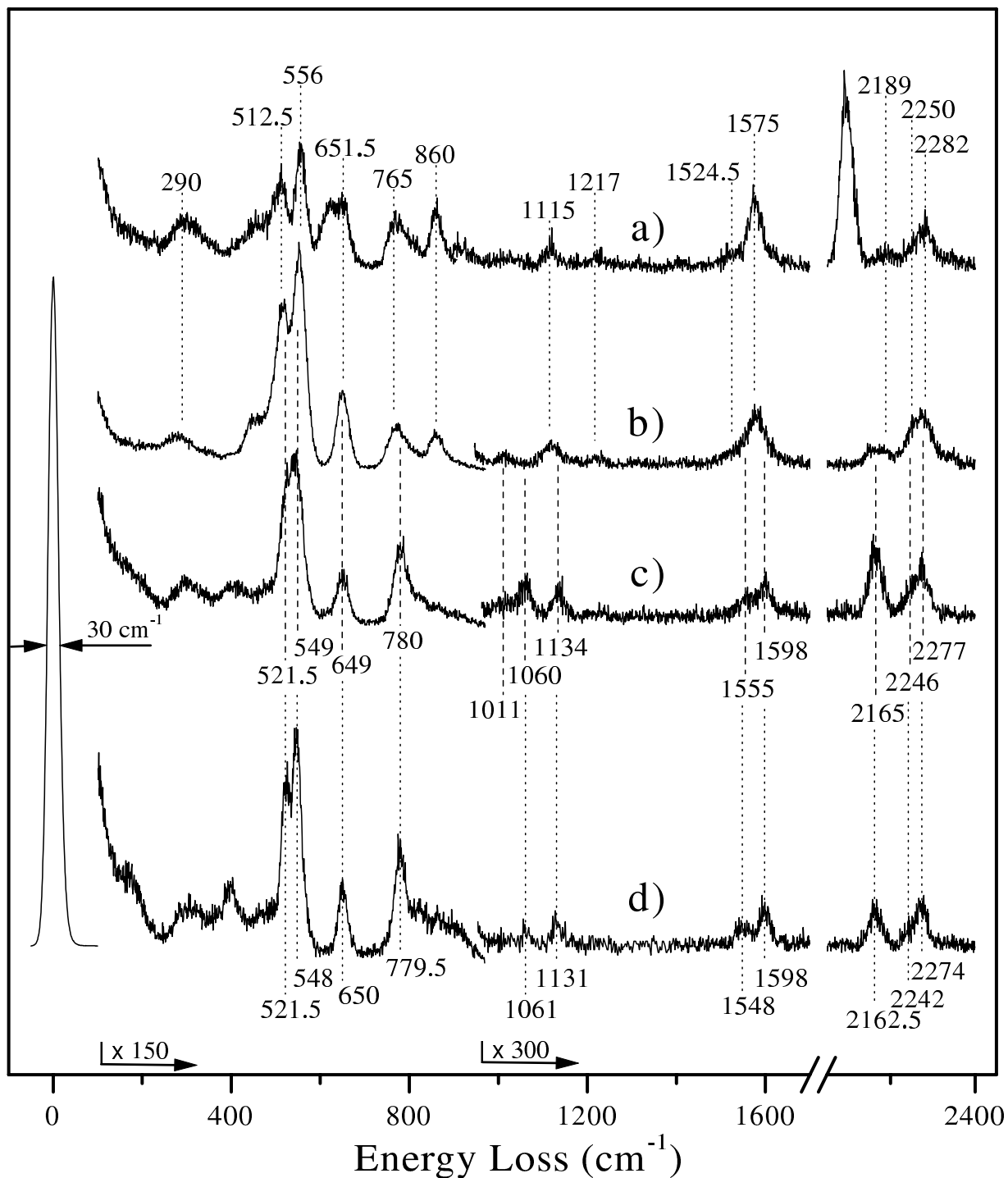


Figure 5.4: HREEL spectra of  $C_6D_6$  adsorbed on a vicinal Si(100) surface. The measurements are performed with 4 eV electron primary energy in the specular direction at 100 K substrate temperature. The spectra are taken on: (a) benzene saturated at 100 K, subsequently annealed to 300 K, after surface passivation (650 K) with 0.4 ML atomic hydrogen; (b) saturated at 100 K and annealed to 300 K clean surface;  $\theta = 0.2$  benzene annealed to (c) 430 K and to (d) 450 K. The two unmarked losses on (a), at  $2100\text{ cm}^{-1}$  and  $621\text{ cm}^{-1}$ , belong to the monohydride vibrations (section 3.3).

respectively. The bands are red shifted but the shape is conserved, suggesting a force constant softening rather than changes in the mode character. The  $C_d-H_d$  stretching is shifted by a factor of two relative to the C-H stretching shift, manifesting that the  $C_d$  atoms are in the center of the structural changes between the different phases. As the carbon-hydrogen bonds are softened the carbon-carbon bonds should become stronger and indeed the symmetric and asymmetric C=C stretchings around  $1600\text{ cm}^{-1}$  are preserved and blue shifted with  $\sim 20\text{ cm}^{-1}$ . For the in-plane ( $1100\div 1350\text{ cm}^{-1}$ ) and out-of-plane ( $650\div 1050\text{ cm}^{-1}$ ) carbon-hydrogen bending modes the shifts can not be simply deduced from the C-H and C-C bond strength changes because both forces, with various portions, are involved in these vibrations. This leads to different in direction shifts of the C-H and  $C_d-H_d$  bending modes. The fully symmetric benzene ring breathing frequencies, at  $605$  and  $876\text{ cm}^{-1}$  for the LTP, are reduced by  $\sim 8\text{ cm}^{-1}$ , suggesting a small portion of the shortened C=C bond. The most dramatic changes occur for the mode related to the  $Si_d-C_d$  stretching plus butterfly motion of the benzene molecule at  $537\text{ cm}^{-1}$  for the LTP. This mode vanishes in the spectra of MTP and HTP. The mode either shifts up in frequency and is not resolved from the neighboring more intensive peak, or it shifts down and in the changed symmetry couples with a substrate phonon band. The former is less probable because this would require a shift of  $\sim 60\text{ cm}^{-1}$ , and also no broadening of the adjacent peak is observed.

Following the excellent correspondence (summarized in Tab. 5.2) between our experimental vibrational characteristics of the LTP and the "first principles" DF calculated values for the "butterfly" geometry [152] we assign this benzene phase to a 1,4-cyclohexadiene-like adsorption complex with a flat-lying molecule which is di- $\sigma$  bonded to the two dangling bonds of a single silicon surface dimer. To verify this assignment we examine the isotope effect on the vibrational characteristics by adsorbing deuterated benzene on the vicinal Si(100) surface. HREEL spectra of the three  $C_6D_6$  phases are presented in Fig. 5.4. As in the case of  $C_6H_6$ , the similarity of the peak positions and ratios is preserved for the three phases within  $\leq 30\text{ cm}^{-1}$  shifts. Again the spectrum of the monolayer is a superposition of the LTP and MTP vibrations, suggesting coexistence of the different phases. In the carbon-deuterium stretching region three bands are resolved which agrees with the theoretical predictions [152]. All three modes are red shifted from LTP to MTP and HTP, manifesting a bond softening. The C=C stretching doublet around  $1580\text{ cm}^{-1}$  is prominent, particularly in the MTP and HTP cases, and undergoes a blue shift. All carbon-deuterium bending modes are isotope shifted to lower frequencies where they coincide and couple with the ring deformation modes. A different coupling is found for the vibration at  $860\text{ cm}^{-1}$  in the LTP compared to the MTP and HTP. In this region three vibrational modes are given from the calculations [152], two of them being totally symmetric. Confirming the observations for  $C_6H_6$ , in the case of  $C_6D_6$  again the LTP has the best correspondence (Table 5.3) to the calculated "butterfly" vibrational modes [152].

In order to extract more information from the HREEL spectra, off-specular measurements have been performed. In Fig. 5.5 HREEL spectra with geometry  $0^\circ$ ,  $5^\circ$  and  $10^\circ$  off the specular direction are presented for the LTP and MTP. The analysis of the loss intensity variations with the off-specular angle shows that only the vibrations at  $537$ ,  $605$  and  $774.5\text{ cm}^{-1}$  for the LTP and at  $595.5$  and  $784\text{ cm}^{-1}$  for the MTP have significant dipole components. All other losses

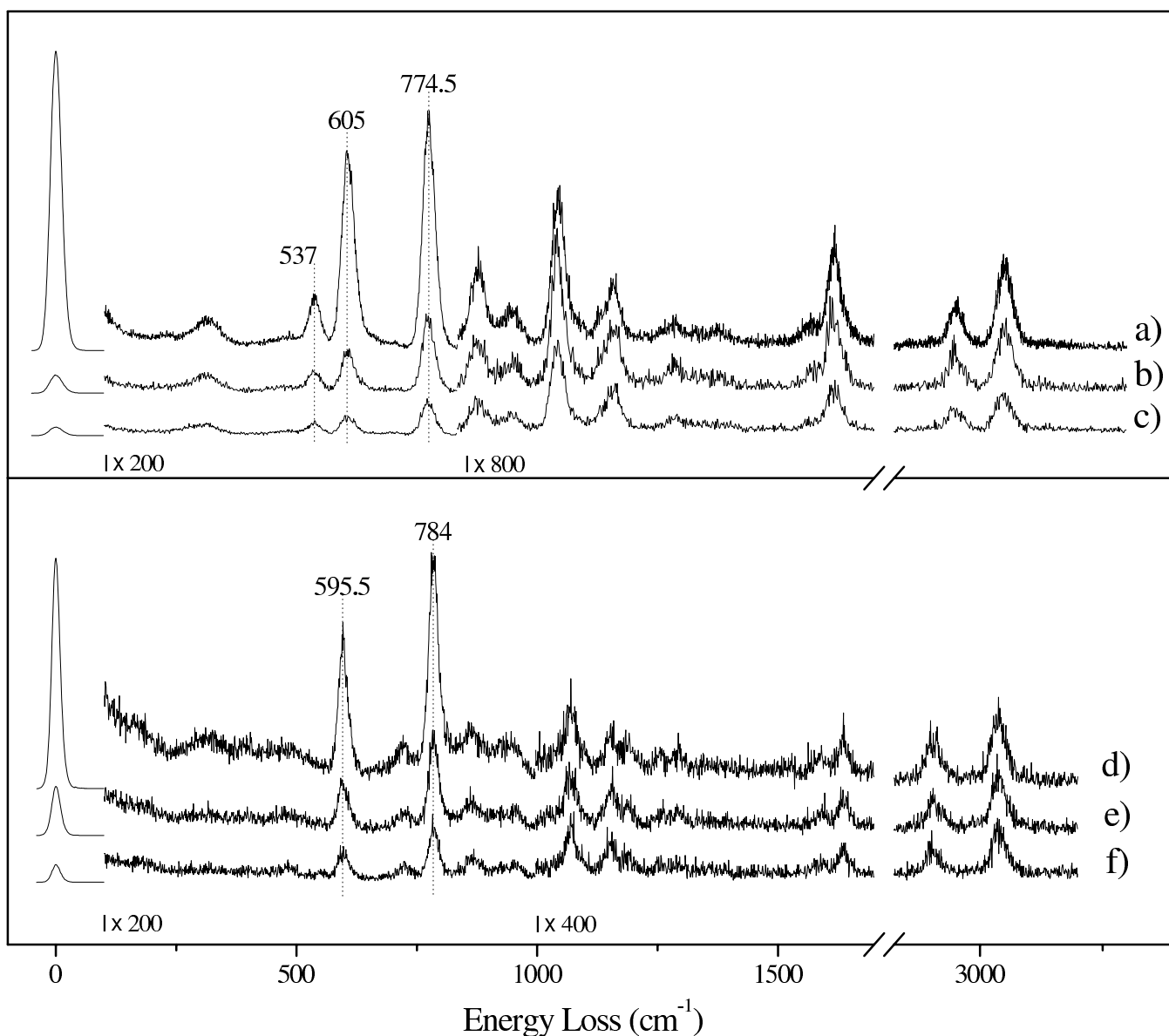


Figure 5.5: Off-specular HREEL spectra of  $C_6H_6$  adsorbed on a vicinal Si(100) surface. The measurements are performed with 4 eV electron primary energy at 100 K substrate temperature. (a), (b) and (c) are spectra of the LTP taken in geometry with  $0^\circ$ ,  $5^\circ$  and  $10^\circ$  off the specular direction, respectively. (d), (e) and (f) are spectra of the MTP measured also with  $0^\circ$ ,  $5^\circ$  and  $10^\circ$  off-angles. Only the frequency values of the modes with significant dipole component are given in the figure.

are excited by the impact scattering mechanism (see subsec. 1.3.1). The missing dipole activity of most of the modes makes it impossible to apply the intensity comparison between the out-of-plane and the in-plane C-H bending vibrations which can be a criterion for the molecular plane orientation relative to the surface. Nonetheless, it is indicative for a flat-lying molecule that all modes with significant dipole component involve atomic motions out of the molecular plane. Apart from the dipole selection rules which can be applied to very few modes, the impact selection rule can be applied in our particular geometry with scattering plane parallel to the

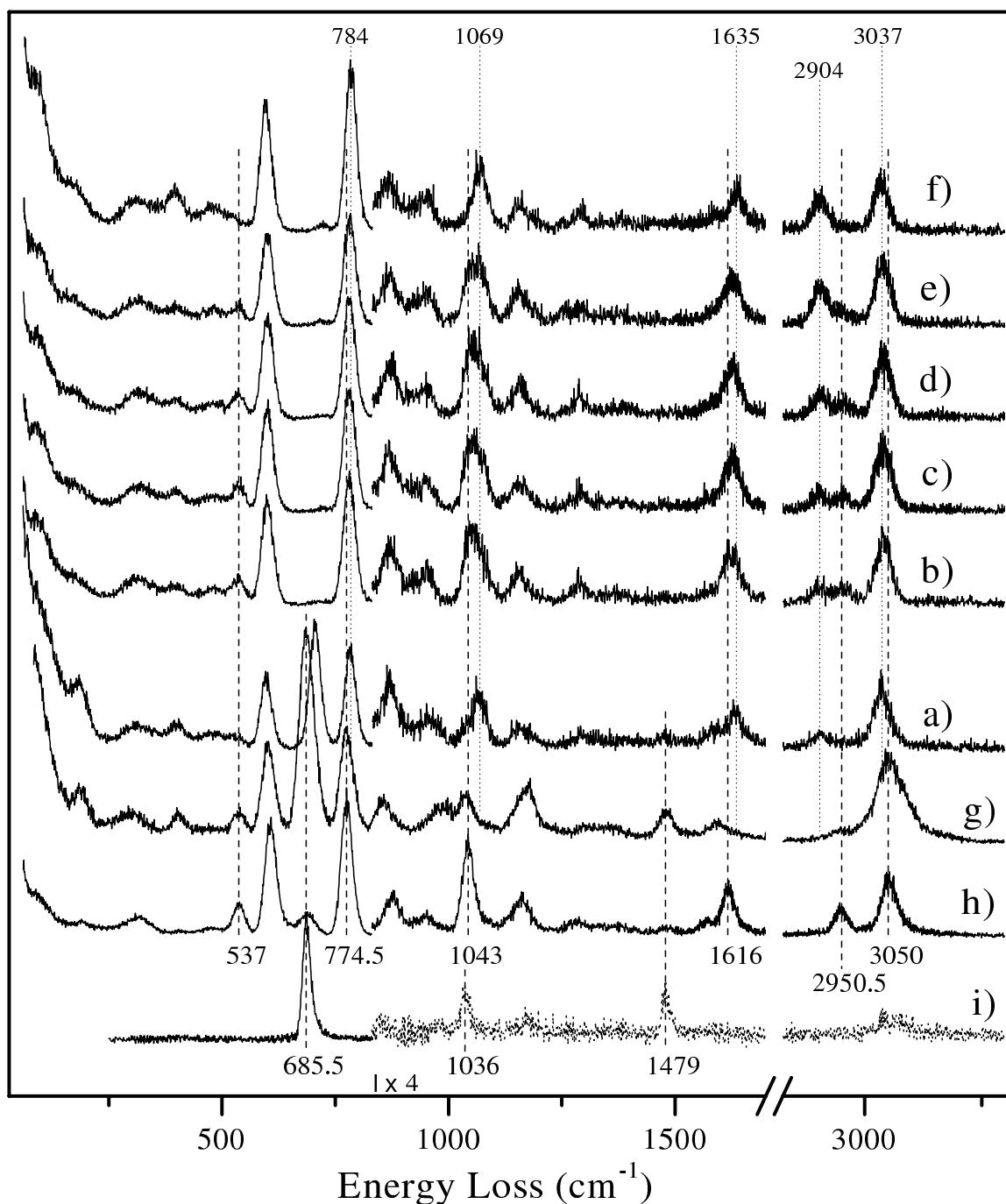


Figure 5.6: HREEL spectra of  $C_6H_6$  adsorbed on a vicinal Si(100) surface as a function of the annealing temperature. The measurements are performed with 4 eV electron primary energy at 100 K substrate temperature. (a–f) are spectra of  $\theta = 0.2$  benzene taken without annealing (a) and after successively annealing for a few seconds up to 200 K (b), 300 K (c), 300 K for 600s (d), 350 K (e) and 440 K (f). (g) is a spectrum of saturated coverage at 100 K. (h) is measured on saturated at 100 K surface, after passivation with 0.40ML hydrogen at 650 K. (i) is an subtraction product of spectra measured on H/Si(100)-(3 $\times$ 1) and on physisorbed benzene covered H/Si(100)-(3 $\times$ 1) surfaces.

silicon dimer bonds. The latter selection rule claims that vibrations with symmetry odd to the scattering plane are suppressed.

As follows, in the  $C_{2v}$  point group of the "butterfly" adsorbate complex the modes belonging to the  $A_2$  and  $B_2$  irreducible representations are impact-forbidden if the scattering plane is aligned with the mirror plane containing the dimer bond. The above-mentioned selection rules operating in the HREELS measurements are applied in the mode assignment of the LTP summarized in Tables 5.2 and 5.3 in the discussion part of this chapter.

STM observations of low benzene coverages adsorbed at 300 K on a Si(100) surface have been interpreted by Lopinski *et al.* [146, 147] as a metastable butterfly structure (Fig. 5.1 a) which converts with time (hours) to a more stable tight bridge configuration (Fig. 5.1 d). Converted into our notations this conclusion claims that the LTP is a metastable adsorption product at 300 K which converts with time to the more stable MTP(HTP). To examine this proposal we have investigated a  $\theta = 0.2$  benzene layer adsorbed at 100 K, as a function of the annealing temperature. The resulting HREEL spectra are plotted in Fig. 5.6. For later comparison the spectrum of physisorbed benzene with vibrations at 685.5, 1036, 1479 and  $\sim 3060 \text{ cm}^{-1}$  is present in Fig. 5.6(i), corresponding to symmetric out-of-plane C-H bending, in-plane C-H bending, C-C stretching and C-H stretching modes, respectively [154]. The vibrations are extracted from a spectrum of physisorbed benzene on H/Si(100)-(3 $\times$ 1) at 100 K, where all silicon dangling bonds are saturated by hydrogen. An observation of the vibrational spectrum of  $\theta = 0.2$  benzene taken without annealing after adsorption at 100 K (Fig. 5.6 a) reveals chemisorbed benzene in the MTP(HTP) with its characteristic modes at 784, 1069 and  $2904 \text{ cm}^{-1}$ , together with a physisorbed phase with a mode at  $705 \text{ cm}^{-1}$ . We can deduce that a site specific MTP(HTP) chemisorption takes place because benzene molecules are randomly distributed over the surface at this temperature. The benzene molecules located not on appropriate surface sites are physisorbed. The out-of-plane C-H bending mode of the latter is perturbed by  $\sim 10 \text{ cm}^{-1}$  relative to benzene physisorbed on a passivated surface (Fig. 5.6 i). Annealing to 200 K (Fig. 5.6 b) is sufficient to convert the physisorbed to chemisorbed benzene in the LTP, manifested by the appearance of its characteristic modes at 537, 1043 and  $2950.5 \text{ cm}^{-1}$  together with the disappearance of the  $705 \text{ cm}^{-1}$  loss. Annealing to 300 K for a few seconds and for 600 sec (Fig. 5.6 c,d) does not alter the vibrational spectrum. After annealing to 350 K the LTP vibration intensities are reduced but still detectable in the spectrum (Fig. 5.6 e) suggesting phase depletion and conversion to the MTP(HTP). This process is supplied by the substrate thermal energy and either occurs at the same surface site or is mediated by benzene transport to an appropriate surface site. Annealing to 440 K, (f) in Fig. 5.6, leaves only HTP on the surface as is also evident from the desorption spectrum (dotted line) in Fig. 5.2(b). Fig. 5.6 (g) and (h) also show spectra of  $\theta > 1$  adsorbed at 100 K on clean and partially passivated surfaces, respectively. In these two cases chemisorption, leading mainly to the LTP, occurs together with a physisorbed phase with unperturbed out-of-plane C-H bending mode. These results imply that saturation of the surface as well as a 0.4 ML monohydride suppress the MTP(HTP) formation at 100 K.

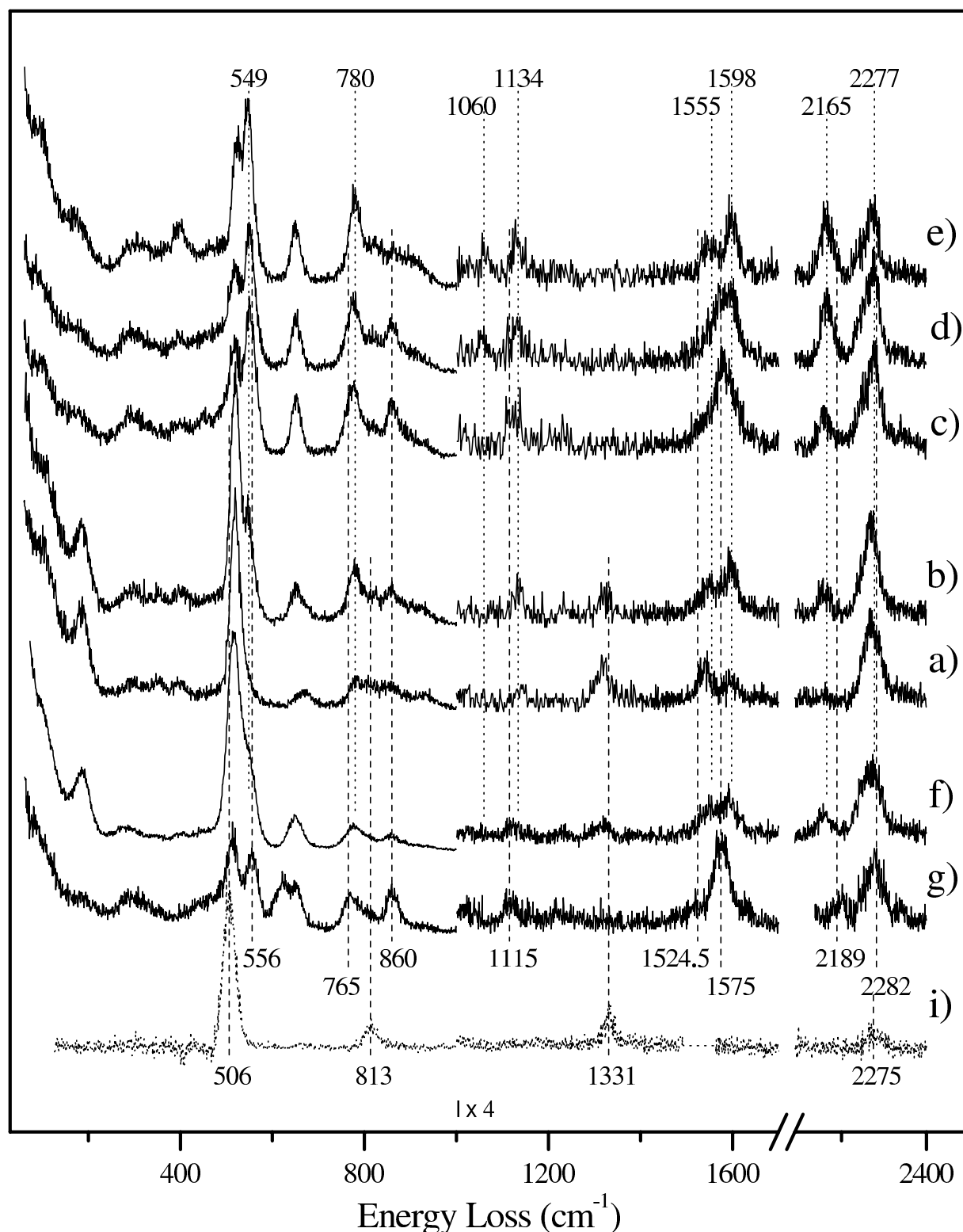


Figure 5.7: HREEL spectra of  $C_6D_6$  adsorbed on a vicinal Si(100) surface as a function of the annealing temperature. The measurements are performed with 4 eV electron primary energy at 40/100 K substrate temperature. (a-e) are spectra of  $\theta = 0.3$  adsorbed at 40 K taken directly after dosing (a) and after successively annealing for a few seconds up to 100 K (b), 300 K (c), 350 K (d), and 440 K (e). (f) is a spectrum of  $\theta > 1$  adsorbed at 100 K. (g) is measured on  $\theta > 1$  adsorbed at 100 K, after passivation with 0.40 ML hydrogen at 650 K. (i) is an subtraction product of spectra measured on D/Si(100)-(2 $\times$ 1) and on physisorbed benzene covered D/Si(100)-(2 $\times$ 1) surface.

Additionally, based on the above results it can be suggested that the physisorption phases acting as precursors for the LTP and for the MTP(HTP) are different; note the out-of-plane C-H bending mode shift from 685.5 to 705  $cm^{-1}$  (Fig. 5.2 a,g).

A  $\theta = 0.3$   $C_6D_6$  layer was also vibrationally investigated in its dependence on the annealing temperature. The resulting HREEL spectra are presented in Fig. 5.7(a-e). The observed behaviour of the deuterated benzene is similar to that of the hydrogenated adsorbate. The spectrum after adsorption of  $\theta = 0.3$  at 40 K and annealed to 100 K (Fig. 5.7 b) again shows a chemisorbed phase with modes at 780, 1134, 1598 and 2165  $cm^{-1}$  characteristic for the MTP(HTP). After annealing to 300 K the LTP appears on the surface with its vibration at 860  $cm^{-1}$  (Fig. 5.7 c), which is reduced in intensity after annealing to 350 K and vanishes after annealing to 440 K (Fig. 5.7 d,e), thus indicating a phase transition at temperatures well above 300 K.  $\theta > 1$  benzene, adsorbed at 100 K, presents a coexistence of chemisorbed benzene in the LTP and in the MTP(HTP) (Fig. 5.7 f). This result differs from the analogous  $C_6H_6$  case but could be a result of the artificial 2-3 times slower dosing in the case of  $C_6D_6$  adsorption.  $\theta > 1$  benzene, adsorbed at 100 K on a 0.4 ML hydrogen-covered surface, shows the presence only of the LTP as a chemisorbed phase (Fig. 5.7 g), in agreement with the results from the hydrogenated adsorbate.

The results presented in this section will be summarized and analyzed together with the benzene adsorption results on the nominally flat Si(100) surface (section 5.2) in the discussion part of this chapter.

## 5.2 Benzene adsorption on a nominally flat Si(100)-(2×1) surface

In order to generalize the results from benzene adsorption on a vicinal Si(100) surface we performed TDS and HREELS investigations of this system also on a highly-oriented (100) silicon crystal. In Fig. 5.8 TPD spectra of regular and deuterated benzene adsorbed at 90 K on a nominally flat Si(100) surface are shown. Again only the temperature range where the chemisorbed phase appears in the desorption spectrum is presented. The TPD spectra are similar to the spectra for benzene adsorption on a 5° vicinal surface (Fig. 5.2). The differences compared to desorption from a vicinal surface are the reduction of the  $\beta_3$  peak area relative to the lower temperature structure and the more prominent double-shape of the latter structure (Fig. 5.8 a,d). The preannealing to 440 and 430 K of the saturated coverage leaves only the  $\beta_2$  and  $\beta_3$  in the TPD spectra (Fig. 5.8 b,e/solid lines), while the same preannealing of  $\theta = 0.2$   $C_6H_6$  shows a single  $\beta_3$  peak (Fig. 5.8 b/dotted line). On a nominally flat Si(100) surface pre-adsorption of 0.25ML hydrogen at 650 K is sufficient to block the  $\beta_3$  and strongly reduce the  $\beta_3$  formation, and results in the appearance of a sharp  $\beta_1$  peak in the TPD spectrum (Fig. 5.8 c,f). Thus analogous to the benzene adsorption on a vicinal surface three benzene phases can be prepared and investigated. Namely, a low-temperature phase (LTP) related to  $\beta_1$ , a middle-temperature phase (MTP) comprising  $\beta_2 + \beta_3$ , and a high-temperature phase (HTP) containing only the  $\beta_3$  peak.

The vibrational spectroscopy has been performed with a scattering geometry in which

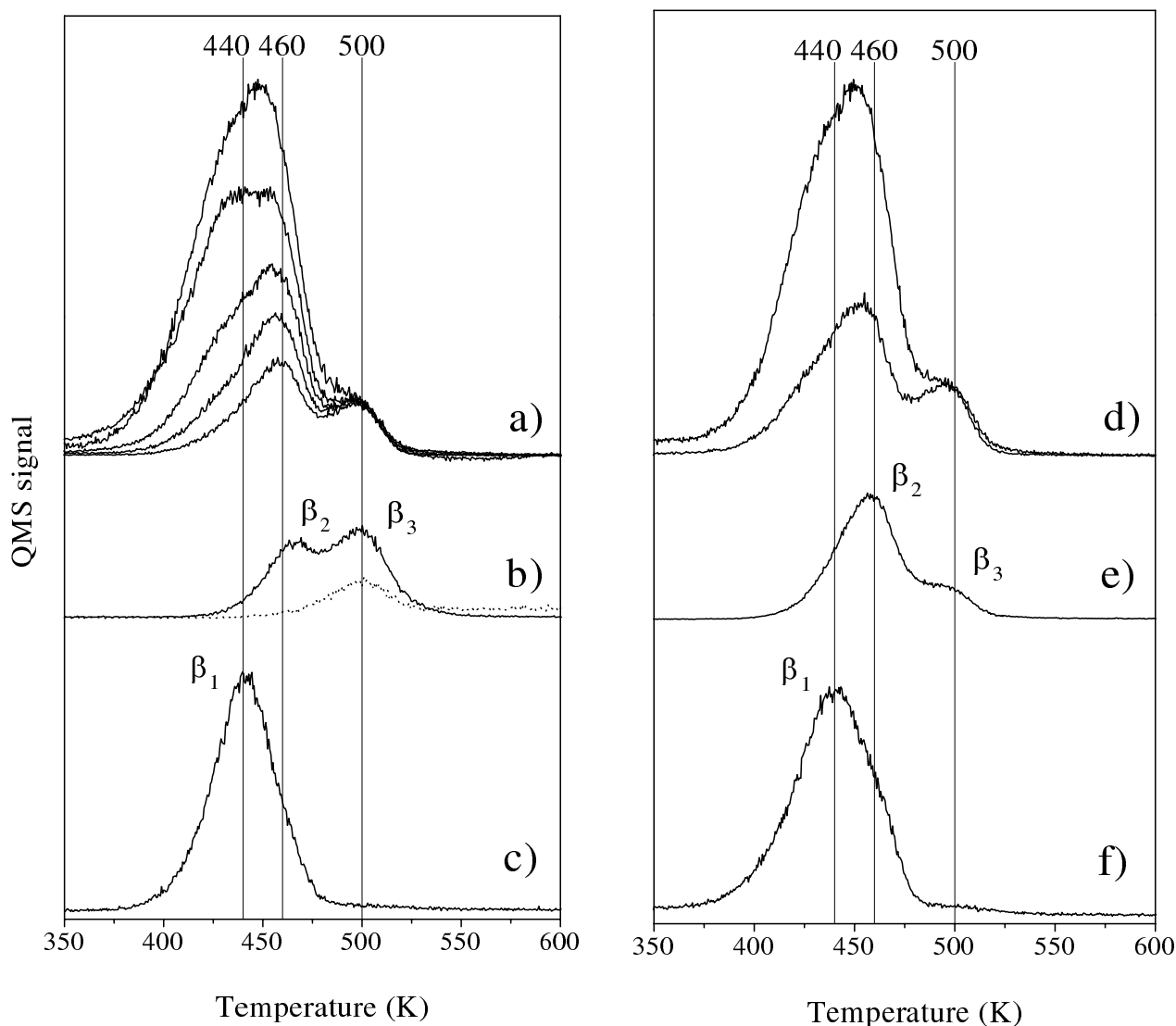


Figure 5.8: TPD spectra (2 K/s) of hydrogenated (a, b, c) and deuterated (d, e, f) benzene adsorbed at 90 K on a nominally flat Si(100) surfaces. Only the chemisorption temperature interval is included. (a) and (d) show spectra taken after successively increased doses. (b) spectra of  $\theta_{C_6H_6} > 1$  (solid line) and  $\theta_{C_6H_6} \approx 0.2$  (dotted line) benzene coverages pre-annealed up to 440 K. (e) spectrum of  $\theta_{C_6D_6} > 1$  pre-annealed to 430 K. (c) and (f) present results of a benzene-saturated surface, after its passivation with  $\theta = 0.25$  hydrogen at 650 K.

the electron scattering plane projection on the surface forms a  $45^\circ$  azimuthal angle ( $\overline{\Gamma M}$  in Fig. 3.8) relative to the silicon dimer bond directions on both orthogonal surface domains (subsection 3.1.1). In Fig. 5.9 HREEL spectrum of the  $C_6H_6$  monolayer, together with spectra of the separated three adsorbate phases, are presented. Comparing the spectrum of the MTP (Fig. 5.9 c) with those of the HTP (Fig. 5.9 d) a strong intensity reduction of the modes above  $500\text{ cm}^{-1}$  is visible. This is a result of the loss intensity dependence on the adsorbate concentration on the surface which is more than twice smaller in the HTP. Thus the modes with small intensity in the spectrum of the MTP are not resolvable in the spectrum of the HTP. The

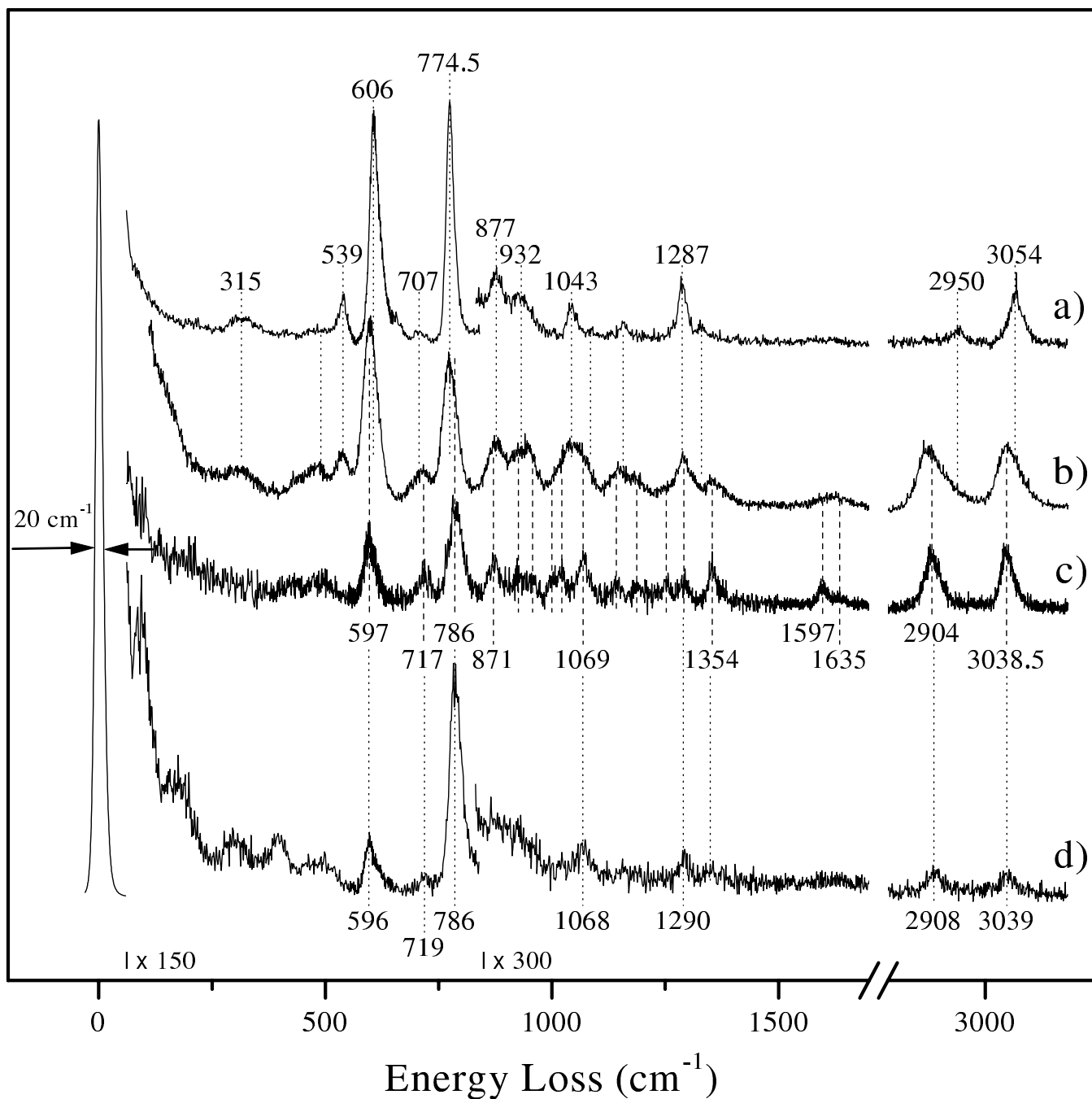


Figure 5.9: HREEL spectra of  $C_6H_6$  adsorbed on a nominally flat Si(100) surface at 90 K with 4 eV electron primary energy in the specular direction. The spectra are taken on: (a)  $\theta_{C_6H_6} > 1$  adsorbed at 90 K on a passivated (650 K) with 0.25 ML atomic hydrogen surface and subsequently annealed to 300 K; (b)  $\theta_{C_6H_6} > 1$  adsorbed on a clean surface at 90 K and subsequently annealed to 300 K;  $\theta_{C_6H_6} = 0.2$  adsorbed at 90 K and annealed to 440 K (c) and to 470 K (d).

significant result is that all strong losses are preserved in the latter spectrum with less than  $4\text{ cm}^{-1}$  shifts, suggesting an almost identical structure of the adsorbate in the MTP and HTP. Comparing the MTP (Fig. 5.9 c) with the LTP (Fig. 5.9 a) vibrational features more significant

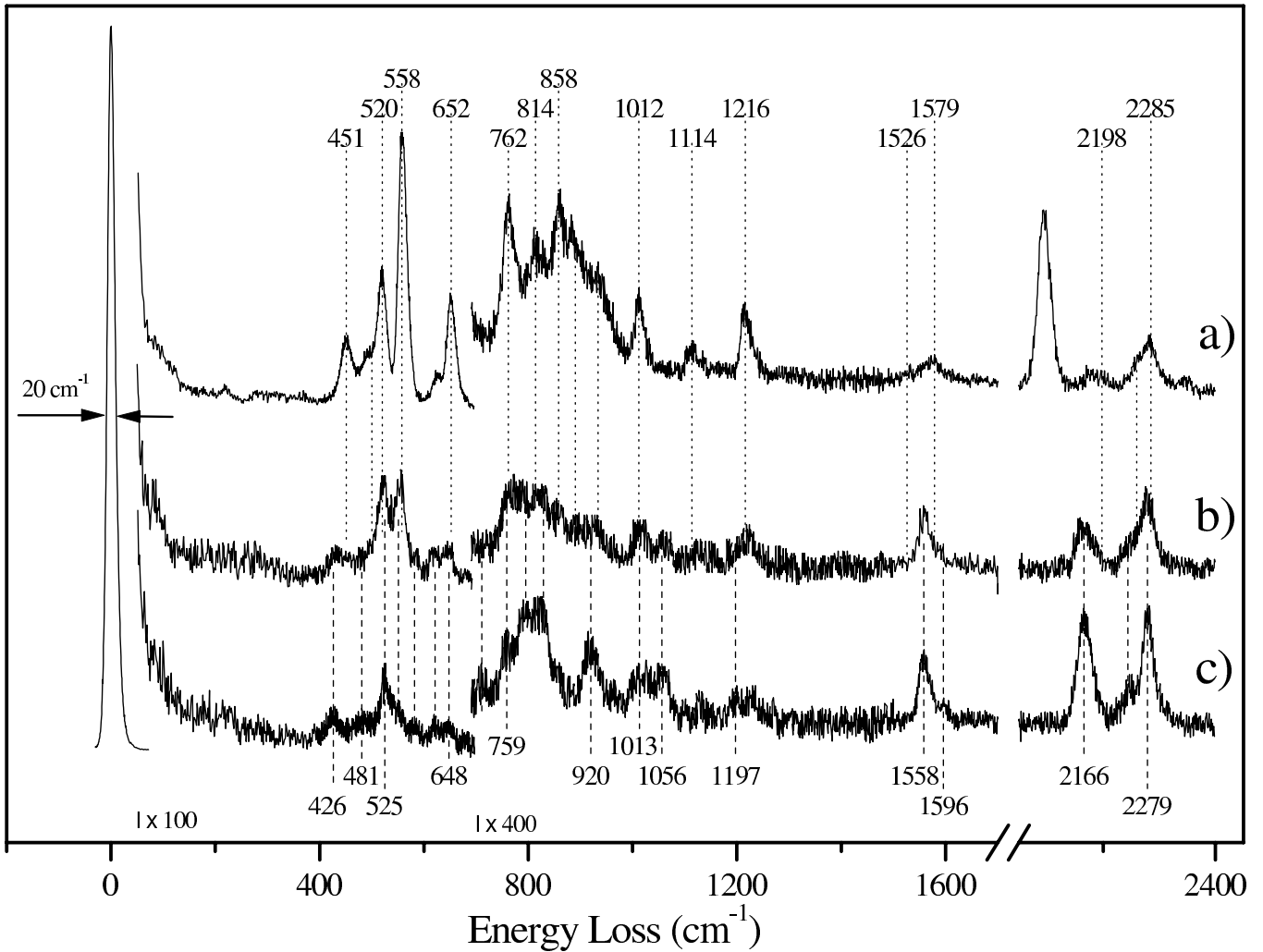


Figure 5.10: HREEL spectra of  $C_6D_6$  adsorbed at 90 K on a nominally flat Si(100) surface. The measurements have been performed with 4 eV electron primary energy in the specular direction at 90 K substrate temperature. The spectra are taken on: (a)  $\theta_{C_6D_6} > 1$  adsorbed at 90 K on a passivated (650 K) with 0.25 ML atomic hydrogen surface and subsequently annealed to 300 K; (b)  $\theta_{C_6D_6} > 1$  adsorbed at 90 K on a clean surface and annealed to 300 K; (c)  $\theta_{C_6D_6} = 0.2$  annealed to 430 K.

differences can be detected. The frequency shifts are up to  $\sim 45 \text{ cm}^{-1}$  and reversed intensity ratios are visible. The  $C_d-H_d$  and C-H stretching modes (for the notations and mode assignment see section 5.1) are red shifted by 46 and  $15.5 \text{ cm}^{-1}$  respectively, suggesting stronger softening of the  $C_d-H_d$  bond. In this particular electron scattering geometry the C=C stretching modes of the LTP are with intensities below our spectroscopy sensitivity. Thus a comparison of the C=C stretching doublet cannot be made. The in-plane ( $1100 \div 1350 \text{ cm}^{-1}$ ) and out-of-plane ( $650 \div 1050 \text{ cm}^{-1}$ ) hydrogen bending modes undergo shifts in different directions manifesting their complex vibrational structure. The benzene ring breathing vibrations at  $606$  and  $877 \text{ cm}^{-1}$  for the LTP are both red shifted by 9 and  $6 \text{ cm}^{-1}$ , respectively. The apparent loss at  $539 \text{ cm}^{-1}$  in the LTP spectrum vanishes in the MTP spectrum probably due to coupling to a substrate phonon band in the modified geometry of the MTP. The spectrum of the benzene monolayer

is a superposition of the losses belonging to the LTP and the MTP demonstrating the coexistence of the two adsorbate phases. The off-specular measurements (not shown here) reveal a significant dipole component only for the LTP modes at 606 and 774.5  $cm^{-1}$ .

In Fig. 5.10 HREEL spectra of deuterated benzene are presented for the monolayer and for the separated LTP and MTP. The HREEL spectrum of the monolayer contains all losses of the two adsorbate phases implying their coexistence. An inspection of the vibrational changes between the LTP and the MTP spectra reveals an almost missing variation of the mode number but significant frequency shifts and altered intra-mode intensity ratios. In the carbon-hydrogen stretching frequency region ( $\sim 2200$   $cm^{-1}$ ) in the LTP spectrum three bands are resolved which undergo a red shift and a relative intensity increase in the MTP. The C=C stretching modes (at 1579  $cm^{-1}$  and 1526  $cm^{-1}$ ) are probably blue shifted with an opposite intensity ratio. As in the case of hydrogenated benzene, the in-plane and out-of-plane deuterium modes show different signs of the frequency shifts. The LTP losses at 558, 652 and 762  $cm^{-1}$  have large intensity reduction in the MTP. The first mode corresponds to the benzene ring deformation with out-of-phase carbon motions. The second two modes are associated with out-of-plane deuterium bending vibrations.

The thermally induced  $C_6H_6$  phase transition has been investigated on the nominally flat Si(100) surface. The resulting HREEL spectra are presented in Fig. 5.11. The HREEL spectrum of  $\theta_{C_6H_6} > 1$  adsorbed at 90 K on the clean surface (Fig. 5.11 e) is dominated by the vibrations of the physisorbed species (Fig. 5.11 f) and the weak losses around 610 and 780  $cm^{-1}$  are not sufficient to resolve which chemisorbed phase is present on that surface. Nonetheless the missing loss at 2904  $cm^{-1}$  could be indicative for the absence of MTP(HTP). In the spectrum of  $\theta = 0.3$  benzene adsorbed at 90 K (Fig. 5.11 a), together with the vibrations of the physisorbed phase weak losses at 600, 785 and 2905  $cm^{-1}$  are detectable. The latter are very close to the characteristic vibrations of the MTP(HTP), suggesting that these phases are present at 90 K. Also the strongest loss of the physisorbed benzene at 695  $cm^{-1}$  is blue shifted by  $\sim 10$   $cm^{-1}$  relative to the physisorbed phase on the fully passivated surface (Fig. 5.11 f). Annealing of this layer up to 200 K converts the physisorbed to a chemisorbed phase and the characteristic losses of the LTP, e.g. the modes at 539, 774.5, 1043, 1287 and 2950  $cm^{-1}$ , appear in the spectrum (Fig. 5.11 b). Annealing to 310 K does not affect the spectrum further (Fig. 5.11 c). After raising the sample temperature up to 380 K a depletion of the LTP in parallel with an increase of the MTP(HTP) related modes is observed, best visible in the disappearance of the modes at 539 and 1043  $cm^{-1}$  together with the increase of the mode at 2904  $cm^{-1}$ . Thus at temperatures between 310 K and 380 K a phase transition from LTP to MTP(HTP) takes place on the surface.

To summarize it can be concluded that the results of benzene adsorption on the nominally flat Si(100) surface qualitatively reproduce the results on the vicinal surface. The quantitative differences will be analyzed in the final section of this chapter.

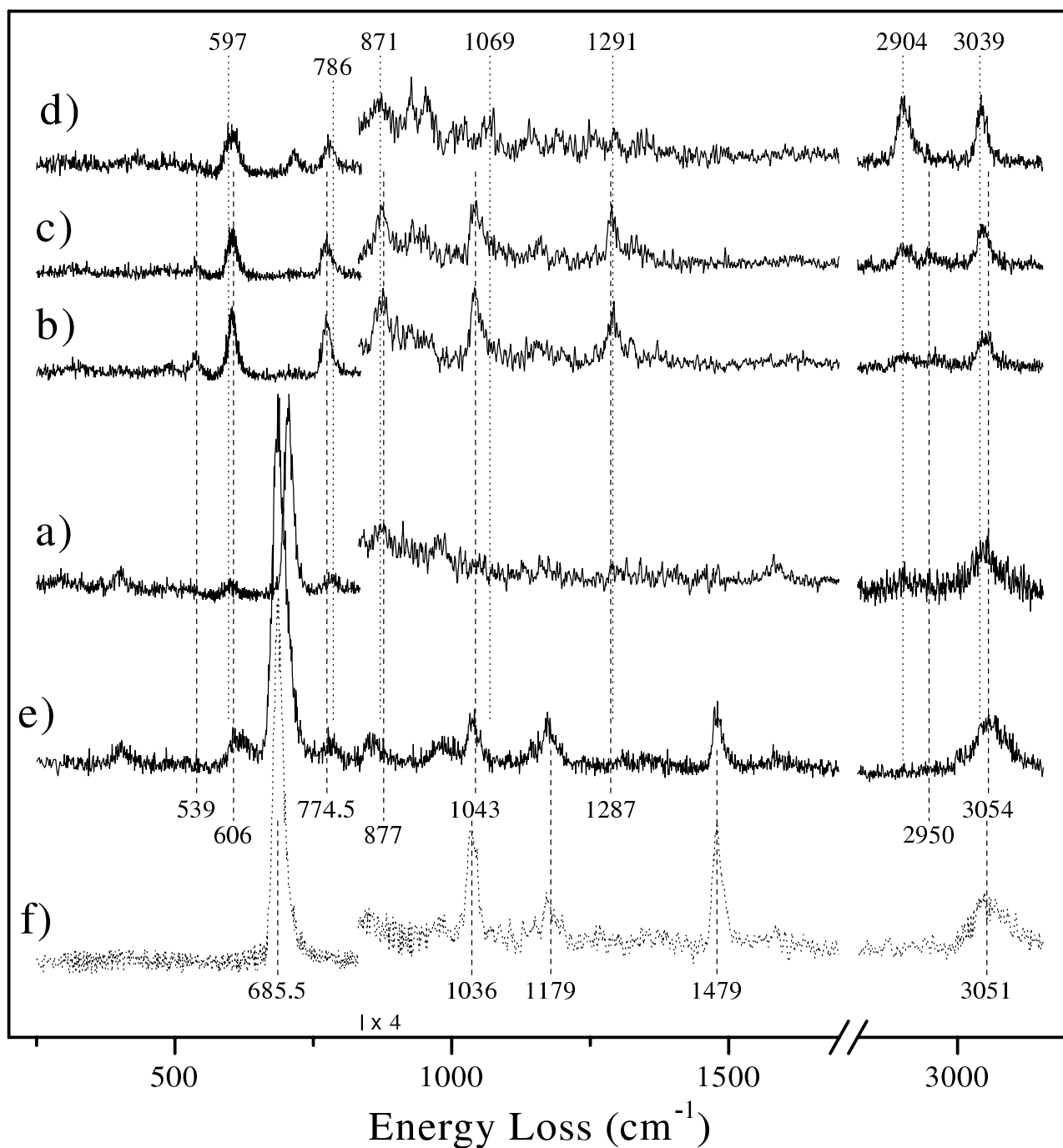


Figure 5.11: HREEL spectra of  $C_6H_6$  adsorbed on a nominally flat Si(100) surface as a function of the annealing temperature. The measurements have been performed with 4 eV electron primary energy at 90 K substrate temperature. (a-d) are spectra of  $\theta = 0.3$  benzene taken without annealing (a) and after successively annealing for a few seconds up to 200 K (b), 310 K (c) and 380 K (d). (e) is a spectrum of  $\theta_{C_6H_6} > 1$  adsorbed at 90 K. (f) is a difference spectrum measured on H/Si(100)-(3 $\times$ 1) and on physisorbed benzene covered H/Si(100)-(3 $\times$ 1) surfaces.

### 5.3 Discussion

Using HREELS the vibrational characteristics of three chemisorbed benzene phases on vicinal and nominally flat Si(100) surfaces have been investigated. All theoretically predicted vibrational modes based on a  $C_{2v}$  symmetry for a butterfly configuration reported by Staufer *et al.* [152] are presented in Tab. 5.1. The HREELS resolved vibrations are marked in the last column of the table. We experimentally resolved totals of 22(22), 15(21) and 14(13)  $C_6H_6(C_6D_6)$  derived modes for the LTP, MTP and HTP respectively, on vicinal and nominally flat Si(100) surfaces. The vibrational frequencies specific for the three phases are summarized in Tab. 5.2 and 5.3 for  $C_6H_6$  and  $C_6D_6$ , respectively. Among the three phases the LTP shows the best correspondence to the calculated vibrational modes of a butterfly geometry [152] with average discrepancy of  $21\text{ cm}^{-1}$  ( $16\text{ cm}^{-1}$ ) between the measured and calculated frequencies above  $500\text{ cm}^{-1}$  and maximum deviation of  $36\text{ cm}^{-1}$  ( $30\text{ cm}^{-1}$ ) for the  $C_6H_6(C_6D_6)$  adsorbate. The small frequency differences between the LTP experimental values on vicinal and flat (100) surfaces come from the different scattering geometries where the cross section of the modes is altered and thus a variation of the shifts due to adjacent peaks in the spectrum takes place. The appearance of new losses, e.g. the modes at 522, 707, 932 and  $1085\text{ cm}^{-1}$ , is also a result of the different experimental geometry with their specific operating scattering selection rules. All ten totally symmetric ( $A_1$ ) modes above  $200\text{ cm}^{-1}$  have been identified in the HREEL spectra of the LTP. Three of them show a significant dipole components of the modes and are marked by an index "d" in Tab. 5.2 and 5.3). The agreement between the symmetric and asymmetric C=C stretching frequencies (modes 35 and 36) is remarkable, especially for the splitting of the C=C stretching modes calculated  $53(55)\text{ cm}^{-1}$  and measured  $49(50)\text{ cm}^{-1}$ . Basing on its vibrational characteristics in comparison with the theoretical results [152] we assign the LTP as the butterfly benzene complex di- $\sigma$  bonded to a single silicon dimer. This assignment is in agreement with the previous works for the monolayer using HREELS with lower resolution [152] as well as using ARUPS [151] for benzene adsorption on a  $4^\circ$  vicinal surface. Here we extend this observation to the flat Si(100) surfaces.

Now we will focus our discussion on the MTP and the HTP of benzene chemisorbed on a Si(100) surface. To visualize the characteristics of the different phases the frequencies of all modes for the butterfly configuration [152] are plotted in Fig. 5.12 together with the loss frequencies of the three phases experimentally resolved in this work. As a fingerprint of the butterfly benzene structure can be taken the C=C stretching doublet which is well separated from the other vibrational modes and is a direct evidence for the presence of more than one carbon-carbon double bond in the adsorbed molecule. Among the stable benzene complexes on the Si(100) surface only the butterfly (1,4-cyclohexadiene-like) and the tilted (1,3-cyclohexadiene-like) geometries have more than one carbon-carbon double bond, namely two C=C bonds (Fig. 5.1 a,b). The tilted configuration with its molecular plane not parallel to the surface has been ruled out by ARUPS [151] and STM [146, 147] investigations. Additionally the splitting of the C=C stretching modes in the gas phase of 1,3-cyclohexadiene is  $\sim 100\text{ cm}^{-1}$  [155] is significantly larger than the splitting of  $\sim 40\text{ cm}^{-1}$  in the MTP and the HTP. Thus the presence of a C=C stretching doublet in the MTP and the HTP manifests the 1,4-cyclohexadiene-like structure of these phases. Relative to the LTP of  $C_6H_6(C_6D_6)$ , the symmetric and asymmetric

N	Assignment	Calc.	Exp.
1	B2 $R_x$ of $C_6H_6-Si_2$ around the dimer bond	86	
2	B1 $T_x$ of $C_6H_6$ + $R_y$ of the dimer (in-ph.)	88	
3	A2 $R_z$ of $C_6H_6$	109	
4	<b>A1</b> $T_z$ of the $C_6H_6-Si_2$ moiety	154	
5	B1 $R_y$ of $C_6H_6-Si_2$ with rotation axis through the benzene	186	
6	B2 $R_x$ of the Si- $C_d$ around Si-Si out-of-ph. with $R_x$ of $C_6H_6$	194	X
7	B1 $R_y$ of $C_6H_6$ in-ph. with $R_y$ of the dimer	310	X
8	<b>A1</b> butt.bend.+ $T_z$ of $C_6H_6-Si_2$ ( $C_d$ in ph.)	318	X
9	B2 $T_y$ of the dimer	381	
10	A2 $R_z$ of the dimer	402	
11	<b>A1</b> Si-Si str.	419	
12	B1 asymm. Si-Cd str.	467	X
13	A2 $R_z$ of the C=C bonds around their centers	474	X
14	<b>A1</b> Si- $C_d$ str. + butt.bend. ( $C_d$ in-ph.)	523	X
15	<b>A1</b> $\langle(C,C_d,C)$ bend.	577	X
16	A2 benzene C-ring (skeleton) shearing along Y	608	
17	B1 asymm. $T_z$ of C and $C_d$ (C and $C_d$ out-of-ph.)	666	X
18	B2 out.of-pl. C-H bend.	678	X
19	<b>A1</b> coll. out-of-pl. C-H and $C_d-H_d$ bend. (in.ph.)	755	X
20	<b>A1</b> benzene breathing	870	X
21	B1 C- $C_d$ str.+C-H bend. following the C and $C_d$ motions	871	X
22	B1 out-of-pl. C-H and $C_d-H_d$ bend.(in-ph.) + skeleton shearing along X	887	X
23	A2 out-of-pl. C-H bend.	910	
24	B1 out-of-pl. C-H and $C_d-H_d$ bend. (out-of-ph.) + skeleton shearing along X	929	X
25	B2 C- $C_d$ str. + C-H, $C_d-H_d$ bend. with the C and $C_d$ motions	945	X
26	<b>A1</b> isolated out-of-pl. $C_d-H_d$ bend.	1016	X
27	A2 C- $C_d$ str.+in-pl. C-H, $C_d-H_d$ bend. following the C and $C_d$ motions	1030	
28	B1 out-of-pl. $C_d-H_d$ bend.	1065	X
29	B2 in-pl. C-H and $C_d-H_d$ bend. (out-of-ph.)	1109	X
30	<b>A1</b> in-pl. C-H bend.	1140	X
31	B2 in-pl. C-H and $C_d-H_d$ bend. (in-ph.)	1253	X
32	A2 in-pl. C-H and $C_d-H_d$ bend. (in-ph.)	1266	X
33	A2 in-pl. C-H and $C_d-H_d$ bend. (out-of-ph.)	1309	X
34	B1 in-pl. C-H bend.	1340	X
35	B2 asymm. C=C str.	1570	X
36	<b>A1</b> symm. C=C str.	1623	X
37	<b>A1</b> $C_d-H_d$ str.	2978	X
38	B1 $C_d-H_d$ str.	2978	
39	A2 C-H str.	3064	
40	B1 C-H str.	3065	X
41	B2 C-H str.	3079	
42	<b>A1</b> C-H str.	3081	X

Table 5.1: Vibrational mode assignment of benzene chemisorbed on a Si(100) surface in a butterfly configuration. The calculated frequencies are in  $cm^{-1}$  [152]. The experimentally observed modes (this work) are marked in the last column.

Num.	symm.	Calc. $C_6H_6$ [152].	Exp.	Exp.	Exp.	Exp.	Exp.	Exp.
			LTP $_{C_6H_6}$ vicinal	LTP $_{C_6H_6}$ nom.flat	MTP $_{C_6H_6}$ vicinal	MTP $_{C_6H_6}$ nom.flat	HTP $_{C_6H_6}$ vicinal	HTP $_{C_6H_6}$ nom.flat
6	B2	194	228	–	–	–	–	–
8	<b>A1</b>	318	311	–	–	–	–	–
12	B1	467	488	490	–	–	–	–
13	A2	474	–	522	–	–	–	–
14	<b>A1</b>	523	537 <sub>d</sub>	539 <sub>d</sub>	–	–	–	–
15	<b>A1</b>	577	605 <sub>d</sub>	606 <sub>d</sub>	597 <sub>d</sub>	597 <sub>d</sub>	596 <sub>d</sub>	596 <sub>d</sub>
18	B2	678	–	707	721	717	721	719
19	<b>A1</b>	755	774.5 <sub>d</sub>	774.5 <sub>d</sub>	784 <sub>d</sub>	786 <sub>d</sub>	784 <sub>d</sub>	786 <sub>d</sub>
20	<b>A1</b>	870	876	877	868	871	864	–
22	B1	887	–	932	927	926	–	–
24	B1	929	952	–	–	–	–	–
25	B2	945	–	–	957	957	950	–
26	<b>A1</b>	1016	1043.5	1043	1069	1069	1068	1068
28	B1	1065	–	1085	–	–	–	–
29	B2	1109	1130	–	1151	1142	1155	1159
30	<b>A1</b>	1140	1160	1157	1187	1187	1195	–
31	B2	1253	–	–	1255	1252	–	–
32	A2	1266	1280	1287	–	–	–	–
33	A2	1309	1328	1330	1293	1291	1291	1290
34	B1	1340	1376	–	–	–	1335	–
35	B2	1570	1567	(1570)	1590	1597	1589	1588
36	<b>A1</b>	1623	1616	(1618)	1635.5	1635	1636	1633
37	<b>A1</b>	2978	2950.5	2950	2904	2904	2904	2908
42	<b>A1</b>	3081	3050	3054	3037	3038.5	3034	3039

Table 5.2: Vibrational modes of three  $C_6H_6$  phases chemisorbed on a Si(100) surface. Index "d" denotes losses with a significant dipole component. The calculated values are for a butterfly adsorbate complex [152].

C=C stretching modes are blue shifted by  $\sim 18(21) \text{ cm}^{-1}$  and  $\sim 25(30) \text{ cm}^{-1}$ , respectively. For  $C_6H_6$  the carbon-hydrogen stretching frequency region contains again two well defined bands, corresponding to the equivalent two and four hydrogen atoms bonded to two  $sp^3$  and four  $sp^2$  hybridized carbon atoms in the benzene ring. Both bands are red shifted by  $46 \text{ cm}^{-1}$  for the  $C_d-H_d$  and by  $15 \text{ cm}^{-1}$  for the C-H stretching modes closer to the corresponding gaseous 1,4-cyclohexadiene values of  $2825 \div 2903 \text{ cm}^{-1}$  and  $3035 \text{ cm}^{-1}$  [155]. In the case of deuterated benzene the three bands in the LTP are also preserved and red shifted by  $28 \text{ cm}^{-1}$  for the  $C_d-D_d$  and by  $10$  and  $5 \text{ cm}^{-1}$  for the other two C-H stretching vibrations. Most of the LTP intensive losses below  $1500 \text{ cm}^{-1}$  have their shifted analogous modes in the HREEL spectra of the MTP and the HTP. Additionally the dipole activity of all modes is conserved. These

Num.	symm.	Calc. $C_6D_6$ [152]	Exp.		Exp.		Exp.
			LTP $_{C_6D_6}$ vicinal	LTP $_{C_6D_6}$ nom.flat	MTP $_{C_6D_6}$ vicinal	MTP $_{C_6D_6}$ nom.flat	HTP $_{C_6D_6}$ vicinal
8	<b>A1</b>	285	290	–	–	–	–
12	B1	438	450	451	–	–	–
13	A2	431	483	500	–	481	–
14	<b>A1</b>	486	512.5 <sub>d</sub>	520 <sub>d</sub>	521.5 <sub>d</sub>	525 <sub>d</sub>	521.5 <sub>d</sub>
15	<b>A1</b>	542	556 <sub>d</sub>	558 <sub>d</sub>	549 <sub>d</sub>	551 <sub>d</sub>	548 <sub>d</sub>
17	B1	589	–	–	–	621	–
18	B2	541	–	–	–	582	–
19	<b>A1</b>	634	651.5 <sub>d</sub>	652 <sub>d</sub>	649 <sub>d</sub>	648 <sub>d</sub>	650 <sub>d</sub>
20	<b>A1</b>	835	860	858	867	–	–
21	B1	689	–	–	–	711	–
22	B1	740	–	–	–	759	–
24	B1	917	–	934	–	–	–
26	<b>A1</b>	747	765	762	780 <sub>d</sub>	795 <sub>d</sub>	779.5 <sub>d</sub>
28	B1	834	–	890	–	–	–
29	B2	788	–	8145	825	829	828
30	<b>A1</b>	835	860	858	912	920	913
31	B2	1105	–	–	1060	1056	1061
32	A2	985	–	1012	1011	1013	–
33	A2	1207	1217	1216	–	1197	–
34	B1	1146	1115	1114	1134	–	1131
35	B2	1528	1524.5	1526	1555	1558	1548
36	<b>A1</b>	1583	1575	1579	1598	1596	1598
37	<b>A1</b>	2193	2189	2198	2165	2165	21625
40	B1	2258	2250	2260	2246	2244	2242
42	<b>A1</b>	2291	2282	2285	2277	2279	2274

Table 5.3: Vibrational modes of three  $C_6D_6$  phases chemisorbed on a Si(100) surface. Index "d" denotes losses with a significant dipole component. The calculated values are for a butterfly adsorbate complex [152].

observations suggest a similar structure of the adsorbate complex in all three phases on the Si(100) surface independent of the surface vicinality. The differences can be attributed to variations of the butterfly-like molecule's azimuthal orientation, relative to the silicon dimer bonds, and to changes of the bond strengths in the adsorption complex. Since a di- $\sigma$  bonded, 1,4-cyclohexadiene-like benzene molecule has local  $C_{2v}$  symmetry, we could find some hints for the molecular orientation by application of impact selection rules. On the nominally flat surface which possesses two 90° rotated (2×1) domains the sample was oriented in such a way that the scattering plane was aligned along a low-symmetry direction at an angle of 45° with respect to the dimer rows (common direction of both domains). On the single domain surfaces the

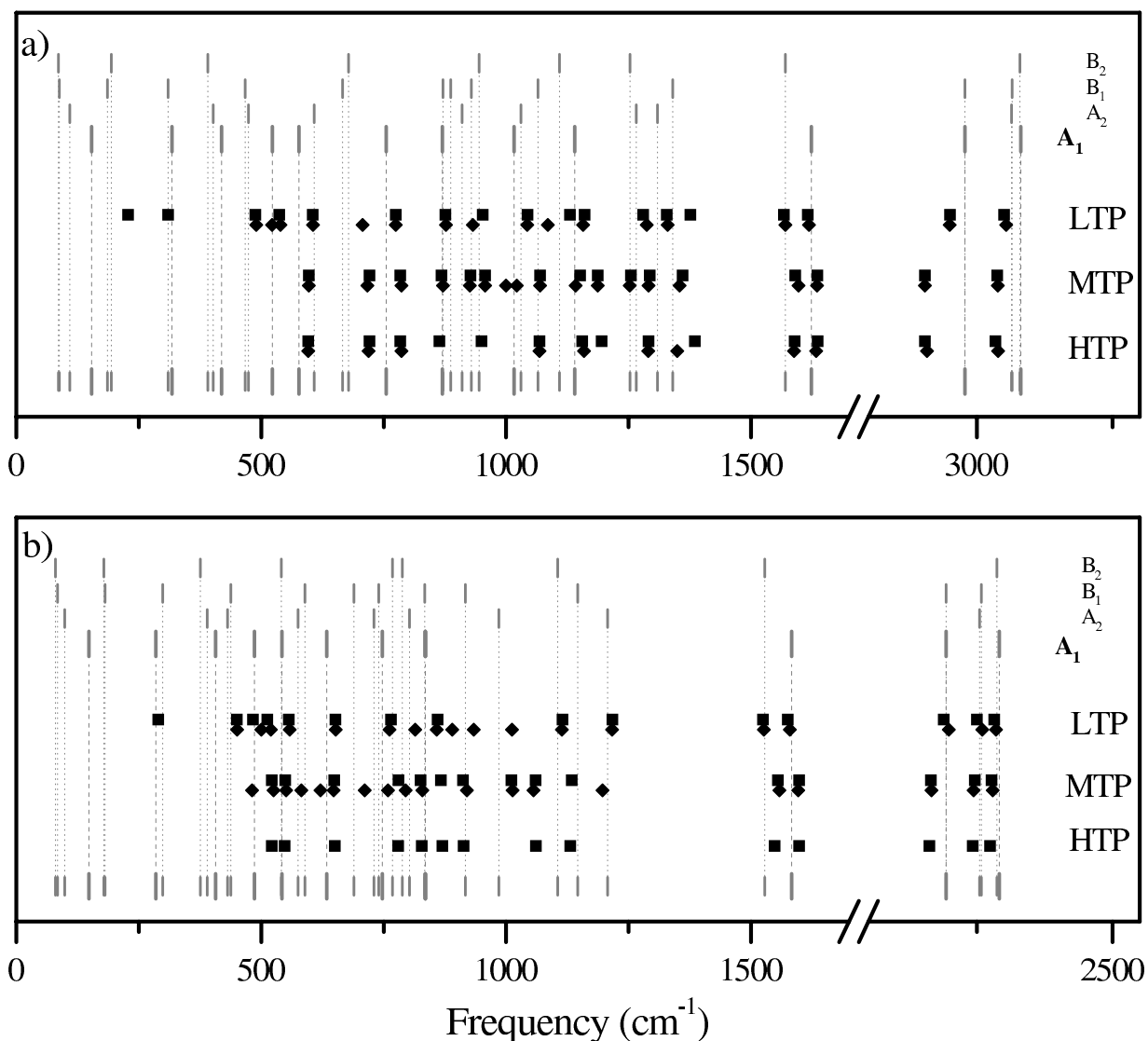


Figure 5.12: Theoretical vibrational modes of the butterfly complex together with the loss frequencies of the three phases of benzene chemisorbed on Si(100) surfaces. (a) and (b) present theoretical (vertical bars) and experimental (squares and diamond symbols) frequencies for C<sub>6</sub>H<sub>6</sub> and C<sub>6</sub>H<sub>6</sub> respectively on vicinal (squares) and nominally flat (diamonds) (100) surfaces.

scattering plane was aligned along the high symmetry direction parallel to the silicon dimer bonds. Thus in the latter case the impact scattering selection rules indicate that modes which are asymmetric with respect to the scattering plane cannot be excited by impact scattering. The vibrations with A<sub>2</sub> and B<sub>2</sub> symmetry are odd and thus are impact-forbidden, while those with A<sub>1</sub> and B<sub>1</sub> symmetry are even, allowed modes. Because the local C<sub>2v</sub> symmetry is slightly distorted due to the surface vicinality [151] the forbidden modes could be observed in the spectra but with strongly reduced intensities. Applying the impact selection rules to the pair of the symmetric (A<sub>1</sub>) and the asymmetric (B<sub>2</sub>) C=C stretching vibrations, the intensity ratio of 5:1 for the LTP is characteristic for an adsorption geometry with the C=C double bonds parallel to the Si-Si dimer bonds (parallel to the scattering plane). The intensity ratios of 2:1 for the

MTP and 3:1 for the HTP show that the benzene molecule in the MTP(HTP) is no longer parallel to the scattering plane (dimer bond direction) and consequently the asymmetric mode is more intensive (not impact-forbidden). The intensity ratios show a difference also between the MTP and HTP. Up to now we have considered these two phases separately but the MTP comprises species which appear as  $\beta_2$  and  $\beta_3$ (HTP) peaks in the TPD spectra. The  $\beta_2 + \beta_3$  and  $\beta_3$  structures show essentially the same vibrational characteristics, independent of the relative population, in contrast to their different desorption energies. The comparison of the MTP and HTP HREEL spectra reveals some frequency shifts but they are close to our experimental uncertainty. Significant variations occur only in the relative loss intensities indicating deviations of the molecule orientation to the scattering plane.

The HREELS investigations of low benzene coverages ( $\theta=0.2\div 0.3$ ) as a function of the annealing temperature reveal the presence of a chemisorbed phase upon adsorption at 100 K. This phase has the vibrational characteristics of the MTP(HTP) and coexists with a physisorbed phase which has altered mode frequencies relative to the multilayers. The physisorbed phase is converted to LTP after annealing to 200 K. Annealing to temperatures above 350 K leads to LTP depletion and increase of the MTP(HTP) population. These results suggest a site-specific chemisorption and probably thermally induced adsorbate diffusion on the surface. Benzene saturation at 100 K or adsorption on a partially hydrogen passivated surface suppresses the MTP(HTP) formation at 100 K and favours the LTP chemisorption. The hydrogen blocking of the MTP and the HTP in the entire temperature interval between 100 K and the desorption temperatures contains important information for the site specific chemisorption on the silicon surface. Atomic hydrogen adsorption on a Si(100) surface at 650 K forms monohydride pairs on a single silicon dimer [113, 109]. At this temperature diffusion of the hydrogen pairs takes place [156] and leads to clustering [113]. The step and defect sites are hydrogen passivated [157] and the strain induced by these surface inhomogeneities is reduced [158]. Therefore, the MTP (HTP) seems to be connected to an adsorption on dimers which are strained by the point defects or steps. This observation is supported by the TPD spectrum of benzene adsorbed on a surface passivated by atomic hydrogen at 400 K as presented in Fig. 5.13 (c).

In this spectrum a  $\beta'_3$  peak with HTP vibrational character is present and shifted to higher temperatures relative to the  $\beta_3$  of benzene adsorbed on a clean surface. The  $\beta_2$  is missing and the  $\beta'_1$  is slightly shifted to lower temperatures relative to  $\beta_1$ . A possible explanation is that a dihydride is formed at 400 K which acts as a missing-dimer-like point defect on the surface and in this way produces the necessary strain for the HTP formation. Hence, the HTP can be assigned to adsorption on silicon dimers near surface defects (point, steps). The  $\beta_2$  phase appears as not defect induced but rather it depends on the free terrace area which is reduced after hydrogen adsorption. The HREELS results suggest that the benzene molecules in the MTP(HTP) are rotated relative to those in the LTP which means that their C=C axes are not parallel to the silicon dimer bond. As all phases exhibit 1,4-cyclohexadiene-like vibrational spectra a butterfly bridge benzene complex di- $\sigma$  bonded to two silicon dimers adjacent in a row is proposed for the MTP and HTP. This butterfly bridge geometry is either defect assisted (HTP) or requires large surface areas free of defects and adsorbates in the low-coverage regime. In the butterfly bridge geometry (MTP, HTP) the benzene ring distortion is opposite to those of

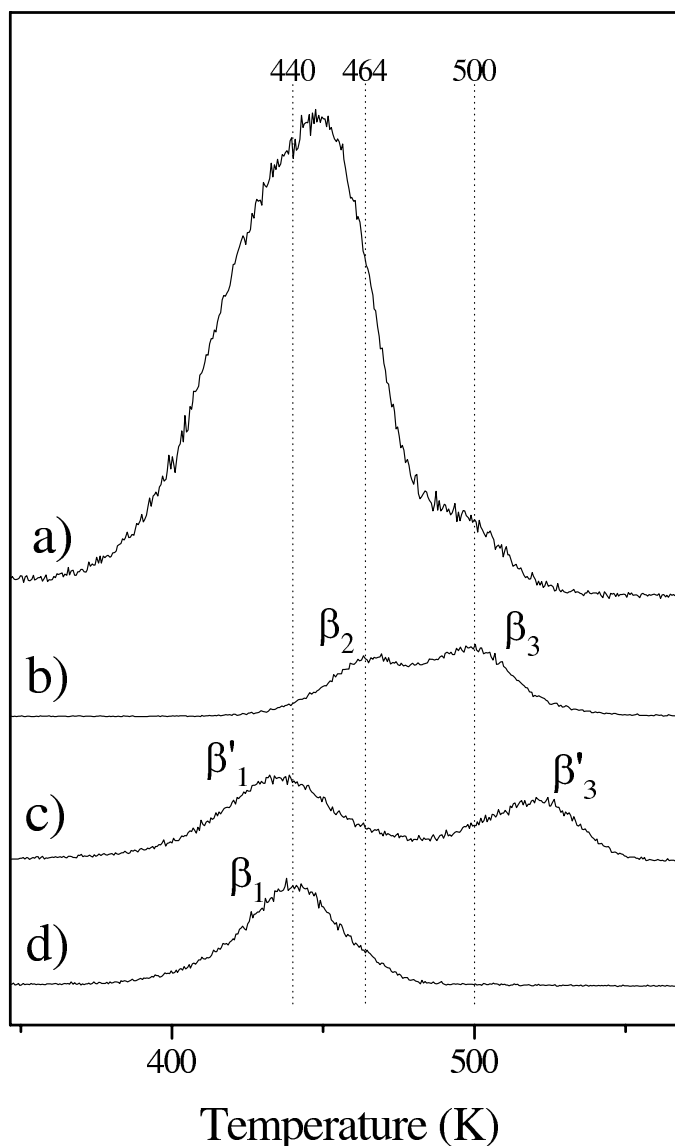


Figure 5.13: TPD spectra of  $C_6H_6$  chemisorbed on a nominally flat Si(100) surface. (a) clean surface saturated at 90 K. (b) saturated coverage annealed to 440 K. (c) benzene saturated surface after 0.25 ML atomic hydrogen adsorption at 400 K. (d) benzene saturated surface after 0.25 ML atomic hydrogen adsorption at 650 K.

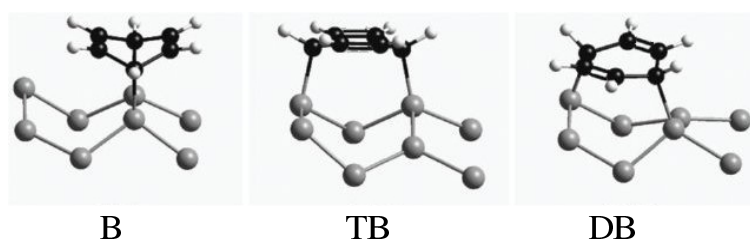


Figure 5.14: The stable 1,4-cyclohexadienelike configurations of benzene on a Si(100) surface. B – butterfly, TB – tilted bridge butterfly, DB – diagonal bridge butterfly. The gray, black and white atoms correspond to silicon, carbon and hydrogen, respectively. [142]

the butterfly geometry (LTP) which can explain the C=C, C-H and  $C_d-H_d$  force strength shifts. The C=C stretching mode undergoes a red shift with the ring angle reduction in cyclohexene, cyclopentene and cyclobutene where its frequency is 1646, 1611 and 1566  $cm^{-1}$ , respectively [27]. We observe an analogous red shift for the LTP compared with the MTP (HTP) C=C stretching modes. Potential candidates for the MTP and the HTP are the TB and DB benzene complexes derived as stable configurations by Silvestreli *et al* [142] based on a theoretical study from

first principles. The three 1,4-cyclohexadienelike configurations are shown in Fig. 5.14. The calculated binding energies in the  $(2\times 1)$  reconstruction are 2.06(B), 2.08(TB) and 1.70(DB) eV. In the  $c(4\times 2)$  reconstruction the binding energies are 2.20 (B), 1.99 (TB) and 2.24 (DB) eV [142]. Apparently the relative binding energies are sensitive to the surface strain in agreement with our experimental observations. An appreciable progress in the different phase assignment can be gained by a comparison with the calculated vibrational spectra of the two stable TB and DB butterfly bridge configurations (Fig. 5.14) as has been demonstrated for the LTP [152].



# Summary and conclusions

The vibrational properties of bare and adsorbate-covered vicinal and nominally flat Si(100) surfaces have been investigated using high resolution electron energy loss spectroscopy (HREELS). The examined adsorbate complexes Si(100)-(2×1)-H, monodeuteride Si(100)-(2×1)-D, Si(100)-(2×1)-C<sub>6</sub>H<sub>6</sub>, and Si(100)-(2×1)-C<sub>6</sub>D<sub>6</sub> represent two typical examples of vibrational coupling, namely when the adsorbate related vibrations have frequencies well above (monohydride) the substrate phonon continuum (0÷550 cm<sup>-1</sup>), or when part of these frequencies fall into this continuum (monodeuteride, benzene).

The technologically important Si(100) surface is the model of a semiconductor surface. The detailed structural and energetic characterization of this surface is fundamental for understanding and predicting its physical and chemical properties upon adsorption and in interfaces. The equilibrium structure of the Si(100) surface, namely its asymmetric dimerization, is well established. Its surface energetics remains not entirely characterized. Surface phonons as an access to the surface dynamics provide information of the bonding structure and the interatomic force constants in the topmost layers. The experimental possibility (HREELS, HAS) of full characterization of the vibrational states of the surface is a basis for the various theoretical models adjustment of the Si(100) surface. In this work for the first time the full surface phonon dispersion spectra on Si(100) single-crystals along the  $\overline{\Gamma J}$ ,  $\overline{\Gamma K}$ , and  $\overline{\Gamma M}$  directions of the (2×1) SBZ at 90 and 300 K are experimentally determined. All high-symmetry points in the (2×1) SBZ have been covered. Eight phonon bands are resolved on the bare surface. The comparison with the theoretical predictions reveals good agreement only with the calculations for a c(4×2) reconstruction of the flat surface [137]. On the vicinal surface the experimental results correspond to calculations of a c(4×2) as well as to a p(2×2) unit cell [137]. The most prominent phonons which have been resolved along the three directions are the acoustic modes (**RW** and **A**) in the  $\leq 110$  cm<sup>-1</sup> (13.6 meV) range and the dimer rocking mode (**r**) at  $\sim 180$  cm<sup>-1</sup> (22.3 meV). Except the **RW** and **A** modes, all other vibrations involve characteristic motions of the dimer atoms. The high-frequency edge of the surface localized phonon bands at  $\sim 500$  cm<sup>-1</sup> (62 meV) is characterized by a **ds**' mode involving dimer stretching vibrations.

For the first time the surface phonon dispersions on monohydride Si(100)-(2×1)-H surfaces have been determined along the  $\overline{\Gamma J}$ ,  $\overline{\Gamma K}$ , and  $\overline{\Gamma M}$  directions of the (2×1)SBZ at 90 and 300 K. When the silicon dangling bonds are saturated by hydrogen, the Si(100) surface reconstructs in parallel rows containing symmetric silicon dimers. The surface phonon dispersion spectrum contains seven bands which are summarized in Tab. 4.2. In general, when referring to bare surfaces, the **RW**, **r**, and **ds**'/s phonons are blue shifted while the other modes reproduce the location of their corresponding modes. The shift of the **r** mode is for the vicinal surface

$\sim 36 \text{ cm}^{-1}$  (4.5 meV) at  $\bar{\Gamma}$ ,  $\sim 44 \text{ cm}^{-1}$  (5.5 meV) at  $\bar{K}$  and  $< 7 \text{ cm}^{-1}$  (0.9 meV) at  $\bar{J}$ , for the nominally flat sample this shift is  $\sim 45 \text{ cm}^{-1}$  (5.6 meV) at  $\bar{\Gamma}$  and  $\sim 37 \text{ cm}^{-1}$  (4.6 meV) at  $\bar{M}$ . The agreement of this shift with the theoretical value  $\sim 40 \text{ cm}^{-1}$  (5.0 meV) at the  $\bar{M}$  point [14] is very good. The **RW** is shifted up at the zone boundaries with  $\sim 37 \text{ cm}^{-1}$  (4.6 meV) at  $\bar{M}$  and  $\bar{K}$ ; no shift is observed at  $\bar{J}$ . The **ds'** and **s** mode probably coincide in the **ds'/s** mode on the hydrogenated surfaces and a new band (**m**) is present in the dispersion spectrum. Based on the position of the monohydride bending mode at  $\sim 620 \text{ cm}^{-1}$  and the stretching mode at  $\sim 2100 \text{ cm}^{-1}$  vibrations which are well above the substrate phonon continuum and the expected small mass effect (H:Si mass ratio of 1:32) the observed changes of the phonon spectrum after hydrogenation are related mainly to structural rearrangement of the substrate topmost layers. The assumption of a negligible mass effect of the adsorbate was confirmed by the examination of the isotope effect after deuterium adsorption (D:Si mass ratio of 2:32) on the phonon spectrum. The phonon dispersion of the monodeuteride Si(100)-(2 $\times$ 1)-D surface along  $\bar{\Gamma K}$  and  $\bar{\Gamma M}$  reveal that the seven bands on the hydrogenated surface are exactly reproduced. The only difference is the appearance of a new band (**Db**) at  $\sim 405 \text{ cm}^{-1}$  (50.2 meV). The new mode is associated with a monodeuteride bending vibration which falls in the substrate phonon continuum in contrast to the stretching mode located far above this continuum at  $1527 \text{ cm}^{-1}$ . In conclusion, among all experimentally observed phonons on the bare Si(100) surface the **RW** at  $\leq 100 \text{ cm}^{-1}$ , **r** at  $\sim 180 \text{ cm}^{-1}$ , and **ds'** at  $\sim 395 \text{ cm}^{-1}$  bands are the most sensitive to the silicon dimer tilting and can be used as a fingerprint for the dimer symmetry.

When the adsorbate-derived vibrations are located above the surface phonon bands, less interaction is expected and they can be approached as decoupled from the substrate by examining of the adsorbate complex only. The benzene adsorption is a model for the aromatic hydrocarbons adsorption on Si(100) and it has been studied experimentally and theoretically in the last fifteen years. On the Si(100) surface we have detected and vibrationally characterized three chemisorbed phases with different relative populations on a vicinal surface compared to a nominally flat one. We have experimentally resolved 22  $\text{C}_6\text{H}_6$  derived modes for the low temperature (desorption) phase (LTP) and the comparison with the theoretical results in Ref. [152] leads to identification of all ten totally symmetric ( $A_1$ ) modes above  $200 \text{ cm}^{-1}$ . The mode identification has been confirmed by the results for the isotope  $\text{C}_6\text{D}_6$  which reveal 22  $\text{C}_6\text{D}_6$  derived modes. The LTP is assigned to a 1,4-cyclohexadiene-like benzene molecule di- $\sigma$  bonded to a single silicon dimer on the flat as well as on the vicinal Si(100) surface.

The middle (MTP) and high (HTP) temperature phases of  $\text{C}_6\text{H}_6(\text{C}_6\text{D}_6)$  have been identified and vibrationally characterized for the first time. A total of 15(21) and 14(13)  $\text{C}_6\text{H}_6(\text{C}_6\text{D}_6)$  derived modes for the MTP and HTP, respectively, have been resolved on vicinal and nominally flat Si(100) surfaces. The MTP and HTP show essentially the same vibrational characteristics, independent of the relative population, in contrast to their different desorption energies. Relative to the LTP of  $\text{C}_6\text{H}_6(\text{C}_6\text{D}_6)$ , in both phases the symmetric and the asymmetric C=C stretching modes are blue shifted by  $\sim 18(21) \text{ cm}^{-1}$  and  $\sim 25(30) \text{ cm}^{-1}$ , respectively. For  $\text{C}_6\text{H}_6$  the carbon-hydrogen stretching frequency region contains again two well-defined bands, corresponding to the equivalent two and four hydrogen atoms bonded to two  $sp^3$  and four  $sp^2$  hybridized carbon atoms in the benzene ring. Both bands are red-shifted by  $46 \text{ cm}^{-1}$  for the

$C_d-H_d$  and by  $15\text{ cm}^{-1}$  for the C-H stretching modes closer to the corresponding gaseous 1,4-cyclohexadiene values [155]. In the case of deuterated benzene the three bands in the LTP are also preserved and red shifted by  $28\text{ cm}^{-1}$  for the  $C_d-D_d$  and by 10 and  $5\text{ cm}^{-1}$  for the other two C-H stretching vibrations. Most of the prominent losses of the LTP below  $1500\text{ cm}^{-1}$  have their shifted analogous modes in the HREEL spectra of the MTP and the HTP. These observations are interpreted as similar 1,4-cyclohexadiene-like structure of the adsorbate complex in all three phases on the Si(100) surface independently of the surface vicinality. The differences are attributed to variations of the butterfly-like molecule's azimuthal orientation, relative to the silicon dimer bond direction, and to changes of the bond strengths in the adsorption complexes. The HREELS investigations of low benzene coverages ( $\theta=0.2\div 0.3$ ) as a function of the annealing temperature reveal the presence of a chemisorbed phase upon adsorption at 100 K. This phase has the vibrational characteristics of the MTP(HTP) and coexists with a physisorbed phase which has altered mode frequencies relative to the multilayers. The physisorbed phase is converted to LTP after annealing to 200 K. Annealing to temperatures above 350 K leads to conversion from the LTP to the MTP(HTP). These results are interpreted as site-specific chemisorption and phase conversion via adsorbate diffusion. Benzene saturation at 100 K or adsorption on a partially hydrogen passivated surface suppress the MTP(HTP) formation at 100 K and favour the LTP chemisorption. Additionally, the presence of dihydride units on the surface leads to HTP formation. It is proposed that the MTP and HTP correspond to a 1,4-cyclohexadiene-like benzene molecule di- $\sigma$  bonded to two silicon dimers adjacent in a row. These butterfly bridge geometries are either defect-assisted (HTP) or require large surface areas free of defects and adsorbates (MTP).



# Appendix A

In order to extract the correct frequencies from the HREEL spectra without application of numeric resolution enhancement methods [159, 160], a simple fitting procedure is applied. In principle it is based on fitting the spectrum structures by a profile of the corresponding elastic peak [116]. The losses(gains) are expected to repeat the elastic peak shape with additional broadening due to their own lifetimes, which is based on an approximation that the transfer function is invariant across the spectrum [160]. Additionally, a discrete gain and loss pair is symmetrically located relative to the zero with gain intensity reduced by the Boltzmann factor  $\exp(-\hbar\omega/k_B T)$ , where  $\hbar\omega$  is the loss energy,  $k_B$  is the Boltzmann constant, and  $T$  is the sample temperature. Based on its ability to fit the elastic peak, we apply the function

$$y = \frac{a (1 + n^2)^{-d} \exp \left\{ -e \left[ \arctan(n) + \arctan \left( \frac{e}{2d} \right) \right] \right\}}{\left( 1 + \frac{e^2}{4d^2} \right)^{-e}}, \quad (5.3.1)$$

where

$$n = \frac{x - \frac{ce}{2d} - b}{c}, \quad (5.3.2)$$

and  $\mathbf{a}$  is the amplitude,  $\mathbf{b}$  is the center,  $\mathbf{c}$  is FWHM and  $\mathbf{e}$  gives the asymmetry of the function. Broadening of the elastic peak with the off-specular angle between 0 and 12% at 100 K and between 0 and 25% at 300 K is observed. Elastic peak intensities as a function of the measured angle were presented in Fig. 4.2. The obtained parameters are used for fitting of the feature in the corresponding spectra.  $\mathbf{d}$  and  $\mathbf{e}$  are fixed,  $\mathbf{a}$  and  $\mathbf{b}$  are varied,  $\mathbf{c}$  is multiplied by a factor between 1 and 2. The multiphonon background is determined using Eq. 5.3.1 applied only to featureless regions in the spectrum,  $\pm 550 \text{ cm}^{-1}$  around the elastic peak. For the rest of the spectra, above  $550 \text{ cm}^{-1}$ , a linear background is used. In the background fitting all parameters are varied, with  $\mathbf{c} > 10 \mathbf{c}_{elastic}$ ,  $\mathbf{b} > 0$  and  $\mathbf{e} < 0$ . Multiphonon backgrounds determined in this way are shown in Fig. 5.15 for two different sample temperatures. The goal is to obtain a monotonic background related to the peaks which does not affect the peak positions and serves mainly for simultaneous deconvolution of the gain and loss parts of the spectra. In this way the error in the background determination concerns mainly the amplitude of the obtained vibrations and less their frequency positions. This is the reason why in this work an analysis of the vibrational mode amplitudes are not presented. When the background is low and the structure is a single peak the former is not involved in the fitting. (Fig. 5.16).

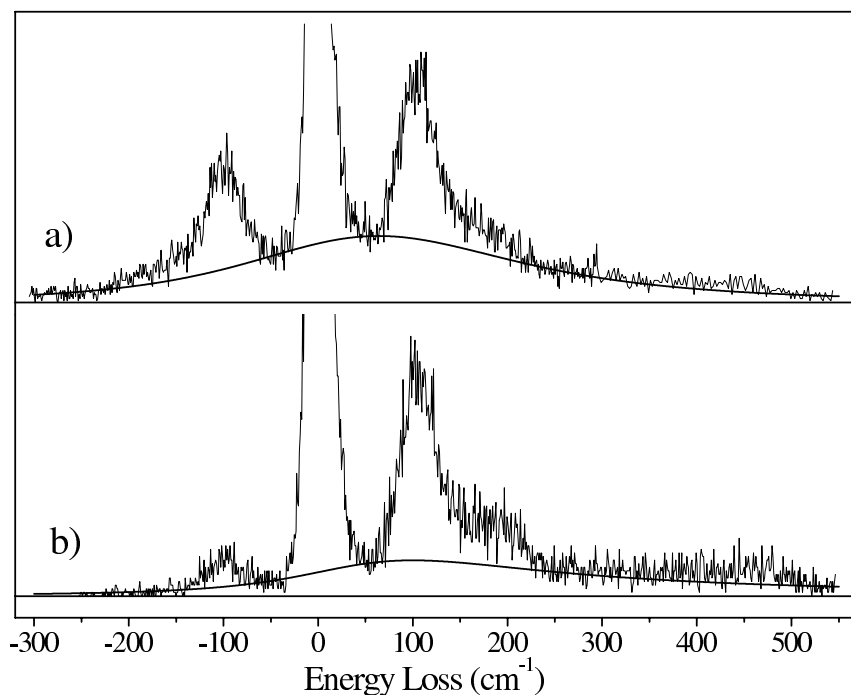


Figure 5.15: HREELS multiphonon background at different sample temperatures. Measurements are with off-specular geometry at 300 K (a) and at 88 K (b). For comparison lines at  $y = 0$  are also plotted.

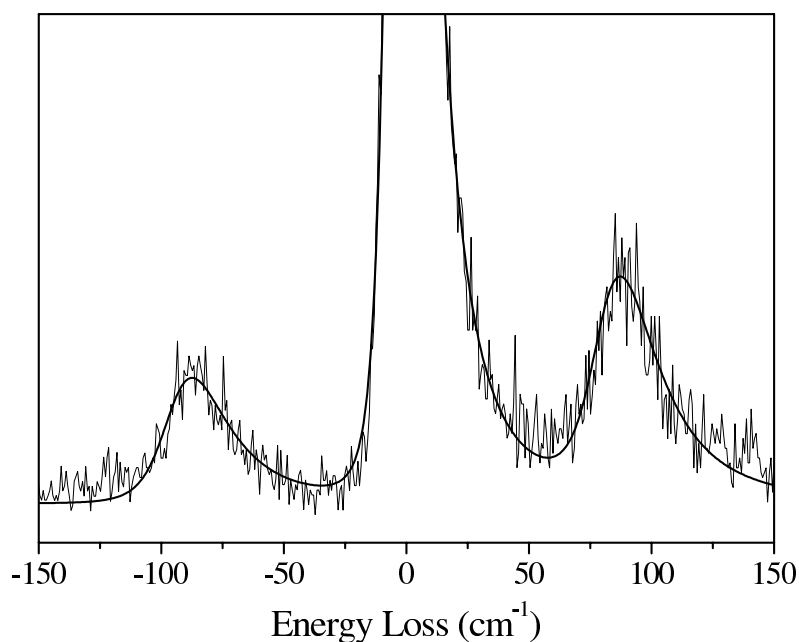


Figure 5.16: Fit of a single peak in a HREEL spectrum with negligible background.

In the critical case with phonons appearing in the tail of the elastic peak, the extraction of the correct frequency by application of a fitting procedure is essential. An example of such a fit is presented in Fig. 5.17. The peaks plotted with a solid line are the only ones taken into account in the analysis performed after the fitting. The peaks plotted by dotted lines are used only for balance in the fitting process. This notation is used in the next figures of this appendix. Another situation is presented in Fig. 5.18, namely a triple structure with a valley in the center. The fit resulting peak at the center (dotted line in Fig. 5.18) is not taken into consideration in the phonon dispersion data.

An example of structure containing losses with significantly different widths is shown in Fig. 5.19, together with the fitting result. The central sharp peak results from adsorbate induced vibrations while the remaining structures are surface resonances (Chapter 1). On the

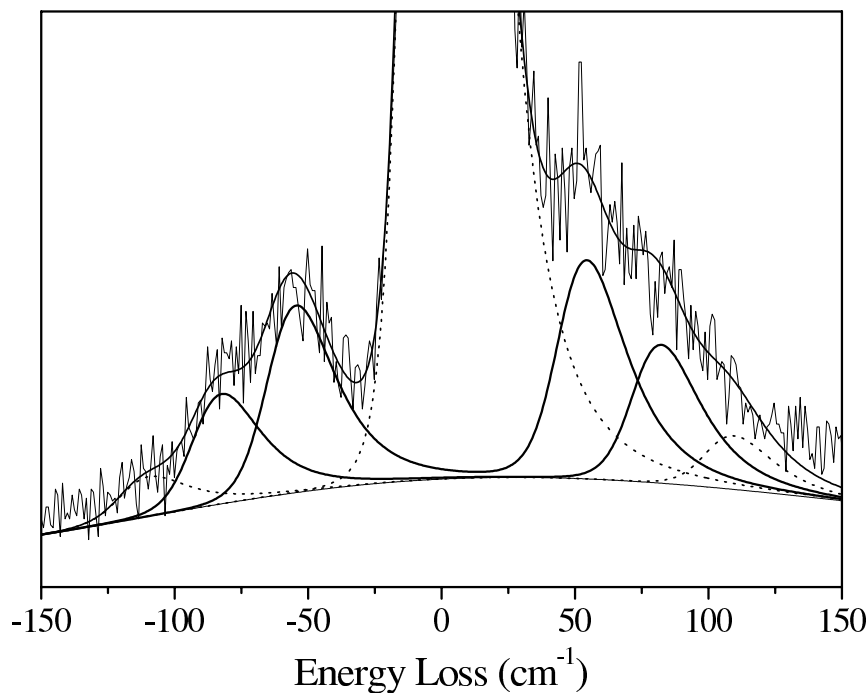


Figure 5.17: Deconvolution of modes positioned near the elastic peak. The solid curves denote vibrations which are accepted as significant, the dotted line peaks are used only for the fitting balance.

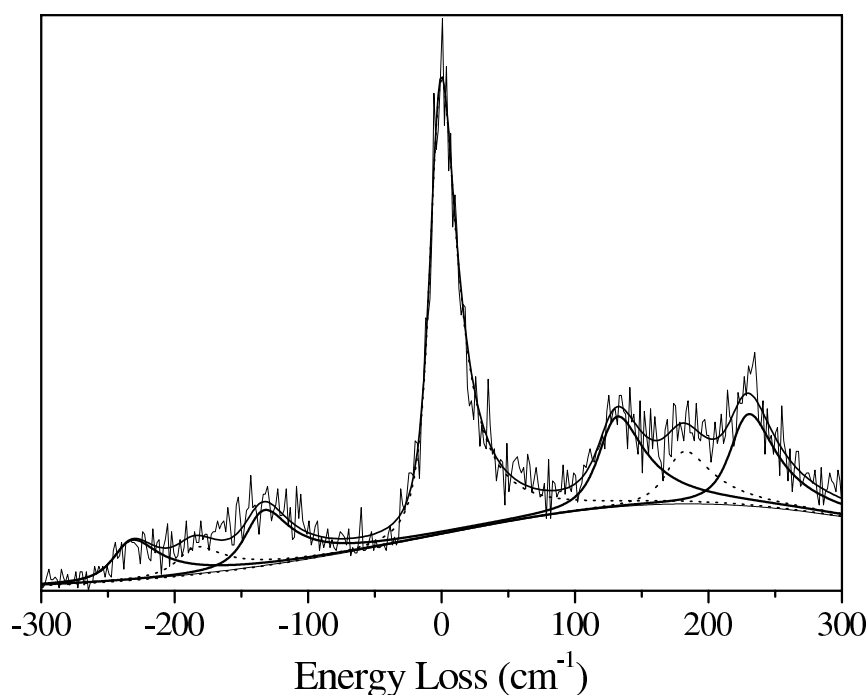


Figure 5.18: Deconvolution of a triple structure. The elastic peak is located at  $0 \text{ cm}^{-1}$ .

left-hand-side of Fig. 5.19 a fit together with the experimental points of the corresponding elastic peak is plotted.

In the typical adsorbate associated frequency region, above the substrate (silicon) phonon continuum  $550 \text{ cm}^{-1}$ , multimode spectral structures are represented in Fig. 5.20. The frequency region where the adsorbate related bending modes are located is presented for H/Si(100)-(2×1) and H/Si(100)-(3×1) surfaces. As in the latter system a dihydride is present together with a monohydride from the former system and the lateral adsorbate interactions are weak, a superposition of the two species vibrational characteristics in the HREEL spectra is expected. The deconvolution products in Fig. 5.20 (a) reveals the preserved monohydride modes from Fig. 5.20 (b) together with new losses coming from the dihydride species.

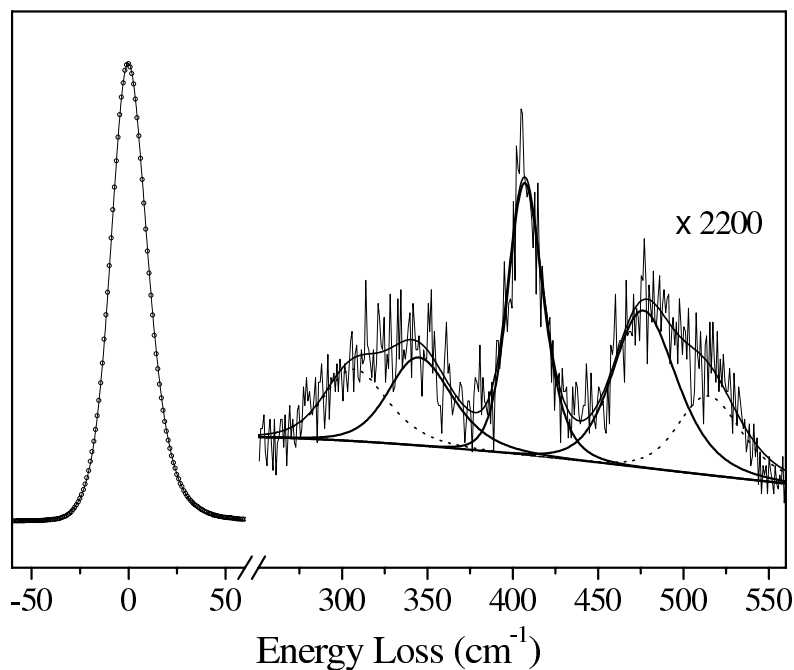


Figure 5.19: Deconvolution of a structure (right-hand-side), containing losses with different widths. The central peak appears with FWHM, smaller by a factor of 1.7 related to the other peaks in the structure. On the left-hand-side of the plot the corresponding elastic peak (open circles) and the parametrization fit (solid line) is shown.

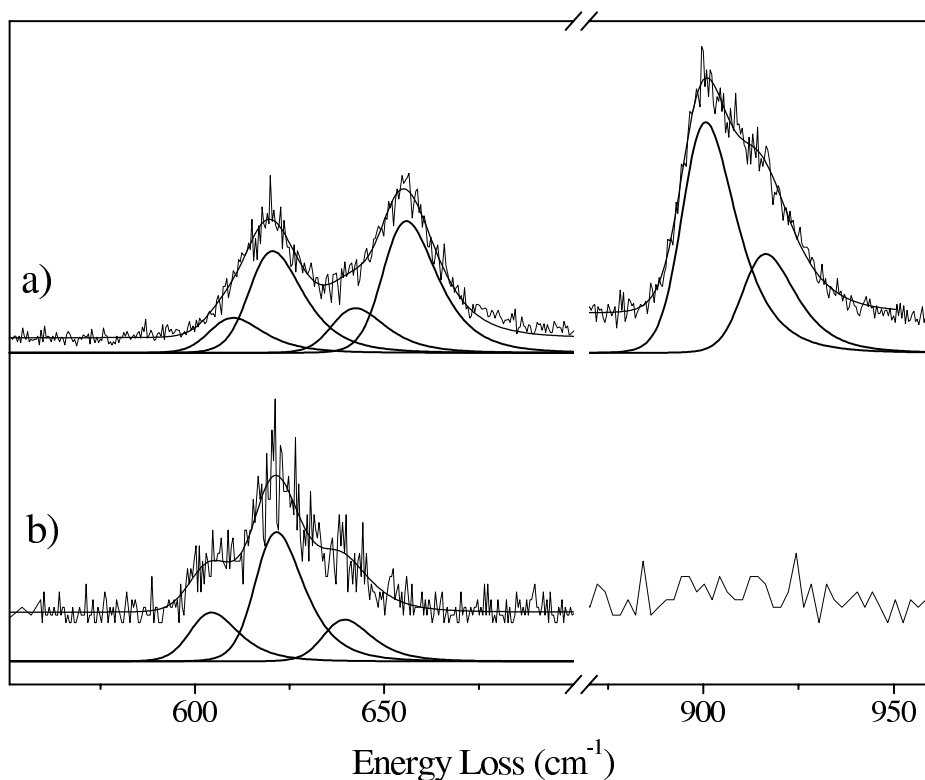


Figure 5.20: Fits of hydrogen induced losses in HREEL spectra. (b) are bending modes on a H/Si(100)-(2 $\times$ 1) surface, (a) are bending and scissor modes on a H/Si(100)-(3 $\times$ 1) surface.

In conclusion, the good correspondence of our data extracted by the above-described simple method with the experimental and theoretical results available in the literature (discussed in Chapters 3, 4 and 5) supports the reliability of such a fitting procedure.

# List of Figures

2.1	UHV setting . . . . .	22
2.2	Sample mounting . . . . .	22
2.3	Evaporators . . . . .	23
2.4	The crystal holder . . . . .	24
2.5	The temperature control scheme . . . . .	24
2.6	The gas dosing system . . . . .	25
2.7	The HREEL spectrometer. . . . .	26
3.1	The asymmetric dimer . . . . .	30
3.2	The surface structures. . . . .	31
3.3	The single-domain Si(100). . . . .	32
3.4	HREELS of a Si(100)-(2×1) surface after adsorption of acetylene and annealing to 1200 K. . . . .	34
3.5	HREELS of a Si(100)-(2×1) surface after one month under UHV at RT. . . . .	36
3.6	LEED patterns of bare Si(100) at 300 and 90 K. . . . .	37
3.7	HREELS of a bare Si(100)-(2×1) surface. . . . .	38
3.8	Measured directions. . . . .	38
3.9	Hydrogen(deuterium) TPD spectra . . . . .	39
3.10	Structures of a hydrogen-saturated Si(100) surface . . . . .	40
3.11	HREEL spectrum of a monohydride saturated Si(100)-(2×1) surface . . . . .	41
3.12	HREEL spectra of monohydride saturated vicinal and nominally flat Si(100)-(2×1) surfaces . . . . .	41
3.13	Off-specular HREELS measurements of a monohydride-saturated vicinal Si(100)-(2×1) surface with 250 eV electron primary energy . . . . .	42
3.14	Off-specular HREELS measurements of a monohydride-saturated vicinal Si(100)-(2×1) surface with 200 eV electron primary energy . . . . .	43
3.15	Off-specular HREELS measurements of a monohydride-saturated nominally flat Si(100)-(2×1) surface with 15 eV electron primary energy . . . . .	43
3.16	LEED patterns of a Si(100)-(3×1)-H surface. . . . .	44
3.17	HREELS spectra of a Si(100)-(3×1)-H, compared with spectra of a Si(100)-(2×1)-H . . . . .	44
3.18	HREEL spectrum of the monodeuteride Si(100)-(2×1)-D surface . . . . .	45
3.19	HREEL spectra of monodeuteride saturated vicinal and nominally flat Si(100)-(2×1) surfaces . . . . .	45

3.20	HREEL spectra of the monohydride Si(100)-(2×1)-H surfaces compared with corresponding elastic peak profiles. . . . .	47
3.21	Dispersions of monohydride related vibrations on Si(100)-(2×1) surfaces. . . . .	48
3.22	HREEL spectra of H/Si(100)-(3×1) surfaces compared with corresponding elastic peak profiles. . . . .	49
4.1	Displacement patterns of the characteristic vibrations on a Si(100)-(2×1) surface.	52
4.2	Elastic peak intensities on bare Si(100) surfaces . . . . .	54
4.3	HREEL spectra on bare Si(100) surfaces for various electron primary energies. . . . .	56
4.4	Off-specular HREEL spectra on bare Si(100) surfaces . . . . .	57
4.5	Phonon dispersions on Si(100) surfaces. . . . .	58
4.6	Comparison with experimental dispersions from literature . . . . .	59
4.7	Phonon dispersion over the PBP . . . . .	60
4.8	Comparison with calculated phonon dispersion for a (2×1) reconstructed Si(100) surface . . . . .	61
4.9	HREELS measurements on a bare Si(100) surface. . . . .	62
4.10	Comparison of experimental and theoretical phonon dispersions on a Si(100) surface. . . . .	63
4.11	HREEL spectra on Si(100)-(2×1)-H surfaces for various electron primary energies.	66
4.12	Off-specular HREEL spectra on Si(100)-(2×1)-H(D) surfaces . . . . .	67
4.13	Phonon dispersions on Si(100)-(2×1)-H(D) surfaces. . . . .	68
4.14	Phonon dispersions on Si(100)-(2×1)-H(D) over the BPP . . . . .	69
4.15	Comparison of the phonon dispersions on bare and monohydride-covered Si(100) surfaces. . . . .	71
4.16	Comparison of the phonon dispersions on monohydride and monodeuteride-covered Si(100) surfaces. . . . .	72
5.1	The stable structures of benzene on a Si(100) surface. . . . .	78
5.2	TPD spectra of benzene adsorbed at 100 K on a vicinal Si(100) surface. . . . .	79
5.3	HREEL spectra of C <sub>6</sub> H <sub>6</sub> adsorbed on a vicinal Si(100) surface. . . . .	81
5.4	HREEL spectra of C <sub>6</sub> D <sub>6</sub> adsorbed on a vicinal Si(100) surface. . . . .	82
5.5	Off-specular HREEL spectra of C <sub>6</sub> H <sub>6</sub> adsorbed on a vicinal Si(100) surface. . . . .	84
5.6	HREEL spectra of C <sub>6</sub> H <sub>6</sub> adsorbed on a vicinal Si(100) surface as a function of annealing temperature. . . . .	85
5.7	HREEL spectra of C <sub>6</sub> D <sub>6</sub> adsorbed on a vicinal Si(100) surface as a function of annealing temperature. . . . .	87
5.8	TPD spectra of benzene adsorbed at 90 K on a nominally flat Si(100) surface. . . . .	89
5.9	HREEL spectra of C <sub>6</sub> H <sub>6</sub> adsorbed on a nominally flat Si(100) surface. . . . .	90
5.10	HREEL spectra of C <sub>6</sub> D <sub>6</sub> adsorbed on a nominally flat Si(100) surface. . . . .	91
5.11	HREEL spectra of C <sub>6</sub> H <sub>6</sub> adsorbed on a nominally flat Si(100) surface as a function of the annealing temperature. . . . .	93
5.12	Theoretical vibrational modes of the butterfly complex together with the loss frequencies of the three phases of benzene adsorbed on Si(100) surfaces. . . . .	98

---

5.13	TPD spectra of $C_6H_6$ adsorbed on a nominally flat Si(100) surface. . . . .	100
5.14	The stable 1,4-cyclohexadienelike configurations of benzene on a Si(100) surface	100
5.15	Multiphonon background at different temperatures . . . . .	108
5.16	Single mode fit . . . . .	108
5.17	Deconvolution of modes positioned near the elastic peak. . . . .	109
5.18	Deconvolution of a triple structure. . . . .	109
5.19	Deconvolution of a multiple structure. . . . .	110
5.20	Fits of adsorbate induced vibrations. . . . .	110



# List of Tables

1.1	Comparison of the vibrational spectroscopies. . . . .	18
3.1	Vibrational modes of water decomposition products on Si(100). . . . .	35
3.2	Vibrational modes of atomic hydrogen(deuterium) adsorption products on Si(100). . . . .	50
4.1	Experimental surface phonon frequencies on a Si(100) surface. . . . .	73
4.2	Experimental surface phonon frequencies on a Si(100)-(2×1)-H surface. . . . .	74
4.3	Experimental surface phonon frequencies on a Si(100)-(2×1)-D surface. . . . .	74
5.1	Vibrational mode assignment of benzene chemisorbed on a Si(100) surface. . . . .	95
5.2	Vibrational modes of C <sub>6</sub> H <sub>6</sub> chemisorbed on a Si(100) surface. . . . .	96
5.3	Vibrational modes of C <sub>6</sub> D <sub>6</sub> chemisorbed on a Si(100) surface. . . . .	97



# Bibliography

- [1] H.C. Gatos. Semiconductor electronics and the birth of the modern science of surfaces. *Surf. Sci.*, 299-300:1–23, 1994.
- [2] H.R. Huff. An electronics division retrospective (1952-2002) and future opportunities in the twenty-first century. *J. Electrochem. Soc.*, 149(5):S35–S58, 2002.
- [3] W. Mönch. *Semiconductor Surfaces and Interfaces*. Springer-Verlag, 1995.
- [4] *The International Technology Roadmap for Semiconductors (ITRS)*. Semiconductor Industry Association, San Jose, CA, 2001.
- [5] W. Kress and F.W. de Wette. *Surface phonons*. Springer-Verlag, 1991.
- [6] J. Fritsch and U. Schröder. Density functional calculation of the semiconductor surface phonons. *Physics Reports*, 309:209–331, 1999.
- [7] J.R. Dutcher, S. Lee, B. Hillebrands, G.J. McLaughlin, B.G. Nickel, and G.I. Stegeman. Surface-Grating-induced zone folding and hybridization of surface acoustic modes. *Phys. Rev. Lett.*, 68(16):2464–2467, 1992.
- [8] N. Takagi, S. Shimonaka, T. Aruga, and M. Nishijima. Surface phonons of the Si(001)(2x1) surface. *Phys. Rev. B*, 60(15):10919–10925, 1999.
- [9] H.E. Ruda. Reactions on semiconductor surfaces. *Science*, 283:646, 2002.
- [10] J.T. Yates, Jr. Surface chemistry: A new opportunity in silicon-based microelectronics. *Science*, 279(5349):335–336 and references therein, 1998.
- [11] A.A. Maradudin. Surface phonon – Theory. In R. Vanselow und R. Howe, editor, *Chemistry and Physics of Solid Surfaces V*, pages 151–182. Springer, 1988.
- [12] M.C. Desjonqueres and D. Spanjaard. *Concepts in surface physics*. Springer, 1993.
- [13] R.F. Wallis and S.Y. Tong. Physics of solid surfaces: Vibrational and excitational properties of surfaces. In G. Chiarotti, editor, *Solid State Physics*, volume 24, pages 433–473. Springer, 1994.
- [14] J. Fritsch, M. Arnold, C. Eckl, R. Honke, P. Pavone, and U. Schröder. Density-functional calculation of the phonons in the adsorbate-covered semiconductor surfaces. *Surf. Sci.*, 427-428:58–63, 1999.

- [15] H. Ibach and D.L. Mills. *Electron energy loss spectroscopy and surface vibrations*. Academic Press, New York, USA, 1982.
- [16] G.P. Alldredge, R.E. Allen, and F.W. de Wette. Studies of vibrational surface modes. III. Effect of an adsorbed layer. *Phys. Rev. B*, 4(6):1682–1697, 1971.
- [17] C.H. Li, S.Y. Tong, and D.L. Mills. Large-angle inelastic electron scattering from adsorbate vibrations: Basic theory. *Phys. Rev. B*, 21(8):3057–3073, 1980.
- [18] V.M. Rozenbaum and S.H. Lin. Local vibrations in systems of interacting adsorbed molecules. *J. Chem. Phys.*, 110(12):5919–5932, 1999.
- [19] M. Rocca. A2. Measuring techniques and surface properties changed by adsorption: Surface phonon dispersion. In *Physics of Covered Solid Surfaces: A. Adsorbed Layers on Surfaces*, volume III/42. Landolt-Börnstein, 2000.
- [20] L.J. Clarke. *Surface crystallography*. John Wiley & Sons, Chichester, UK, 1985.
- [21] G. Ertl and J. Küppers. *Low energy electrons and surface chemistry*. VCH, Germany, 1985.
- [22] H. Lüth. *Surfaces and Interfaces of Solid Materials*. Springer-Verlag, 1995.
- [23] G.J. Schulz. Resonances in electron impact on diatomic molecules. *Rev. Mod. Phys.*, 45(3):423–486, 1973.
- [24] J.E. Demuth, D. Schmeisser, and P. Avouris. Resonance scattering of electrons from N<sub>2</sub>, CO, O<sub>2</sub> and H<sub>2</sub> adsorbed on a silver surface. *Phys. Rev. Lett.*, 47(16):1166–1169, 1981.
- [25] L. Sanche and M. Michaud. Resonance-enhanced vibrational excitation in electron scattering from O<sub>2</sub> multilayer films. *Phys. Rev. Lett.*, 47(14):1008–1011, 1981.
- [26] R. Franchy, F. Bartolucci, F. Buatier de Mongeot, F. Cemic, M. Rocca, U. Valbusa, L. Vattuone, S. Lacombe, K. Jacobi, K.B.K. Tang, R.E. Palmer, J. Villette, D. Teillet-Billy, and J.P. Gauyacq. Negative ion resonances of O<sub>2</sub> adsorbed & on Ag surfaces. *J. Phys.: Condens. Matter*, 12:R53–R82, 2000.
- [27] N.B. Colthup, L.H. Daly, and S.E. Wiberley. *Introduction to infrared and Raman spectroscopy*. Academic press INC., London, UK, 1990.
- [28] H.J. Kreuzer and Z.W. Gortel. *Physisorption kinetics*. Springer-Verlag, 1986.
- [29] D. Menzel. Desorption phenomena. In R. Gomer, editor, *Interactions on Metal Surfaces*, pages 101–142. Springer Verlag, 1975.
- [30] D. Menzel. Thermal desorption. In R. Vanselow und R. Howe, editor, *Chemistry and Physics of Solid Surfaces IV*, pages 389–406. Springer, 1982.
- [31] M. Vollmer and F. Träger. Analysis of Fractional Order Thermal Desorption. *Surf. Sci.*, 187:445–462, 1987.

- [32] J.B. Miller, H.R. Siddiqui, S.M. Gates, J.N. Russell, Jr., J.T. Yates, Jr., J.C. Tully, and M.J. Cardillo. Extraction of kinetic parameters in temperature programmable desorption: A comparison of methods. *JCP*, 87(11):6725–6732, 1987.
- [33] P.A. Redhead. Thermal desorption of gases. *Vacuum*, 12:203–211, 1962.
- [34] E. Habenschaden and J. Küppers. Evaluation of flash desorption spectra. *Surf. Sci.*, 138:L147–L150, 1984.
- [35] H. Schlichting and D. Menzel. Techniques for attainment, control, and calibration of cryogenic temperatures at small single-crystal samples under ultrahigh vacuum. *Rev. Sci. Instrum.*, 64(7):2013–2022, 1993.
- [36] A. Fink. *Organische Moleküle auf Halbleitern: Adsorption und elektronische Struktur ungesättigter Kohlenwasserstoffe auf Si(100), Ge/Si(100) und Ge(100) Oberflächen*. PhD thesis, Technische Universität München, Institut E20, 2001.
- [37] S. Gokhale, A. Fink, P. Trischberger, K. Eberle, W. Widdra, and D. Menzel. Silicon bonding for ultrahigh vacuum surface science studies. *J. Vac. Sci. Technol. A*, 19(2):706–708, 2001.
- [38] H. Schlichting. *Methoden und Mechanismen der thermischen Desorption: Adsorptions-, Desorptions-Kinetik, Epitaxie und Ordnung von Edeltgaschichten auf Ru(001)*. PhD thesis, Technische Universität München, Institut E20, 1990.
- [39] H. Ibach. *Electron energy loss spectrometers*. Springer-Verlag, Germany, 1991.
- [40] Th. Moritz. . PhD thesis, Technische Universität München, Institut E20, 2002.
- [41] P. Feulner and D. Menzel. Simple ways to improve "flash desorption" measurements from single crystal surfaces. *J. Vac. Sci. Technol.*, 17(2):662–663, 1980.
- [42] Charles Kittel. *Introduction to Solid State Physics*. JW&S, New York, USA, seventh edition, 1996.
- [43] R.F. Schlier and H.E. Farnsworth. Structure and adsorption characteristics of clean surfaces of germanium and silicon. *J. Chem. Phys.*, 30(4):917–926, 1959.
- [44] M.J. Cardillo and G.E. Becker. Diffraction of he atoms at a Si(100) surface. *Phys. Rev. Lett.*, 40(17):1148–1151, 1978.
- [45] R.J. Hamers, R.M. Tromp, and J.E. Demuth. Scanning tunneling microscopy of Si(100). *Phys. Rev. B*, 34(8):5343–5357, 1986.
- [46] D. J. Chadi. Atomic and Electronic Structures of Reconstructed Si(100) Surfaces. *Phys. Rev. Lett.*, 43(1):43–47, 1979.
- [47] D. J. Chadi. Si(100) surfaces: Atomic and electronic structures. *J. Vac. Sci. Technol.*, 16(5):1290–1296, 1979.

- [48] F. J. Himpsel and D.E. Eastman. Photoemission studies of intrinsic surface states on Si(100). *J. Vac. Sci. Technol.*, 16(5):1297–1299, 1979.
- [49] J. Pollmann, P. Krüger, A. Mazur, and G. Wolfgarten. Atomic, Electronic and Vibrational structure of semiconductor surfaces. *Appl. Phys. A*, 41:21–38, 1986.
- [50] S.B. Healy, C. Filippi, P. Kratzer, E. Penev, and M. Scheffler. Role of electronic correlation in the Si(100) reconstruction: A quantum Monte Carlo study. *Phys. Rev. Lett.*, 87(1):013105–1/4, 2001.
- [51] H. Over, J. Wasserfall, W. Ranke, C. Ambiatello, R. Sawitzki, D. Wolf, and W. Moritz. Surface atomic geometry of Si(001)-(2x1): A low-energy electron-diffraction structure analysis. *Phys. Rev. B*, 55(7):4731–4736, 1997.
- [52] J. Fritsch and P. Pavone. Ab initio calculation of the structure, electronic states, and the phonon dispersion of the Si(100) surface. *Surf. Sci.*, 344:159–173, 1995.
- [53] T. Tabata, T. Aruga, and Y. Murata. Order-Disorder Transition on Si(001):c(4x2) to (2x1). *Surf. Sci.*, 179:L63–L70, 1987.
- [54] R.A. Wolkow. Direct observation of an increase in buckled dimers on Si(001) at low temperature. *Phys. Rev. Lett.*, 68(17):2636–2639, 1992.
- [55] J. Gryko and R.E. Allen. Energy surface and dynamics of Si(100). *J. Vac. Sci. Technol. A*, 10(4):2052–2054, 1992.
- [56] A.I. Shkrebtii, R. Di Felice, C.M. Betroni, and R. Del Sole. Ab initio study of structure and dynamics of the Si(100) surface. *Phys. Rev. B*, 51(16):11201–11204, 1995.
- [57] K. Hata, Y. Sainoo, and H. Shigekawa. Atomically resolved local variation of the barrier height of the flip-flop motion of the single buckled dimers of Si(100). *Phys. Rev. Lett.*, 86(14):3084–3087, 2001.
- [58] R.J. Hamers and U.K. Köhler. Determination of the local electronic structure of atomic-sized defects on Si(001) by tunneling spectroscopy. *J. Vac. Sci. Technol. A*, 7(4):2854–2859, 1989.
- [59] D. Badt, H. Wengelnik, and H. Neddermeyer. Scanning tunneling microscopy at low temperatures on the c(4x2)/(2x1) phase transition of Si(100). *J. Vac. Sci. Technol. B*, 12(3):2015–2017, 1994.
- [60] A.R. Smith, F.K. Men, K.-J. Chao, Z. Zhang, and C.K. Shih. Scanning tunneling microscopy investigation of the dimer vacancy-dimer vacancy interaction on the Si(001)2x1 surface. *J. Vac. Sci. Technol. B*, 14(2):909–913, 1996.
- [61] T. Yokoyama and K. Takayanagi. Suppressive influence of steps on a phase transition of the Si(001) surface. *Phys. Rev. B*, 57(8):R4226–R4229, 1998.

- [62] D.J. Chadi. Stability of single-layer and bilayer steps on Si(001) surface. *Phys. Rev. Lett.*, 59(15):1691–1694, 1987.
- [63] M. Henzler and J. Clabes. Structural and electronic properties of stepped semiconductor surfaces. *Japan. J. Appl. Phys. Suppl.2, Pt.2*, pages 389–396, 1974.
- [64] P.E. Wierenga, J.A. Kubba, and J.E. Griffith. Tunneling images of biatomic steps on Si(001). *Phys. Rev. Lett.*, 59(19):2169–2172, 1987.
- [65] O.L. Alerhand and A.N. Berker, J.D. Joannopoulos, D. Vanderbilt, R.J. Hamers, and J.E. Demuth. Finite-temperature phase diagram of vicinal Si(100) surfaces. *Phys. Rev. Lett.*, 64(20):2406–2409, 1990.
- [66] B. S. Swartzentruber, N. Kitamura, M.G. Lagally, and M.B. Webb. Behavior of steps on Si(001) as a function of vicinality. *Phys. Rev. B*, 47(20):13432–13441, 1993.
- [67] S. van Dijken, H. J. W. Zandvliet, and B. Poelsema. Energetics and structure of the stable and unstable biatomic step edges of Si(001). *Surf. Rev. Lett.*, 5(1):15–20, 1998.
- [68] H.J.W. Zandvliet. Energetics of Si(001). *Reviews of Modern Physics*, 72(2):593–602, 2000.
- [69] B. S. Swartzentruber, Y.-W. Mo, M.B. Webb, and M.G. Lagally. Scanning tunneling microscopy studies of structural disorder and steps on Si surfaces. *J. Vac. Sci. Technol. A*, 7(4):2901–2905, 1989.
- [70] K. Hata, T. Kimura, S. Ozawa, and H. Shigekawa. How to fabricate a defect free Si(001) surface. *J. Vac. Sci. Technol. A*, 18(4):1933–1936, 2000.
- [71] A.R. Smith, F.K. Men, A.R. Smith, K.-J. Chao, Z. Zhang, and C.K. Shih. Dimer-vacancy-dimer-vacancy interaction on the Si(001) surface: The nature of the  $2\times n$  structure. *Phys. Rev. B*, 52(12):R8650–R8653, 1995.
- [72] K. Kato, T. Ide, S. Miura, A. Tamura, and T. Ichinokawa. Si(100) $2\times n$  structures induced by Ni contamination. *Surf. Sci.*, 194:L87–L94, 1988.
- [73] V.A. Ukraintsev and J.T. Yates, Jr. The role of nickel in si(001) roughening. *Surf. Sci.*, 346:31–39, 1996.
- [74] H.J. Osten, M. Methfessel, G. Lippert, and H. Rucker. Observation of the formation of a carbon-rich surface layer in silicon. *Phys. Rev. B*, 52(16):12179–12183, 1995.
- [75] F. Boszo, J. T. Yates, Jr. , W. J. Choyke, and L. Muehlhoff. Studies of sic formation on si(100) by chemical vapor deposition. *J. Appl. Phys.*, 57(8):2771–2778, 1985.
- [76] K. Miki, K. Sakamoto, and T. Sakamoto. Is the  $c(4\times 4)$  reconstruction of the Si(001) associated with the presence of carbon? *Appl. Phys. Lett.*, 71(22):3266–3268, 1997.

- [77] R. Kosugi, S. Sumitami, T. Abukawa, Y. Takakuwa, S. Suzuki, and S. Sato. X-ray photoelectron diffraction study of the Si(001)c(4x4)-C surface. *Surf. Sci.*, 411:55, 1998.
- [78] M. Stoffel, L. Simon, D. Aubel, J.L. Bischoff, and L. Kubler. Carbon-associated Si(001)-(4x4) reconstruction dosed with hydrogen. *Surf. Sci.*, 454-456:201–206, 2000.
- [79] R. Butz and H. Lüth. The surface morphology of Si(100) after carbon deposition. *Surf. Sci.*, 411:61–69, 1998.
- [80] O. Leifeld, D. Grützmacher, B. Müller, K.Kern, E. Kaxiras, and P.C. Kelires. Dimer pairing on the C-alloyed Si(001) surface. *Phys. Rev. Lett.*, 82(5):972–975, 1999.
- [81] S.T. Jemander, H.M. Zhang R.I.G. Uhrberg, and G.V. Hansson. Surface structure of Si(100) with submonolayer coverage of C. *Mater. Sci. Eng. B*, 89:415–419, 2002.
- [82] T. Balster, V.M. Polyakov, H. Ibach, and J.A. Schaefer. A study of surface band bendings and charge density of SiC(001)2x1 and c(2x2) by high-resolution electron-energy-loss spectroscopy. *Surf. Sci.*, 416:177–183, 1998.
- [83] V.M. Polyakov, T. Balster, S. Sloboshanin, F.S. Tautz, H. Ibach, and J.A. Schaefer. Surface state-derived electronic transitions of SiC(001). *Surf. Sci.*, 420:87–94, 1999.
- [84] D. Chen, W.Y. Cheung, and S.P. Wong. Ion beam induced crystallization effect and growth kinetics of buried SiC layers formed by carbon implantation into silicon. *Nucl. Instrum. Methods B*, 148:589–593, 1999.
- [85] W. Widdra, S.I. Yi, C. Huang, and W.H. Weinberg. Coadsorption of hydrogen with ethylene and acetylene on si(100)-(2x1). *J. Chem. Phys.*, 105(13):5605–5617, 1996.
- [86] J. Schmidt, C. Stuhlmann, and H. Ibach. Adsorption and decomposition of diethylsilane and diethyldichlorosilane on Si(100)(2x1) and Si(111)(1x1). *Surf. Sci.*, 302:10–24, 1994.
- [87] J.L. Armstrong, E.D. Pylant, and J.M. White. Thermal chemistry of biacetyl on Si(100). *J. Vac. Sci. Technol. A*, 16(1):123–130, 1998.
- [88] K. Sakamoto, M. Harada, H. Ashima, T. Suzuki, T. Wakita, A. Kasuya, and S. Suto. SiC islands grown on Si(111)-(7x7) and Si(001)-(2x1) surfaces by C<sub>60</sub> precursor. *J. Electron Spectrosc. Rel. Phen.*, 88-91:897–903, 1998.
- [89] K.W. Kolasinski, W. Nessler, A. de Meijere, and E. Hasselbrink. Hydrogen adsorption on and desorption from Si: Considerations on the applicability of detailed balance. *Phys. Rev. B*, 72(9):1356–1359, 1994.
- [90] P. Kratzer, E. Pehlke, M. Scheffler, M.B. Raschke, and U. Höfer. Highly Site-Specific H<sub>2</sub> Adsorption on Vicinal Si(001) Surfaces. *Phys. Rev. Lett.*, 81(25):5596–5599, 1998.
- [91] Y. Bu and M.C. Lin. Interaction of CO with silicon single-crystal surfaces studied by HREELS, UPS and TPD. *Surf. Sci.*, 298:94–100, 1993.

- [92] A.B. Gurevich, B.B. Stefanov, M.K. Weldon, Y.J. Chabal, and K. Raghavachari. Heterogeneous nucleation of oxygen on silicon: Hydroxyl-mediated interdimer coupling on Si(100)-(2x1). *Phys. Rev. B*, 58(20):R13434–R13437, 1998.
- [93] M.K. Weldon, B.B. Stefanov, K. Raghavachari, and Y.J. Chabal. Initial H<sub>2</sub>O-induced oxidation of Si(100)-(2x1). *Phys. Rev. Lett.*, 79(15):2851–2854, 1997.
- [94] F. Meyer. Ellipsometric study of adsorption complexes on silicon. *Surf. Sci.*, 27:107–116, 1971.
- [95] K. Fujiwara. Localized bond model for H<sub>2</sub>O chemisorption on silicon surfaces. *Surf. Sci.*, 108:125–134, 1981.
- [96] D. Schmeisser, F.J. Himpsel, and G. Holliger. Chemisorption of H<sub>2</sub>O on Si(100). *Phys. Rev. B*, 27(12):7813–7816, 1983.
- [97] H. Ibach, H. Wanger, and D. Bruchmann. Dissociative chemisorption of H<sub>2</sub>O on Si(100) and Si(111) - A vibrational study. *Solid State Comm.*, 42(6):457–459, 1982.
- [98] Y.J. Chabal and S.B. Christman. Evidence of dissociation of water on the Si(100)2x1 surface. *Phys. Rev. B*, 29(12):6974–6976, 1984.
- [99] S. Ciraci and H. Wagner. Dissociation of water molecules on Si surfaces. *Phys. Rev. B*, 27(8):5180–5183, 1983.
- [100] L. Andersohn and U Köhler. In situ observation of water adsorption on Si(100) with scanning tunneling microscopy. *Surf. Sci.*, 284:77–90, 1993.
- [101] K. Raghavachari, Y.J. Chabal, and L.M. Struck. Vibrational interactions at surfaces: H<sub>2</sub>O on Si(100). *Chem. Phys. Lett.*, 252:230–235, 1996.
- [102] Y.J. Chabal. Infrared study of the chemisorption of hydrogen and water on vicinal Si(100)2x1 surfaces. *J. Vac. Sci. Technol. A*, 3(3):1448–1451, 1985.
- [103] X.L. Zhou, C.R. Flores, and J.M. White. Adsorption and decomposition of water on Si(100): a TPD and SSIMS study. *Appl. Surf. Sci.*, 62:223–237, 1992.
- [104] Y.K. Sun, D.J. Bonser, and T. Engel. Spatial inhomogeneity and void-growth kinetics in the decomposition of ultrathin oxide overlayers in Si(100). *Phys. Rev. B*, 43(17):14309–14312, 1991.
- [105] T. Sakurai and H.D. Hagstrum. Interplay of the monohydride phase and a newly discovered dihydride phase in chemisorption of H on Si(100)2x1. *Phys. Rev. B*, 14(4):1593–1596, 1976.
- [106] F. Stucki, J.A. Schaefer, J.R. Anderson, G.J. Lapeyre, and W. Göpel. Monohydride and dihydride formation at Si(100)2x1: A high resolution electron energy loss spectroscopy study. *Solid State Comm.*, 47(10):795–801, 1983.

- [107] Y.J. Chabal and K. Raghavachari. Surface infrared study of Si(100)-(2x1)H. *Phys. Rev. Lett.*, 53(3):282–285, 1984.
- [108] U. Höfer, L. Li, and T.F. Heinz. Desorption of hydrogen from Si(100)2x1 at low coverages: The influence of  $\pi$ -bonded dimers in the kinetics. *Phys. Rev. B*, 45(16):9485–9488, 1992.
- [109] W. Widdra, S.I. Yi, R. Maboudian, G.A. Briggs, and W.H. Weinberg. Adsorption, Abstraction, and Pairing of Atomic Hydrogen on Si(100)-(2x1). *Phys. Rev. Lett.*, 74(11):2074–2077, 1995.
- [110] J.J. Boland. Structure of the H-Saturated Si(100) Surface. *Phys. Rev. Lett.*, 65(26):3325–3328, 1990.
- [111] J.E. Northrup. Structure of Si(100)H: Dependence on the H chemical potential. *Phys. Rev. B*, 44(3):1419–1422, 1991.
- [112] Y.J. Chabal and K. Raghavachari. New Ordered Structure for the H-saturated Si(100) Surface: The (3x1) Phase. *Phys. Rev. Lett.*, 54(10):1055–1058, 1985.
- [113] J.J. Boland. Evidence of pairing and its role in the recombinative desorption of hydrogen from the Si(100)-2x1 surface. *Phys. Rev. Lett.*, 67(12):1539–1542, 1991.
- [114] J.J. Boland. *Scanning tunneling microscopy of the interaction of hydrogen with silicon surfaces*. Advances in Physics. New York, USA, 1993.
- [115] C.C. Cheng and J.T. Yates, Jr. H-induced surface restructuring on Si(100): Formation of higher hydrides. *Phys. Rev. B*, 43(5):4041–4045, 1991.
- [116] F.S. Tautz and J.A. Schaefer. Ultimate resolution electron energy loss spectroscopy at H/Si(100) surface. *J. Appl. Phys.*, 84(12):6636–6643, 1998.
- [117] J.H. Kang, S.K. Jo, J. Lee, B. Gong, D. Lim, J.M. White, and J.G. Ekerdt. Molecular hydrogen evolution from bulk crystalline silicon pretreated with thermal hydrogen atoms. *Phys. Rev. B*, 59(20):13170–13175, 1999.
- [118] A. Dinger, C. Lutterloh, and J. Küppers. Kinetic of D abstraction with H atoms from the monodeuteride phase on Si(100) surface. *Chem. Phys. Lett.*, 311:202–208, 1999.
- [119] S.K. Jo, J.H. Kang, X.M. Yan, J.M. White, J.G. Ekerdt, J.W. Keto, and J. Lee. Direct Adsorption of Gas-Phase Atomic Hydrogen by Si(100): A Narrow Temperature Window. *Phys. Rev. Lett.*, 85(10):2144–2147, 2000.
- [120] U. Bischler and E. Bertel. Simple source of atomic hydrogen for ultrahigh vacuum applications. *J. Vac. Sci. Technol. A*, 11(2):458–460, 1992.
- [121] B.N.J. Persson. Vibrational energy and phase relaxation at surfaces. *J. Phys. C*, 17:4741–4750, 1984.

- [122] J.W. Gadzuk and A.C. Luntz. On vibrational lineshapes of adsorbed molecules. *Surf. Sci.*, 144:429–450, 1984.
- [123] P. Jakob, Y.J. Chabal, and K. Raghavachari. Lineshape analysis of the Si-H stretching mode of the ideally H-terminated Si(111) surface: the role of dynamical dipole coupling. *Chem. Phys. Lett.*, 187(3):325–333, 1991.
- [124] J.C. Tully, Y.J. Chabal, K. Raghavachari, J.M. Bowman, and R.R. Lucchese. Infrared linewidths and vibrational lifetimes at surfaces: H on Si(100). *Phys. Rev. B*, 31(2):1184–1186, 1985.
- [125] E.J. Mele, D.C. Allan, O.L. Alerhand, and D.P. di Vincenzo. Phonons in reconstructed silicon surfaces. *J. Vac. Sci. Technol. B*, 3(4):1068–1073, 1985.
- [126] T. Angot, D. Bolmont, and J.J. Koulmann. High resolution electron energy loss spectroscopy study of the Si(001)3x1 hydrogenated surface. *Surf. Sci.*, 352-354:401–406, 1996.
- [127] Y.J. Chabal. Infrared spectroscopy of hydrogen on silicon surfaces. *Physica B*, 170:447–456, 1991.
- [128] W.B. Pollard and G. Lucovsky. Phonons in polysilane alloys. *Phys. Rev. B*, 26(6):3172–3180, 1982.
- [129] M.K. Weldon, K.T. Queeney, A.B. Gurevich, B.B. Stefanov, Y.J. Chabal, and K. Raghavachari. Si-H bending modes as a probe of local chemical structure: Thermal and chemical routes to decomposition of H<sub>2</sub>O on Si(100)-(2x1). *J. Chem. Phys.*, 113(6):2440–2446, 2000.
- [130] D.C. Allan and E.J. Mele. Surface vibrational excitation on Si(001)2x1. *Phys. Rev. Lett.*, 53(8):826–829, 1984.
- [131] D.C. Allan and E.J. Mele. Response of [161]. *Phys. Rev. Lett.*, 57(14):1812–1812, 1986.
- [132] O.L. Alerhand and E.J. Mele. Surface reconstruction and vibrational excitations of Si(001). *Phys. Rev. B*, 35(11):5533–5546, 1987.
- [133] E.J. Mele. Surface phonons and dimer ordering transitions on Si(001) surface. *Surf. Sci.*, 278:L135–L140, 1992.
- [134] A. Mazur and J. Pollmann. Anisotropy of the mean-square displacements at the Si(001)-(2x1) surface. *Surf. Sci.*, 225:72–80, 1990.
- [135] P.C. Weakliem and E.A. Carter. Constant temperature molecular dynamics simulations of Si(100) and Ge(100): Equilibrium structure and short-time behavior. *J. Chem. Phys.*, 96(4):3240–3250, 1992.
- [136] H.M. Tütüncü, S.J. Jenkins, and G.P. Srivastava. Theoretical studies of atomic vibrations on the Si(001)(2x1) surface. *Phys. Rev. B*, 56(8):4656–4664, 1997.

- [137] W. Stigler. *Modellrechnungen zur Struktur und Dynamik von Elementhalbleitern und deren Oberflächen auf der Basis von Ab-initio-Daten*. PhD thesis, Universität Regensburg, 2000.
- [138] W. Stigler, P. Pavone, U. Schröder, J. Fritsch, G. Brusdeylins, T. Wach, and J.P. Toennies. Manifestation of the dimer correlation in the phonon dispersion of Ge(001). *Phys. Rev. Lett.*, 79(6):1090–1093, 1997.
- [139] Y. Taguchi, M. Fujisawa, T. Takaoka, T. Okada, and M. Nishijima. Adsorbed state of benzene on the Si(100) surface: Thermal desorption and electron energy loss spectroscopy studies. *J. Chem. Phys.*, 95(9):6870–6876, 1991.
- [140] Y. Taguchi, Y. Ohta, T. Katsumi, K. Ichikawa, and O. Aita. Photoemission study of benzene adsorbed on Si surfaces. *J. Electron Spectrosc. Rel. Phen.*, 88-91:671–676, 1998.
- [141] B.I. Craig. A theoretical examination of the chemisorption of benzene on Si(100)-(2×1). *Surf. Sci.*, 280(3):L279–L284, 1993.
- [142] P.L. Silvestrelli, F. Ancilotto, and F. Toigo. Adsorption of benzene on Si(100) from first principles. *Phys. Rev. B*, 62(3):1596–1599, 2000.
- [143] H.D. Jeong, S. Ryu, Y.S. Lee, and S. Kim. A semi-empirical study of the chemisorbed state of benzene on Si(100)-(2×1). *Surf. Sci.*, 344(3):L1226–L1230, 1995.
- [144] K.W. Self, R.I. Pelzel, J.H.G. Owen, C. Yan, W. Widdra, and W.H. Weinberg. Scanning tunneling microscopy study of benzene adsorption on Si(100)-(2x1). *J. Vac. Sci. Technol. A*, 16(3):1031–1036, 1998.
- [145] B. Borovsky, M. Krueger, and E. Ganz. Metastable adsorption of benzene on the Si(001) surface. *Phys. Rev. B*, 57(8):R4269–R4272, 1998.
- [146] G.P. Lopinski, D.J. Moffatt, and R.A. Wolkow. Benzene/Si(100): metastable chemisorption and binding state conversion. *Chem. Phys. Lett.*, 282:305–312, 1998.
- [147] G.P. Lopinski, T.M. Fortier, D.J. Moffatt, and R.A. Wolkow. Multiple bonding geometries and binding state conversion of benzene/Si(100). *J. Vac. Sci. Technol. A*, 16(3):1037–42, 1998.
- [148] R.A. Wolkow, G.P. Lopinski, and D.J. Moffatt. Resolving organic molecule-silicon scanning tunneling microscopy features with molecular orbital method. *Surf. Sci.*, 416:L1107–L1113, 1998.
- [149] W.A. Hofer, A.J. Fisher, G.P. Lopinski, and R.A. Wolkow. Adsorption of benzene on Si(100)-(2x1): Adsorption energies and STM image analysis by ab initio methods. *Phys. Rev. B*, 63(8):085314–1/7, 2001.
- [150] U. Birkenheuer, U. Gutdeutsch, and N. Rösch. Geometrical structure of benzene adsorbed on Si(001). *Surf. Sci.*, 409:213–228, 1998.

- [151] S. Gokhale, P. Trischberger, H. Dröge, H.P. Steinrück, U. Gutdeutsch, U. Birkenheuer, N. Rösch, D. Menzel, and W. Widdra. Electronic Structure of Benzene Adsorbed on Single-Domain Si(001)-(2×1): A Combined Experimental and Theoretical Study. *J. Chem. Phys.*, 108(3):5554–5564, 1998.
- [152] M. Staufer, U. Birkenheuer, T. Belling, F. Nörtemann, N. Rösch, K.L. Kostov, T. Moritz, D. Menzel, and W. Widdra. The vibrational Structure of Benzene adsorbed on Si(100). *J. Chem. Phys.*, 112:2498–2506, 2000.
- [153] M.J. Kong, A.V. Teplyakov, J.G. Lyubovitsky, and S.F. Bent. NEXAFS studies of adsorption of benzene on Si(100)-(2×1). *Surf. Sci.*, 411(3):286–293, 1998.
- [154] P. Jakob and D. Menzel. Benzene multilayers: A model for their anisotropic growth from vibrational spectroscopy and thermal desorption. *Surf. Sci.*, 220:70–95, 1989.
- [155] National Institute of Standards and Technology. *Chemistry WebBook*. NIST, <http://webbook.nist.gov/chemistry>, 2002.
- [156] D.R. Bowler, J.H.G. Owen, K. Miki, and G.A.D. Briggs. Diffusion of paired hydrogen on Si(001). *Phys. Rev. B*, 57(15):8790–8793, 1998.
- [157] M.B. Raschke and U. Höfer. Equilibrium and nonequilibrium hydrogen coverages on vicinal Si(001) surfaces: Diffusion barriers and binding energies. *Phys. Rev. B*, 59(4):2783–2789, 1999.
- [158] E. Pehlke and P. Kratzer. Density-functional study of hydrogen chemisorption on Si(001) surfaces. *Phys. Rev. B*, 59(4):2790–2800, 1999.
- [159] Y. Wang and W.H. Weinberg. Ultrahigh-Resolution Electron Energy Loss Spectroscopy via Digital Signal Processing Techniques. *Phys. Rev. Lett.*, 69(23):3326–3329, 1992.
- [160] B.G. Frederick, B.B. Frederick, and N.V. Richardson. Multiple scattering contributions and defining the background for resolution enhancement in HREELS. *Surf. Sci.*, 368:82–95, 1996.
- [161] A. Mazur and J. Pollmann. Surface vibrational excitations on Si(001)-(2×1). *Phys. Rev. Lett.*, 57(14):1811–1812, 1986.



# Publications

- (1) B.Naydenov and W.Widdra, "HREELS study of hydrogen terminated Si(100) surfaces: Dispersion of adsorbate-derived vibrations", in preparation.
- (2) B.Naydenov and W.Widdra, "Surface phonon dispersion on Si(100) surfaces", in preparation.
- (3) B.Naydenov and W.Widdra, "Benzene adsorption on Si(100)-(2×1) surfaces: Vibrational characterization of different chemisorbed phases", in preparation.



# Acknowledgements

To all who have contributed to the successful completion of this work I would like to warmly thank.

First of all I would like to thank to Prof. Dr. D.Menzel for the opportunity to be a member of his excellent scientific group (E-20) with its brilliant humane relations. The state-of-the-art equipment in his laboratories allowed me to enrich my experimental skills. The profound approach of Prof. Menzel to the physical phenomena, demonstrated in the regular seminars of the group, has had a strong pedagogical influence on me.

During my PhD studentship in E-20 I have received a great support and understanding from my supervisor Prof. Dr. W.Widdra. His high motivation and efficiency were very infectious. I had the possibility to be in touch with his versatile knowledge. Prof. Widdra not only efficiently led my experimental work and data analysis but also had an essential tutorial influence on my result representation skill. For all above I would like to heartily thank to Prof. Widdra and express my hope that our successful relations will continue in the future.

The performance of the present PhD work will not be possible without the high-quality education offered in the Semiconductor Physics Department of the Faculty of Physics in the Sofia University. For basics in Surface Science I have to acknowledge Prof. Dr.L.Surnev from the Bulgarian Academy of Science. During my work in his group I have received big support also from Dr. Joro Boishin concerning the specific UHV investigation techniques.

I am thankful to my colleague Thomas Moritz who has shared with me his experience in the HEELS laboratory. I am very obliged to the great experimentalist Prof. Dr. Krasimir Kostov for his useful advices and to the theoretical chemist Dr. G.Vayssilov for the fruitful discussions. Thanks to the diploma student Ingo Schweiger I had a merry-maker in as well as out of the Lab. From the very beginning of my PhD studentship my colleagues Dr. Andreas Fink, Dr. Ralf Romberg, Dr. Andreas Schlapka, Dr. Thomas Niedermayer and engineer Karl Eberle have readily responded to my questions and have involved me in the facilities available in E-20 and this responsiveness has continued during the writing time of this thesis. Special position has my colleague Ruth Weimar with her participation in a symphonic orchestra which concerts have made a great pleasure to me and my family. Irreplaceable help I have had from engineer Max Glanz, Dr. Hartmut Schlichting and Dr. Peter Averkamp in overcoming the appearing computer problems. For the "express" and qualitative crystal polishing and orientation I want to thank to Mrs. Hannelore Eichele. For the expert and often tutorial assistance in the mechanical workshop I want to thank to Mr. Hans Eggstein and Mr. Karl Kölbl.

I am grateful to Dr. Peter Feulner and Dr. Peter Jakob who have always respond to my requests for help concerning experiments and physics. This was especially important for me at

the time when my supervisor have moved to another institute. I can not omit in my acknowledgement the fundamental questions of Prof. Dr. Wilfried Wurth during my seminars and the amazing demonstrations of Prof. Dr. Christian Ucke.

I am obliged to Dr. Ivan Bachvarov and Dr. Veselinka Koch who have put me in touch with Prof. Widdra.

The extraordinary friendly people engineer Norbert Heckmair and family Schindler from Dietersheim have made my life as foreigner in the wonderful Bavaria much more easier. My adaptation in the unknown environment have been strongly supported also by the bulgarian PhD-student group in TU-München. To all of them-warmly thanks.

Special thaks I owe to my parents Georgi and Pasha Markovi for their acceptance of my decision to study physics. In my privat and professional life exclusive is the position of my wife Dr. Izabela Naydenova. As woman and physicist she have ensured an atmosphere of tranquility and understanding which help me to succeed in my present work. I am grateful to my small daughter Pressiana who had to often miss her father at home. I would like to thank to my friends and colleges Rosen and Dimana Nazarovi as well as to my sister Rumiana and her husband Borislav Budinov. Not in the last place I am sincerely obliged to Dr. Georgi and Rosica Tsolovi for their moral and financial support during the difficult time of political transitions in Bulgaria.

I am thankful to Vasilka Stamatova for the emendation of this thesis.